A P P L I C A T I O N S O F B E T A R A Y S P E C T R O S C O P Y

Thesis by

William Frank Hornyak

In Partial Fulfillment of the Requirements

For the Degree of

Doctor of Philosophy

California Institute of Technology

Pasadena, California

1949

ACKNOWLEDGMENTS

It is a pleasure to acknowledge the many helpful suggestions and active assistance of Professor T. Lauritsen in connection with this problem. I am also indebted to Professors C.C. Lauritsen, W.A. Fowler, and R.F. Christy for valuable advice and consultations. This work was assisted by the joint program of the Office of Naval Research and the Atomic Energy Commission.

ABSTRACT

The design procedure is discussed for the construction of a lens type beta ray spectrometer having a large solid angle and capable of focusing electrons with energies up to 20 Mev. The observed performance of the instrument is compared with theory.

The application of beta ray spectroscopy to the energy determination of γ-rays by use of both the photoelectric and Compton effects is considered. The effects of converter thickness and finite instrumental resolution are treated extensively. The analysis of the experimental data, employing these techniques, leads to the determination of excited states in Li^7 at 476.7 ± 0.9 Kev; B^{10} at 713.8 ± 1.3 Kev; Ni^{60} at 1172.4 ± 1.8 and 1330.9 ± 2.1 Kev; and C^{13} at 3092. ± 12 Kev.

The continuous beta spectra from the radioactive elements Li^8, B^{12}, and N^{13} were studied. The upper energy limits for these spectra were determined as 15.8 ± 0.1 Mev, 13.43 ± 0.06 Mev, and 1.202 ± .005 Mev respectively. Experimental evidence is given to show that the beta decay of Li^8 proceeds mainly to a broad excited state at ~ 3 Mev, the transitions to the ground state being estimated at less than 2 percent. Evidence for possible highly excited states in Be^8 and C^{12} is presented and discussed.

TABLE OF CONTENTS

TABLE OF CONTENTS (CONT.)

I. SPECTROMETER DESIGN

General Introduction

Beta ray spectroscopy has proved to be a very useful tool in the investigation of nuclear processes and nuclear structure. In addition to the determination of the electron spectra in the β-decay disintegration of radioactive nuclei the β-ray spectrometer can also be used in the analysis of the secondary electron spectrum arising from the interaction of γ-radiation and matter. Such an analysis can be made to give both the energy and intensity of the γ-radiation. Information concerning the lifetime of certain γ-ray emitting states in nuclei, although of a less precise nature, can also be obtained. The study of internal conversion electrons and pairs as well fall within the scope of investigation of the β-ray spectrometer.

Since for most of the reactions of interest, intensity considerations required a fairly large solid angle, it was decided to construct a lens type spectrometer of the type built by Deutsch, Elliott and Evans[1]. Although the lens type of spectrometer has an ultimate resolution which is inferior to that of the best designed semi-circular instruments, when the main factor in the figure of merit is intensity, the larger solid angles available with lens type spectrometer are in its favor. In this respect also the lens type spectrometer compares favorably with the various double focusing type spectrometers.

In order to obtain the maximum flexibility in the shape of the focusing field, the spectrometer coil was constructed in

four separate units. Thus actually, the field shape may be varied continuously from the thin lens type of Deutsch, Elliott, and Evans through the uniform axial field of Witcher[2] to the "U" shaped field giving minimum spherical aberration discussed by K. Siegbahn[3], by merely adjusting the coil spacings appropriately. No iron was used to form the magnetic fields in this design mainly to avoid the uncertain hysteresis effects inherent in instruments involving iron. Thus an obvious advantage of the air circuit spectrometer is that the focusing coil current is directly proportional to the momentum of the observed particles while for the iron formed magnetic field spectrometer a magnetometer must be used to determine the momentum. The maximum energy electrons that could be focused with the coils most judiciously disposed was set at 20 Mev. With this field configuration protons and alpha particles up to kinetic energies of 250 Kev or deuterons up to 125 Kev could also be focused.

Theoretical Considerations

The theory of the lens type spectrometer has been frequently discussed in the literature, with perhaps the most recent surveys given by Zworykin et al[4], and K. Siegbahn[5]. Only the briefest discussion, mostly for orientation, will be given here. Consider an axially symmetric magnetic field, the axis of symmetry being the Z-axis of Fig. 1a. Let r, θ, and z be the coordinates of an electron sheet S. Then for paraxial rays, the trajectory can be shown to be given by

SPECTROMETER TRAJECTORIES

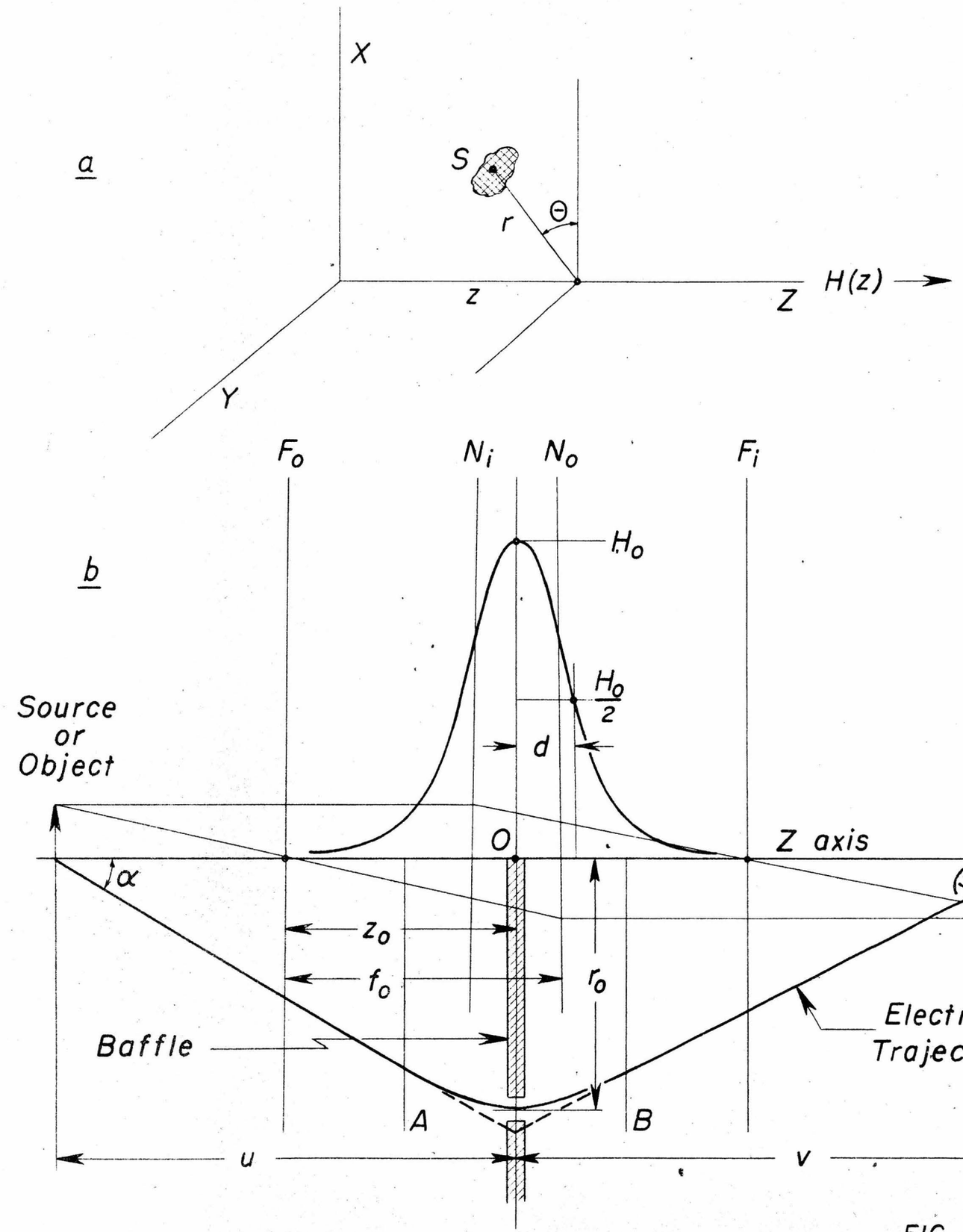

FIG. 1

$$\frac{d^2r}{dz^2} = -\frac{H^2(z)}{4(B\rho)^2} \cdot r \quad * \qquad (1)$$

where $H(z)$ is the magnetic field along the axis at the z coordinate of the sheet and $B\rho$ is the "momentum". The electron sheet is presumed to be monoenergetic.

A typical "thin lens" type arrangement is shown in Fig. 1b. For such configurations the source is located on the Z-axis at a point where the magnetic field is considerably reduced from its peak intensity, such that $u/d \gg 1$ (Fig. 1b). When the magnetic field is set high enough, electrons that pass through the spectrometer baffle opening will again cross the axis after following trajectories somewhat as shown in the figure, the exact path being governed by equation (1).

At this point it may prove instructive to give an approximate solution to eq. (1). Referring to Fig. 1b, planes A and B are located intersecting the Z axis at points where the magnetic field is small compared to its maximum intensity. Integrating equation (1) from plane A to Bthere results

$$\left(\frac{dr}{dz}\right)_B - \left(\frac{dr}{dz}\right)_A = -\frac{1}{4(B\rho)^2} \int_A^B r H^2(z)\, dz \quad , \qquad (2)$$

now under the prevailing conditions r is essentially a constant equal to r_0 in the interval A to B and may be taken outside the integral. Further the limits of integration may be taken as in-

---

* See Appendix I.

definitely large in each extension. Thus equation (2) may be rewritten as

$$\left(\frac{dr}{dz}\right)_B - \left(\frac{dr}{dz}\right)_A \approx -\frac{r_0}{4(B\rho)^2}\int_{-\infty}^{\infty} H^2(z)\,dz \qquad (3)$$

Equation (1) shows that since $H(z)$ is very small in the region from the source to plane A, and from plane B to the image the curvature of the trajectory is small, hence $\left(\frac{dr}{dz}\right)_A \approx \tan\alpha = r_0/u$ and $\left(\frac{dr}{dz}\right)_B \approx \tan\beta \approx -r_0/v$. Then substituting these in equation (3)

$$\frac{1}{u} + \frac{1}{v} \approx \frac{1}{4(B\rho)^2}\int_{-\infty}^{\infty} H^2(z)\,dz \qquad (4)$$

We thus see that this system behaves very much like the optical focusing of a thin lens, where it is customary to write

$$\frac{1}{u} + \frac{1}{v} = \frac{1}{f} \qquad (5)$$

provided one takes the focal length as

$$f = \frac{4(B\rho)^2}{\int_{-\infty}^{\infty} H^2(z)\,dz} \qquad (6)$$

An exact analysis can be carried out for certain field shapes. The field shape typically observed may be approximately fitted by the equation

$$H(z) = \frac{H_0}{\left[1 + (z/a)^2\right]^{\mu}} \qquad (7)$$

where $a = \frac{d}{\sqrt{2^{1/\mu} - 1}}$ and d is the half width at half maximum. With $H(z)$ in this form, equation (1) becomes, letting $X = \frac{z}{a}$

$$\frac{d^2r}{dx^2} = -\frac{H_0^2a^2}{4(B\rho)^2}\frac{r}{(1+x^2)^{2\mu}} = -K_\mu^2\frac{r}{(1+x^2)^{2\mu}} \qquad (8)$$

with $K_\mu^2 = \dfrac{H_0^2a^2}{4(B\rho)^2}$.

This equation has been treated by Glaser[6] for the case $\mu = 1$. As a first approximation when $\mu \neq 1$, substitute $\xi = \sqrt{\mu}\, x$ in equation (8), there results when the right hand side is expanded in a power series

$$\frac{1}{r}\frac{d^2r}{d\xi^2} = -\frac{K_\mu^2}{\mu}\left[1 - 2\xi^2 + \left(2 + \frac{1}{\mu}\right)\xi^4 + \cdots\right] . \qquad (9)$$

Then to the extent that the series inside the brackets is independent of μ this equation is of the same type as obtained with $\mu = 1$. The first approximation then is to take the solution of equation (8) with $\mu = 1$, using for K^2 the value K_μ^2/μ , and using the scale factor implied in the substitution $\xi = \sqrt{\mu}\, x$. The convergence of the series in equation (9) has been discussed by Siegbahm[5]. While the expansions discussed in connection with equation (9) hold only for $\xi < 1$ (Z of the order of d), the region in which $\xi > 1$ is a comparatively weak field region and as equation (1) shows, has a relatively smaller effect in determining the trajectories. It is of particular interest to note the limit which equation (7) approaches as $\mu \to \infty$ and d is held fixed. We take

$$y = \left[1 + \left(\frac{Z}{d}\right)^2\right]^\mu = \left[1 + \left(\frac{Z}{d}\right)^2\left(2^{1/\mu} - 1\right)\right]^\mu$$

and

$$\ln y = \frac{\ln\left[1 + \left(\frac{Z}{d}\right)^2\left(2^{1/\mu} - 1\right)\right]}{1/\mu}$$

Then using L'Hospital's rule

$$\lim_{\mu\to\infty} \ln y = \lim_{\mu\to\infty} \frac{-\dfrac{1}{1+\left(\frac{z}{d}\right)^2\left(2^{1/\mu}-1\right)}\cdot\left(\frac{z}{d}\right)^2 2^{1/\mu}\ln 2\cdot\frac{1}{\mu^2}}{-1/\mu^2}$$

hence $$\lim_{\mu\to\infty} \ln y = \left(z/d\right)^2 \ln 2$$

or $$y = e^{(z/b)^2} \qquad \text{with} \qquad b = \frac{d}{\sqrt{\ln 2}}$$

finally then equation (7) becomes

$$H(z) = H_0 e^{-\left(\frac{z}{b}\right)^2} .$$

Thus with this value of $H(z)$ equation (8) becomes if $x = z/b$ and $K_\infty = \dfrac{H_0^2 b^2}{4(B\rho)^2}$,

$$\frac{1}{r}\frac{d^2 r}{dz^2} = -K_\infty^2 e^{-2x^2} = -K_\infty^2\left[1-2x^2+2x^4+\cdots\right] .$$

Thus again to a first approximation the solution to equation (8) with $\mu = 1$ may be used, here however K_1^2 is replaced by K_∞^2, also noting the difference in the definition of x.

The solution of equation (8) for $\mu = 1$ may be carried out exactly (see Appendix II) giving

$$r = \frac{1}{\sin\omega}\left\{C_1 \sin\left[\left(K_1^2+1\right)^{1/2}\omega\right] + C_2 \cos\left[\left(K_1^2+1\right)^{1/2}\omega\right]\right\} \qquad (10)$$

with $\omega = \arctan x$, $-\pi < \omega < 0$, and C_1 and C_2 arbitrary constants.

The "focal length" which was given approximately by equation (6) as well as the location of the "focal plane", may be determined exactly for the field shape used here. Consider a paraxial ray entering from the left in Fig. 1b at a distance r_0

from the axis. Then for $X \to \infty$, $\omega \to 0$ hence we must take $C_2 = 0$ and $C_1 = \frac{r_0}{(K_1^2+1)^{1/2}}$, where upon equation (10) becomes

$$\frac{r}{r_0} = \frac{\sin\left[(K_1^2+1)^{1/2}\omega\right]}{(K_1^2+1)^{1/2}\sin\omega}, \qquad -\pi < \omega < 0 . \tag{11}$$

Equation (11) has zeros at $(K_1^2+1)^{1/2}\omega = -n\pi$ or

$$\frac{Z_n}{d} = -\operatorname{ctn}\frac{n\pi}{(K_1^2+1)^{1/2}} \qquad n = 1,2,3 \cdots\cdots n_{max} \tag{12}$$

and $n_{max} < (K_1^2+1)^{1/2}$.

In a practical case the baffles are set so that only the first zero is of interest. Then the location of the focal plane from the plane of symmetry (i.e. $Z=0$) is approximately for the general field shape of equation (7)

$$\frac{Z_{1\mu}}{a/\sqrt{\mu}} = -\operatorname{ctn}\frac{\pi}{(K\mu^2/\mu+1)^{1/2}} \tag{13}$$

$$\frac{Z_{1\infty}}{b} = -\operatorname{ctn}\frac{\pi}{(K_\infty^2+1)^{1/2}} .$$

We note that for a thin lens $\left(\frac{K\mu^2}{\mu} \ll 1\right)$, $Z_{1\mu}$ is positive, thus the paraxial rays entering at the left of Fig. 1b are brought to a focus to the right of the plane of symmetry ($Z=0$). As the strength of the lens is increased $Z_{1\mu}$ eventually becomes zero ($\frac{K\mu^2}{\mu} = 3$) and finally becomes negative ($\frac{K\mu^2}{\mu} > 3$). The conditions of equation (12) show that for a thin lens $n_{max} = 1$, and thus paraxial rays cross the lens axis but once, however, as the lens becomes stronger many nodes appear, their number being given by n_{max}.

To find the focal length for paraxial rays we use the analogy with the optical case and take

$$\frac{1}{f_n} = \frac{1}{r_0}\tan\phi = \frac{\left|\frac{dr}{dz}\right|_{z_n}}{r_0} = \frac{1}{d}\sin\frac{n\pi}{(K_1^2+1)^{1/2}} \qquad (14)$$

$$n = 1, 2, 3 \cdots n_{max} < (K_1^2+1)^{1/2}.$$

Thus for $n=1$, the approximate focal length for the general field shape of equation (7) is

$$\frac{f_{1\mu}}{a/\sqrt{\mu}} = \csc\frac{\pi}{(K_\mu^2/\mu+1)^{1/2}}$$

$$\frac{f_{1\infty}}{b} = \csc\frac{\pi}{(K_\infty^2+1)^{1/2}} \qquad (15)$$

Since by inspection of equations (13), and (15) and related equations it is seen that $|f_{n\mu}| > |z_{n\mu}|$ the location of the unit plane which is $z_{n\mu} - f_{n\mu}$, is in all cases negative. Thus the object unit plane is located on the image side of the plane of symmetry (image space) and vice versa even for thin lens case, and in this respect differs from the usual optical case for thin symmetric converging lenses. The location of the unit planes and focal planes is illustrated in Fig. 1b.

For completeness it should be observed that equation (7) substituted into equation (6) gives for $\mu = 1$ to $\mu = \infty$

$$f_{11} = \frac{4(B\rho)^2}{H_0^2 d^2}\cdot\frac{d}{\int_{-\infty}^{\infty}\left[1+\left(\frac{z}{d}\right)^2\right]^{-2}\frac{dz}{d}} = \frac{2d}{\pi K_1^2}$$

$$f_{12} = \frac{4(B\rho)^2}{H_0^2 a^2} \frac{a}{\int_{-\infty}^{\infty} [1 + (z/a)^2]^{-4} \frac{dz}{a}} = \frac{a}{\pi K_2^2} \cdot \frac{16}{5}$$

$$f_{1\mu} = \frac{4(B\rho)^2}{H_0^2 a^2} \frac{a}{\int_{-\infty}^{\infty} [1 + (z/a)^2]^{-2\mu} \frac{dz}{a}} = \frac{a}{\pi K_\mu^2} 2^{4\mu} \frac{(4\mu-1)[(2\mu)!]^2}{4\mu \; (4\mu)!}$$

(16)

$$f_{1\mu} \approx \frac{a}{\pi K_\mu^2} 2\sqrt{\mu} \cdot \sqrt{\frac{\pi}{2}}$$

using Stirling's approximation

$$f_{1\infty} = \frac{4(B\rho)^2}{H_0^2 b^2} \frac{b}{\int_{-\infty}^{\infty} e^{-2(z/b)^2} \frac{dz}{b}} = \frac{2b}{\pi K_\mu^2} \sqrt{\frac{\pi}{2}}$$

While equation (15) when expanded for $\frac{K_\mu^2}{\mu} \ll 1$ (i.e. a thin lens) gives

$$f_{11} = \frac{2d}{\pi K_1^2}$$

$$f_{12} = \frac{a}{\pi K_2^2} 2\sqrt{2} \qquad (17)$$

$$f_{1\mu} = \frac{a}{\pi K_\mu^2} 2\sqrt{2}$$

$$f_{1\infty} = \frac{2b}{\pi K_\infty^2}$$

Thus the focal lengths predicted by equation (15) for a thin lens are too small by a factor

$$\rho = \frac{2^{4\mu-1}}{\sqrt{\mu}} \cdot \frac{4\mu-1}{4\mu} \frac{[(2\mu)!]}{(4\mu)!} \qquad (18)$$

which gives $\rho = 1$ for $\mu = 1$, and rapidly approaches $\sqrt{\frac{\pi}{2}}$ for large μ. While equation (15) is exact for the field shape $\mu = 1$ and is probably a fair approximation for any μ and mod-

erately thick lenses (i.e. u and v comparable to d, since for such lenses the higher powers in the expansion of equation (9) are relatively less important and it is just here that the approximation lies) it would be expected that equations (6) and (16) should be more exact for the thin lens case.

Finally then the thick lens formula to be used is

$$\frac{1}{u + h_{1\mu}} + \frac{1}{v + h_{1\mu}} = \frac{1}{f_{1\mu}} \tag{19}$$

where $h_{1\mu} = f_{1\mu} - z_{1\mu}$ and where u and v are the object and image distances respectively measured from the plane of symmetry (see Fig. 1b). Thus when $u = v$ (unit magnification) the "length" of the spectrometer is

$$L_1 = 2u = 2\,(f_{1\mu} + z_{1\mu}) \tag{20}$$

This last equation may be combined with equations (13) and (15) to give

$$L_{1\mu} = \frac{2a}{\sqrt{\mu}} \tan \frac{\pi}{2(K_\mu^2/\mu + 1)^{1/2}} \tag{21}$$

$$L_{1\infty} = 2b \tan \frac{\pi}{2(K_\infty^2 + 1)^{1/2}}$$

Design Procedure

A. Vacuum Chamber and Accessories

It was decided that for a reasonable field utilization, the best compromise between obtaining of a large solid angle and small aberration was to be had by using a spectrometer vacuum

chamber approximately 10 inches in diameter. Hard drawn brass seamless pump liner having an I.D. = 10,000" and a wall thickness of .148" was commercially available, and was therefore used. A 48" long section of this tubing was used as the "vacuum box" in the series of experiments described later; a shorter length of 36" was also available.

The vacuum in the spectrometer must be hard enough to prevent excessive scattering and energy loss of the electrons being focused. The curve of Fig. 2 gives the collision mean free path for high energy electrons in air as a function of the pressure. It will be observed that to have the mean free path greater than the length of the spectrograph requires a vacuum that is better than 2×10^{-4} mm Hg. A 2" diameter, 2 stage oil diffusion pump backed with a Megavac mechanical fore pump was used to obtain the desired vacuum. In some of the arrangements to be discussed the spectrometer vacuum system was connected to that of an electrostatic accelerator. The diffusion pump was connected directly to the vacuum chamber by a short length of 2" diameter brass tubing (see Fig. 3). The pump down time to obtain a hard vacuum starting with a cold diffusion pump was about 30 minutes. An air lock, see Fig. 3, was provided to permit a rapid change of target or source assemblies, it being but a matter of a few minutes to change sources by this device. The air lock unit was provided with a set of adjusting screws which permitted one to change the position of the source by small amounts to insure its accurate location. The end plate at the source end of the spectrometer contained a 3" diameter lucite window.

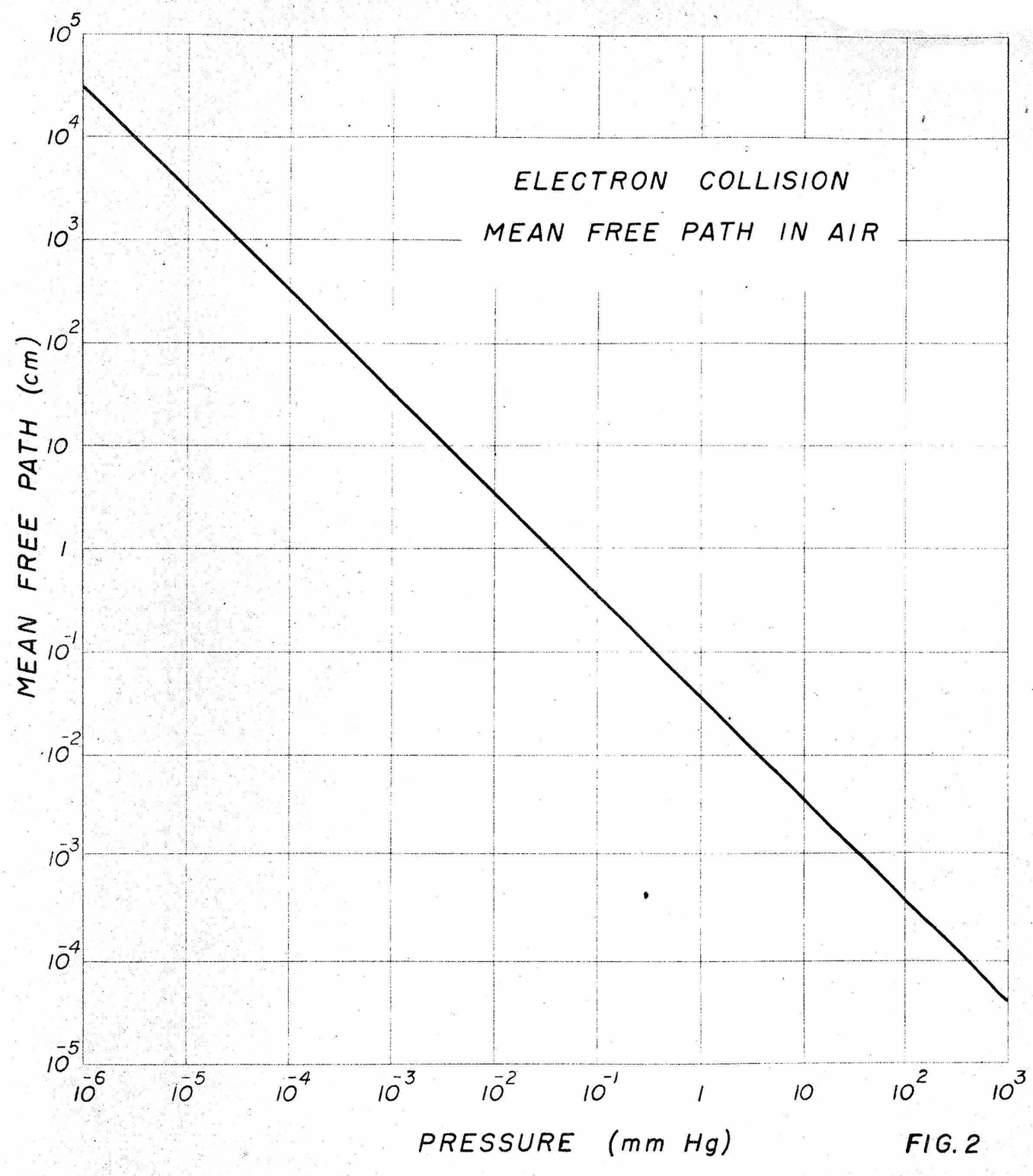
ELECTRON COLLISION
MEAN FREE PATH IN AIR
MEAN FREE PATH (cm)
10^{5}
10^{4}
10^{3}
10^{2}
10
1
10^{-1}
10^{-2}
10^{-3}
10^{-4}
10^{-5}
10^{-6}
10^{-5}
10^{-4}
10^{-3}
10^{-2}
10^{-1}
1
10
10^{2}
10^{3}
PRESSURE (mm Hg)

FIG. 2

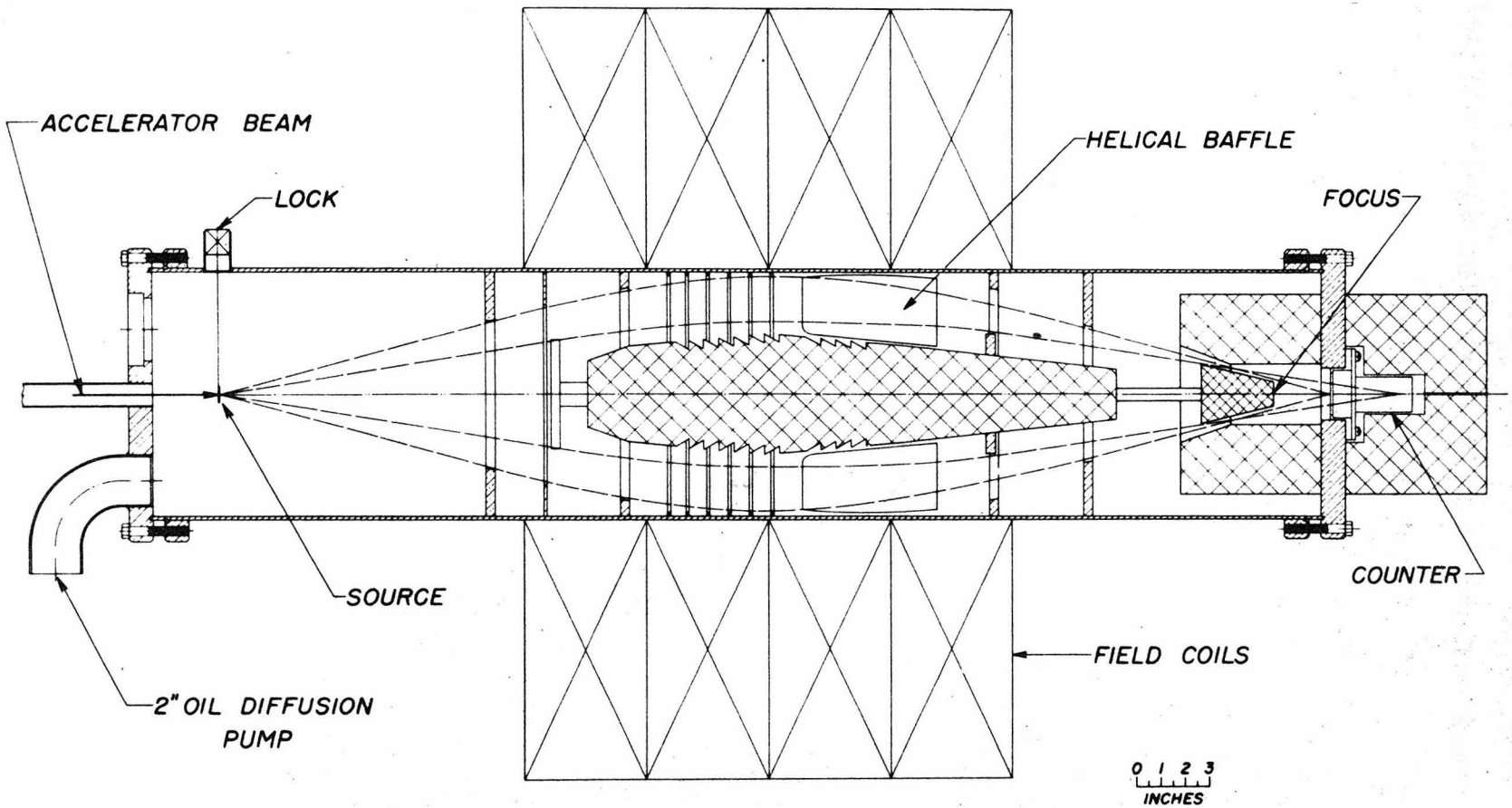
ACCELERATOR BEAM
LOCK
HELICAL BAFFLE
FOCUS
SOURCE
COUNTER
FIELD COILS
2" OIL DIFFUSION PUMP
0 1 2 3
INCHES

FIG. 3

A small wattage bulb was sealed inside the spectrometer which could be used to illuminate the source assembly which in turn was readily visible through the end plate window. A small rod pointer which could be accurately relocated was used to indicate where the target or source center should come. This pointer could be swung into place or moved out of the way through a vacuum seal connection. With the pointer in place the air lock set screws could then be used to align the source.

When the beam of the electrostatic accelerator was brought into the spectrograph to bombard the target in place, the axis of the spectrograph was carefully aligned with the direction of the beam. A small quartz disc with fine copper wire "cross hairs" could be swung into the target position by a lever extension through a vacuum gland. The arm holding the quartz disc and "cross hairs" was mounted on the source end of the center baffle slug. This disc was carefully centered on the spectrometer axis and permanently in place. When the fluorescent spot produced by the beam striking the quartz discs was centered in the cross hairs for both quartz discs, the beam and spectrometer were judged to be coaxial.

B. Focusing Coils

The field coils were constructed in four separate sections as shown in Fig. 3. in order to obtain a high degree of flexibility in shape of the focusing field of the spectrometer. The highest energy electrons will be focused however when the four sections are used as the closest spaced unit, centered midway

between the source and the detecting window. When the obtaining of the maximum converging power of the lens (minimum focal length) is not the prime consideration the coils may be separated and various field shapes can then be achieved. Since the most adverse electrical and thermal conditions arise when the spectrograph is operated at its maximal converging power the design is considered for the case in which the four coils operate as a single unit.

To obtain the highest converging power for the least expenditure of electrical power it is apparent that the axial length of the coil ℓ (see Fig. 4) should be made as long as possible (up to a point $\ell < L$) and that the radii R_{min} and R_{max} should be made as small as possible. Such a configuration will make the best use of the ampere turns in producing useful magnetic fields in the spectrometer itself. The versatility obtained by separating the coils is somewhat enhanced by keeping ℓ substantially smaller than L. In the present design L is fixed at 45 inches and R_{min} at 5.6 inches from the considerations of solid angle and aberrations. With L and R_{min} thus determined a reasonable value for the length of the coil is $\ell \approx L/2$; the actual value of ℓ in this design was taken as 20 inches.

To a fair degree of approximation the field along the coil axis can be represented by:

$$H(z) = H_0 e^{-\frac{z^2}{b^2}} .$$

From which it follows using Ampere's circuital law that

$$\frac{4\pi N i}{10} = \int_{-\infty}^{\infty} H(z)\,dz = H_0 b \sqrt{\pi} \quad , \qquad (22)$$

SCHEMATIC FIELD COIL CROSS-SECTION

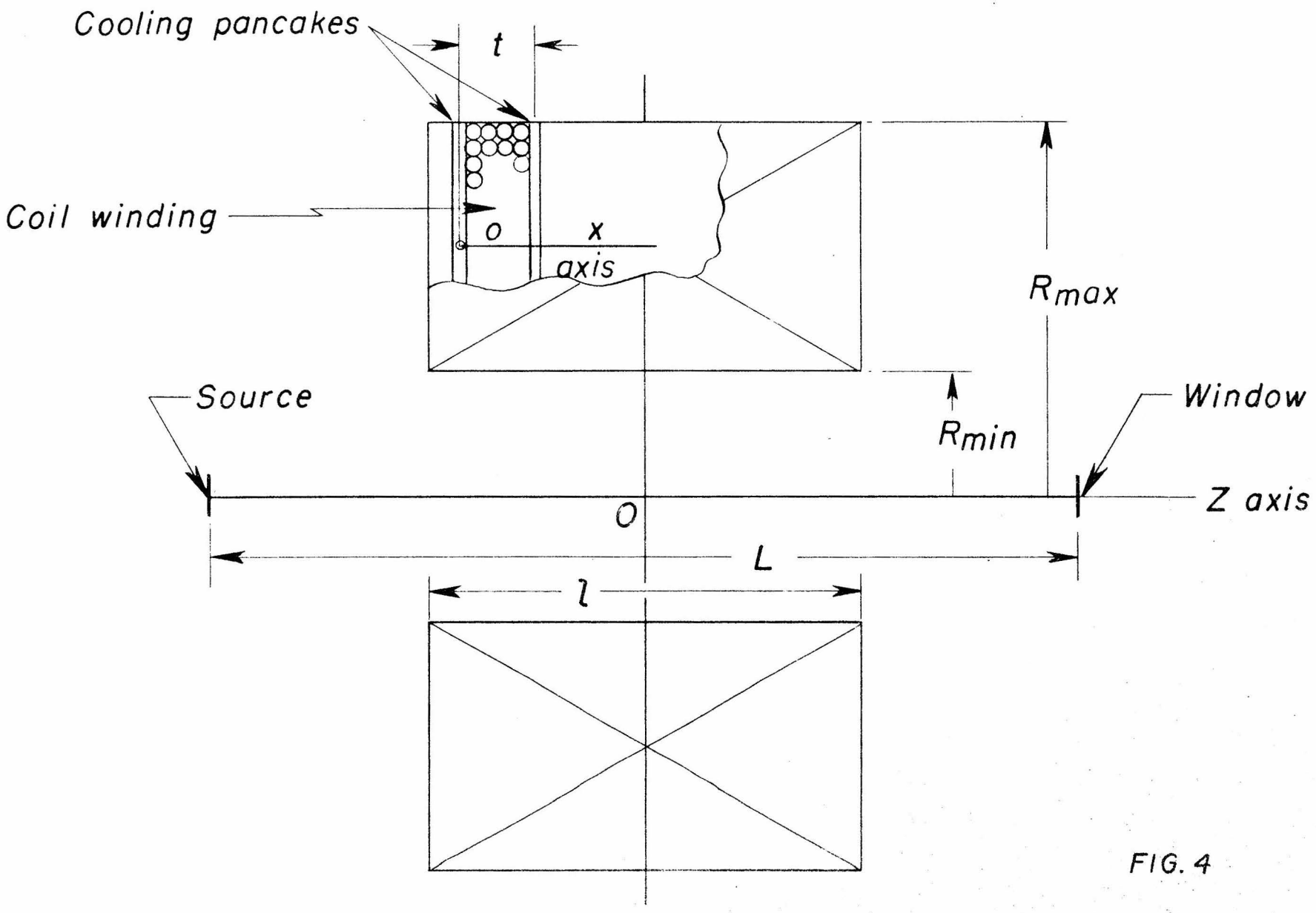

FIG. 4

where N is the total number of turns in the coil and i the coil current in amperes while H_0 is in gauss and b in centimeters. Using the thin lens approximation for unit magnification from equation (6)

$$L = 4f = \frac{16(B\rho)^2}{H_0^2 \int_{-\infty}^{\infty} e^{-2z^2/b^2} dz} = \frac{16(B\rho)^2}{H_0^2 b \sqrt{\frac{\pi}{2}}} . \qquad (23)$$

Combining this equation with equation (22) there results for the total ampere turns required

$$Ni = 10 B\rho \sqrt{\frac{b}{\pi L}} \sqrt{2/\pi} = 4.60 B\rho \sqrt{\frac{d}{L}} \qquad (24)$$

where $d = \frac{b}{\sqrt{\ln 2}}$.

It was proposed to use water cooling in the present design by having cooling pancakes distributed within the coil spaced t inches apart, see Fig. 4. With a current density of j amp/in^2 in the copper wire itself and a coil space factor S (cross sectional area of copper per square inch of the winding) the power generated is:

$$W = S\sigma j^2 \quad \text{watts/in}^3$$

where σ is the resistivity of copper (8.9 x 10^{-7} ohms-in at 100°C). Then approximately (see Fig. 4 for coordinate system)

$$\frac{d^2T}{dx^2} = -\frac{S\sigma}{K} j^2$$

at equilibrium where T is the temperature and K is the effective thermal conductivity for the winding. The temperature distribution within the winding then is:

$$T = -\frac{S\sigma j^2}{2K}(x^2 - xt) + T_0 \qquad (25)$$

and the difference in temperature between the hot spot and the cooling pancake is

$$T_{max} - T_o = \frac{S\rho t^2}{8K} j^2 \quad . \tag{26}$$

The actual difference in temperature will be somewhat greater than this amount when the number of layers of winding between the cooling pancakes is small rather than the continuum of distribution assumed in this treatment. An estimated value of K which was later confirmed by a performance test is $K = 0.01$ watts/in°C for uniformly spaced double cotton covered round copper wire of diameter greater than AWG 12 with some impregnation. Since $S = 0.7$ for such wire, equation (26) gives

$$j \approx \frac{350.}{t} \sqrt{T_{max} - T_o} \quad amps/in^2 \tag{27}$$

with t in inches and $T_{max} - T_o$ in degrees centigrade. With a cooling plate every inch and an 80°C temperature rise to the hot spot, j = 3100 amps/in^2. If the overall coil space factor is ϵ then in the notation of Fig. 4 the ampere turns are given by

$$Ni = \epsilon j \ell \left[R_{max} - R_{min} \right] . \tag{28}$$

Then since $\ell \approx L/2$ and it has been decided to take $\ell \approx \frac{L}{2}$, combining equation (28) with equation (24) gives

$$\epsilon j L \left[R_{max} - R_{min} \right] = 4.60 B\rho \tag{29}$$

Hence since j = 3100 amps/in^2, L = 45 inches, and R_{min} = 5.6 inches a value of ϵ = 0.4 requires that R_{max} = 16.8 inches in

order to focus 20 Mev. electrons (6.8×10^4 gauss-cm.). In the actual design $R_{max} = 15$ inches was used. The total power dissipated is

$$W = \sigma j^2 V = \sigma j^2 \epsilon \pi \ell \left[R_{max}^2 - R_{min}^2 \right] \qquad (30)$$

which corresponds to 46 K.W. under the present design conditions.

With an efficient design of the cooling pancake the temperature T_o should be the mean between the exit and entrance temperature of the cooling water or

$$T_o = \frac{T_{in} + T_{exit}}{2} \qquad (31)$$

Since the value of T_{max} beyond which it is not safe to go is 110°C and since the design was for an 80°C rise, $T_o = 30°C$. With tap water being used for cooling $T_{in} = 15°C$, hence $T_{exit} = 45°C$. Then the rate of flow of water must be

$$F = \frac{W - W_o}{4180 (T_{exit} - T_{in})} \quad liters/sec \qquad (32)$$

with W, the power generated in watts and the temperatures in degrees centigrade and where W_o is the power dissipated by radiation and convection to the air. Under actual performance only 39 K.W. peak power was required instead of the 46 K.W. calculated from equation (30). The dissipation of heat into the air was estimated to be 1 K.W. for the peak heating by using Newton's law of cooling

$$W_o \approx 7.5 \times 10^{-3} (T_s - T_A) \quad watts/in^2 \qquad (33)$$

where T_S and T_A are the surface and room temperatures respectively in degrees centigrade, in the present design $T_S - T_A \approx 30°C$ while the total surface area is approximately 3500 in^2. Thus the rate of flow required under the actual operating conditions is F = 0.30 liters/sec. The water pressure head obtainable in the laboratory was 70 psi. The cooling pancakes were made out or rolled down copper tubing as shown in Fig. 5. Each of the four units of the focusing coil was originally designed to have four cooling pancakes spaced every inch of actual winding. The separate spirals were connected in series on one plate while the pancakes (total of 16) were in turn connected in parallel to lower the water impedance. If necessary a large number of other ways of connecting the spirals and pancakes was available. The net water load for the arrangement used consisted of 16 parallel sections of rolled down 5/16"O.D. copper tubing ($\approx$ 0.110 x 0.300" inside dimensions) each approximately 4 times 33, or 132 feet long.

The pressure head for the required flow through such a system may be readily calculated. The characteristic dimension or mean hydraulic diameter for such tubing is

$$d = \frac{2ab}{a+b} = \frac{2 \times .110 \times .300}{.410} = 0.161''$$

and since the kinematic viscosity ν of water at 30°C is 8.6 x 10^{-6} ft^2/sec, while the flow of 0.3 liters/sec requires a flow velocity of v = 2.9 ft/sec, the Reynolds number R becomes

$$R = \frac{vd}{\nu} = \frac{2.9 \times .161}{8.6 \times 10^{-6} \times 12} = 4.5 \times 10^4.$$

SPECTROGRAPH PARTS
COOLING PLATE ASSEMBLY

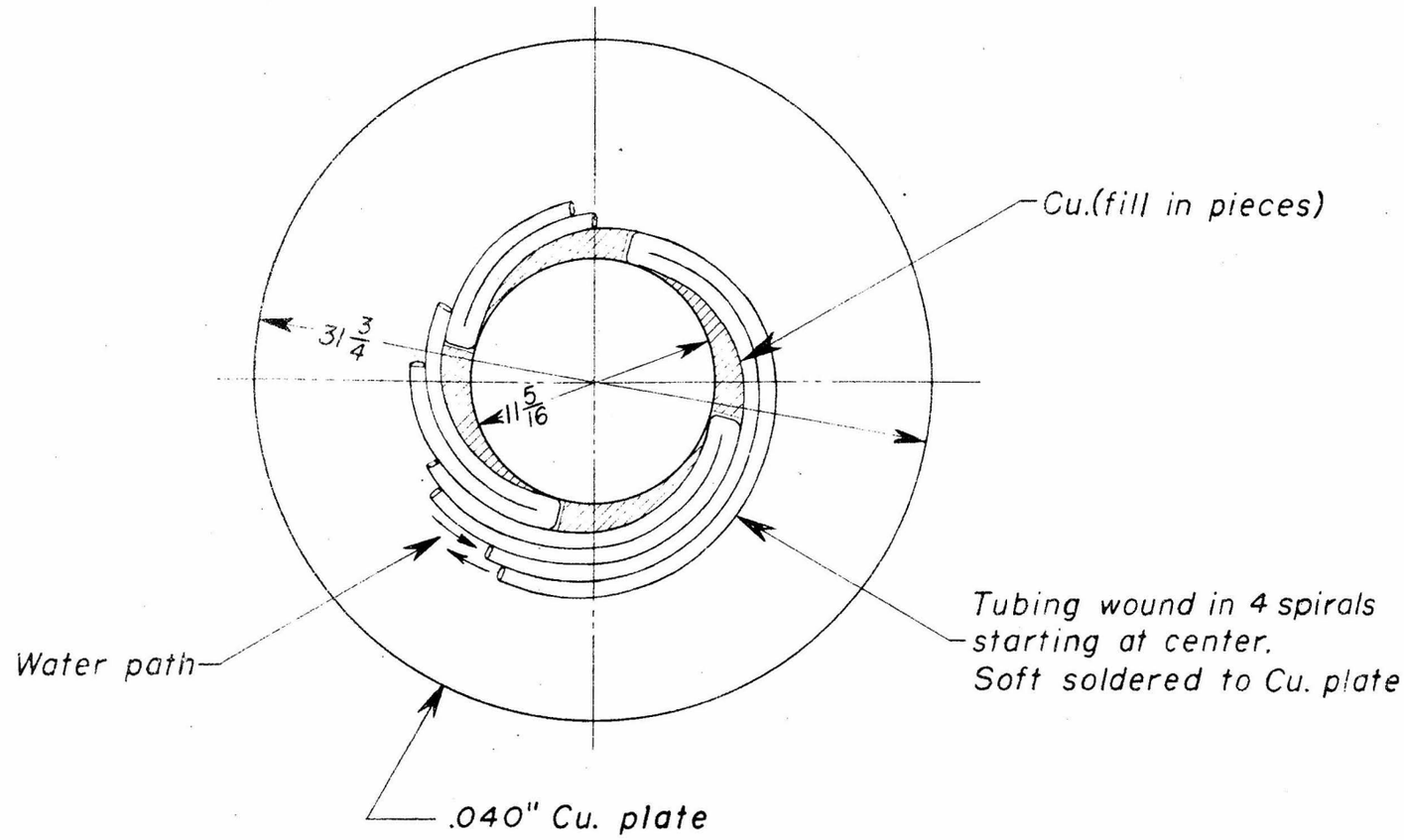

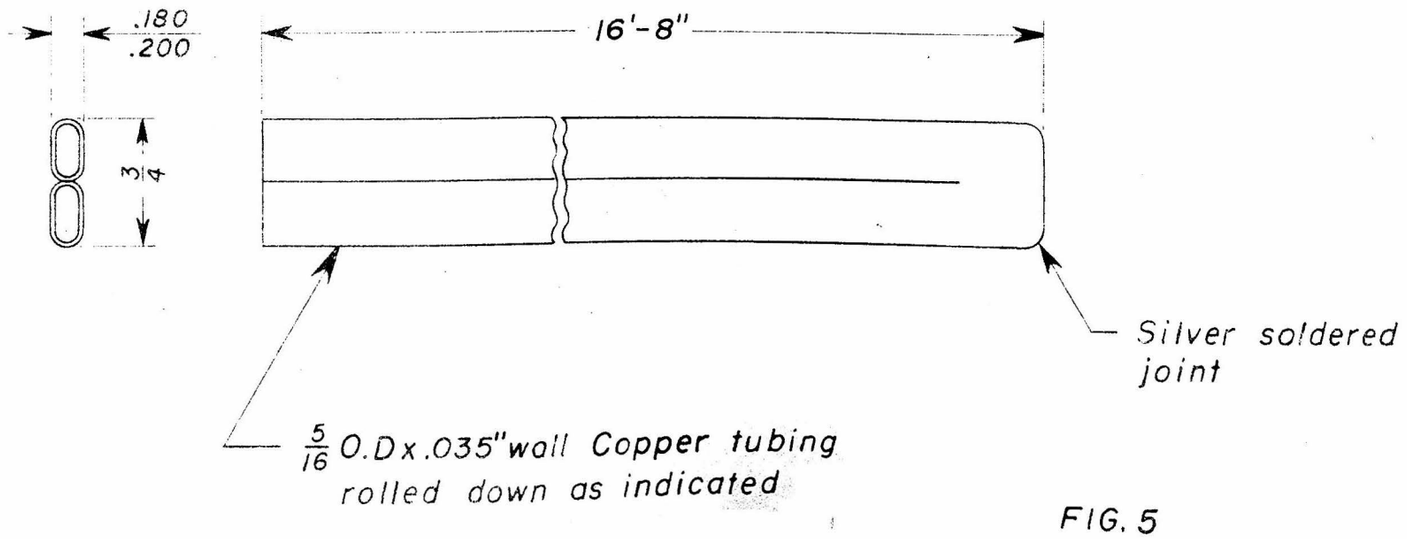

FIG. 5

Since this value is much larger than the critical Reynolds number of 1-2 x 10^3 the flow will be turbulent. From the point of view of getting an efficient cooling system where the pressure head available is large enough so as not to be a limiting factor turbulent flow is desirable. The relationship between the pressure head h in feet of water and the velocity of flow in feet per second is

$$h = \frac{v^2}{2g}\left(1 + \phi_1 + f\frac{l}{d} + \phi_3 + \phi_4\right) + h_o \qquad (34)$$

with h_o = head lost in entrance and exit pipes in feet of water.

g = acceleration of gravity 32.2 ft/sec^2.

ϕ_1 = friction loss in entrance to the tubing $\sim$ 1.

f = friction factor for the tubing.

l = length of tubing.

d = the hydraulic diameter.

ϕ_3 = friction loss at bends $\sim$ 1 per 90° bend.

ϕ_4 = friction loss at valves etc.

The friction factor for smooth pipes and tubing is approximately given by the formula of Blazius

$$f = \frac{.316}{R^{.25}} \qquad (35)$$

or may be obtained from various engineering books[7]. The value of f in the present case is 0.022 while estimates of ϕ_1, ϕ_3, and ϕ_4 are 1, 12, and 5 respectively, and $h_o \approx 15$ feet, thus the head required is h = 46 feet or 20 psi. In the actual construction only one unit had 4 pancakes the other three units

had 3 pancakes each, this load (higher impedance than used in the above calculations) gave a flow rate of .29 liters/sec at a 70 psi head.

A generator capable of delivering 60 K.W. to a load of 1.0 ohm was available to supply the power required. The wire size of the winding could therefore be calculated. It was decided that in addition to having the coil separated into four individual units each such unit should have four sub units, one between each pair of cooling pancakes, with all the electrical connections brought out. Number 6 AWG double cotton covered wire was readily available and proved to satisfy all the requirements. The winding scheme is illustrated in Fig. 6, and had 212 turns per sub unit or 848 turns per unit. The resistance of one half a sub unit is 0.26 ohms at 70°C, hence connecting the two halves of one sub unit in parallel gives 0.13 ohms. Connecting all the subunits then in series gives a total resistance of 2.1 ohms. The copper wire was designed to run at a current density of 3100 amps/in^2 and since the wire cross sectional area is .0206 in^2 this gives a wire current of 65 amps or a generator current of 130 amps. Thus in spite of the impedance mismatch by a factor of two the required current can still be supplied by the generator operating at its rated terminal voltage. While winding the coils, two of them had copper-constantan thermocouple junctions embedded near the expected hot spot region. The 4 subsections of each coil unit were held together by an end plate assembly shown in Fig. 7.

SPECTROGRAPH PARTS
COIL SUB UNIT

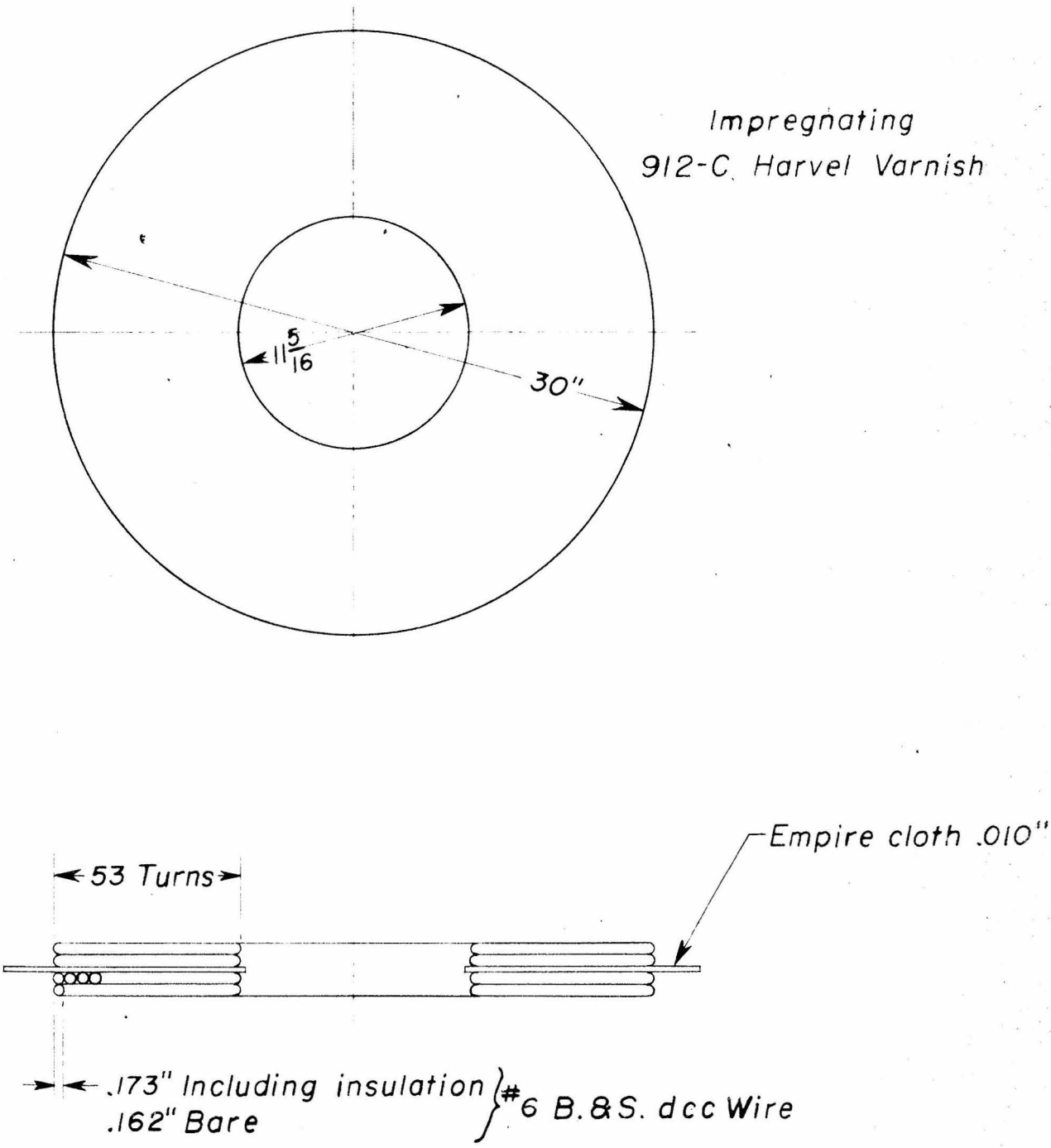

FIG. 6

SPECTROGRAPH PARTS
END PLATE ASSEMBLY

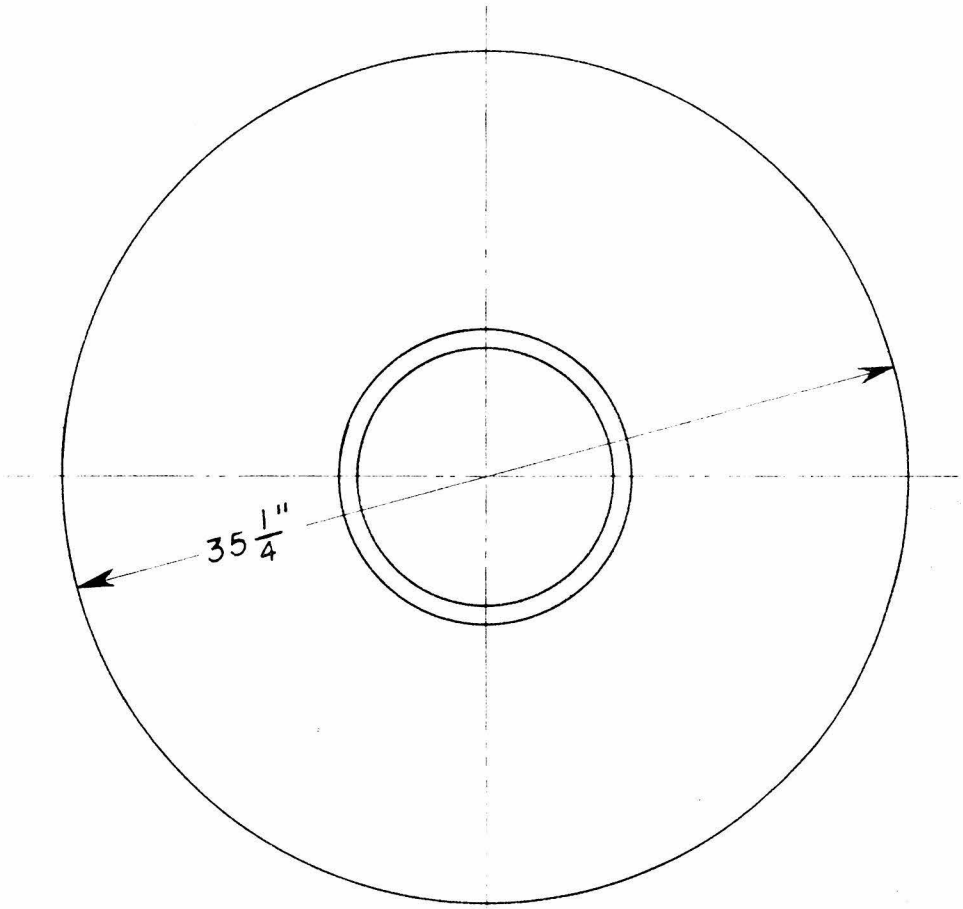

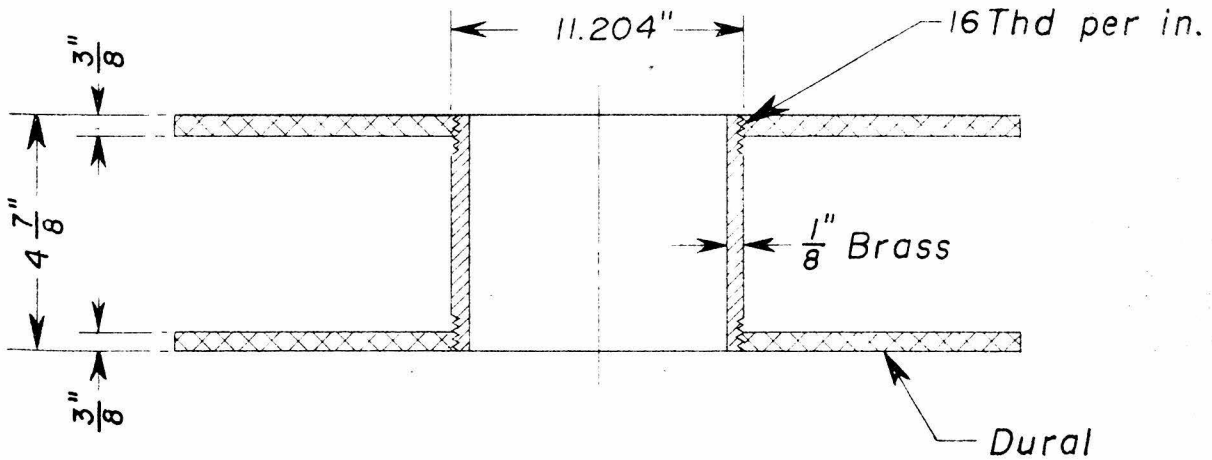

FIG. 7

To protect the coil against the high voltage stresses that would result if its current was inadvertantly interrupted while at a high value, a selenium oxide rectifier was placed directly across the coil with the polarity opposed to the supply voltage and with all the switches beyond the rectifier. Thus if the current from the supply is interrupted the polarity of the rectifier is proper to permit a circulating current to flow between it and the coil until the energy stored in the magnetic field is dissipated.

With the coil connected as described (i.e. paralleled subunits which are all in turn hooked in series), the inductance has been estimated at 0.70 henries. The requirements on the rectifier unit are that it operate at a forward voltage of 250 and block even at an inverse voltage of 250, take a maximum surge current of 130 amperes and dissipate a transient power represented by this peak current flowing for 40 milli-seconds.

The spectrometer coil was supported on a large wooden cradle based on some 4 x 4 beams. The vacuum chamber was also supported by this cradle through four legs which were adjustable in length. The adjustment of these lengths permitted the relative motion of the chamber with respect to the coils. The cradle in turn was supported on a wooden frame, through the agency of four grease pads which had adjusting screws provided to facilitate making small adjustments in the position of the spectrometer as a whole. The frame legs consisted of jacks so that the spectrometer could be raised or lowered and leveled.

C. Baffle System

The spectrometer was provided with a series of baffles to lower the scattering within the vacuum chamber and to aid in defining the desired focused trajectories. A large fluted lead center slug was used to prevent direct radiation from entering the detector window. Various annular stops were provided as illustrated in Fig. 3. Some of these stops were moveable by the agency of rods that extended through vacuum seals. A large set of square wire rings equally spaced were used to line the inside of the vacuum chamber wall near the central region (refer to Fig. 3) principally to lower the wall area "visible" from both the source and the detector window and thus lower scattering. A "paddle wheel" type baffle of the type discussed by Deutsch, Elliott and Evans was provided to select the positrons from the electrons. The fins of this baffle were along the helical paths of the desired trajectories. The pitch of the helical baffle could be adjusted through a vacuum seal. The transmission of this baffle to particles of the proper sign was approximately 70 percent while to those of the opposite sign it was very close to zero.

While it was decided to have the source far away from possible scattering material, a large amount of lead shielding was used around the detector window as shown in Fig. 3. The conical aperture in the large lead shield in conjunction with a small adjustable conical lead plug were used to set the "ring focus". The location of the ring focus was determined experimentally.

D. Detector Unit

A bell jar counter of the type made by the Radiation Counter labs, Chicago, having a 1-1/16 inch diameter 1.5 mg/cm^2 mica window was used. In all the ring focus configurations the full counter aperture was utilized. These counters have a plateau of approximately 200^v and a dead time of the order of 200 μ sec.

The quench circuit used with this counter was of the multivibrator type discussed by Korff[8] and first devised by Getting[9]. This type quench circuit has numerous advantages. Among these may be listed: a low output impedance which enables one to use long leads from the quench unit to the scaling unit; the recovery time of the Geiger tube can be matched by adjusting the circuit time constants; the output pulse is independent of the counter tube characteristics; the quench tubes operate only at normal voltages; the adjusting of the bias on the normally off tube gives a certain amount of discriminator action of the Schmitt type and helps cut down multiples.

A standard scale of 16 scaling circuit of the type designed by Higinbotham at Los Alamos Scientific Lab was used in conjunction with a mechanical counter.

It is perhaps desirable at this point to make a slight digression and review some of the criteria governing counter statistics. With the aid of these criteria and the known magnitude of the statistical errors that can be tolerated proper counting rates and scaling units can be selected.

The derivation in Appendix III has lead to Poisson's law

which gives the probability that precisely N pulses be observed in the time interval t for random pulses having a long time average rate $\bar{n} = \frac{1}{\tau}$. This expression is equation (34) of the Appendix

$$P_N(t) = \frac{t^N e^{-t/\tau}}{N!\,\tau^N} \quad . \tag{36}$$

Consider a source of random pulses with a long time average rate $\bar{n} = \frac{1}{\tau}$ feeding into a perfect scaling circuit of scale N (i.e. for every N pulses into this unit one output pulse appears), the output of which in turn goes to a mechanical counter of dead time t . Then the probability that one or more output pulses in addition to the reference pulse come within the dead time of the mechanical counter is:

$$\Pi = P_N(t) + P_{N+1}(t) + P_{N+2}(t) + \cdots$$

or $$\Pi(t) = e^{-t/\tau} \sum_{j=N}^{\infty} \frac{(t/\tau)^j}{j!}$$

Or if $n_0 = \frac{N}{t}$ is the uniformly spaced pulse rate into the scaler at which the mechanical counter just jams

$$\Pi_N = e^{-\frac{\bar{n}}{n_0}N} \sum_{j=N}^{\infty} \left(\frac{\bar{n}N}{n_0}\right)^j \frac{1}{j!} \quad . \tag{37}$$

This is precisely the formula that comes up in telephone congestion problems[10].

Constant error curves are given in Fig. 8 which illustrate the "smoothing action" of a scale of N circuit. For example, a mechanical counter which just jams at 100 pulses per sec. supplied by an oscillator can count random pulses at a rate of only

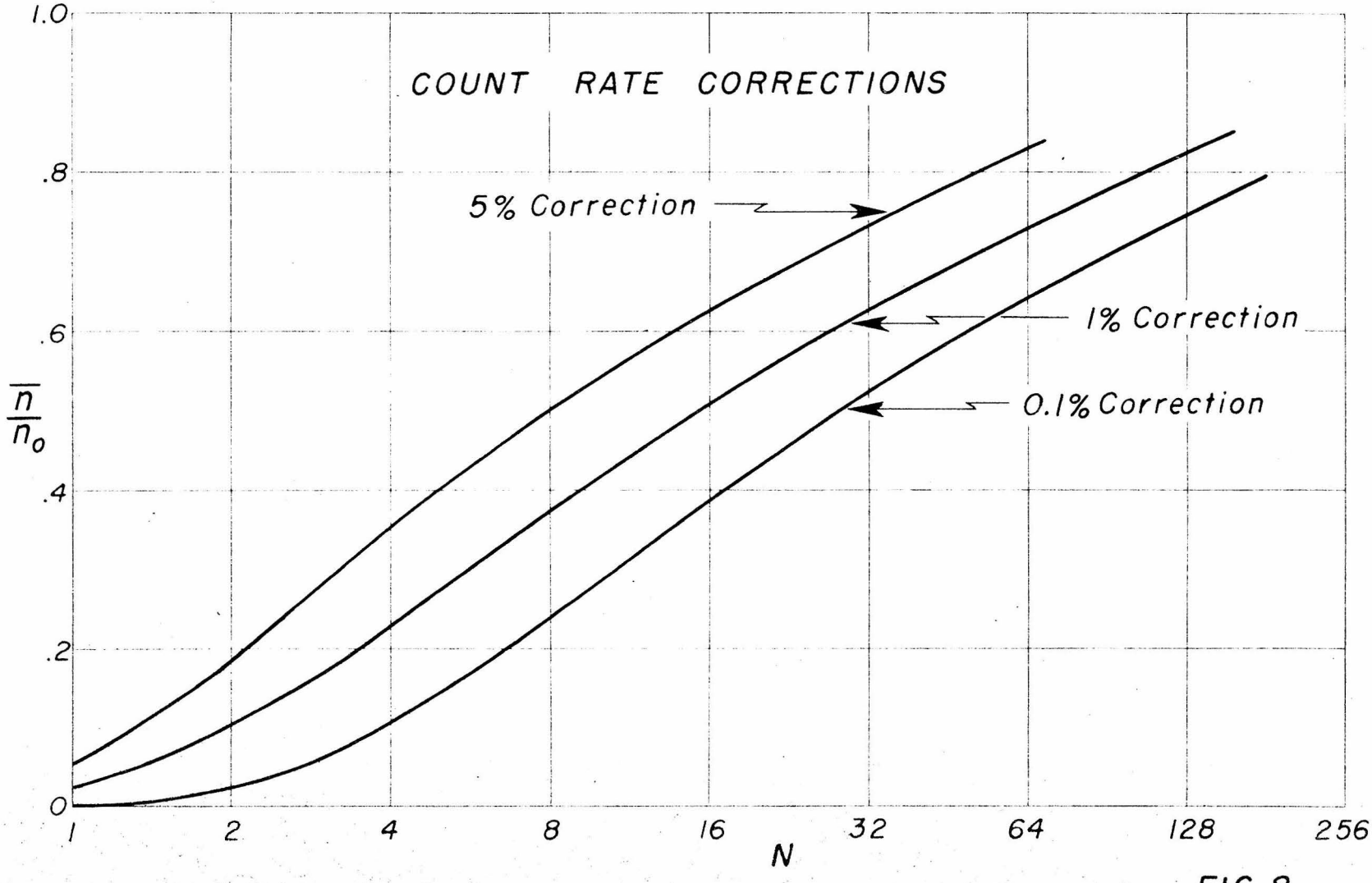
COUNT RATE CORRECTIONS
5% Correction
1% Correction
0.1% Correction
1.0
.8
.6
.4
.2
0
$\frac{n}{n_0}$
1
2
4
8
16
32
64
128
256
N

FIG. 8

1 per sec. for a loss of only 1% in the pulses recorded. If a perfect scale of 4 scaler is inserted between the source of random pulses and the mechanical counter a 1% error in the pulses recorded is not reached until a long time average random count rate into the scaler is .23 x 4 x 100 (see Fig. 8) or 92 counts per sec. Thus by far the largest increase is due to the smoothing of the statistics rather than the obvious factor of 4 gained by the raising of n_0 .

For small N equation (37) is better written as

$$\mathcal{I}_N = 1 - e^{-\frac{\bar{n}}{n_0}N} \sum_{0}^{N-1} \left(\frac{\bar{n}N}{n_0}\right)^j \frac{1}{j!} \qquad (38)$$

for $N = 1$ this just becomes

$$\mathcal{I}_1 = 1 - e^{-\frac{\bar{n}}{n_0}} \quad . \qquad (39)$$

The case of count loss inherent in the geiger counter itself which has a dead time $\frac{1}{n_0} = t_c$ can be treated using equation (39). If the true long time average count rate is $\bar{n}$ the counts lost per unit of time n_m are $\bar{n}\mathcal{I}_1$ or

$$n_m = \bar{n}\left(1 - e^{-\bar{n}t_c}\right)$$

hence the observed count rate n_c is

$$n_c = \bar{n} - n_m = \bar{n}e^{-\bar{n}t_c} \quad . \qquad (40)$$

This enables $\bar{n}$ to be determined when a count rate n_c is observed, if t_c is known. In practice $\bar{n}\,t_c$ is held small compared to unity when equation (40) may be approximated since $n_c \approx \bar{n}$ as,

$$n_c = \bar{n}e^{-\bar{n}t_c} \approx \bar{n}e^{-n_c t_c} \approx \bar{n}(1 - n_c t_c)$$

or finally

$$\bar{n} \approx n_c (1 + n_c t_c) \quad . \tag{41}$$

An interesting method for determining t_c for a geiger counter is the so called "two source method". As the name of the method implies two radio active sources are required; first one source is brought near the counter, the other being at a very large distance, and the observed count rate C_1 is recorded, then the other source is brought near, the position of the first source and counter tube being held fixed and the observed count rate S is recorded, finally the first source is removed to a large distance again keeping the position of the counter tube and remaining source fixed, and the rate C_2 is recorded. Care must be taken that when the two sources are present the presence of one does not change the flux of particles from the other striking the counter by scattering or the additional conversion of γ-radiation in the shield of the other source for example. The natural background in the absence of the two sources B is recorded. Then with N_1 and N_2 being the individual true count rates from sources #1 and #2 respectively, while N_0 is the true background rate we have

$$\begin{aligned} C_1 &= (N_1 + N_0) e^{-t_c (N_1 + N_0)} \\ C_2 &= (N_2 + N_0) e^{-t_c (N_2 + N_0)} \\ S &= (N_1 + N_2 + N_0) e^{-t_c (N_1 + N_2 + N_0)} \\ B &= N_0 e^{-t_c N_0} \quad . \end{aligned} \tag{42}$$

With the count rates such that $(N_1+N_2+N_0)t_c \ll 1$ we have approximately

$$\begin{aligned} C_1 &\approx N_1+N_0-t_c(N_1+N_0)^2 \\ C_2 &\approx N_2+N_0-t_c(N_2+N_0)^2 \\ S &\approx N_1+N_2+N_0-t_c(N_1+N_2+N_0)^2 \\ B &\approx N_0-t_cN_0^2 \end{aligned} \tag{43}$$

$$\therefore C_1+C_2-S-B = t_c\left[(N_1+N_2+N_0)^2+N_0^2-(N_1+N_0)^2-(N_2+N_0)^2\right]$$
$$\approx t_c\left(S^2+B^2-C_1^2-C_2^2\right)$$

or finally

$$t_c \approx \frac{C_1+C_2-S-B}{S^2+B^2-C_1^2-C_2^2} \quad . \tag{44}$$

In general, very good statistics must be obtained in determining the various rates since as formula (44) shows the small differences between these rates are the important factors. This method gave a dead time of some 200 μsec for the bell jar counters used throughout the experiments to be described. Estimates of the desired rates on the counter showed that a scale of 16 was adequate to reduce the errors in mechanical recording to a negligible quantity.

E. Stray Field Compensation

The spectrometer axis was along the magnetic meridian. Thus only the vertical component of the earth's field, which was measured as 0.3 ± 0.1 gauss, was effective in producing a defocusing action. Various arrangements were used to compensate this component of the earth's field; in the final version

a pair of large frame rectangular coils 46" x 88" suspended in parallel horizontal planes symmetricallyplaced with respect to the spectrometer and separated by 31" was used. Fields up to several gauss could be produced in the center of the coils. When the electrostatic accelerator beam was brought into the spectrometer a large analyzing and deflecting magnet some 7 feet from the spectrometer had to be used, which produced a stray horizontal field roughly the order of the .1-.5 gauss. A set of large frame coils 41" x 60" separated 37" symmetrically placed was used to compensate this field.

The remaining component of the earth's field which was along the axis of the spectrometer required that a slight correction be made for the spectrometer momentum calibration. This point will be discussed later.

General Performance and Comparison with Theory

The magnetic field shape was calculated for the centered coil configuration using the expression

$$\frac{H_0}{i} = \frac{2\pi n}{10}\left[\left(z+\frac{\ell}{2}\right)\ln\left\{\frac{a_2+\left|a_2^2+\left(z+\frac{\ell}{2}\right)^2\right|^{1/2}}{a_1+\left|a_1^2+\left(z+\frac{\ell}{2}\right)^2\right|^{1/2}}\right\}-\left(z-\frac{\ell}{2}\right)\ln\left\{\frac{a_2+\left|a_2^2+\left(z-\frac{\ell}{2}\right)^2\right|^{1/2}}{a_1+\left|a_1^2+\left(z-\frac{\ell}{2}\right)^2\right|^{1/2}}\right\}\right] \quad (45)$$

where $n = \dfrac{N}{\ell(a_2-a_1)}$

N = total number of turns = 3390

ℓ = length of coil = 20.0"

a_1 = minimum radius, previously called R_{min} = 5.7"

a_2 = maximum radius, previously called R_{max} = 15.0"

z = distance along the axis from the center of the coil, as before.

i = the coil wire current, one half of the supply generator current for the electrical connections used.

This expression is exact for a rectangular cross section coil as shown by Deutsch, Elliott and Evans[1]. The half width at half maximum is 10.4" and the value of H_o is 65.0 gauss per ampere. The field shape is plotted in Fig. 9 as well as the approximations for $\mu = 1$ and $\mu = \infty$. It will be seen that the Gaussian fit ($\mu = \infty$) gives a fairly good match in the region where the field is intense. The use of equation (22) gives $\frac{H_o}{i}$ = 76 guass/amp for $b = \frac{10.4}{\sqrt{\ln 2}}$ = 12.5", which is not greatly in error and indicates the reliability of such design calculations.

A series of experiments was done in which the point focus was used, the opening in front of the counter window being $\frac{1}{4}$" in diameter. The shield in which the window was cut was movable through a vacuum seal, thus the source to detector window could be changed by small amounts. A stop was placed in the center of the spectrometer which permitted three narrow zones that were cut in this stop to illuminate the detector window, the zones were $\frac{1}{4}$" in radial extent and had mean radii of 2.62", 3.88", and 4.87". The source consisted of a thin deposit of $Th\,B$ on a .0005" Al foil. The generator supply currents required to focus the "F" line ($B\rho$ = 1385) are tabulated in Table A; the resolution was $\sim$ 2%.

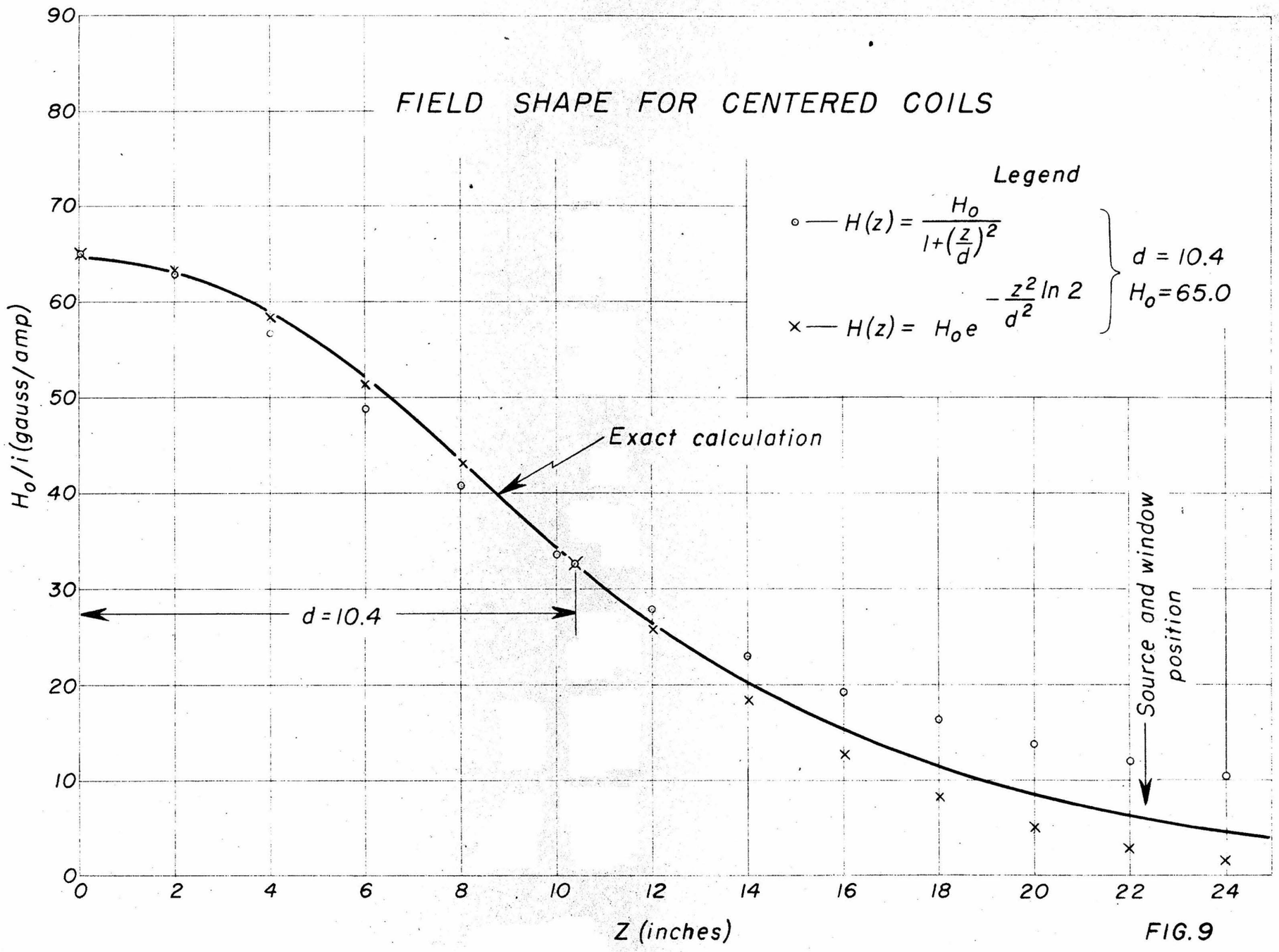
FIELD SHAPE FOR CENTERED COILS
Legend
$\circ$ — $H(z) = \frac{H_0}{1+(\frac{z}{d})^2}$
$\times$ — $H(z) = H_0 e^{-\frac{z^2}{d^2} \ln 2}$
$d = 10.4$
$H_0 = 65.0$
Exact calculation
d = 10.4
Source and window position
H_0/i (gauss/amp)
Z (inches)
0
10
20
30
40
50
60
70
80
90
0
2
4
6
8
10
12
14
16
18
20
22
24

FIG. 9

TABLE A

Zone Mean Radius	Source to Window Distance		
	42.5"	43.5"	44.5" (Normal)
4.87"	----	3.035	2.998
3.88"	3.178	3.142	3.095
2.62"	3.285	3.240	3.195
zero extrapolation	3.358	3.319	3.272

The use of equation (21) permits the prediction of the generator current to focus the ThB-F line. For the source to window distance of 44.5" and d = 10.4" (see Fig. 9) the value of K_∞ is 1.095 which corresponds to a focusing field of H_0 = 95.7 gauss for the F line. This focusing field requires a coil current of 1.48 amperes and a generator current twice this or 2.96 amps., this is to be compared to the zero extrapolated value of the observed currents of 3.27 amperes.

It is of some interest to plot the trajectory for paraxial rays in the present configuration as predicted by equation (10). With the value K_∞ = 1.095 the curve of Fig. 10 results, where for comparison the trajectory for paraxial rays in a uniform field is also given. The values of ξ given on the figure, namely ξ = 1.26 and $\frac{\pi}{2}$, for the centered coils and the uniform field respectively, represent the extrapolation of the initial trajectories to the plane of symmetry of the spectrometer as $z = 0$ (see Fig. 1).

Equation (20) of Appendix I given below for convenience

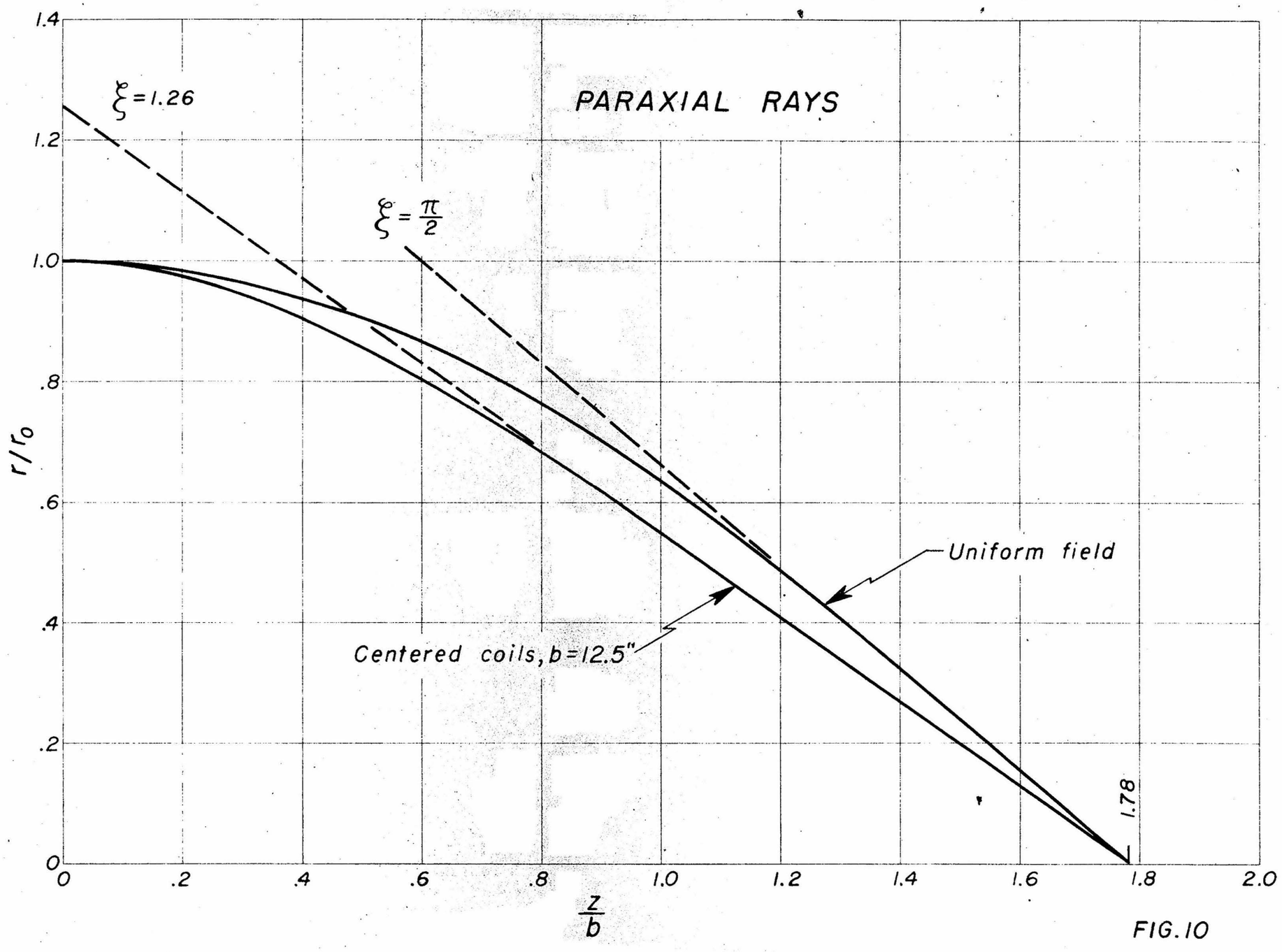
PARAXIAL RAYS
$\xi = 1.26$
$\xi = \frac{\pi}{2}$
Uniform field
Centered coils, b=12.5"
1.78
r/r₀
z/b
0
.2
.4
.6
.8
1.0
1.2
1.4
1.6
1.8
2.0

FIG. 10

$$\frac{\Delta i}{i} = -\frac{r_0^2}{b^2}\left[\frac{b}{L\sqrt{\pi}} + \frac{1}{4}\right], \qquad (46)$$

gives the change in focusing current caused by the aberrations for a mean zone radius r_0. Since this expression was derived for the thin lens case more appropriately r_0 should be replaced by Σr_0, then if i_0 is the focusing current for paraxial rays (i.e. $r_0 = 0$) then the focusing current i for a general ray will be

$$i \approx i_0\left(1 - \frac{\Sigma^2 r_0^2}{b^2}\left[\frac{b}{L\sqrt{\pi}} + \frac{1}{4}\right]\right). \qquad (47)$$

The data presented in Table A has been plotted in Fig. 11, showing the focusing current required for a given zone r_0 as a function of r_0^2, with the source to window distance L as a parameter. The approximation to the curves by straight lines as predicted by equation (47) is seen to be quite satisfactory. The slope divided by the y-intercept of the line for $L = 44.5"$ is from Fig. 11 — .00354 in^{-2} while the value predicted by equation (47) is — .00415 in^{-2}.

The variation of focal current with the source to window distance L can be obtained from equation (21) which for $\mu = \infty$ becomes

$$\frac{dL_{/\infty}}{di} = -\frac{\pi b K_\infty}{(K_\infty^2+1)^{3/2}} \sec\frac{\pi}{2(K_\infty^2+1)^{1/2}} \cdot \frac{dK_\infty}{di} \qquad (48)$$

Using the value of $K_\infty = 1.095$ there results $\frac{dL}{di} = 16.2$ inches per ampere of generator current while from Table A the observed variation is $\sim$ 21"/amp.

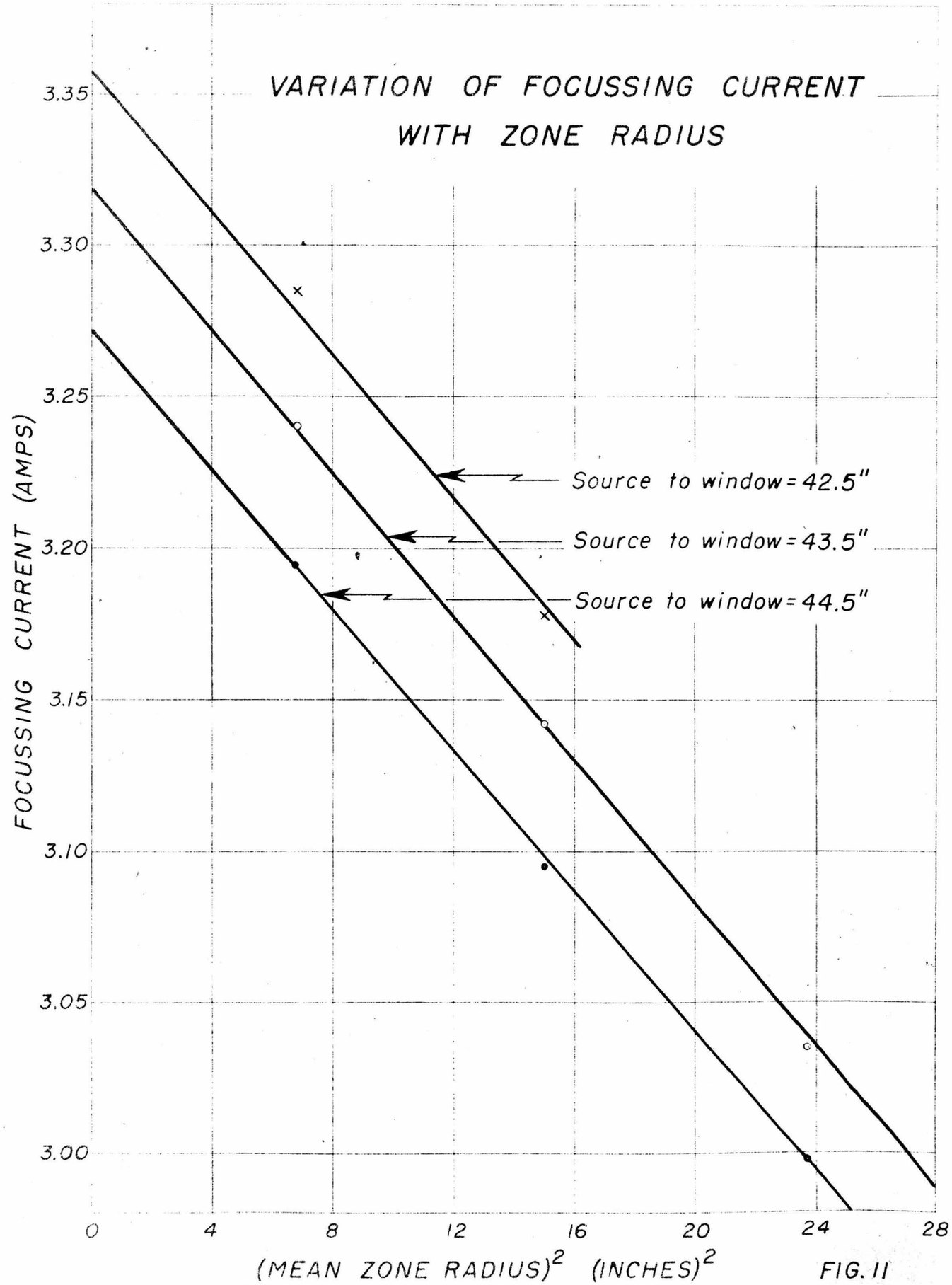
VARIATION OF FOCUSSING CURRENT
WITH ZONE RADIUS
FOCUSSING CURRENT (AMPS)
3.35
3.30
3.25
3.20
3.15
3.10
3.05
3.00
Source to window = 42.5"
Source to window = 43.5"
Source to window = 44.5"
0
4
8
12
16
20
24
28
(MEAN ZONE RADIUS)² (INCHES)²

FIG. 11

The data presented in Table A can also be used to determine the location of the "ring focus" stop. The crossover points on the axis for the various zonal rays at the current setting which just focuses the outer zone rays at 44.5" from the source as well as the approximate trajectories based on equation (10) are shown in Fig. 12. The relative location of the bell jar geiger counter and its window is also illustrated. The actual lead stops are not shown in this figure, but may be seen on Fig. 3.

As a matter of interest the equivalent optical lens for the centered coil arrangement has been calculated, using the equations in Drude[11]. In the present notation

$$f_{1\mu} = \frac{n}{2(n-1)} \frac{r^2}{nr - d(n-1)}$$
$$z_{1\mu} = d + f_{1\mu} - \frac{rd}{nr - d(n-1)} \qquad (49)$$

where n is the index of refraction and r is the radius of curvature of the lens surface (taken as symmetric) with d the half axial lens thickness (taken as the half width at half maximum of the axial magnetic field). The result of these calculations is shown in Fig. 13 for $\mu = \infty$ and $d = 10.4"$, and $K_\infty = 1.095$. The index of refraction becomes $n = 1.48$, while the radius of curvature is $r = 5.67"$. The pertinent dimensions are given on the figure.

The resolution obtained for the centered coil and ring focus arrangement was adjustable; however, the best overall performance was at 1.47 percent resolution, the corresponding solid angle being estimated at 0.5 percent of a sphere. The mean acceptance angle of the spectrometer for this configuration was

SPECTROMETER TRAJECTORIES

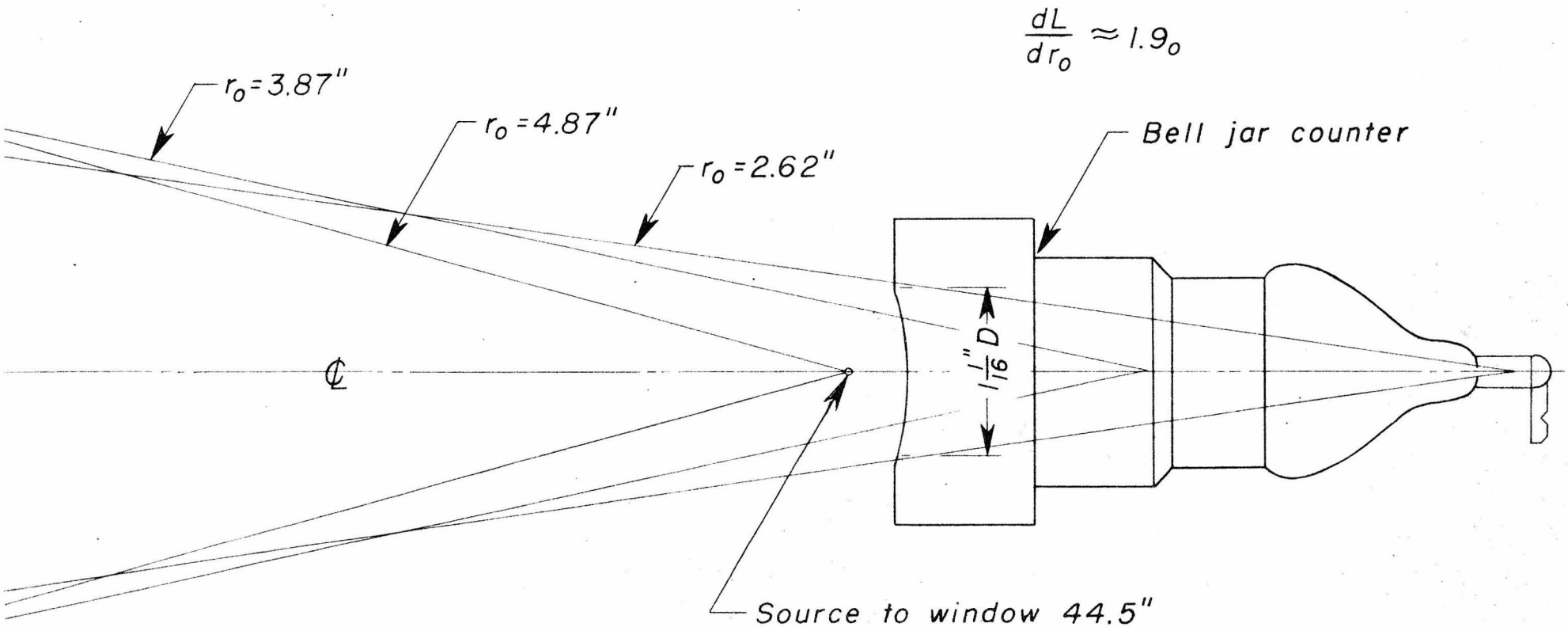

Scale 1=1

FIG. 12

EQUIVALENT OPTICAL LENS

$$\frac{1}{u+7.06} + \frac{1}{v+7.06} = \frac{1}{14.65}$$

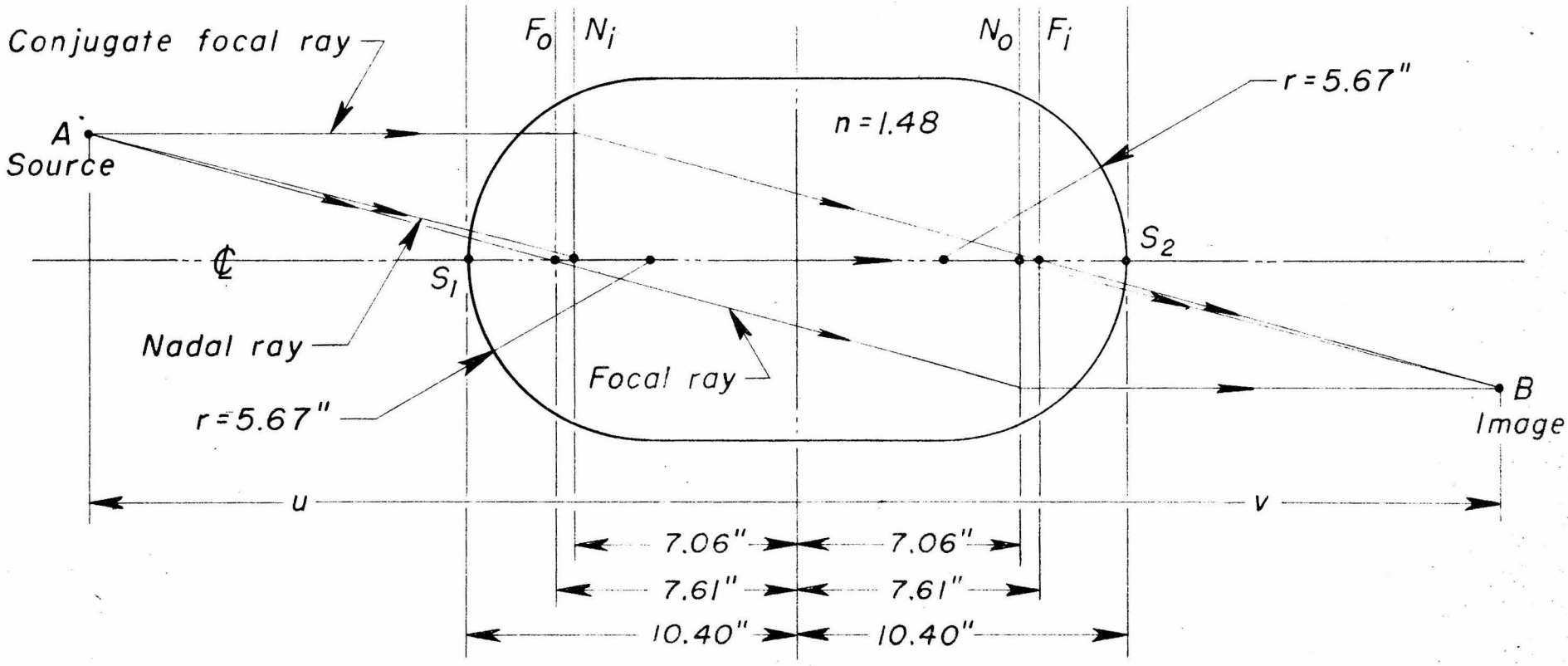

FIG. 13

13°. The observed resolution consists partly of the spread produced by the source size and partly of the smearing caused by the spectrometer aperture geometry. The spread produced by the source for the thin lens approximation has been estimated by Cosslett[12] and Deutsch, Elliott and Evans and is given by the expression

$$\frac{\Delta(B\rho)}{B\rho} \approx \frac{S}{4\xi r_0} \qquad (50)$$

where S is the source radius and r_0 is the mean zonal radius. The usual internal conversion source used was .090" in radius which with r_0 = 4.0" makes the source contribution $\sim$ .45%, which means that most of the spread was produced by the instrument itself. A more detailed discussion of the effect of source size and instrument spread has been given by DuMond[13] and Persico[14] as well as Deutsch, Elliott, and Evans. In addition to the centered coil configuration, experiments with the coils separated into two groups with various separations have been tried. Such configurations generally give a larger ratio of solid angle to resolution, by observed increases as much as a factor of 5. The maximum energy electrons which can be focused is considerably reduced, by as much as a factor of 2 for an extreme case. In general the alignment of the spectrometer becomes more critical and the source centering must be done very precisely.

It will be seen (see equations (1), (8), and related equations) that for a fixed spectrometer stop geometry, source to window distance, and a given field shape, K_μ is determined and

hence the focusing current (through H_0) must be proportional to the $B\rho$ of the focused electrons. In fact the focusing current will be proportional to $B\rho$ for any field shape provided only that H_0 be strictly proportional to the focusing current. This is a great advantage of spectrometers not employing magnetic substances. The focusing current was determined by measuring the milli-volt drop across one of a set of carefully inter-calibrated manganin shunts. The inter-calibration of the shunts was better than 0.05%. The shunt drop was measured with a type K-Leeds and Northrup potentiometer. The output of the potentiometer in addition to being indicated on a sensitive galvanometer was also used to supply a signal to the current regulator. The potentiometer output was transformed into a square wave by interruption at alow signal level employing a Western Electric sealed pressure relay. This square wave signal was amplified by approximately 100 db and was used to control the output of a $\frac{1}{2}$ K.W. amplidyne through a phase sensitive push pull amplifier stage using $6L6's$. The amplidyne output in turn controlled the field of the 60 K.W. generator supplying the spectrometer current. Appropriate feedback was used in the amplifier to improve the stability. The spectrometer current was thus held to better than 2 parts in 10,000 on the average.*

---

* I am particularly indebted to C. Dougherty, W. Gibbs, and G. Downs for the design and construction of the regulating circuit.

II. GAMMA RAY ENERGY DETERMINATIONS USING THE PHOTOELECTRIC EFFECT

General Introduction

A method which has become widely used in the determination of γ -ray energies and intensities is the study of the secondary electron and positron spectra that γ -rays give rise to when they are allowed to irradiate foils of various materials. Of these secondary processes the photoelectric effect is in principle perhaps the most suitable since it produces electron lines of intrinsically high homogeneity in momentum. To utilize this effect it is necessary to make use of an instrument of fairly high resolution such as is available in the various forms of β -ray spectrographs. Intensity considerations then lead to the use of foils consisting of high atomic number elements and having thicknesses large enough to require a consideration of the scattering and energy loss suffered by the photo conversion electrons in emerging from the foil. Even at best, however, the use of the photoelectric effect is limited to γ -rays having energies less than 4 Mev or so; both because of the unfavorably small cross sections at the higher energies and because of the increasing difficulty in resolving the photo electric lines from the Compton effect electrons.

When monochromatic energy γ -radiation irradiates a thin foil a certain amount of photo electric conversion of the γ -radiation throughout the volume of the foil takes place. One

such process is illustrated schematically in Fig. 14 as taking place at point b within the foil. The photo electron so produced will then emerge from the foil at some point c after having followed a path $\underline{bc}$ which will depend on the initial direction of emission of the electron and the amount of scattering it experiences along the path. If the γ -ray source and the converter are imagined to be discs placed concentrically with the axis of a lens type β -ray spectrograph and further if for the given magnetic field setting of the spectrograph the emergent electron has both the proper momentum and a trajectory that emerges at an angle θ_o with the spectrograph axis which is within the angular acceptance of the instrument it will be detected. The spectrum of the electrons from the converter as a function of the momentum (i.e. a function of the magnetic field setting of the spectrometer) can then be obtained. The result may be somewhat as illustrated in Fig. 15. The line shape will depend on a number of important factors listed below:

a. Nature of γ -Ray Sources.

b. The Photoelectric Conversion Process.

c. Source and Converter Geometry.

d. Scattering of Electrons in the Converter.

e. Straggling and Energy Loss for Electrons Emerging from the Converter.

f. Instrumental Resolution.

SCHEMATIC DRAWING OF SOURCE ASSEMBLY

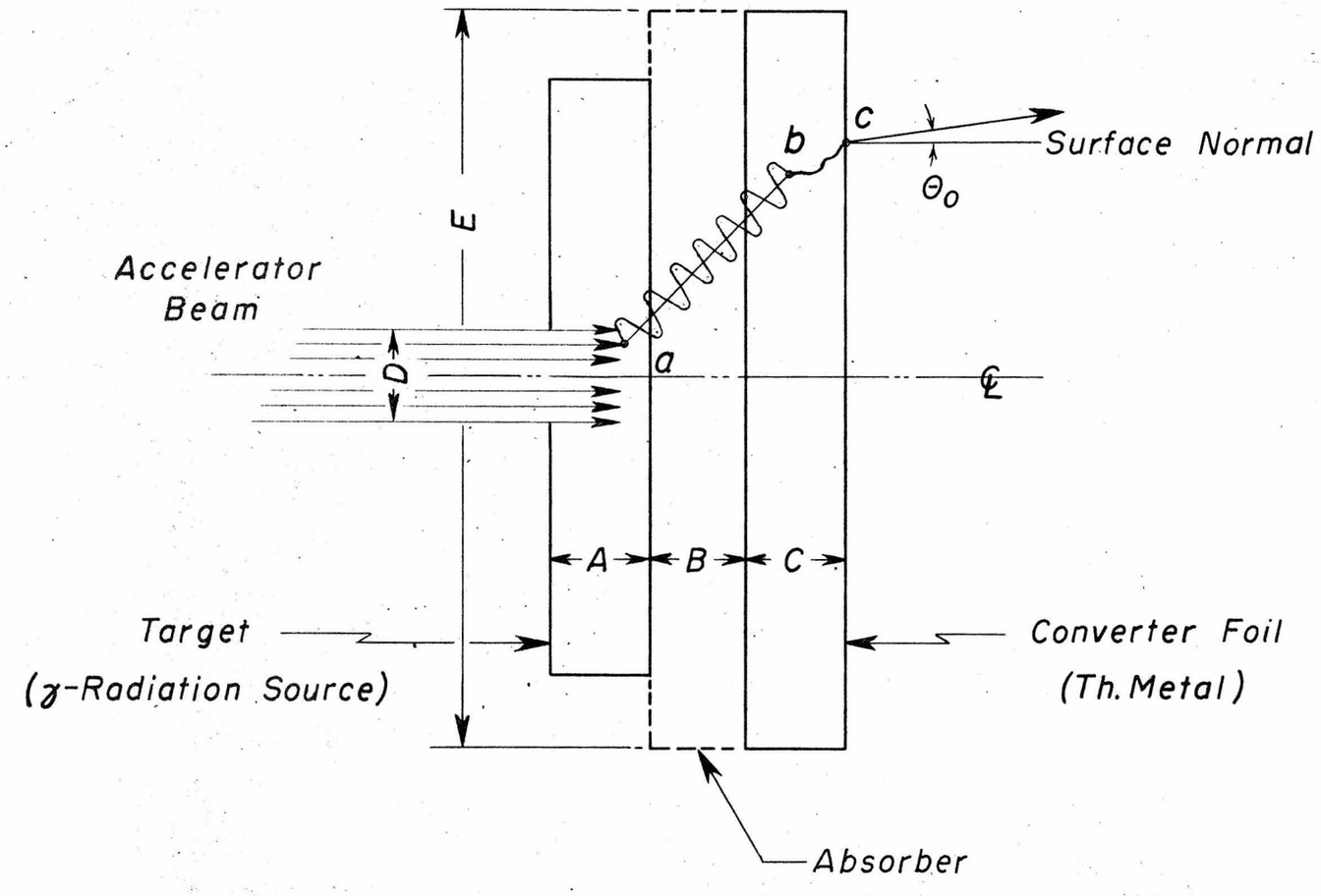

Typical Dimensions	
A	.0001 - .010"
B	0 - .030"
C	.00025 - .005"
D	.080"
E	.375"
Θ_o	13°

FIG. 14

CONVERTER ELECTRON SPECTRUM

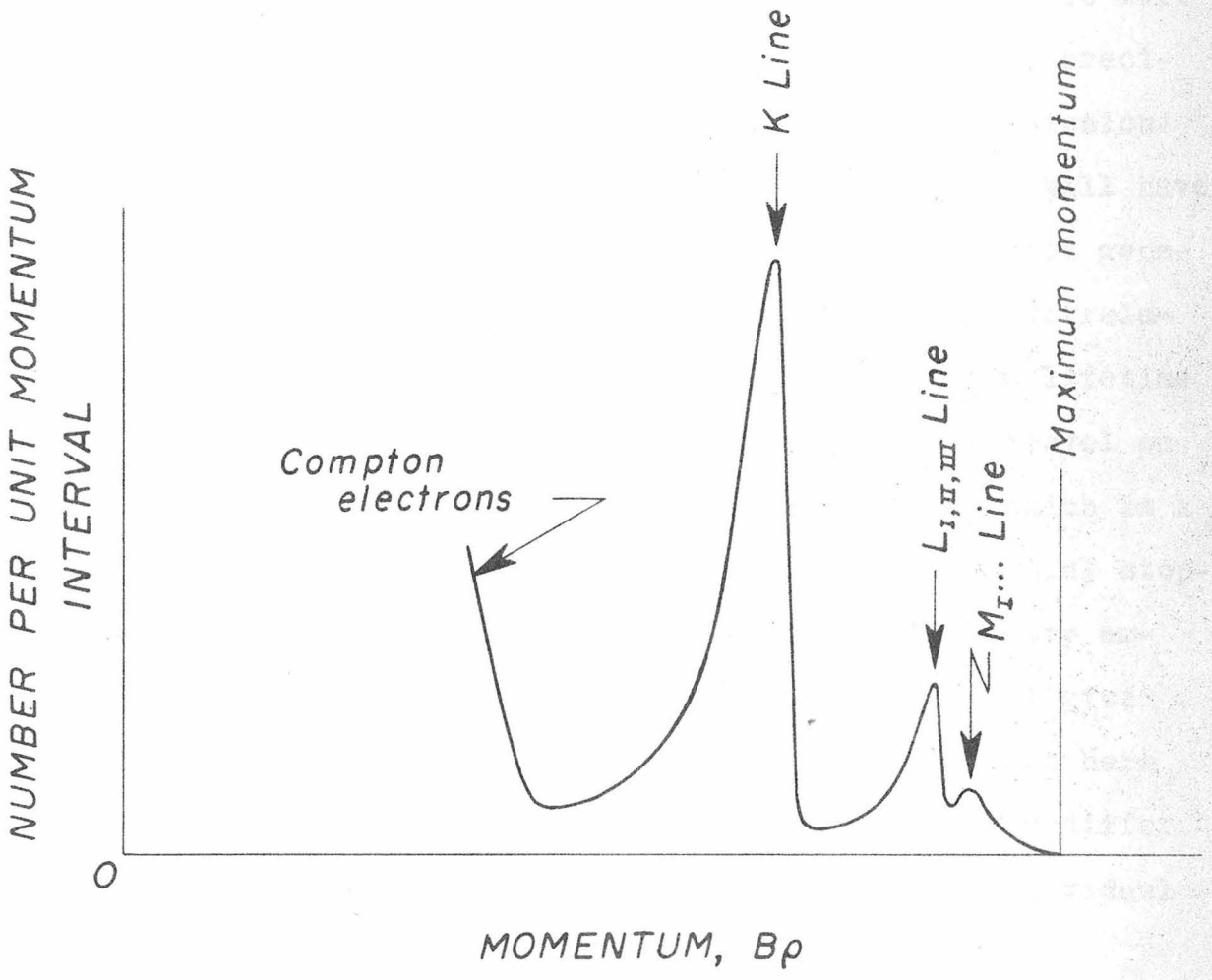

FIG. 15

Nature of Gamma Ray Sources

Since the lifetime of a nuclear state decaying by γ-ray emission may be comparatively short for example 10^{-7} to about 10^{-13} sec for dipole radiation, the γ-ray will have an intrinsic energy spread. Such γ-ray widths are in general of the order of 100 ev to .01 ev or so and may be neglected for the present purposes.

In a nuclear reaction in which a residual nucleus is left in an excited state the residual nucleus may have an appreciable velocity at the time when it decays by γ-ray emission. The γ-ray that is emitted under these circumstances will have a Doppler shift in energy which will depend on the exact geometry of the observation and any possible anisotropic correlations inherent in the nuclear process itself. If the lifetime of the excited state is long enough the nucleus may travel, on the average, a distance before emitting the γ-ray which is a considerable part of its range, thus resulting in partial stopping. This effect combined with the particular geometry employed in the target bombardment for the reaction will give rise to further complications. The effects encountered here are by no means negligible in all cases, however, they differ markedly enough from example to example to require individual treatment.

The Photoelectric Conversion Process

An electron ejected from an atomic system through the photoelectric effect will have an angular correlation both with the

direction of propagation of the γ-ray and the direction of polarization of the γ-ray. An expression for these angular correlations has been worked out by F. Sauter[15] for the relativistic case using the Born approximation $\frac{2\pi\alpha Z}{\beta} \ll 1$ where $\beta = v/c$ and $\alpha = \frac{1}{137}$. Thus even for $v \approx c$ the distribution function is rigorous only for $Z \ll 20$ or so, and although the interest here is in converter material with $Z \approx 90$ this solution will be used to a first approximation. An integration of Sauter's result over all directions of polarization consistent with a given direction of propagation gives the differential photoelectric cross section as:

$$d\sigma = const \times \frac{\sin^3\theta}{(1-\beta\cos\theta)^3}\left[\frac{\sqrt{1-\beta^2}}{(1-\beta\cos\theta)} + \frac{3(1-\sqrt{1-\beta^2})-2\beta^2}{2(1-\beta^2)}\right]d\theta, \quad (51)$$

where θ is the angle between the direction of propagation of the γ-ray and of the electron. A plot of this function for photo electron kinetic energies E of 0.0, 0.20, 0.50, and 1.00 Mev is given in Fig. 16. The various curves were normalized to give the same maximum $d\sigma$. To a good first approximation the half angle $\theta_{1/2}$ of a cone with the direction of propagation of the γ-ray as its axis which includes one half of the total number of photo electrons is given by the expression:

$$\cos\theta_{1/2} \approx \beta \quad (52)$$

The maximum in the distribution occurs at a somewhat smaller angle as the following table indicates.

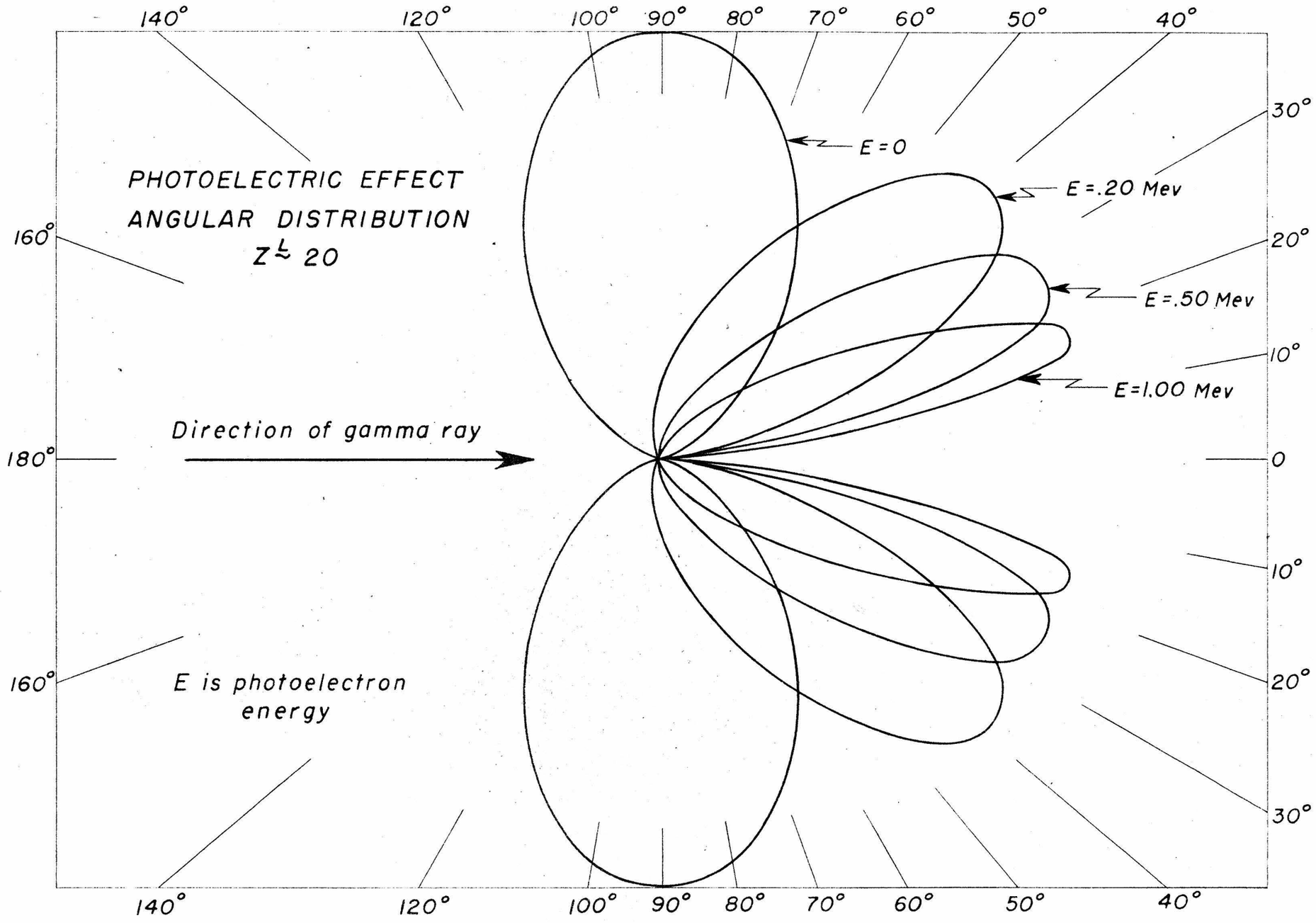
PHOTOELECTRIC EFFECT
ANGULAR DISTRIBUTION
Z ≲ 20
E = 0
E = .20 Mev
E = .50 Mev
E = 1.00 Mev
Direction of gamma ray
E is photoelectron energy
140°
120°
100°
90°
80°
70°
60°
50°
40°
30°
20°
10°
0
160°
180°

FIG. 16

TABLE B

E MEV.	β	$\theta_{1/2}$	θ_{max}
0	0	90°	90°
0.20	.695	46.0°	38°
0.50	.863	30.4°	25°
1.00	.9411	19.7°	16.5°

It will be seen then, by an examination of Fig. 16 and equation (52), that for high energy γ-radiation the photo-electrons are ejected to a larger and larger extent in a lobe in the forward direction, while the width of the lobe becomes progressively narrower as the γ-ray energy is increased.

Source and Converter Geometry

In the analytical treatment which will be given later the concept of the surface brightness i for electron radiation from various portions of the surface area of a lamina of thickness dx into which the converter foil is imagined to be subdivided will prove useful. By analogy with the optical case the surface brightness will be defined as the number of electrons emitted per second per unit solid angle per unit of projected area of the surface. In the general case the brightness of a surface element may depend on the direction of observation with respect to the normal to the surface element. Consider the flux of radiation per second dL in the solid angle $d\Omega$ having an angle θ with the emitting surface element $d\sigma$ illustrated in Fig. 17a. Let t be the effective thickness of the radiating matter, and

SURFACE BRIGHTNESS

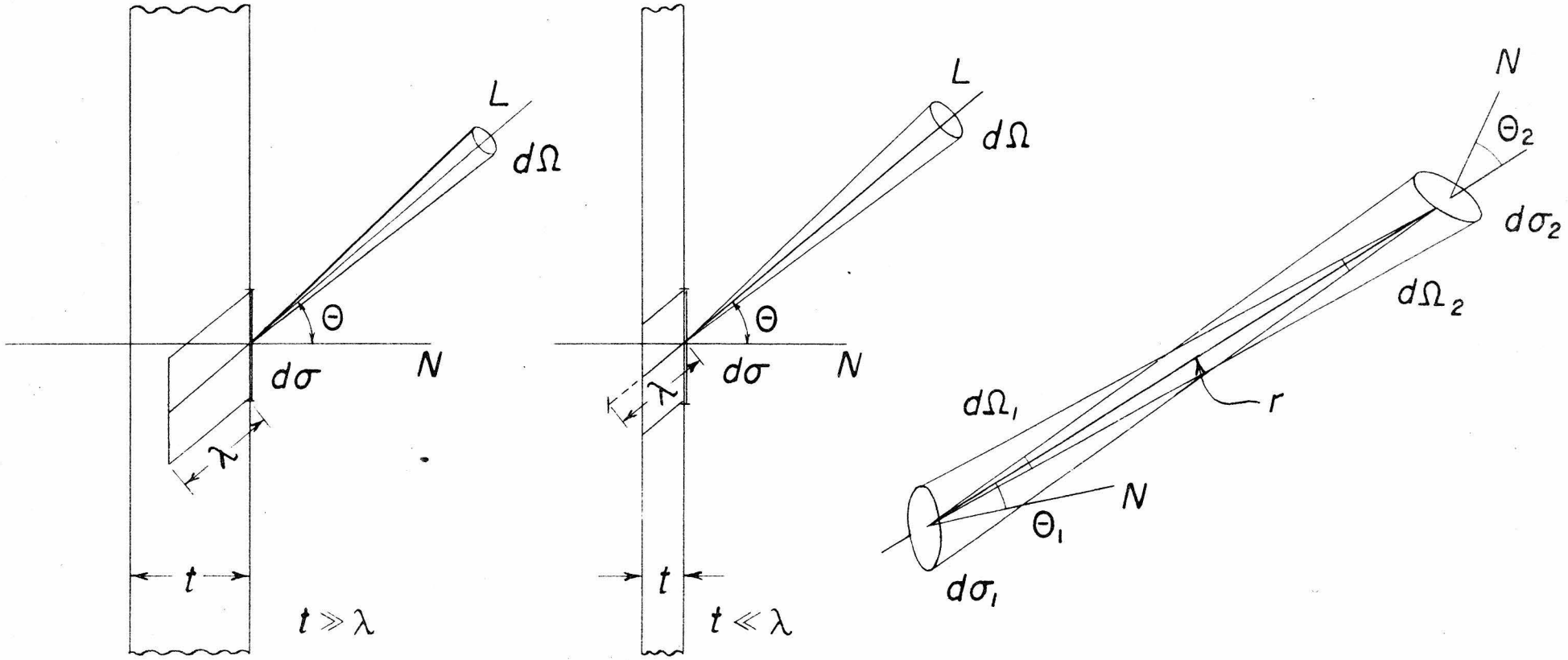

FIG. 17

let λ be the mean free path for absorption of the radiation; then the effective volume of sources is, if $t \gg \lambda$:

$$\lambda \cos\theta \, d\sigma$$

and hence for isotropic sources,

$$dL = \alpha \lambda \cos\theta \, d\sigma \, d\Omega \tag{53}$$

while from the definition of the surface brightness

$$dL = i(\theta) \cos\theta \, d\sigma \, d\Omega \tag{54}$$

consequently

$$i(\theta) = \alpha\lambda \tag{55}$$

Thus when $t \gg \lambda$, which is essentially the definition of a black body, the brightness is independent of θ or is said to obey Lambert's law. For the other limiting case $t \ll \lambda$, as illustrated in Fig. 17b, the effective volume of sources is:

$$t \, d\sigma$$

hence again for isotropic sources

$$dL = \alpha t \, d\sigma \, d\Omega \tag{56}$$

and consequently

$$i(\theta) = \frac{\alpha t}{\cos\theta} \quad . \tag{57}$$

Thus when $t \ll \lambda$ the surface brightness is inversely proportional to $\cos\theta$, while the intensity of radiation $\frac{dL}{d\Omega}$ is a constant which is characteristic of isotropic radiators.

The $1/e$ total absorption length in various materials for γ-rays having energies between 0.5 and 10.0 $m_o c^2$ is given in table C[16] below.

TABLE C

$h\nu/m_0c^2$	λ_{Pb} *	λ_{Cu} *	λ_{Al} *
0.5	~ .20	.92	3.5
1	.59	1.4	4.6
2	1.3	2.0	6.3
5	2.1	2.9	10.
10	2.1	3.5	13.

* in centimeters

Since in all the experiments considered later the effective thickness $t/\cos\theta$ over the range of angles θ which is of consequence for the γ-ray sources used is much less than any of the λ's appearing in table C, the γ-ray sources may be considered as isotropic radiators. The situation, however, is entirely different for the source of conversion electrons and a detailed investigation of $i(\theta)$ for these converters will be given later.

It is of interest at this point to recall a well known reciprocity relationship from Optics. Consider the two differential areas $d\sigma_1$, and $d\sigma_2$ orientated at random illustrated in Fig. 17c; let r be the distance between these areas and θ_1 and θ_2 be the angles r makes with the surface normals. Then if surface $d\sigma_1$ is radiating with a uniform surface brightness $i(\theta_1)$, the flux per second falling on the element $d\sigma_2$ is:

$$dL_2 = i(\theta_1)\cos\theta_1\, d\sigma_1\, d\Omega_1, \tag{58}$$

where $d\Omega_1$ is the solid angle $d\sigma_2$ subtends at $d\sigma_1$. This may be

written as:

$$dL_2 = i(\theta_1)\cos\theta_1\, d\sigma_1 \frac{d\sigma_2 \cos\theta_2}{r^2} = i(\theta_1)\cos\theta_2\, d\sigma_2\, d\Omega_2 \qquad (59)$$

where $d\Omega_2$ is the solid angle surface $d\sigma_1$ subtends at $d\sigma_2$. If on the other hand surface $d\sigma_2$ were the one radiating with the same surface brightness that $d\sigma_1$ had in the previous consideration, the rate of flux falling on $d\sigma_1$ would be;

$$dL_1 = i(\theta_2)\cos\theta_2\, d\sigma_2\, d\Omega_2 \qquad (60)$$

hence

$$i(\theta_1)dL_1 = i(\theta_2)dL_2 \qquad (61)$$

The concentric disc γ-ray source -- converter combination discussed in the General Introduction is pictured in an isometric view in Fig. 18. In the extreme case with $h\nu \to \infty$, and hence also very large photo electron energies, the scattering of the photo electron in the converter can be neglected and further the path of the electron may be considered collinear with that of the γ-ray. In the case of the geometry of Fig. 18, $\theta_1 = \theta_2 = \theta$ and hence in equation (61), $dL_1 = dL_2$. Thus the surface area $d\sigma_2$ of the γ-ray source effective in the ejection of photo electrons from area $d\sigma_1$ of the converter into the solid angle $d\Omega$ having directions θ and ϕ, is just that included within the solid angle $d\Omega$ at the γ-ray source as illustrated. The photo electron surface brightness of the converter at (ρ, ψ) in the direction (θ, ϕ) will be independent of ϕ for the range 123, and will be zero for values outside this range as Fig. 18 reveals. If the thickness of the converter dx is very small compared to the $1/e$ absorption for the γ-radiation then the photo electron surface brightness of the

SOURCE GEOMETRY

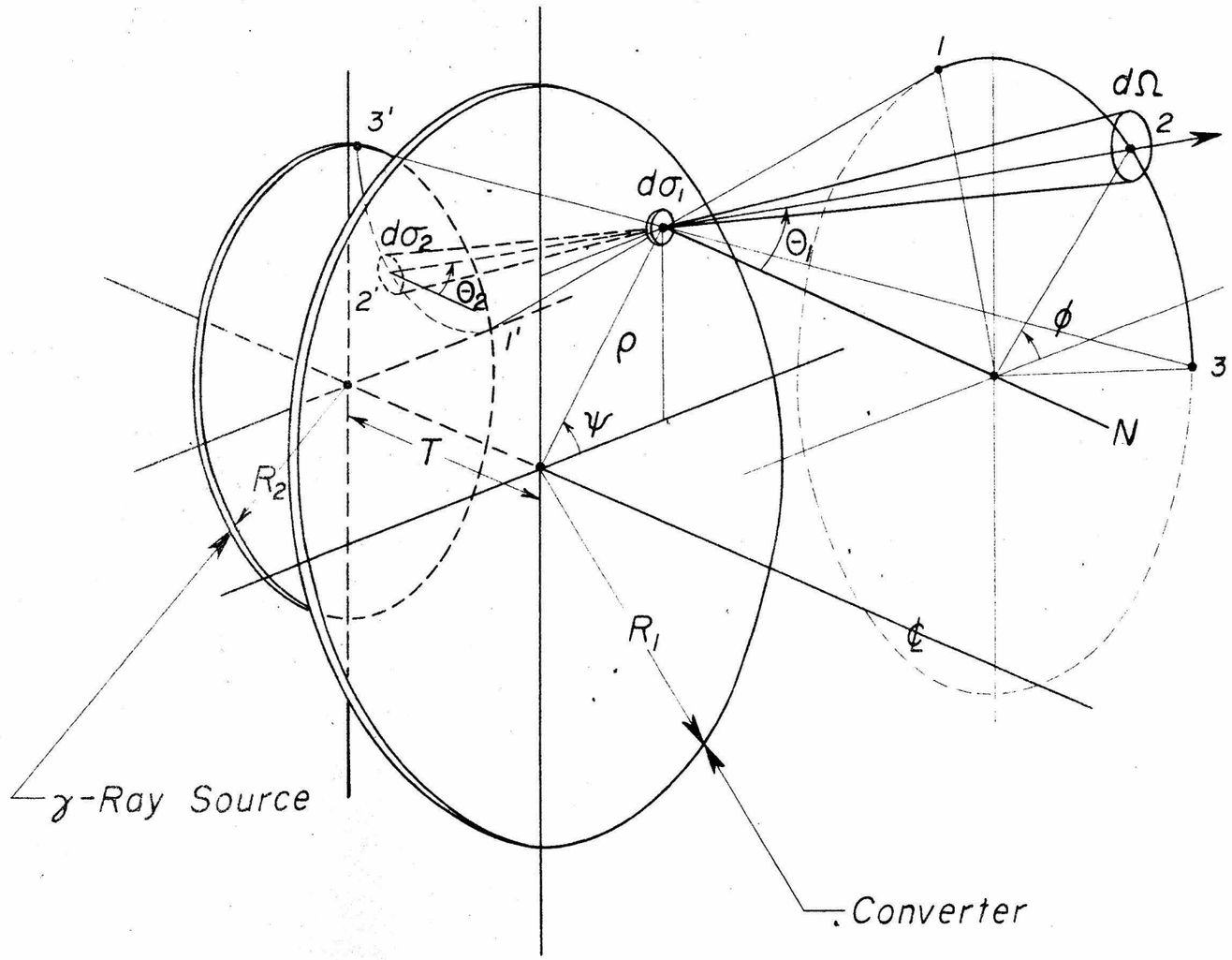

FIG. 18

converter will be

$$i(\theta_1,\phi)=\begin{cases}\dfrac{C\,dx}{\cos^2\theta_1} & \phi \text{ in range 123}\\ 0 & \text{otherwise}\end{cases} \qquad (62)$$

where C is a parameter that depends only on the γ-ray energy and intensity and the material of the converter.

In Fig. 19 the intensity per unit area, $I = i(\theta_1,\phi)\cos\theta_1$, for $\phi=\psi$ is plotted as a function of θ_1 for various values of ρ. In addition to the extreme case $E\to\infty$, but still ignoring scattering, a rough sketch for $E\approx .5$ Mev is included. The geometry illustrated is a typical experimental case drawn to a scale of x20. In the case illustrated, as in all other cases of interest here, the total converter thickness is very small compared to R_2, the radius of the γ-ray source, and hence to a first approximation each lamina of thickness dx, into which the converter is imagined to be subdivided, is an exact replica of any other lamina.

For the case $E\to\infty$ and an acceptance angle θ_0 the converter out to $\rho'=R_2-T\tan\theta_0$ will have $i(\theta_0,\phi)$ non vanishing for any ϕ while beyond $\rho''=R_2+T\tan\theta_0$, $i(\theta_0,\phi)$ will be zero for all ϕ. For the entire range of θ_0 ($\theta_0 \max = 30^\circ$) used in the experiments, T was often essentially zero and at most was approximately equal to R_2 (see Fig. 14). Hence each lamina dx had essentially a uniform surface brightness out to $\rho=R_2$ which was independent of ϕ, beyond $\rho\approx R_2$ the surface brightness was essentially zero. For the case E finite the variation of surface brightness is more gradual and extends out

SOURCE GEOMETRY

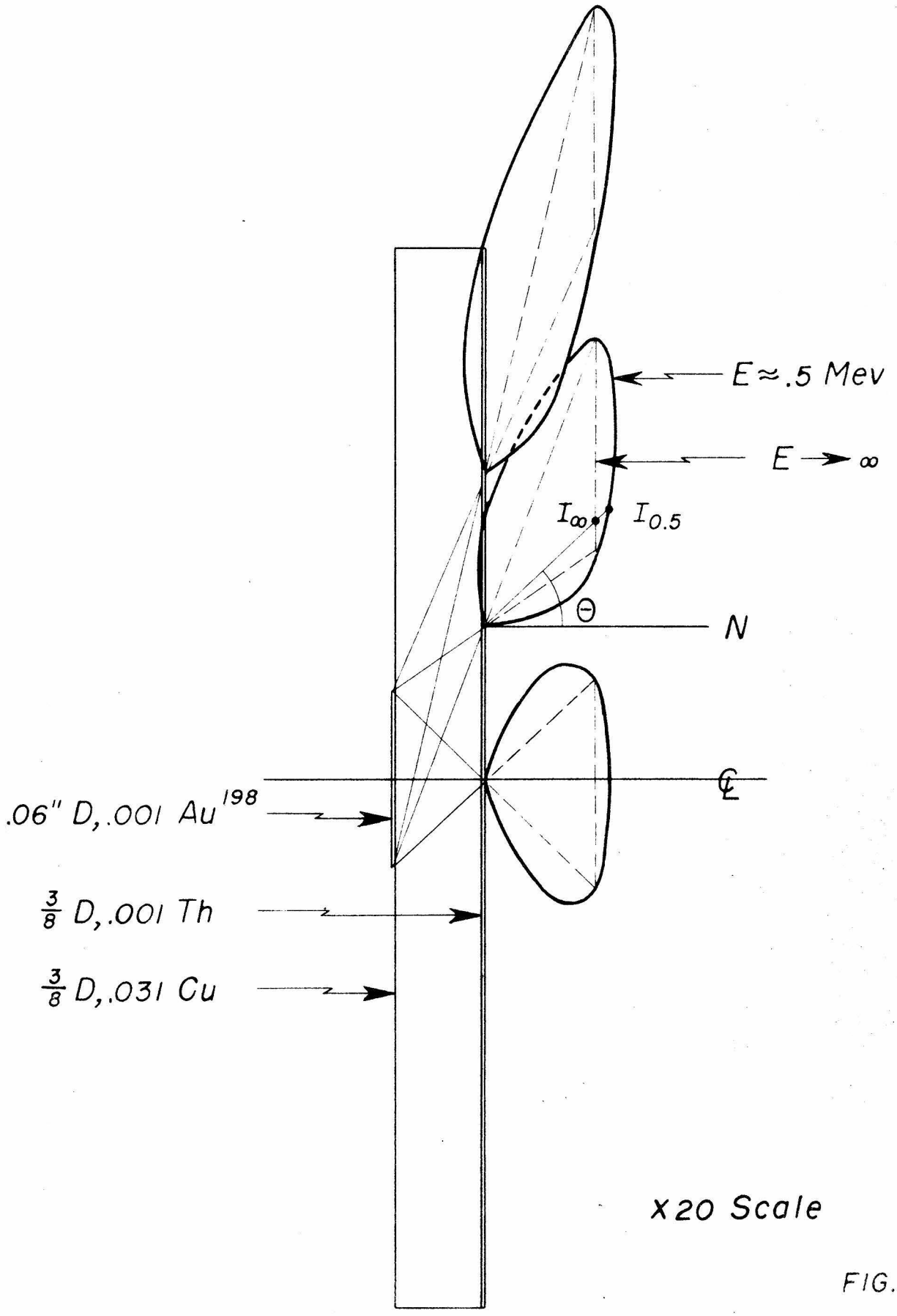

FIG. 19

to a larger ρ. The case which turns out to be easiest to solve is the one in which the whole effective surface of the lamina is considered to have a uniform brightness depending only on θ. Admittedly this approximation is not very accurate, but it will be taken as a reasonable first approximation.

Scattering of Electrons in the Converter

The behavior of electrons in penetrating matter is an extremely difficult problem to investigate theoretically. To simplify the investigation it is common to separate the various discernable effects and to treat them individually. This will be the approach used here.

The photo electron originating at point b in Fig. 14, while traversing the path $\underline{bc}$ in emerging from the converter, will in general undergo a comparatively large number of small angle elastic scatterings principally through its interaction with the nuclear Coulomb field of the converter atoms. To a much smaller extent (amplitude amounting to essentially $1/Z$ times the nuclear case) scattering will also occur from the interactions with the extra-nuclear electronic structure of the atoms of the converter material. These collisions are, however, inelastic and give rise to an energy loss which is statistical in nature and depends markedly on the path length $\underline{bc}$.

It is desirable at this point to consider the equation of state of a system of electrons in matter when only elastic scattering is assumed to occur. Let the density of electrons in the six dimensional coordinate and velocity space be $f(\underset{\sim}{r}, \underset{\sim}{u}, t)$,

where $\underset{\sim}{r}$ is the position vector and $\underset{\sim}{u}$ is a unit vector in the direction of motion and t is the time. Thus for example the number of electrons having coordinates ranging from x to $x+dx$, y to $y+dy$, z to $z+dz$ and velocities ranging from v_x to v_x+dv_x, v_y to v_y+dv_y, v_z to v_z+dv_z is

$$f(x,y,z,v_x,v_y,v_z,t)\,dx\,dy\,dy\,dv_x\,dv_y\,dv_z .$$

Now f will vary with time due to the convection or drift from cell to cell in phase space and also due to the relatively discontinuous changes in velocity caused by the scattering the electrons undergo in the matter. The change in f due to drift may be written as

$$(\Delta f)_d = -\left(\frac{\partial f}{\partial x}v_x + \frac{\partial f}{\partial y}v_y + \frac{\partial f}{\partial z}v_z + \frac{\partial f}{\partial v_x}a_x + \frac{\partial f}{\partial v_y}a_y + \frac{\partial f}{\partial v_z}a_z\right)dt.$$

If the terms involving the acceleration of the system are taken as zero, since it is assumed that there are no external fields present, the result may be written in a more compact form

$$(\Delta f)_d = -v\,\underset{\sim}{u}\cdot\nabla_r f\,dt. \tag{63}$$

Let $\sigma(\alpha, v)$ be the scattering cross section for deflecting an electron through an angle α, then $\sigma(\alpha,v)d\Omega$ is the probability per scattering center that an electron get deflected into the solid angle $d\Omega$ in a direction α with the original direction of motion. If N is the number of scattering atoms per unit volume than in the time dt

$$f(\underset{\sim}{r},\underset{\sim}{u},t)\,Nv\,dt\int_\Omega \sigma(\alpha,v)\,d\Omega = f(\underset{\sim}{r},\underset{\sim}{u},t)\,Nv\,dt\int_\Omega \sigma(\alpha,v)\sin\alpha\,d\alpha\,d\beta .$$

electrons are lost per unit cell in phase space while

$$N v\, dt \int_{\Omega} f(\underset{\sim}{r}, \underset{\sim}{u}', t)\, \sigma(\alpha, v) \sin\alpha\, d\alpha\, d\beta$$

electrons are gained per unit cell in phase space. Fig. 20a illustrates a scattering event accompanied by a change in direction of α. Thus f will change due to scattering a net amount

$$(\Delta f)_s = N v\, dt \int_{\Omega} \sigma(\alpha, v) \sin\alpha \left[f(\underset{\sim}{r}, \underset{\sim}{u}', t) - f(\underset{\sim}{r}, \underset{\sim}{u}, t) \right] d\alpha\, d\beta \,. \tag{64}$$

Finally then combining equations (63) and (64) there results,

$$\frac{1}{v}\frac{\partial f}{\partial t} = -\underset{\sim}{u}\cdot\nabla_r f + \int_{\Omega} N\sigma(\alpha, v) \sin\alpha \left[f(\underset{\sim}{r}, \underset{\sim}{u}', t) - f(\underset{\sim}{r}, \underset{\sim}{u}, t) \right] d\alpha\, d\beta \tag{65}$$

This equation was first considered by L. Boltzmann[17] and is known as Boltzmann's equation of state. The scattering cross section $\sigma(\alpha, v)$ as developed in the theory of single scattering is large only for small angles α and rapidly decreases as α increases, hence to a first approximation α will be considered as a small angle. Write $\underset{\sim}{u}' = \underset{\sim}{u} + \underset{\sim}{w}$ with $|w| = 2\sin\frac{\alpha}{2} \ll 1$. Now $f(\underset{\sim}{r}, \underset{\sim}{u}', t)$ may be expanded in a Taylor expansion in powers of $\underset{\sim}{w}$ on a unit sphere. Then

$$f(\underset{\sim}{r}, \underset{\sim}{u}', t) - f(\underset{\sim}{r}, \underset{\sim}{u}, t) = w_x \frac{\partial f}{\partial u_x} + w_y \frac{\partial f}{\partial u_y} + \frac{1}{2} w_x^2 \frac{\partial^2 f}{\partial u_x^2} + \frac{1}{2} w_y^2 \frac{\partial^2 f}{\partial u_y^2} + w_x w_y \frac{\partial^2 f}{\partial u_x \partial u_y} \tag{66}$$

where $w_x = w\cos\beta$, $w_y = w\sin\beta$

Integrating equation (65) over the azimuth β using equation (66), only the terms in w_x^2 and w_y^2 remain and there results

$$\frac{1}{v}\frac{\partial f}{\partial t} = -\underset{\sim}{u}\cdot\nabla_r f + \pi N \left(\frac{\partial^2 f}{\partial u_x^2} + \frac{\partial^2 f}{\partial u_y^2} \right) \int_{\alpha} \sigma(\alpha, v)(1 - \cos\alpha) \sin\alpha\, d\alpha \,,$$

SCATTERING GEOMETRY

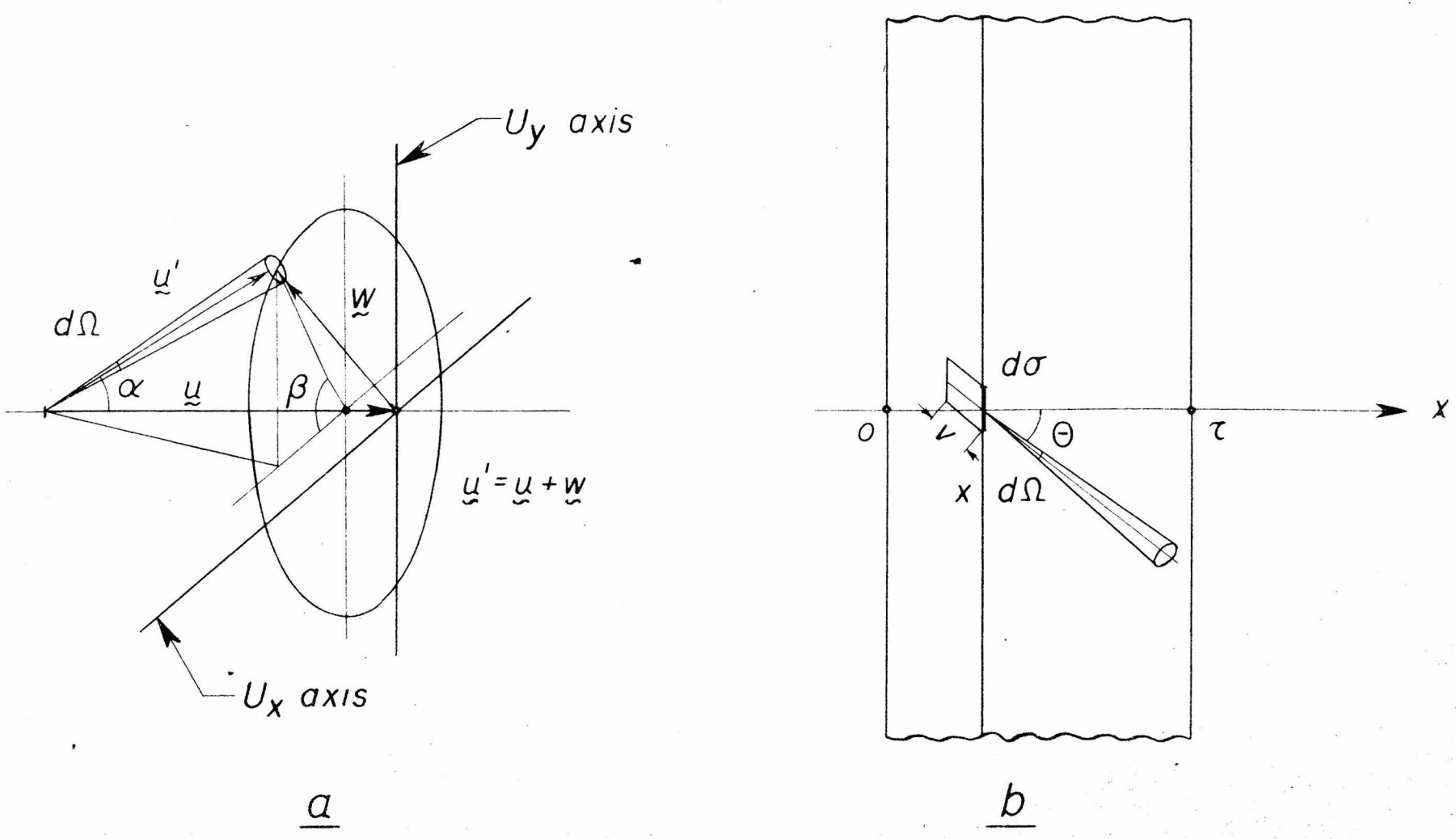

FIG. 20

or letting
$$K = 2\pi N \int_{\alpha} \sigma(\alpha, v)(1-\cos\alpha)\sin\alpha \, d\alpha \tag{67}$$

and writing
$$\frac{\partial^2}{\partial u_x^2} + \frac{\partial^2}{\partial u_y^2} = \frac{1}{\sin\theta}\frac{\partial}{\partial\theta}\left(\sin\theta\frac{\partial}{\partial\theta}\right) + \frac{1}{\sin^2\theta}\frac{\partial^2}{\partial\phi^2} = \nabla_u^2 \tag{68}$$

$$\frac{1}{v}\frac{\partial f}{\partial t} = -\underset{\sim}{u}\cdot\nabla_r f + \frac{K}{2}\nabla_u^2 f \tag{69}$$

Equation (69) which is correct up to fourth derivatives must be obeyed by all electron systems experiencing only elastic scattering, quite irrespective of the geometry.

Consider now an infinite plane slab of thickness z illustrated in Fig. 20b, extending from $X=0$ to $X=z$. Let f depend only on the phase space variables X and θ, thus this requires the distribution f to be uniform over any surface $X=X$ and $\underset{\sim}{u}$ to be independent of the azimuth angle ϕ. Since equation (69) assumes no interaction between electron systems having different velocities v, consider the systems to be homogeneous in velocity. Under steady state conditions, that is dynamic equilibrium $\frac{\partial f}{\partial t} = 0$, hence equation (69) becomes

$$\frac{K}{2}\frac{1}{\sin\theta}\frac{\partial}{\partial\theta}\left(\sin\theta\frac{\partial f}{\partial\theta}\right) - \cos\theta\frac{\partial f}{\partial X} = 0$$

$$\text{or} \quad \frac{\partial^2 f}{\partial\theta^2} + \cot\theta\frac{\partial f}{\partial\theta} - \frac{z}{K}\cos\theta\frac{\partial f}{\partial X} = 0 \tag{70}$$

This equation was first derived by Bothe[18] and given careful consideration by him and also later by Bethe, Rose, and Smith[19].

Take the surface area $d\sigma$ at a depth X and consider the number of electrons per second entering the solid angle $d\Omega$ making an angle θ with the surface normal as in Fig. 20b, then

$$\frac{dn}{dt} = v \cos\theta \, d\sigma f(x,\theta) \, d\Omega$$

But from the concept of surface brightness

$$\frac{dn}{dt} = i(x,\theta) \cos\theta \, d\sigma \, d\Omega$$

hence

$$v f(x,\theta) = i(x,\theta) \quad . \tag{71}$$

But since is a constant, equation (70) may be written as

$$\frac{\partial^2 i}{\partial \theta^2} + \cot\theta \frac{\partial i}{\partial \theta} - \frac{2}{K} \cos\theta \frac{\partial i}{\partial x} = 0 \tag{72}$$

Thus if the surface brightness at the surface, for example $X = 0$, is known then equation (72) governs the propagation of this surface brightness through the slab.

As an interesting sidelight into the nature of equation (72) consider the case in which $\theta \ll \frac{\pi}{2}$ then

$$\frac{\partial^2 i}{\partial \theta^2} - \frac{1}{\theta} \frac{\partial i}{\partial \theta} - \frac{2}{K} \frac{\partial i}{\partial x} = 0$$

which has as a particular integral solution

$$i = \frac{1}{2\pi K x} e^{-\theta^2/2Kx} \quad , \tag{73}$$

and corresponds to the transmission of a parallel beam of electrons through a thin slab of thickness x , normalized to give $\int_0^\infty i \, 2\pi\theta \, d\theta$. Note that from equation (73) $\overline{\theta^2}$ is given by

$$\overline{\theta^2} = \int_0^\infty \frac{\theta^2 e^{-\frac{\theta^2}{2Kx}}}{2\pi K x} 2\pi\theta \, d\theta = 2xK$$

and hence $2K$ is just the mean square scattering angle for a unit thickness of slab; this is of course just what equation

(67) gives for small angle scattering. To find the total number of electrons within a cone of half angle Θ and having as its axis the surface normal we have

$$n(\Theta) = n_0 \int_0^{\Theta} 2\pi\theta \frac{e^{-\frac{\theta^2}{2\kappa x}}}{2\pi\kappa x} d\theta = n_0 \left(1 - e^{-\frac{\Theta^2}{2\kappa x}}\right), \qquad (74)$$

The term in the bracket being the transmission factor for the slab. The experimental results of many investigators, in fact, show that when such a mono-energetic parallel beam of electrons traverses thin foils the beam will become spread out having an angular distribution which is essentially Gaussian in nature[20,21]. The evaluation of the integral in equation (67) requires quite a degree of refinement in order to properly set the lower limit, which if taken as zero would cause the integral to diverge. The cutoff is obtained by considering the electron screening of the nuclear Coulomb potential. Using this cut off, Bothe derives an expression for κ which he then compares with experiment through equations (73) and (74). By slightly readjusting the value of the cut off he obtained what might be called a semi-empirical fit and gives

$$\sqrt{\kappa x} = 8.0 \frac{V+511}{V(V+1022)} Z \sqrt{\frac{\rho x'}{A}} \quad \text{radians} \qquad (75)$$

where V = kinetic energy of electron in Kev

x' = foil thickness in 10^{-4} cm.

ρ, A, and Z are the density, atomic weight and atomic number for the material of the foil.

Values of κ based on this formula are given in table D for

Thorium metal foils and various electron energies and foil thicknesses.

TABLE D

	E (mev)								
mils	0.10	0.20	0.40	0.60	1.0	2.0	4.0	6.0	10.0
.24	--	64.5°	35.5°	25.3°	16.6°	9.2°	5.0°	3.4°	2.1°
.55	--	--	53.3°	38.0°	24.9°	13.8°	7.5°	5.2°	3.2°
.87	--	--	67.2°	48.0°	31.4°	17.5°	9.5°	6.5°	4.0°
2.8	--	--	--	85.5°	56.0°	31.1°	16.9°	11.6°	7.1°
5.2	--	--	--	--	77.0°	42.7°	23.2°	16.0°	7.8°

To return to the more general case we note that equation (29) is separable; take $i(x,\theta) = g(\theta)\,h(x)$ then

$$\frac{d^2g}{d\theta^2} + \cot\theta\,\frac{dg}{d\theta} + \frac{2\alpha}{K}\cos\theta\cdot g = 0$$

$$\frac{dh}{dx} + \alpha h = 0 \qquad (76)$$

whence $$h(x) = C\,e^{-\alpha x} \qquad (77)$$

Bothe has noticed that in many experiments $i\left(x,\frac{\pi}{2}\right)$ is essentially zero, hence he forced equation (76) to have the general boundary condition $g\left(\frac{\pi}{2}\right) = 0$. This leads to eigen values for the separation constant α say α_s and the corresponding eigen functions $g_s(\theta)$. Thus the general solution is

$$i(\theta,x) = \sum_{s=1}^{\infty} C_s\,g_s(\theta)\,e^{-\alpha_s x} \qquad (78)$$

Bothe has shown that approximately

$$\alpha_1 \approx 1.33K \;,\quad \alpha_2 \approx 9.15K \;,\quad \alpha_3 \approx 23.3K$$

$$g_1(\theta) \approx 2\cos\theta \tag{79}$$

$$g_2(\theta) \approx 2\sqrt{\tfrac{2}{3}}\,(5\cos^3\theta - 3\cos\theta)$$

$$g_3(\theta) \approx \tfrac{2}{\sqrt{15}}\,(63\cos^5\theta - 70\cos^3\theta + 15\cos\theta)\,.$$

Hence if $i(X=0,\theta)$ is known (Fig. 20b) then it may be expanded in the functions $g_s(\theta)$, and the $C_s's$ of equation (78) are then determined and $i(X,\theta)$ is then known. Note that because of the rapid damping of the solutions $S \geq 2$, $i(X,\theta)$ can be taken as simply

$$i(X,\theta) \approx 2C_1\cos\theta\, e^{-1.33KX} \qquad X \geq \tfrac{2}{K} \tag{80}$$

Bothe finds that this angular distribution fits experimental data well although the "mass absorption coefficient" α_1/ρ does not check experiment too well insofar as the Z dependence is concerned, the absorption being less pronounced than indicated by α_1/ρ for the larger atomic numbers.

Bethe, Rose, and Smith use a boundary condition which simply requires $i(X,\theta)$ to be finite for all θ rather than the one used by Bothe who took $i(X,\tfrac{\pi}{2}) = 0$. The resulting eigen values for the less restricted boundary condition are $\alpha_S = 3.22\,(S+\tfrac{1}{2})^2 K$, since even for $S=1$ the solution is too rapidly attenuated, Bethe, Rose, and Smith suggest that the singular solution

$$i(\theta,X) = \alpha + \beta\,(\cos\theta - KX) \tag{81}$$

be used along with the exponential solutions. A matching of the boundary conditions at the surface $X = 0$ is then used in determining the constants α and β, for $X \gtrsim \frac{.4}{K}$ the solution represented by equation (81) alone may be used.

In the actual application of the scattering theory which will be made only electrons which have suffered comparatively small energy loss will be considered. As will be seen later the energy loss depends on the actual path length of the electron which in turn is affected by scattering. Thus electrons that suffer a large angular scattering will in general also travel greatly increased paths and thereby lose large amounts of energy before emerging from the converter. For this reason perhaps Bothe's boundary condition is to be preferred since it effectively supplies a sink for electrons having been scattered through large angles.

Straggling and Energy Loss for Electrons Emerging from the Converter

As has been mentioned, fast electrons in moving through matter will lose energy mostly through the encounters they make with the electrons bound to the atoms of this material. In such encounters, however, the energy transfer is not uniquely determined, but is governed by quantum mechanical considerations. Thus even for electrons that have made a definite specified number of encounters the energy loss can only be given as a spectrum. When the average number of encounters characterized by a certain energy loss in traversing a certain thickness of ma-

terial is comparatively small, there will be a considerable spread in the actual number of encounters for various electrons due to the statistical nature of this phenomenon. Both these phenomena combine then in preventing the association of a unique energy loss with a specified thickness. While for the motion of heavy particles (such as α -particles, protons and deuterons) through matter it has been customary to refer only to the statistical fluctuations as "straggling", the term will be applied through what follows in a general sense to indicate the degree to which the energy loss and thickness cannot be correlated uniquely.

A quantitative investigation, essentially combining the results of Landau[22] and Bohr[23] on the most probable energy loss for a given thickness of material traversed, has been undertaken by Christy and Cohen[24]. They have shown that the most probable energy loss Δ per length of path X may be written as

$$\frac{\Delta}{X} = \epsilon = \xi \left[\ln \frac{X}{a_0} + \ln F_c^3 - (1 - F_c)\beta^2 + 0.37 \right] \qquad (82)$$

where $F_c = \dfrac{\eta^{1/2}}{1 + \eta^{1/2}}$

$a_0 = \hbar^2 / m_0 c^2$ = Bohr radius = 0.528×10^{-8} cm

$\beta = v/c$

$\xi = \dfrac{2\pi N e^4 \rho Z}{m_0 v^2 A}$

and $\eta^{3/2}(1+\eta^{1/2}) = \gamma^2 \dfrac{4\pi N \hbar^2 e^2 Z \rho}{A m_0 I^2} = \gamma^2 \dfrac{\hbar^2 \nu^2}{I^2}$, $\nu^2 = \dfrac{4\pi N e^2 Z \rho}{A m_0}$

E = total electron energy = $\gamma m_0 c^2$

I = mean ionization potential = $13.5\, Z$ ev.

Equation (82) actually is an approximation in that it is assumed that $\gamma m_0 c^2 \gg \xi x \gg I$. Fig. 21 shows the most probable energy loss per unit path length ϵ in Kev/mil for various thicknesses and electron kinetic energies in thorium metal.

An effect which has so far not been considered is the increase in X , the path length, due to the actual zig-zag nature of the electron motion caused by the scattering in the material. For an electron starting at a depth X within a thin foil, with its original direction being along the normal to the foil surface, the actual path length ℓ has been calculated by Christy and Cohen to be

$$\ell = -x_m \ln\left(1 - \frac{x}{x_m}\right)$$

where

$$x_m = \frac{A}{N\rho}\left(\gamma - \frac{1}{\gamma}\right)^2\left(\frac{m_0c^2}{e^2}\right)^2\left[2\pi Z^2 \ln\frac{4(\gamma^2-1)}{\alpha^2 Z^{2/3}}\right]^{-1} \qquad (83)$$

with the notation the same as for equation (82) and $\alpha = \frac{1}{137}$. Figure 22 gives ℓ/x_m as a function of x/x_m while Fig. 23 gives x_m as a function of the electron energy, for thorium metal. The nature of the approximations involved in the derivation of equation (83) make the correction for the path length reasonably reliable only if this correction is such that $\ell/x \lesssim 2$.

Since the electrons accepted within the solid angle of the spectrometer can start making a range of angles with the surface normal of the foil, the true length is further increased to

$$\ell' = \frac{\ell}{\cos\theta}$$

Here $\cos\theta$ should be some type of mean cosine for the range of initial angles under discussion. For high energy electrons this

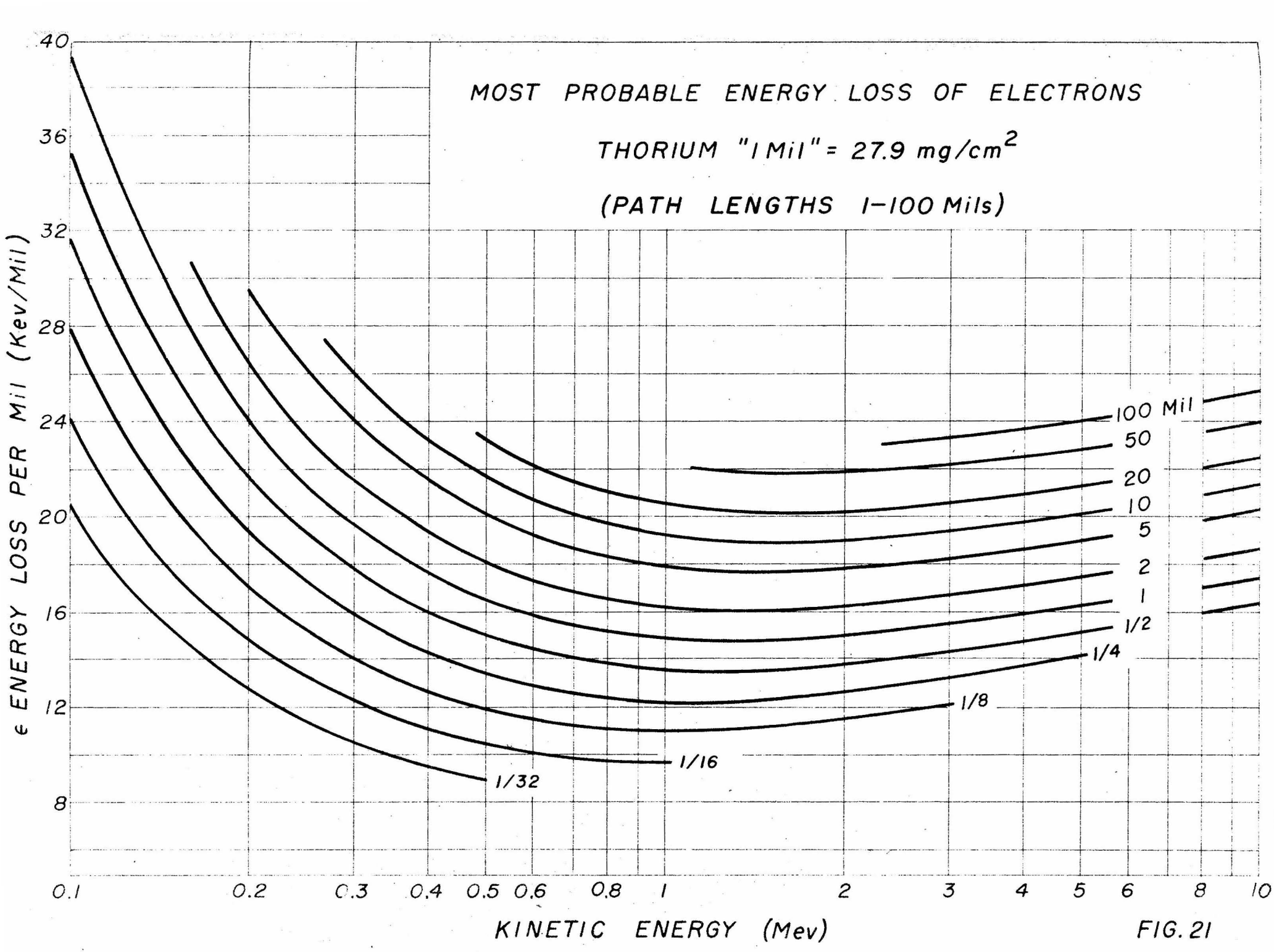
MOST PROBABLE ENERGY LOSS OF ELECTRONS
THORIUM "1 Mil" = 27.9 mg/cm²
(PATH LENGTHS 1–100 Mils)
ε ENERGY LOSS PER Mil (Kev/Mil)
KINETIC ENERGY (Mev)
40
36
32
28
24
20
16
12
8
0.1
0.2
0.3
0.4
0.5
0.6
0.8
1
2
3
4
5
6
8
10
100 Mil
50
20
10
5
2
1
1/2
1/4
1/8
1/16
1/32

FIG. 21

532

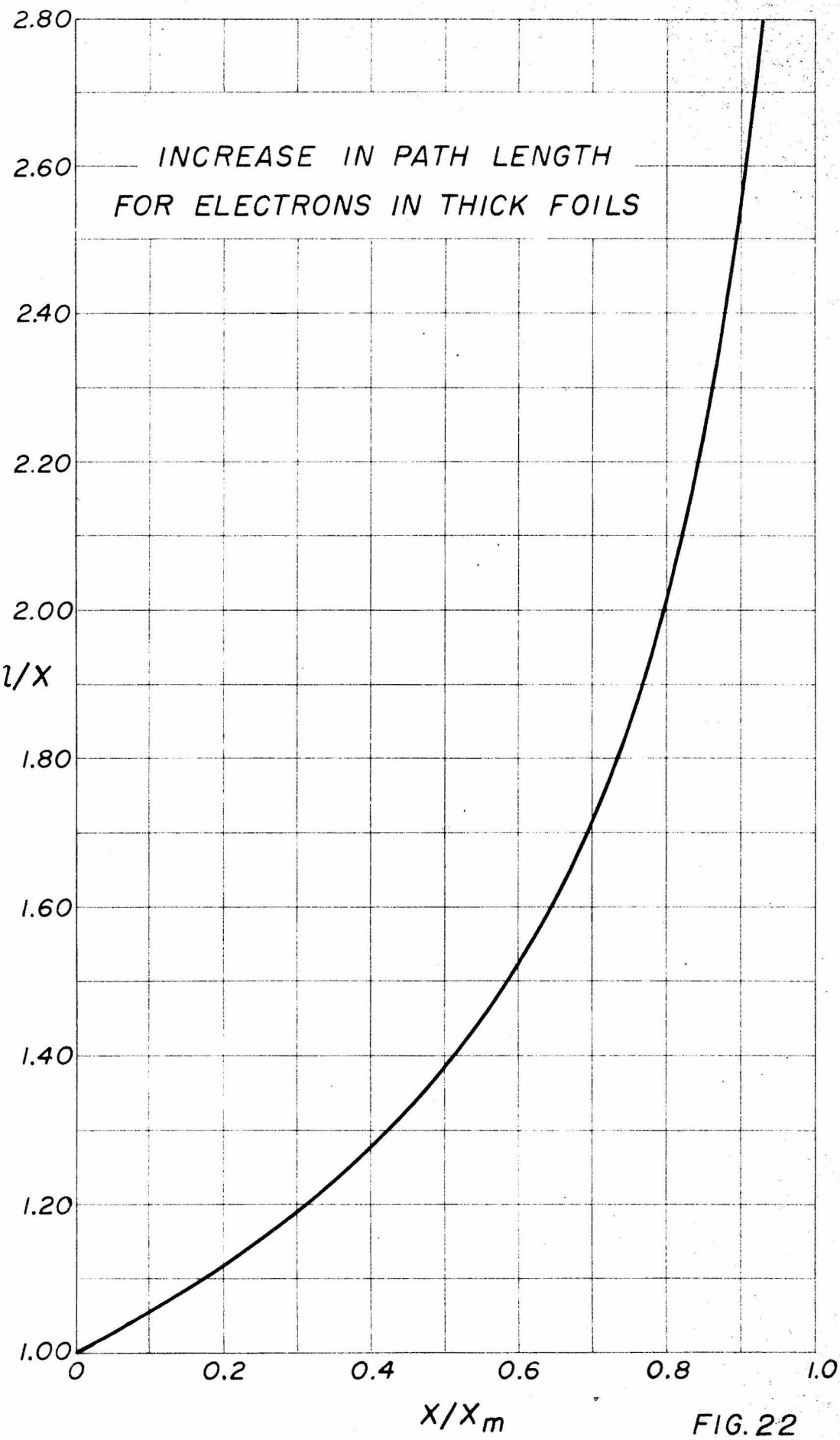
INCREASE IN PATH LENGTH
FOR ELECTRONS IN THICK FOILS
2.80
2.60
2.40
2.20
2.00
1.80
1.60
1.40
1.20
1.00
l/X
0
0.2
0.4
0.6
0.8
1.0
X/Xm

FIG. 22

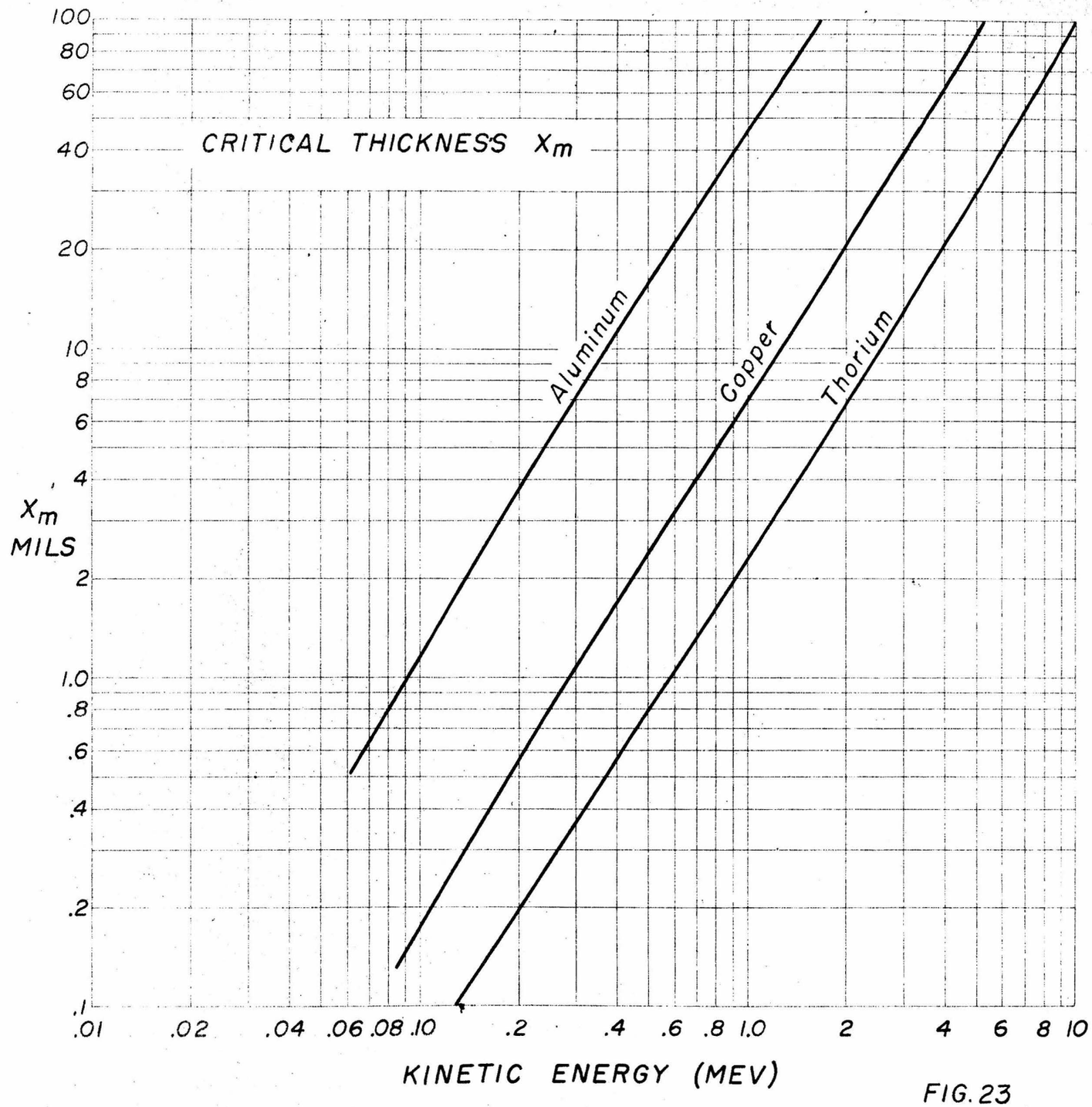
CRITICAL THICKNESS X_m
Aluminum
Copper
Thorium
X_m MILS
100
80
60
40
20
10
8
6
4
2
1.0
.8
.6
.4
.2
.1
.01
.02
.04
.06
.08
.10
.2
.4
.6
.8
1.0
2
4
6
8
10
KINETIC ENERGY (MEV)

FIG. 23

mean is essentially $\cos\theta_0$, where θ_0 is the mean angle of acceptance of the spectrometer. To a first approximation then

$$\ell' = \frac{\ell}{\cos\theta_0} \tag{84}$$

which can be assumed to be the same for all energy electrons.

The classical experiments of White and Millington[25] treat the problem of straggling in energy loss for a wide range of electron energies in thin mica foils ranging in thickness for 2 - 15 mg/cm^2. They find that to a fair degree of approximation the monoenergetic line source of electrons is spread into a spectrum which has a universal shape factor. Thus if the distribution of electrons in the spectrum $g(x)$ is plotted as a function of the energy loss X, in units that give $X = 29$, for the most probable energy loss, the curve of Fig. 24 results, which is independent of the absorbing foil thickness.

Although they found indications of absorption for the thicker foils the experimental results were only able to confirm the order of magnitude of the absorption predicted by Bothe. They, as well as many other investigators, have found that the actual thickness to be associated with an absorbing foil is greater than its measured thickness. The results of White and Millington are in no essential variance with those predicted from equation (83).

It should perhaps be pointed out that if the results of the White and Millington experiments are applied to a case in which the electrons originate throughout the volume of the absorbing foil (as for example in the case of photoelectric conversion in

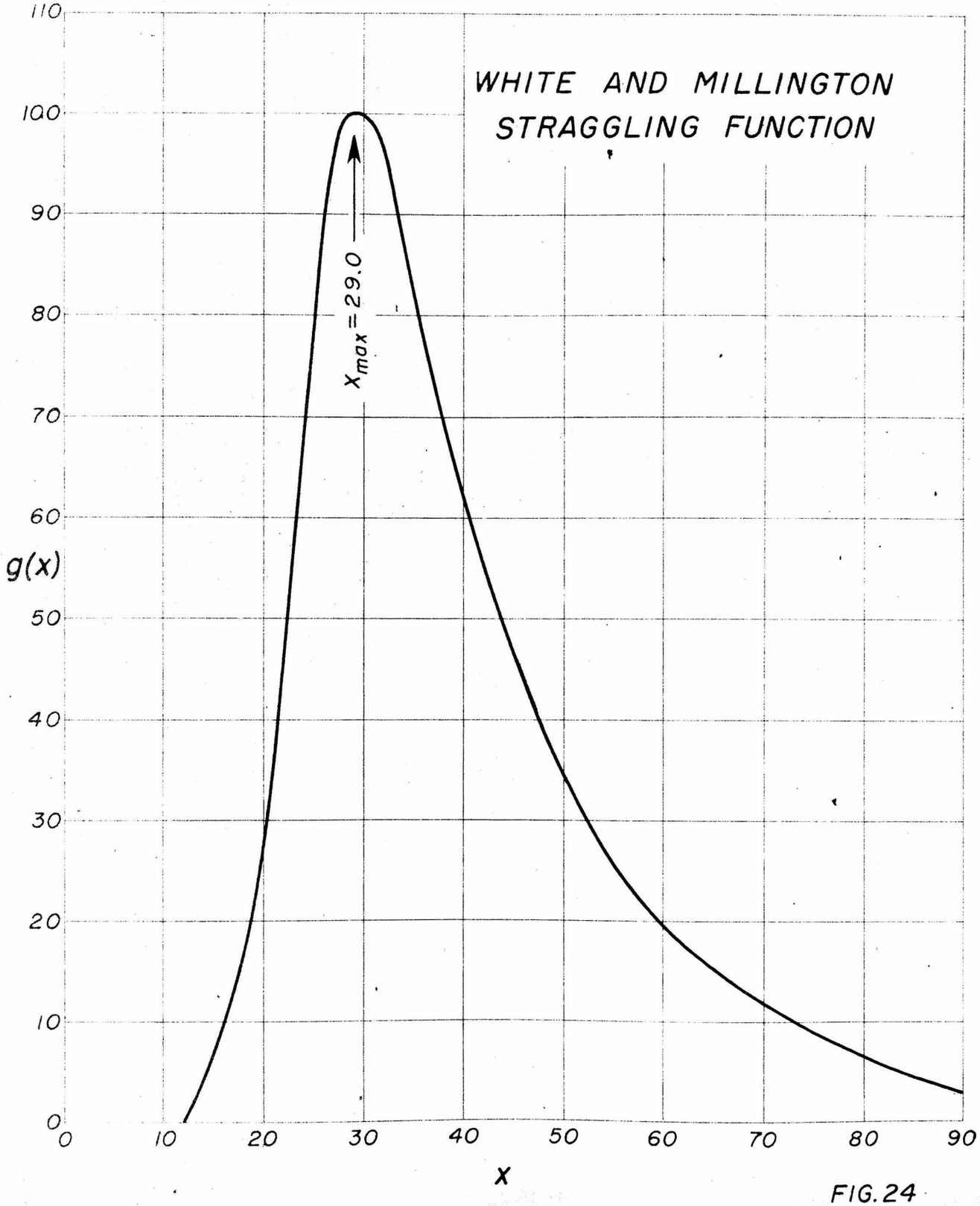
WHITE AND MILLINGTON
STRAGGLING FUNCTION
$X_{max} = 29.0$
g(x)
X
0
10
20
30
40
50
60
70
80
90
100
110

FIG. 24

a foil) an integration of $g(x)$ properly normalized may be used as a first approximation in obtaining the spectrum, however, not without some error. In the volume source arrangement the electron distribution reaching the foil surface, from a thin lamina within the depth of the foil, will depend not only on the depth of this lamina (i.e. the thickness of foil which must be penetrated to arrive at the surface) but also on the amount of material backing up this lamina through the phenomenon of back scattering. These experiments do not include this effect of back scattering. Further, while the curve of Fig. 24 may be of a universal nature for the range of foils covered in these experiments it is clear that for both very thin and very thick absorbing foils this cannot be the case. For very thick foils the treatment based on a complete diffusion theory is known to be an accurate description and this gives results which are not in agreement with the idea of a universal curve. For very thin foils (foil thicknesses of Thorium say for which the most probable energy loss is less than $\sim$ 1 Kev) a finite number of electrons will succeed in penetrating the foil with zero energy loss. The number of such electrons will increase at a rapid rate as the thickness is decreased in this range. The curve of Fig. 24 permits no electrons below $\frac{12}{29}$ the most probable energy loss and hence must be in error for such small thicknesses.

Instrumental Resolution

All selective observational instruments reflect in the data the effects of their own resolution or stated in the usual terminology such instruments give a result which is the "fold" of their own window curves into the distribution being observed.

Let $P(p,j)$ be the probability that an electron of momentum p directed at random with respect to the spectrograph axis be detected when the spectrograph current is set to j. Let $f(p)dp$ be the number of electrons in the spectrum being observed that have momenta between p and $p+dp$. Let the total number of electrons detected at the current setting j be $F(j)$.

Due to the focusing property of the spectrograph, units may be introduced in which $[p] = [j]$

Then

$$F(j) = \int_p P(p,j) f(p) dp \quad . \tag{85}$$

Now when the spectrum $f(p)$ is a delta function as in the case of an internally converted γ-ray which gives a line β-spectrum $f(p)$ may be taken as

$$f(p) = \delta(p - p_o)$$

where p_o is the momentum of the electron line. Therefore:

$$F(j) = \int_p P(p,j)\, \delta(p - p_o)\, dp$$

or $$F(j) = P(p_o, j) \quad .$$

Experimentally it is observed that for the lens type β-ray spectrograph used and in the momentum range 1 - 10 kilo gauss-cm.

$$F(j) = \frac{\Omega}{4\pi} e^{-\frac{(j-j_0)^2}{\Delta^2 j j_0}} \qquad (86)$$

for such internally converted lines, where

Ω = solid angle of spectrograph

$\Delta = \frac{\sigma}{2\sqrt{\ln 2}}$ and σ is defined as the instrument resolution.

$j_0 = p_0$

hence

$$P(p,j) = \frac{\Omega}{4\pi} e^{-\frac{(j-p)^2}{\Delta^2 p j}}$$

Thus in general the spectrum of the data $F(j)$ and the spectrum being observed $f(p)$ are connected through the relationship

$$F(j) = \frac{\Omega}{4\pi} \int_p e^{-\frac{(j-p)^2}{\Delta^2 p j}} f(p)\, dp . \qquad (87)$$

The experiments to be discussed later show the striking extent to which equation (86) fits the experimental observation for typical window curves, (see Figures 32 and 47).

Now if $\Delta \ll 1$ and if $\frac{\partial f(p)}{\partial p} \cdot p\Delta \ll f(p)$ then

$$F(j) \approx \frac{\Omega}{4\pi} f(j) \int_0^\infty e^{-\frac{(j-p)^2}{\Delta^2 j^2}} dp$$

Introducing the variable $x = \frac{p-j}{\Delta j}$, $\therefore \frac{dp}{\Delta j} = dx$

$$F(j) = \frac{\Omega}{4\pi} f(j) \Delta j \int_{-\frac{1}{\Delta} \approx -\infty}^{\infty} e^{-x^2} dx = \frac{\Omega \Delta}{4\sqrt{\pi}} j f(j) \qquad (88)$$

Thus the spectrum $f(j)$ and hence $f(p)$ can be obtained from $F(j)$ with the aid of equation (88).

Consider the integral $\int_0^\infty \frac{F(j)}{j} dj$, then

$$\int_0^\infty \frac{F(j)}{j}\,dj = \frac{\Omega}{4\pi}\int_0^\infty\int_\phi^\infty \frac{e}{j}^{-\frac{(j-\phi)^2}{\Delta^2\phi j}} f(\phi)\,d\phi\,dj \,.$$

Or

$$= \frac{\Omega}{4\pi}\int_\phi \left[\int_0^\infty e^{-\frac{1}{\Delta^2 j}\left(\frac{j}{\phi}-1\right)^2}\frac{dj}{j}\right] f(\phi)\,d\phi$$

Using the substitution $y = j/\phi$, $\therefore \frac{dj}{j} = \frac{dy}{y}$ there results

$$= \frac{\Omega}{4\pi}\int_\phi \left[\int_0^\infty e^{-\frac{1}{\Delta^2 y}(y-1)^2}\frac{dy}{y}\right] f(\phi)\,d\phi \,.$$

The integral inside the braces converges and is only a function of Δ, hence may be set equal to $T(\Delta)$. Finally then

$$\int_0^\infty \frac{F(j)}{j}\,dj = \frac{\Omega\, T(\Delta)}{4\pi}\int_\phi f(\phi)\,d\phi \,. \tag{89}$$

But $\int_\phi f(\phi)\,d\phi$ is just the total intensity of the source, thus the area under the $\frac{F(j)}{j}$ curve is proportional to the source strength.

For small Δ, $T(\Delta)$ may be readily evaluated since

$$T(\Delta) = \int_0^\infty e^{-\frac{1}{\Delta^2 y}(y-1)^2}\frac{dy}{y} \approx \int_{0\approx-\infty}^{\infty} e^{-\frac{(y-1)^2}{\Delta^2}}\,dy = \Delta\sqrt{\pi} \tag{90}$$

This result of course could be obtained directly from equation (88).

In all that has been said so far the source was assumed to be an isotropic radiator; if this is not the case, then since the spectrograph accepts only particles in the angular range θ_o

to $\theta_0 + d\theta_0$, the ratio of the total intensity to that within the solid angle Ω must be known and the proper corrections made.

It is convenient in some cases to obtain an inversion formula, that is obtaining $f(j)$ when $F(j)$ is known, which is one degree of approximation better than that given in equation (88). As in the derivation of that equation assume $\Delta \ll 1$, then as before equation (87) may be written

$$F(j) = \frac{\Omega}{4\pi} \int_0^\infty e^{-\frac{(j-p)^2}{\Delta^2 j^2}} f(p)\, dp \quad .$$

Introduce the substitution $p - j = z$ then

$$F(j) = \frac{\Omega}{4\pi} \int_{-j \approx -\infty}^{\infty} e^{-\frac{z^2}{\Delta^2 j^2}} f(z+j)\, dz , \qquad (91)$$

now $f(z+j)$ may be expanded in a Taylor series about j

$$f(z+j) = f(j) + z f'(j) + \frac{z^2}{2} f''(j) + \cdots \quad .$$

When this is substituted into equation (91) and integrated term by term there results,

$$F(j) = \frac{\Delta j}{4\sqrt{\pi}} \left[f(j) + \frac{\Delta^2 j^2}{4} f''(j) + \cdots \right] . \qquad (92)$$

We now introduce the function $\phi(j) = \frac{F(j)}{j}$, then

$$\frac{4\sqrt{\pi}}{\Delta} \phi(j) = f(j) + \frac{\Delta^2 j^2}{4} f''(j) + \cdots \quad ;$$

now since the second term in the right membrum is a small correction term, $\frac{4\sqrt{\pi}}{\Delta} \phi(j)$ may be taken equal to $f(j)$ in this

term, hence

$$f(j) = \frac{4\sqrt{\pi}}{\Delta}\left[\phi(j) - \frac{\Delta^2 j^2}{4}\phi''(j) + \cdots\right] . \qquad (93)$$

Thus while equation (87) may be viewed as the fold of the window curve into the primary distribution, equation (93) may be taken as the first approximation in the unfolding to obtain the primary spectrum. This approximation equation has been indicated by Owen and Primakoff[26].

The Energy Spectrum of the Electrons from the Converter based on an Approximate Theoretical Treatment

The discussion thus far has been in general terms with only occasional references to the problem of determining the observable spectrum of the electrons produced by the photoelectric effect in foils of finite thickness. Because of the effects of scattering and straggling in the foil, the number of electrons emerging in a given energy interval will decrease as the energy loss increases, leading to a primary spectrum with a maximum value for zero energy loss, tailing off monotonically toward lower energies at a rate determined by the initial photo electron energy and the converter thickness and atomic number. The observation of such a distribution with an instrument of finite resolution will in general result in a shifting of the peak and extrapolated front edge of the curve by a magnitude depending on the resolution and on the exact shape of the spectrum. We shall now turn to specific attempts to account for these effects.

Consider now that the foil illustrated in Fig. 20b is just the photo electron converter discussed above, and further consider only that part of the electron surface brightness at $X = X$ due to the conversion of γ-rays within a thickness dx at X. This surface brightness will be taken as uniform over the surface $X = X$ and independent of X as has already been discussed. This surface brightness can then be expanded in terms of the functions $g_s(\theta)$ and then imagined to propogate to the surface $X = \tau$ where it will be assumed that only the first term of the series need be considered. Hence,

$$i_{\tau-x}(\theta) = 2C_1' \cos\theta \, e^{-1.33K(\tau-x)} dx . \qquad (94)$$

It will be assumed that the energy loss may be correctly taken into account by simply considering the energy these electrons will lose in penetrating the thickness $\tau - X$, rather than modifying the differential equation (69). Further, if for the thicknesses of interest the straggling in energy loss is small compared to the most probable energy loss all the photoelectrons produced at the depth $\tau - X_o$ with energies E_o will arrive at $X = \tau$ with an energy

$$E = E_o - \left[\epsilon(\tau - x)\right] \cdot \left[\frac{l}{\tau - x}\right] \cdot \frac{\tau - x}{\cos\theta_o} \qquad (95)$$

where the functions $\epsilon(\tau - x)$ and $\frac{l}{\tau - x}$ are the ones discussed under the previous sections.

Unfortunately this assumption that the straggling can be neglected even over a small range of foil thicknesses and elec-

tron energies is not a very good one. For the time being, however, we shall proceed with this assumption to see what general conclusions result. We shall return to this point again later.

The location of the peak of the observed photo-line with respect to E_o the energy of the photo electron just at ejection is of interest. The electrons in the spectrum immediately in the neighborhood of the maximum are those which have suffered a percentage loss in energy roughly of the order of the resolution of the instrument or less and hence will not have undergone extensive scattering in the converter. Hence the $\frac{\ell}{\tau - x}$ term may be taken as unity approximately, further $\epsilon(\tau - x)$ may be replaced by a mean energy loss $\epsilon_m(\tau, K)$, therefore

$$dE \approx \frac{\epsilon_m}{\cos\theta_o} dx .$$

If for simplification we consider a shift in the origin of the distribution such that $E_o = 0$ and consider indefinitely thick foils, the number of electrons having energies between E and $E + dE$ in the primary spectrum is

$$dn = 4\pi C' e^{\frac{1.33 K \cos\theta_o E}{\epsilon_m}} dE \tan\theta_o d\theta_o , \qquad (96)$$

and the observed spectrum becomes

$$N = \frac{1}{\sigma}\sqrt{\frac{2}{\pi}}\, const(\sigma, \Omega, \theta_o) \cdot \int_{-E_o \approx -\infty}^{0} e^{1.33\frac{K}{\epsilon_m}\cos\theta_o E - \frac{(E-E_1)^2}{2\sigma^2}} dE \qquad (97)$$

where σ is proportional to the instrument resolution and will be taken constant over the range of integration.

Let W_o be the full width at half maximum of the window curve then writing

$$E = x \quad , \quad E_1 = X_1$$
$$1.33\,K/\epsilon_m \cos\theta_0 = \beta \qquad (98)$$
$$2\sigma^2 = .360\,W_0^2$$

equation (97) becomes,

$$y(X_1) = C_N \int_{-\infty}^{0} e^{\beta x} e^{-\frac{(x-X_1)^2}{.360\,W_0^2}}\,dx \quad . \qquad (99)$$

The plot of Fig. 25 shows y as a function of X_1 in units of W_0 for various values of β in units of $1/W_0$. The value of C_N was adjusted to give unity for the maximum value of the function y. The high energy extrapolated edge X_c is determined by extending the slope at the point of inflection and is also shown in this figure. The largest value of this extrapolated edge occurs for the window curve itself, that is $\beta = \infty$ and has the value $\frac{X_c}{W_0} = .850$, while the smallest value is $\frac{X_c}{W_0} = .583$ for the case $\beta = 0$. If we let W represent the observed full width at half maximum, Fig. 26 gives X_c/W_0 as a function of W_0/W . While the values of X_c/W_0 are limited to within a comparatively narrow range of values, the displacement of the peak X_p from the peak of the window curve $\frac{X_1}{W_0} = 0$, ranges from zero for $\beta = \infty$ to an indefinitely large value for $\beta = 0$. Fig. 27 shows X_p/W_0 as a function of βW_0.

It will be shown later after a somewhat more general treatment, that in the range of electron energies E_0 from 0.2 to 1.0 Mev and for instrument resolution widths less than about 5% the peak shift cannot exceed the half width at $1/e$ of the maximum of the

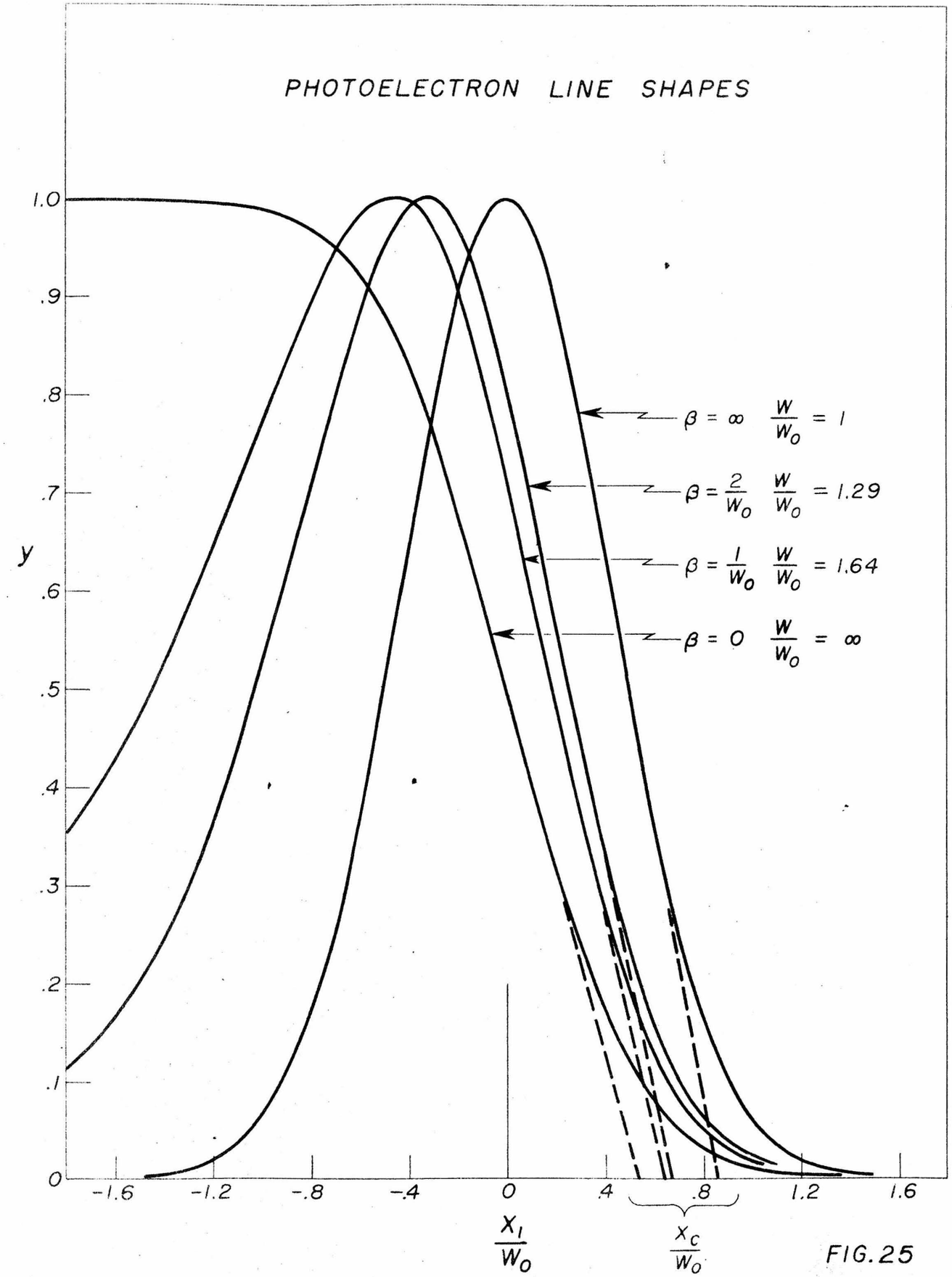
PHOTOELECTRON LINE SHAPES
1.0
.9
.8
.7
y
.6
.5
.4
.3
.2
.1
0
β = ∞ W/W0 = 1
β = 2/W0 W/W0 = 1.29
β = 1/W0 W/W0 = 1.64
β = 0 W/W0 = ∞
-1.6
-1.2
-.8
-.4
0
.4
.8
1.2
1.6
X1/W0
Xc/W0

FIG. 25

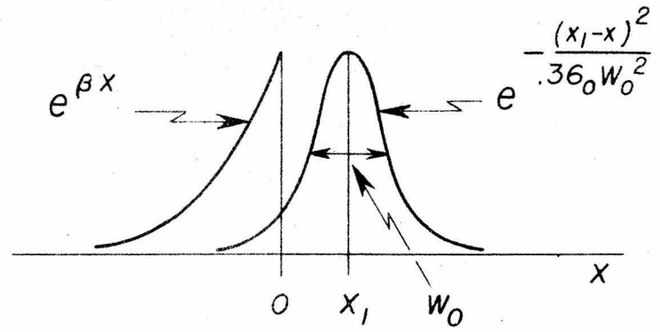

$$y = C_N \int_{-\infty}^{0} e^{\beta x} \, e^{-\frac{(x_1-x)^2}{.36_0 W_0^2}} \, dx$$

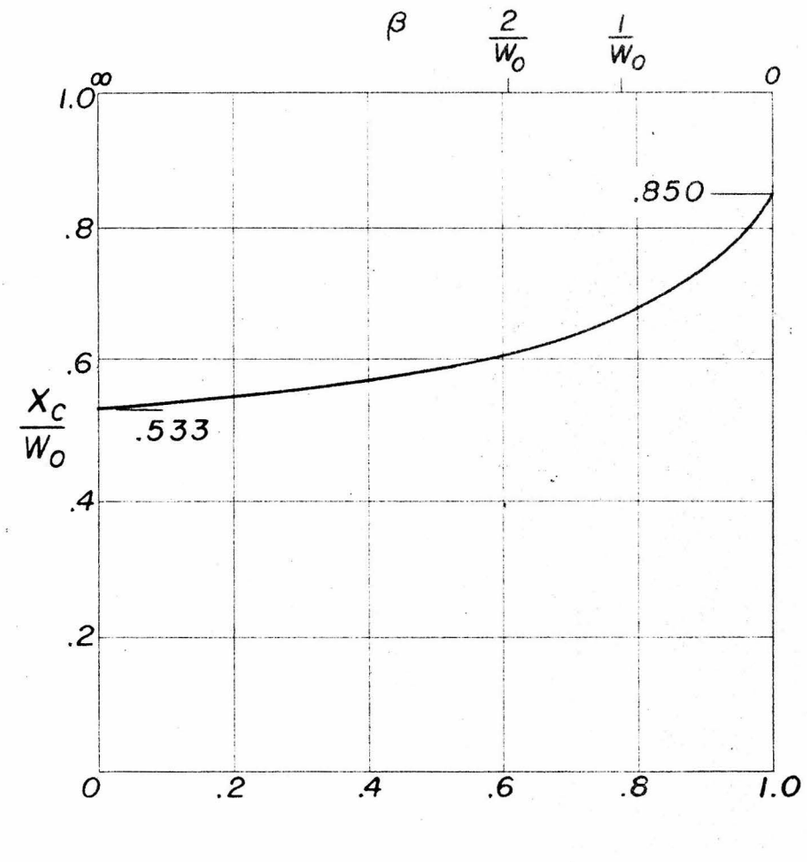

W_0 = Full width at half maximum of window

W = Observed full width at half maximum

$\frac{X_c}{W_0}$ = Extrapolated front edge

FIG. 26

PEAK SHIFT FUNCTION

$$y = C_N \int_{-\infty}^{0} e^{\beta x} e^{-\frac{(X_1 - X)^2}{.36_0 W_0^2}} dx$$

W_0 = Full width at half maximum of window

$\frac{X_p}{W_0}$ = Peak shift

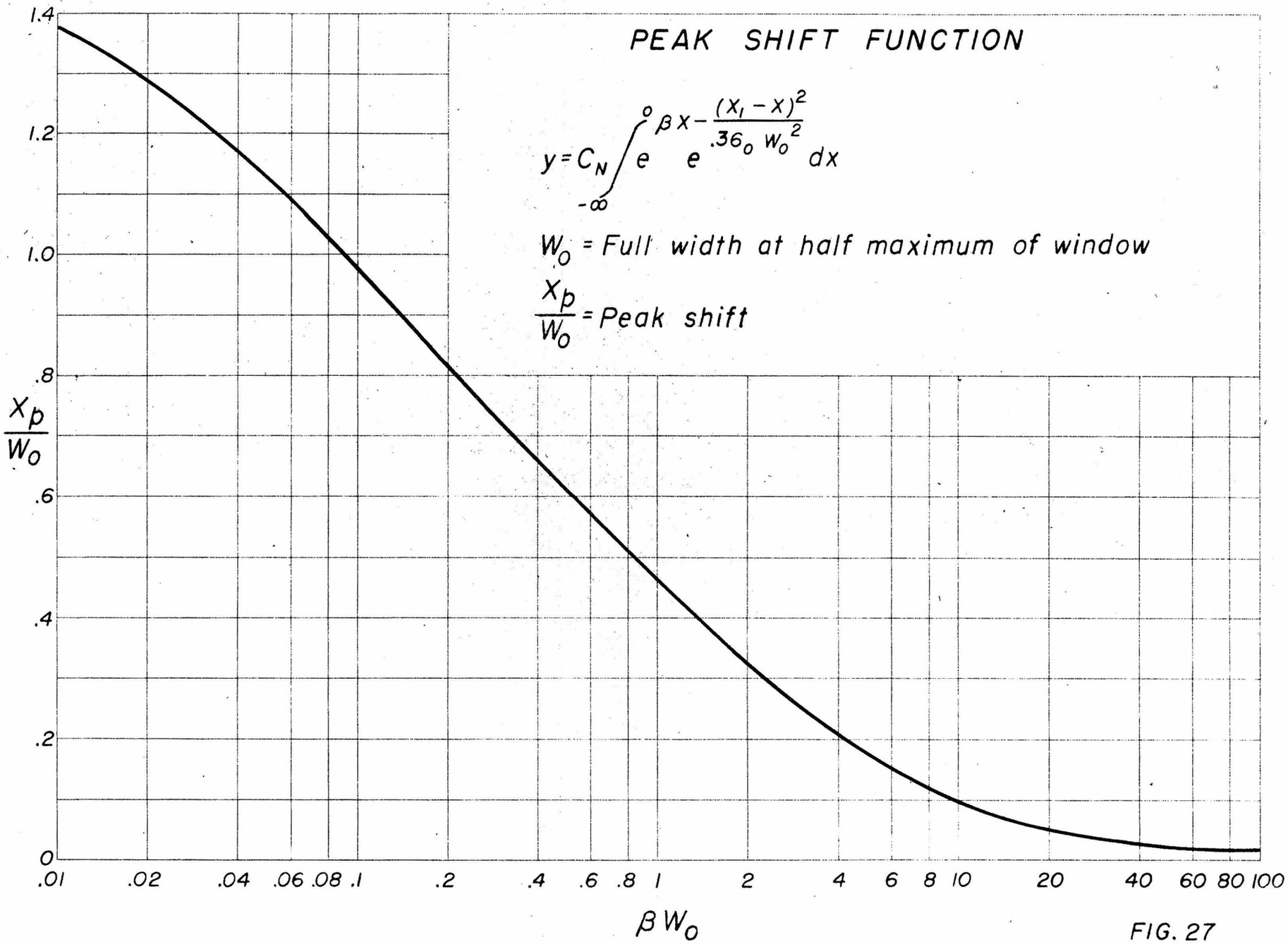

FIG. 27

PEAK SHIFT FUNCTION

$$y = C_N \int_{-\infty}^{0} e^{\beta x} e^{-\frac{(X_1 - X)^2}{.36_0 W_0^2}} dx$$

W_0 = Full width at half maximum of window

$\frac{X_p}{W_0}$ = Peak shift

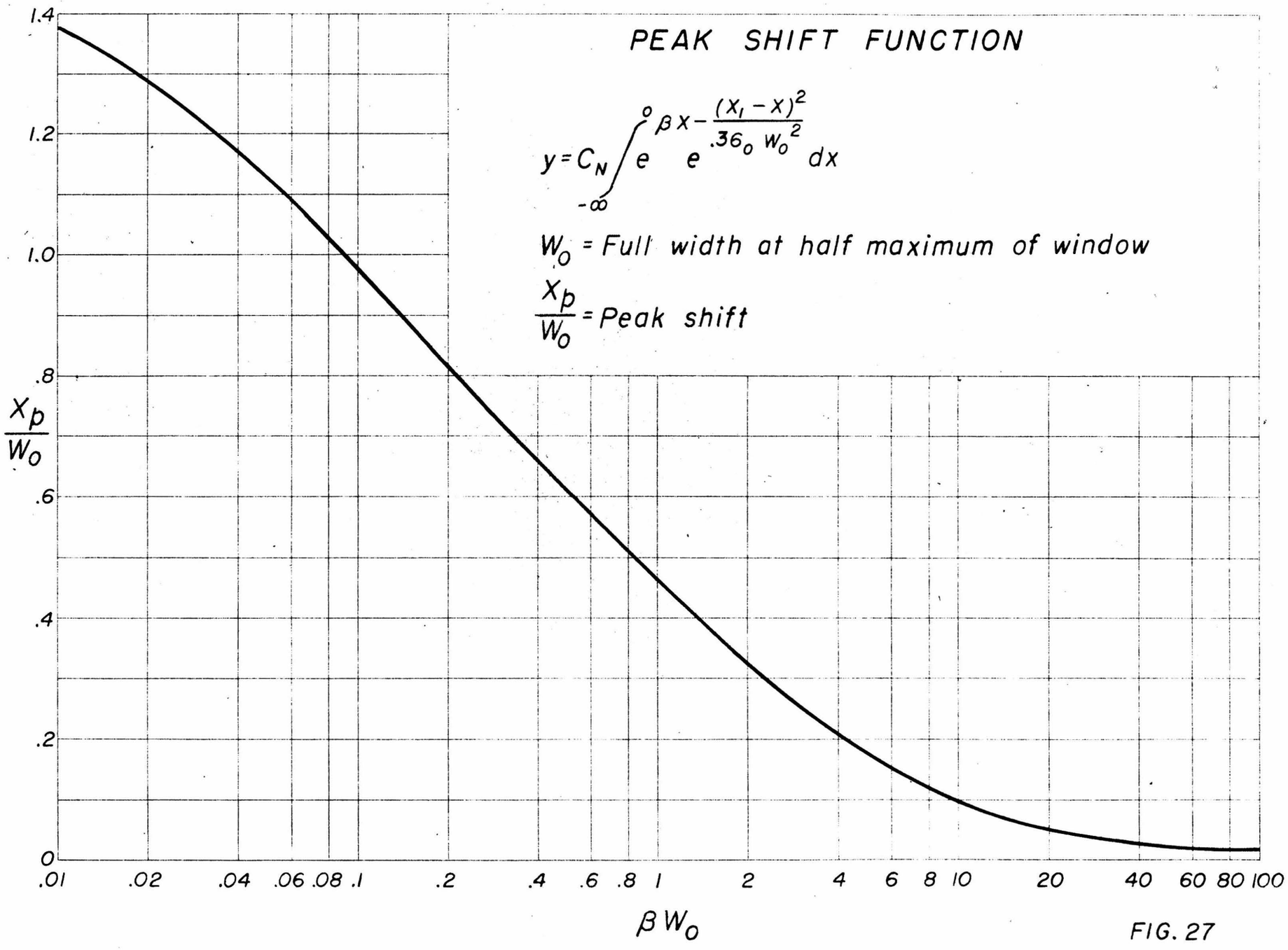

FIG. 27

window curve. This limit is quite insensitive to the exact shape of the primary distribution and depends only on the fact that the primary distribution which decreases monotonically from a maximum at zero energy loss to half intensity at a value corresponding roughly to the most probable energy loss in the "transport mean free path". The transport mean free path is defined as the distance in which the root mean square scattering angle becomes of the order of $\pi/4$.

It will be instructive at this point to consider the other extreme case, namely that of "thin" converters. For thin converters, in which the energy loss is small compared to the resolution width, Jensen, Laslett, and Pratt[27] have pointed out that, if straggling is neglected, the primary distribution can be approximated by a rectangle of width equal to the average energy loss in the foil, and that the resulting peak shift is one-half this width. The straggling in energy loss due to the relatively infrequent close collision is as has been discussed, however, an appreciable factor, and will have the effect of spreading the electron distribution on the low energy side. Since the average energy loss is heavily weighted by the small fraction of electrons which have lost large amounts of energy and which thus will have little influence on the peak location, it would seem reasonable that the effective width of the distribution is better measured by the most probable energy loss, which gives more equitable weighting to the majority of the electrons. The importance of straggling effects even in the

region from 1 to 3 Mev may be judged from the fact that the most probable energy loss is about a factor of two lower than the average energy loss.

As a slightly more refined calculation than has been carried out so far the case of a finite thickness of converter may be considered. Returning to the case with the origin of the distribution at zero energy, we have, referring to equation (96),

$$dn = 4\pi C' e^{-1.33 \frac{K\gamma}{\epsilon_m} \cos\theta_0 (E_0 - E)} dE \tan\theta_0 d\theta_0 \qquad (100)$$

The factor γ has been introduced to permit an adjustment of the "absorption coefficient" to match the experimental results which will be considered later. Thus the following results will be taken as semi-empirical in nature with γ to be appropriately adjusted.

The most probable energy for the electrons originating from the extreme depth of the foil is

$$E_2 = E_0 - \epsilon(\tau)\left[\frac{l}{\tau}\right]\frac{\tau}{\cos\theta_0} \quad . \qquad (101)$$

Thus integrating equation (100) from E_2 to E_0 we have an approximation to the spectrum for a finite thickness of foil; this integral is

$$N = \frac{1}{\sigma}\sqrt{\frac{2}{\pi}}\, const(\sigma, \Omega, \theta_0) \cdot \int_{E_2}^{E_0} e^{-1.33 \frac{K\gamma}{\epsilon_m} \cos\theta_0 (E_0 - E) - \frac{(E - E_1)^2}{2\sigma^2}} dE \, . \qquad (102)$$

It will be expedient to introduce the parameter

$$\alpha = 1.33 \frac{K\gamma}{\epsilon_m} \cos\theta_0$$

Thus expanding and regrouping the exponent gives

$$N = \frac{C}{\sigma}\sqrt{\frac{2}{\pi}} \int_{E_2}^{E_0} e^{-\frac{1}{2\sigma^2}\left[E^2 - 2(E_1+\alpha\sigma^2)E + E_1^2 + 2\alpha\sigma^2 E_0\right]} dE$$

Completing the square gives

$$N = \frac{2C}{\sqrt{\pi}} e^{-\alpha(E_0-E_1)} e^{\frac{\alpha^2\sigma^2}{2}} \int_{E_2}^{E_0} e^{-\frac{1}{2\sigma^2}\left[E-(E_1+\alpha\sigma^2)\right]^2} \frac{dE}{\sqrt{2}\sigma}$$

now letting $\xi = \dfrac{E-(E_1+\alpha\sigma^2)}{\sqrt{2}\sigma}$ there results

$$N = \frac{2C}{\sqrt{\pi}} e^{-\alpha(E_0-E_1)} e^{\frac{\alpha^2\sigma^2}{2}} \int_{\frac{E_2-(E_1+\alpha\sigma^2)}{\sqrt{2}\sigma}}^{\frac{E_0-(E_1+\alpha\sigma^2)}{\sqrt{2}\sigma}} e^{-\xi^2} d\xi \quad .$$

Finally this last equation may be readily integrated in terms of the error function to give

$$N(E_1) = Ce^{-\alpha(E_0-E_1)} e^{\frac{\alpha^2\sigma^2}{2}} \left\{ erf\left(\frac{E_0-E_1-\alpha\sigma^2}{\sqrt{2}\sigma}\right) + erf\left(\frac{E_1-E_2+\alpha\sigma^2}{\sqrt{2}\sigma}\right)\right\} .$$

Here again σ has been taken as constant over the range of integration, however, it will be considered as a function of E_0. Introducing the variables u, w, Z and collecting the various definitions,

$$\alpha = 8.45\times10^{5}\frac{\gamma\cos\theta_0}{\epsilon_m}\left[\frac{E_0+511}{E_0(E_0+1022)}\right] \qquad \text{for Thorium}$$

$$\sigma = .425\,\frac{E_0(E_0+1022)}{E_0+511}\left(\frac{dB\rho}{B\rho}\right)$$

$$u = \frac{\alpha\sigma}{\sqrt{2}} = 2.54\times10^{5}\frac{\gamma\cos\theta_0}{\epsilon_m}\,\frac{E_0+511}{E_0(E_0+1022)}\left(\frac{dB\rho}{B\rho}\right) \qquad (103)$$

$$w = \frac{E_0 - E_1}{\sqrt{2}\,\sigma}$$

$$z = \frac{\epsilon(z)}{\sqrt{2}\,\sigma}\left[\frac{l}{z}\right]\frac{z}{\cos\theta_0}$$

where the energy unit is the Kev and the unit of length is the mil and $100\left(\frac{dB\rho}{B\rho}\right)$ is the full width at half maximum of the window curve of the spectrometer expressed percentagewise, then we have

$$N(w) = Ce^{-2uw}e^{u^2}\left\{\operatorname{erf}(w-u) + \operatorname{erf}(u-w+z)\right\}. \quad (104)$$

The peak of this distribution is given by

$$\frac{\partial N(w)}{\partial w} = 0$$

or

$$u\sqrt{\pi}\left\{\operatorname{erf}(w'-u) + \operatorname{erf}(u-w'+z)\right\} = e^{-(w'-u)^2} - e^{-(u-w'+z)^2} \quad (105)$$

The shift of the peak from E_0 is then $\Delta = \sqrt{2}\,\sigma w'$. A plot of w' as a function of u with z as a parameter is given in Fig. 28 *a* and *b* . Note that for large E_0, that is $u \to 0$, equation (105) gives

$$u'^2 = u'^2 - 2u'z + z^2 \qquad \text{or} \qquad u' = \frac{z}{2}$$

hence

$$\Delta = \frac{\epsilon(z)}{2}\left[\frac{l}{z}\right]\frac{z}{\cos\theta_0} \quad (106)$$

which is just the peak shift discussed under the "thin" foil approximation.

For thick foils $z \to \infty$, and hence equation (105) becomes

$$u\sqrt{\pi}\left\{\operatorname{erf}(w'-u) + 1\right\} = e^{-(w'-u)^2}$$

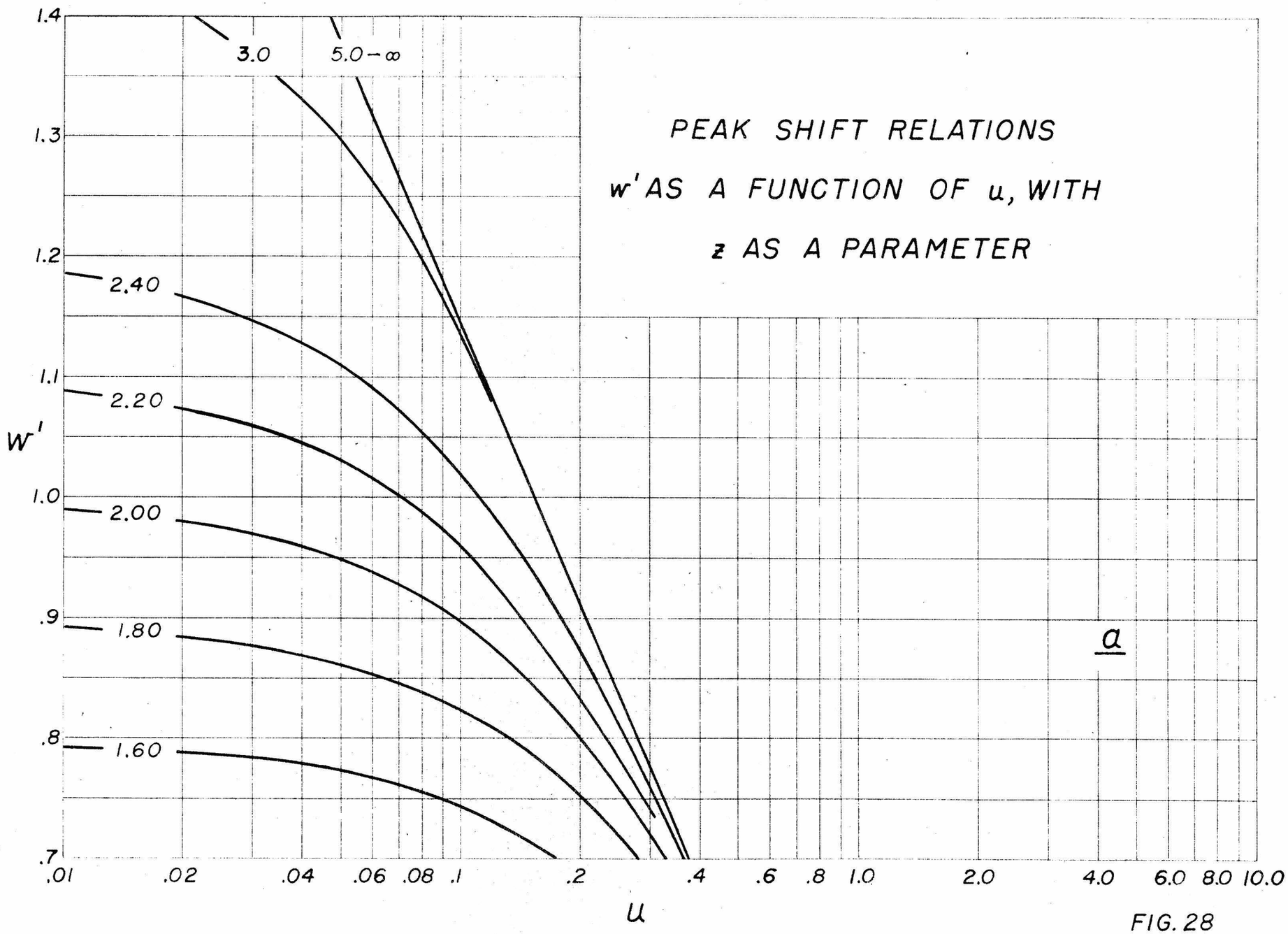
PEAK SHIFT RELATIONS
w' AS A FUNCTION OF u, WITH
z AS A PARAMETER
3.0
5.0 – ∞
2.40
2.20
2.00
1.80
1.60
w'
1.4
1.3
1.2
1.1
1.0
.9
.8
.7
.01
.02
.04
.06
.08
.1
.2
.4
.6
.8
1.0
2.0
4.0
6.0
8.0
10.0
u
a

FIG. 28

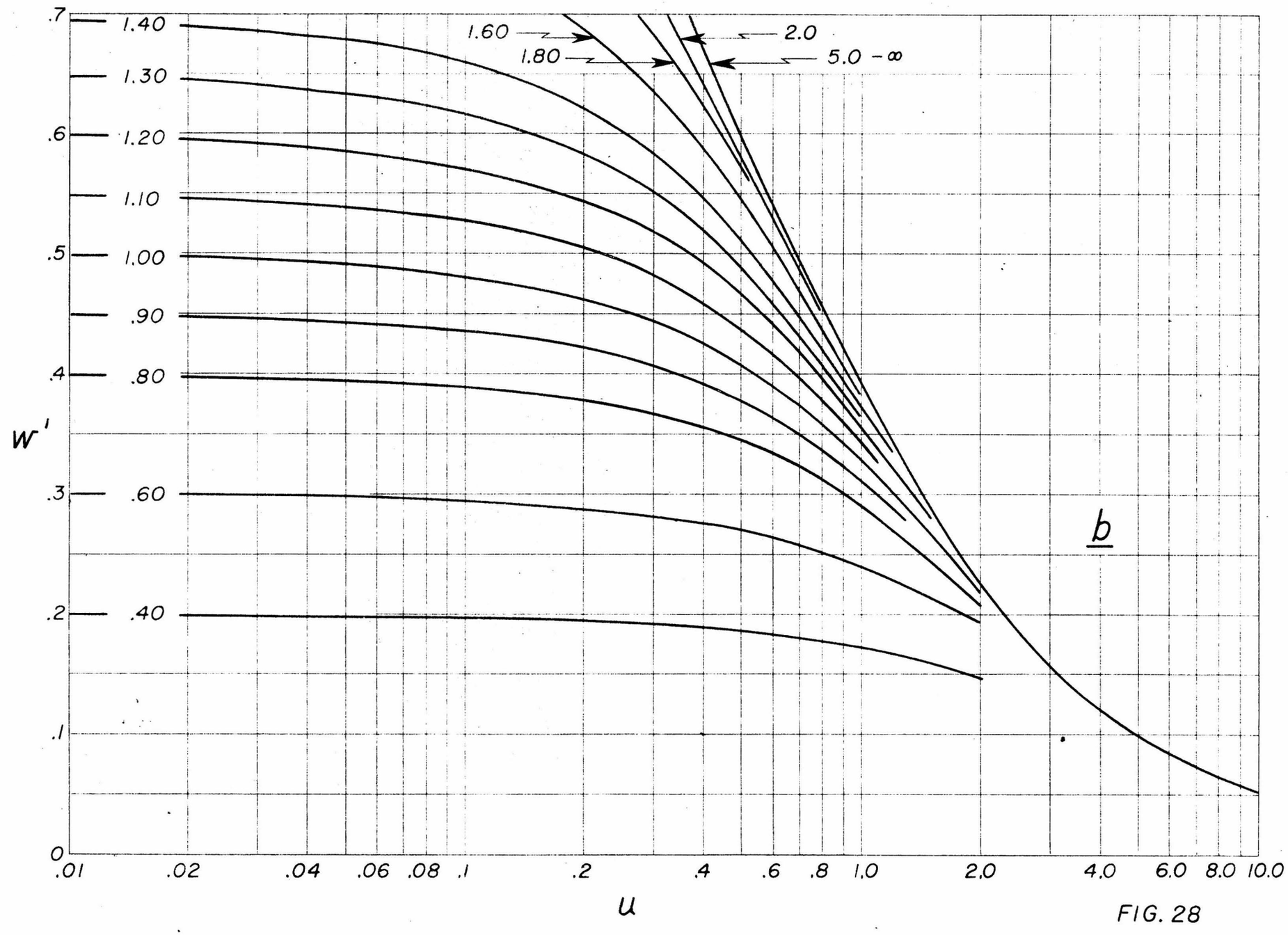
.7
.6
.5
.4
.3
.2
.1
0
W'
1.40
1.30
1.20
1.10
1.00
.90
.80
.60
.40
1.60
1.80
2.0
5.0 - ∞
b
.01
.02
.04
.06
.08
.1
.2
.4
.6
.8
1.0
2.0
4.0
6.0
8.0
10.0
u

FIG. 28

now if further $|w' - u| < 1$

$$\operatorname{erf}(w'-u) = \frac{2}{\sqrt{\pi}}\left[(w'-u) - \frac{(w'-u)^3}{3} + \cdots\right]$$

$$e^{-(w'-u)^2} = 1 - (w'-u)^2 + \frac{(w'-u)^4}{2} + \cdots$$

whence $$u\sqrt{\pi}\left\{1 + \frac{2}{\sqrt{\pi}}(w'-u) + \cdots\right\} = 1 - (w'-u)^2 + \cdots$$

or $$u\sqrt{\pi} + 2uw' - 2u^2 = 1 - w'^2 + 2uw' - u^2$$

hence $$w' = \sqrt{1 + u^2 - \sqrt{\pi}\,u}$$

which implies

$$\Delta \approx \sqrt{2}\,\sigma\sqrt{1 + u^2 - \sqrt{\pi}\,u} \quad . \qquad (107)$$

Combining the definition of ϵ from equation (82) with the definition of u from equation (103)

$$u = \frac{2.54\times10^5\,\gamma\cos\theta_0}{2\pi N e^4 \rho\, Z/A}\left[\ln\frac{2F_c}{a_0}^3 + 0.37 - (1-F_c)\beta^2\right]^{-1}\left(\frac{dB\rho}{B\rho}\right)\frac{511}{E_0+511} \quad .$$

The function within the bracket is very slowly energy dependent hence as far as the energy dependence is concerned

$$u = (\text{essentially const})\cdot\left(\frac{dB\rho}{B\rho}\right)\cdot\frac{511}{E_0+511} \quad .$$

For resolutions better than 5% and for energies E_0 in the range 0.2 - 1.0 Mev for thorium converter, the approximation that leads to equation (107) is fairly reliable and $u < \sqrt{\pi}$; hence Δ is always less than $\sqrt{2}\,\sigma$ which is the half width at $1/e$ of the maximum of the window curve. Further, to the extent that the factor $\frac{511}{E_0+511}$ may be considered to be independent

of E_o , Δ is proportional to σ. Thus for thick converters the peak shift depends mostly on the instrument resolution. This result has also been obtained by Jensen, Laslett, and Pratt based on somewhat different qualitative arguments.

To recapitulate then, the limiting cases for thick and thin converters are founded on general considerations and do not depend markedly on the exact form of the distribution of equation (100). The curves of Fig. 28 as applied to intermediate cases should be viewed essentially as a method of interpolation between these extreme limits. In this connection the constant γ is available for adjustment to match experimental data. Thus while the assumptions made in obtaining equation (100) may have seemed a little severe the applicability of the results is established.

Another approach to the problem of accounting for the primary spectrum and thereby studying such effects as peak shift and extrapolated edge shift is to make use of the universal nature of the straggling curves of White and Millington. Unfortunately since this method cannot be applied analytically a numerical integration must be performed for each converter thickness and each electron energy E_o.

The procedure is to divide the converter into a number of laminae of equal thickness. Assume that all the electrons produced within one such lamina originate at the center of the lamina and must traverse the remainder of the foil equal in thickness to $d_n = (n - \frac{1}{2})\,\delta$ where δ is the laminar thick-

ness and the n^{th} lamina from the front face of the foil is under consideration. The most probable energy loss for d_n is then calculated and energy units in which $X = 29$ corresponds to this loss are taken, then

$$y_n = \frac{1}{d_n} g_n(x) e^{-\frac{1.33K}{\cos\theta_0} d_n}$$

represents the distribution from the n^{th} lamina. Here $g_n(x)$ is taken from Fig. 24 and Bothe's absorption factor has been used; d_n appears in the denominator to normalize $g_n(x)$ to unit area. The total primary distribution is then given by a smooth curve through

$$y = \sum_{n=1}^{t/\delta} \frac{g_n(x)}{(n-\frac{1}{2})\delta} e^{-\frac{1.33K\delta}{\cos\theta_0}(n-\frac{1}{2})} \qquad (108)$$

As an example of this approach a foil thickness and energy have been selected which may be compared with experimental results later. A Thorium metal converter having a thickness of .0005" was taken and an electron energy $E_0 = 300$ Kev used; the value of θ_0 was 13°. The foil was divided into 10 equal laminae. The curve in Fig. 29 shows the resulting curves; the first few y_n functions are given as well as the resultant sum. The dotted curve is for the sum of the first 5 laminae only. More will be said of these curves later, under the section discussing the experimental results.

A type of diffusion theory which is useful in treating the problem of neutron slowing down theory[28] has been applied in a modified form to investigate the nature of the primary distri-

DISTRIBUTION PREDICTED FROM
WHITE AND MILLINGTON CURVES
411 KEV Au^{198}
THORIUM CONVERTER

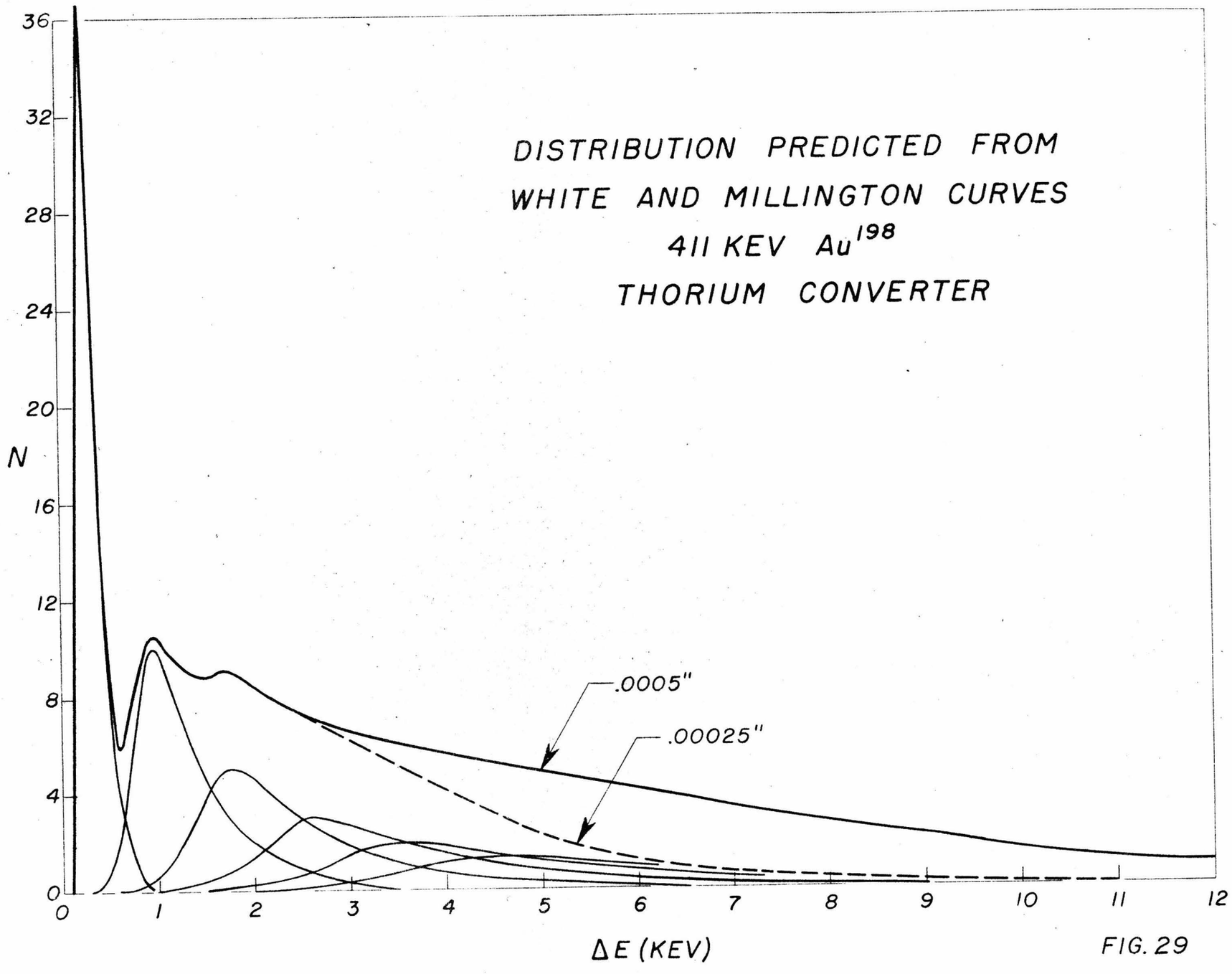

FIG. 29

bution for comparatively large energy losses. We define q as the number of electrons crossing energy E per cm^3 per sec. The Fermi age equation then governs the behavior of the electrons in their motion through the matter of the converter; this equation is

$$\nabla^2 q = \frac{\partial q}{\partial \tau} ,$$

which for a two dimensional problem simply gives

$$\frac{\partial^2 q}{\partial x^2} = \frac{\partial q}{\partial \tau} \tag{109}$$

Here X is the coordinate measured along the surface normal of the foil, the origin being taken at the extreme depth of the foil as illustrated in Fig. 30a; $X = a$ gives the front face of the foil. The variable τ is the so called "age" given by

$$\tau = \int_E^{E_0} \frac{\lambda_s \lambda_d}{3\xi} \frac{dE}{E} \tag{110}$$

where ξ is the number of collisions per second and λ_s and λ_d are the mean free paths for scattering and diffusion respectively. This last equation may be written approximately as,

$$\tau = \int_E^{E_0} \frac{\lambda_s}{3} \frac{dE}{\partial E/\partial x} \approx \frac{\lambda_s}{3} \frac{\Delta E}{\partial E/\partial x} , \quad \Delta E = E_0 - E \tag{111}$$

We try the solution

$$q = f(x)\, g(\tau)$$

in equation (109) which gives upon separation of variables

$$\begin{aligned} \frac{\partial^2 f}{\partial x^2} + \gamma^2 f &= 0 \\ \frac{\partial g}{\partial \tau} + \gamma^2 g &= 0 \end{aligned} \tag{112}$$

SLOWING DOWN THEORY

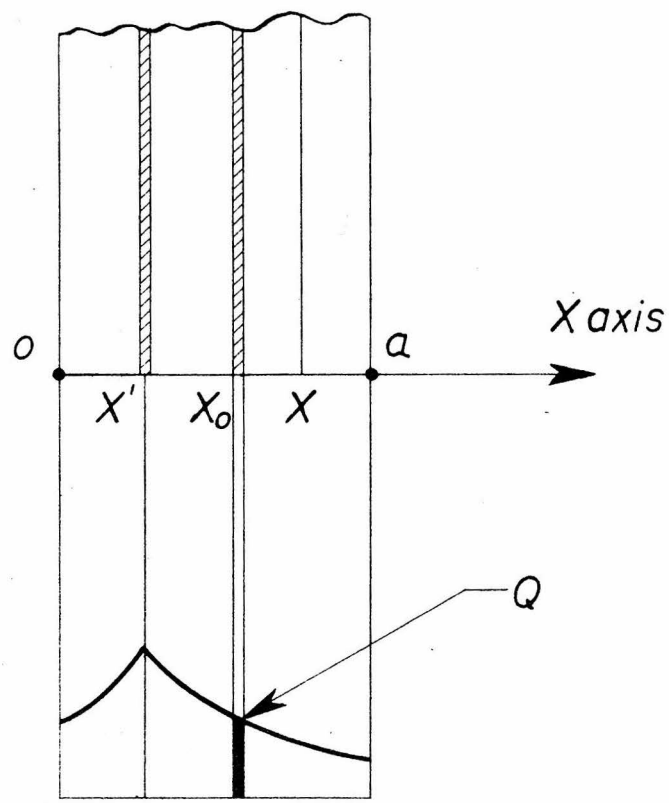

a

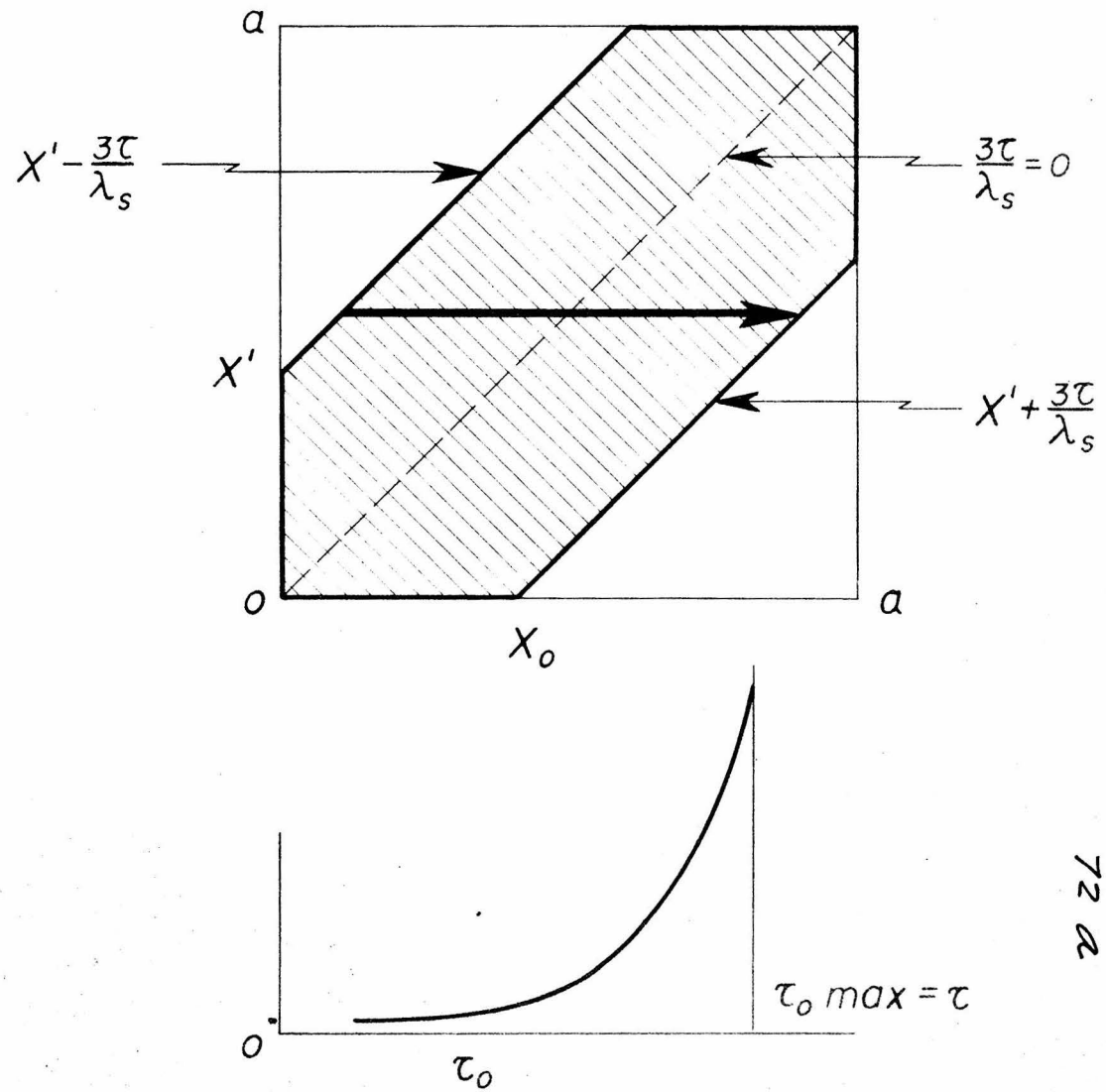

b

FIG. 30

72 a

with $-\gamma^2$ as the separation constant. The solutions are

$$g = Ce^{-\gamma^2 \tau}$$
$$f = A \sin \gamma x + B \cos \gamma x \qquad (113)$$

Now $g = 0$ at $x = 0$, $x = a$ hence $B = 0$ and $\gamma = \frac{\pi n}{a}$, thus the general solution is

$$g = \sum_{n=1}^{\infty} C_n \sin \frac{\pi n}{a} x \, e^{-\frac{\pi^2 n^2}{a^2} \tau} .$$

The physical processes occuring within the converter are imagined to consist firstly, in the uniform liberation of photo-electrons throughout the volume of the foil which then propagate in accordance with Bothe's multiple scattering formula to a mean distance λ_s, secondly these electrons are then taken as diffusion sources and continue their existence as diffusion electrons. With this picture in mind, for $\tau = \tau_0$,

$$g = Q \delta(x - x_0)$$

and $$\int_0^a \sin \frac{\pi m}{a} x \, Q \delta(x - x_0) dx = \sum_{n=1}^{\infty} \int_0^a C_n \frac{\pi n}{a} e^{-\frac{\pi^2 n^2 \tau_0}{a^2}} \sin \frac{\pi n}{a} x \sin \frac{\pi m}{a} x \, dx$$

or $$Q \sin \frac{\pi n}{a} x_0 = C_n \frac{a}{\pi n} \left(\frac{a}{2} \frac{\pi n}{a} \right) e^{-\frac{\pi^2 n^2}{a^2} \tau_0}$$

$$\therefore \quad C_n = \frac{2Q}{a} \sin \frac{\pi n}{a} x_0 \, e^{\frac{\pi^2 n^2}{a^2} \tau_0} \qquad (114)$$

with $$Q = Q' e^{-\frac{|x' - x_0|}{\lambda_s}} dx' dx_0$$

where Q' is constant depending only on the γ-ray intensity and photoelectric cross-section. The processes involved may perhaps be better visualized by referring to Fig. 30a. Thus

$$g = \frac{2Q'}{a} \sum_{n=1}^{\infty} \sin \frac{\pi n}{a} x_0 \sin \frac{\pi n}{a} x \, e^{-\frac{\pi^2 n^2}{a^2} (\tau - \tau_0)} e^{-\frac{|x' - x_0|}{\lambda_s}} dx' dx_0 \qquad (115)$$

The actual density of electrons will result upon integration over all the sources,

$$\rho = \frac{2Q'}{a}\int_0^a dx' \int_{X_{0min}}^{X_{0max}} dX_0 \sum_{n=1}^{\infty} \sin\frac{\pi n}{a}X_0 \sin\frac{\pi n}{a}x\, e^{-\frac{\pi n^2}{a^2}(\tau-\tau_0)} e^{-\frac{|x'-X_0|}{\lambda_s}} \qquad (116)$$

with $\tau_0 \approx \frac{\lambda_s}{3}|x'-X_0|$ which represents the "aging" in going from the primary source at x' to the secondary source at X_0. It is clear that since τ_0 represents the minimum aging $\tau > \tau_0$ hence $X_0 - \frac{3\tau}{\lambda_s} < x' < X_0 + \frac{3\tau}{\lambda_s}$ provided the left membrum of this inequality is positive and the right membrum is less than a. A typical path of integration over dX_0 is illustrated by the horizontal arrow in Fig. 30b. This figure also shows the behavior of the term $\exp-\left[\frac{\pi n^2}{a^2}(\tau-\tau_0)\right]$. The limits on the integral of equation (116) are

$$X_{0max} \quad \left\{ \begin{matrix} x' + \frac{3\tau}{\lambda_s} \\ a \end{matrix} \right\} \qquad \text{which ever is smaller}$$

$$X_{0min} \quad \left\{ \begin{matrix} x' - \frac{3\tau}{\lambda_s} \\ 0 \end{matrix} \right\} \qquad \text{which ever is larger}$$

The gradient of ρ at the surface $x = a$ then gives the distribution of electrons desired, or

$$y = \frac{\partial \rho}{\partial x}\Big|_{x=a} = F\left(\frac{\tau}{a^2}, \frac{a}{\lambda_s}\right) \qquad (117)$$

where it will be recalled,

$$\tau/a^2 = \frac{\lambda_s}{3a^2}\,\frac{\Delta E}{\epsilon_m} \quad ;$$

here a mean value for the most probable energy loss ϵ has been used. Thus y may be obtained as a function of ΔE, the energy

loss. The integration of equation (116) has been carried out, the algebraic complications are too great to reproduce here, and equation (117) applied for a = .0005", E_o = 300 Kev, θ_o = 13°, ϵ_m = 16.7 Kev/mil and using Bothe's theory,

$$\lambda_s = \frac{1}{1.33K} = 1.18 \times 10^{-6} \left[\frac{E_o(E_o+1022)}{E_o+511} \right]^2 \text{ cm.}$$

The results are given in Fig. 31; they are expected to be reliable for energy losses in excess of $\epsilon \lambda_s$ = 4.7 Kev. The expectation is that in the region of zero energy loss this theory is inapplicable.

Before concluding this section on approximate treatments it would be desirable to investigate the possibility of finding coordinates which would enable one to compare primary, that is unfolded, experimental spectra of widely different electron energies and foil thicknesses. For these purposes the universality of the White and Millington curve will be used, thus the results will not be expected to apply for very small energy losses, as discussed. The arguments presented will be in broad general terms. Again it will be supposed that the electron behavior within the matter of the converter can be thought of in terms of scattering and straggling in energy loss separately. Thus the primary distribution in depth dN, that is the number of electrons in the primary spectrum originating from a lamina dx at a depth x, will depend in some way on x/λ_s due to scattering absorption; here $\lambda_s = \frac{1}{1.33K}$ is the mean free path in Bothe's theory. While the solutions proposed by Bothe on the

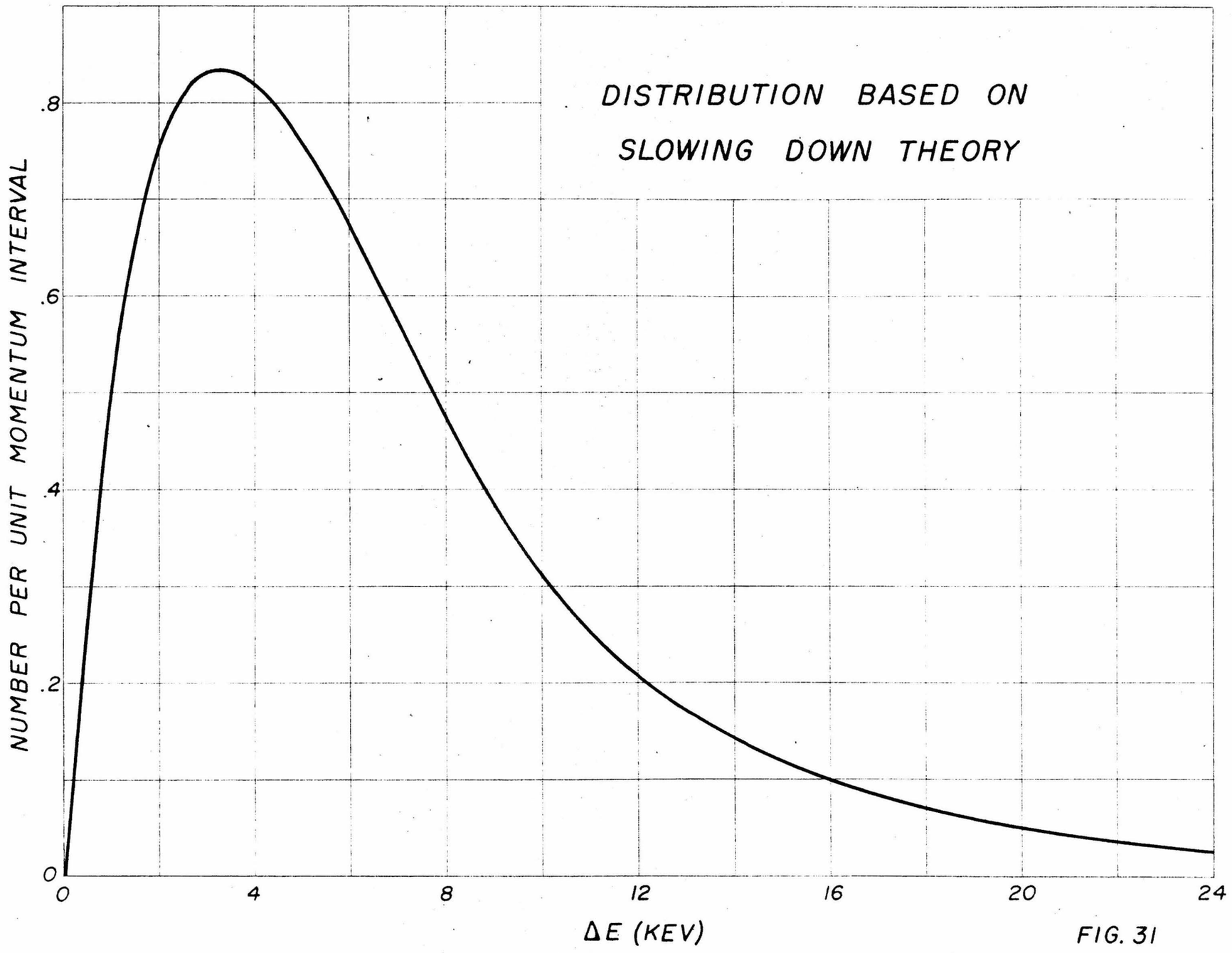
DISTRIBUTION BASED ON
SLOWING DOWN THEORY
NUMBER PER UNIT MOMENTUM INTERVAL
.8
.6
.4
.2
0
0
4
8
12
16
20
24
ΔE (KEV)

FIG. 31

one hand and Bethe, Rose, and Smith on the other hand do not agree as to the nature of the expression for dN they both agree that it is a function of x/λ_s. The effects of back scattering would be expected to depend on a/λ_s, where a is the foil thickness. Hence we take

$$dN = f(x/\lambda_s, a/\lambda_s)\,dx. \tag{118}$$

Again using the technique discussed under the numerical integration of the White and Millington curve, these dN electrons will experience energy loss and straggling resulting in an energy distribution

$$dy = \frac{1}{\epsilon_m x \mu}\, g\left(\frac{\Delta E}{\epsilon_m x \mu}\right) dN \tag{119}$$

where ϵ_m is the mean most probable energy loss for the range of thickness of interest and $\mu = \ell'/x$ is the factor by which the scattering increases the path length. It will be recalled under the discussion of path length corrections that μ is a function of x/x_m, however, x_m is just λ_s up to some multiplicative constants, hence $\mu = \mu(x/\lambda_s)$. Integrating equation (119) then gives the desired distribution,

$$y = \int_0^a \frac{1}{\epsilon_m x \mu} f\left(\frac{x}{\lambda_s}, \frac{a}{\lambda_s}\right) g\left(\frac{\Delta E}{\epsilon_m x \mu}\right) dx .$$

Introducing the variable $z = x/\lambda_s$ we have,

$$y = \frac{1}{\epsilon_m} \int_0^{\frac{a}{\lambda_s}} \frac{1}{z\mu(z)} f\left(z, \frac{a}{\lambda_s}\right) g\left[\frac{\Delta E}{\epsilon_m \lambda_s} \cdot \frac{1}{z\mu(z)}\right] dz .$$

Thus

$$y = \frac{1}{\epsilon_m} F'\left(\frac{\Delta E}{\epsilon_m \lambda_s}, a/\lambda_s\right). \qquad (120)$$

We note that the function F of equation (117) discussed under the slowing down theory depends on the same factors that F' above does, namely $\frac{\Delta E}{\epsilon_m \lambda_s}$ and a/λ_s. Thus except for very small energy losses the unfolded distributions when plotted as a function of $\frac{\Delta E}{\epsilon_m \lambda_s}$ with a/λ_s as parameters would give curves of a universal nature.

Unfortunately as yet there is no adequate theory to properly take into consideration the distribution at very low energy losses ΔE. This part of the distribution will be relegated to an empirical survey only.

Experimental Results*

The experimental work on the photoelectric effect and its application to the problem of determining γ-ray energies was mainly done with two instrument configurations. Some work was done with only two focusing coils separated 29" on centers and spaced symmetrically with respect to the source and detector window. The resolution used was 3.0% for this arrangement and $\theta_o = 30^o$. Work of somewhat higher intrinsic accuracy was done using all four focusing coils in the centered configuration. For this arrangement a resolution of 1.5% was used, and $\theta_o = 13^o$ The solid angle was estimated to be 0.5% of a sphere. In both

---

* Most of the results described here and in the next section have been taken from a paper; Hornyak, Lauritsen, and Rasmussen (to appear).

coil configurations the 48" length vacuum chamber described earler under the section on the design of the spectrometer was used. A more detailed account of the spectrometer structure can be found in that section, as well as a discussion of the current regulation.

In some applications a vacuum connection to a 1.4 Mev. electrostatic accelerator enabled suitable targets at the source position to be bombarded by high energy protons or deuterons for the study of prompt and short lived radioactive gamma radiation. Gamma rays produced at the source position ejected secondary electrons from a heavy element converter immediately adjacent. The schematic diagram shown earler in Fig. 14 illustrates a typical source assembly. The source and converter were supported by a thin wire and the region around the source was completely free of scattering materials for a minimum of three inches. Particular care was taken to reproduce accurately the centering and axial locations of the sources as has been described previously and, while the diversity in the nature of the gamma ray sources required some variation in techniques, the geometry of the source assembly was standardized as much as possible.

The internal parts of the spectrometer were centered with respect to the tube at assembly. Further adjustment of the geometrical alignment was made by moving the tube with respect to the axis of the coils in such a way as to maximize the observed intensity of the high energy internal conversion "X" line ($B\rho$ = 10,000 gauss cm) of ThD. Stray lateral magnetic fields

were then compensated, by means of two large, mutually perpendicular coils as dicussed before, to give maximum intensity for the comparatively low energy "F" line from ThC ($B\rho$ = 1385 gauss cm), the "I" line ($B\rho$ = 1750 gauss cm) being used as an auxiliary check. It was observed that when the compensation was properly set, the instrument resolution was the same for all of the internal conversion lines. When the compensation was incorrect the first sign of maladjustment was a line broadening and loss in intensity which was progressively worse the lower the line energy. Only after a considerable amount of maladjustment of the compensation were the line shapes asymmetrical or noticeably shifted. Because the component of stray field parallel to the spectrometer axis was not compensated, a small correction to the observed line position was made for the 1.5% resolution work. At the time when the lower resolution data was taken, this correction was not thought to be significant hence no measurement of this component of the stray field was made, nor was the direction of the focusing field recorded, thus later no correction could be made. The fact that this correction was not made is partly reflected in the higher probable error attached to this data. For the high resolution experiments, this correction is

$$\frac{\delta M.V.}{M.V.} = \frac{22\,S}{B\rho}$$

where S is the axial component of the stray field in gauss, $B\rho$ the momentum of the line in gauss cm, and $M.V.$ is the millivolt reading on the potentiometer indicating the spectrometer coil

current. Since in this experiment a value of $S = 0.3_0 \pm 0.1$ gauss was measured, the correction at 2000 gauss cm, for example, is $0.3_3\%$.

At this point it will prove expedient to discuss the higher resolution experiments separately. When all this experimental data has been presented we shall return to consider the 3.0% resolution experiments.

In the final high resolution configuration, the spectrometer yielded a symmetric curve, with a shape well approximated by a Gaussian function (Fig. 32) of width at half maximum of $1.5_2\%$. In general this width will depend on the instrument aperture arrangement and the source size. An investigation showed that for the range of source sizes used here, the line shapes were comparatively independent of source size.

Internal conversion photoelectrons provide a particularly simple indication of the gamma ray energy, if the available intensity is great enough to permit the use of a source of such thickness that the energy loss of the electrons may be ignored. In such cases, the observed electron distribution is simply the window or resolution curve of the instrument and the determination may be made directly in terms of either the peak or the extrapolated edge positions. Comparison with a known line of the same character then provides the calibration. As an example of this technique, and for a calibration required for subsequent work, an intercomparison of the internal conversion lines of the gamma radiation of ThD (X line) and Au^{198} (K and L lines) was made. The former line was measured by Ellis[39] in terms of

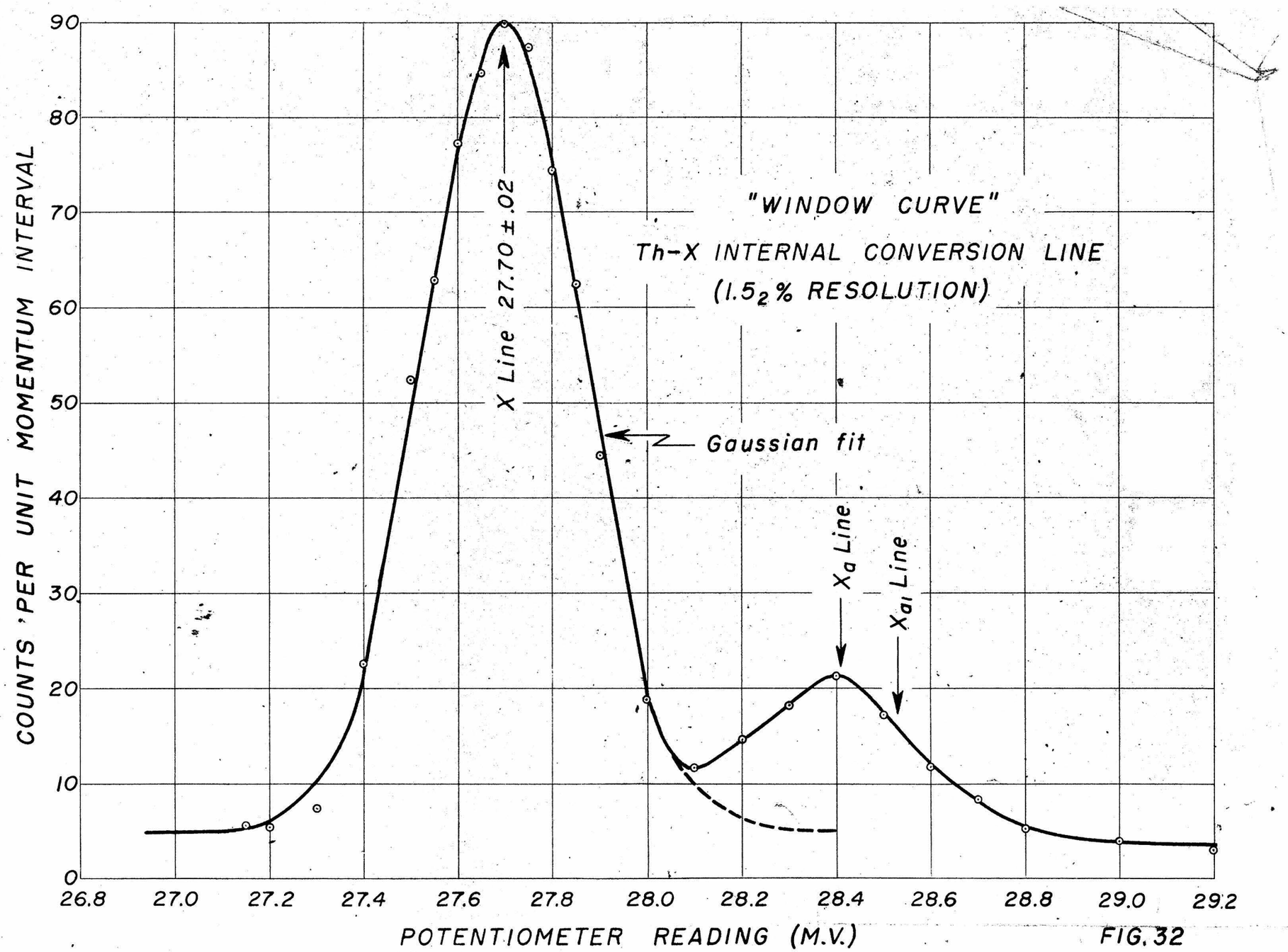
"WINDOW CURVE"
Th-X INTERNAL CONVERSION LINE
(1.5₂% RESOLUTION)
X Line 27.70 ± .02
Gaussian fit
Xa Line
Xa1 Line
COUNTS PER UNIT MOMENTUM INTERVAL
0
10
20
30
40
50
60
70
80
90
26.8
27.0
27.2
27.4
27.6
27.8
28.0
28.2
28.4
28.6
28.8
29.0
29.2
POTENTIOMETER READING (M.V.)

FIG. 32

the I line for which he obtained an absolute value by measurement of the magnetic field. Siegbahn[30] measured the absolute values of the I and F lines by comparing the difference with X-ray spectroscopic values and obtained momenta on the average 0.11% lower than those given by Ellis. Taking the mean of the two I line determinations and using Ellis' X/I ratio, one obtains a momentum value of 10,000 ± 14 gauss cm, or 2.618 ± .004 Mev for the gamma ray energy.*

The gamma radiation of Au^{198} has been measured in a curved crystal spectrometer by DuMond, Lind and Watson[31] who give 411.2 ± 0.1 kev for the energy, yielding values of $B\rho$ = 2219.7 gauss cm for the K conversion line and $B\rho$ = 2502.1 gauss cm for the L line. The K and L binding energies used here were determined from the critical absorption wave length table of Compton and Allison[32]. Since the L_I, L_{II}, and L_{III} lines were not resolved, a weighted mean value for the L shell energy was used. Table E gives the pertinent values for the elements used in these experiments.

---

* See Appendix IV.

TABLE E

K and L Shell Energies

Element	E_K (kev)	E_{L_I} (kev)	$E_{L_{II}}$ (kev)	$E_{L_{III}}$ (kev)	$\bar{E}_L$ (kev)
Thorium	109.8	20.5	19.7	16.3	20.1
Lead	88.0	15.8	15.2	13.0	15.6
Mercury	83.1	14.8	14.2	12.3	14.5
Nickel	8.3_4	--	--	--	--

For the "X" line measurements, sources of $\sim$ 4 mm diameter of ThB were prepared by electrostatic collection from Tn gas on .0005" Al foils. The thin (essentially mono-molecular) deposits so obtained were covered by an additional layer of .0005" Al foil to prevent recoil ThC" nuclei from escaping. The Au^{198} source was plated from solution on a .0005" Cu foil and had a thickness of less than 0.1 mg/cm^2.* The total activity of these sources was of the order of 20 μ curies. Typical curves obtained are reproduced in Fig. 32 and Fig. 33 and the resulting peak and edge calibration values in terms of millivolts drop across a standard shunt presented in Table F.** The indicated locations of the X_a and X_{a1} lines in Fig. 32 are

---

* I am indebted to the Atomic Energy Commission for their cooperation in supplying the Au^{198} and Co^{60} sources and to Mr. J.H. Sullivan for the chemical preparations involved in certain of the applications.

** The focusing current for lines having momenta greater than 4500 gauss cm was measured on a shunt having $.1330_3$ times the resistance of the standard shunt.

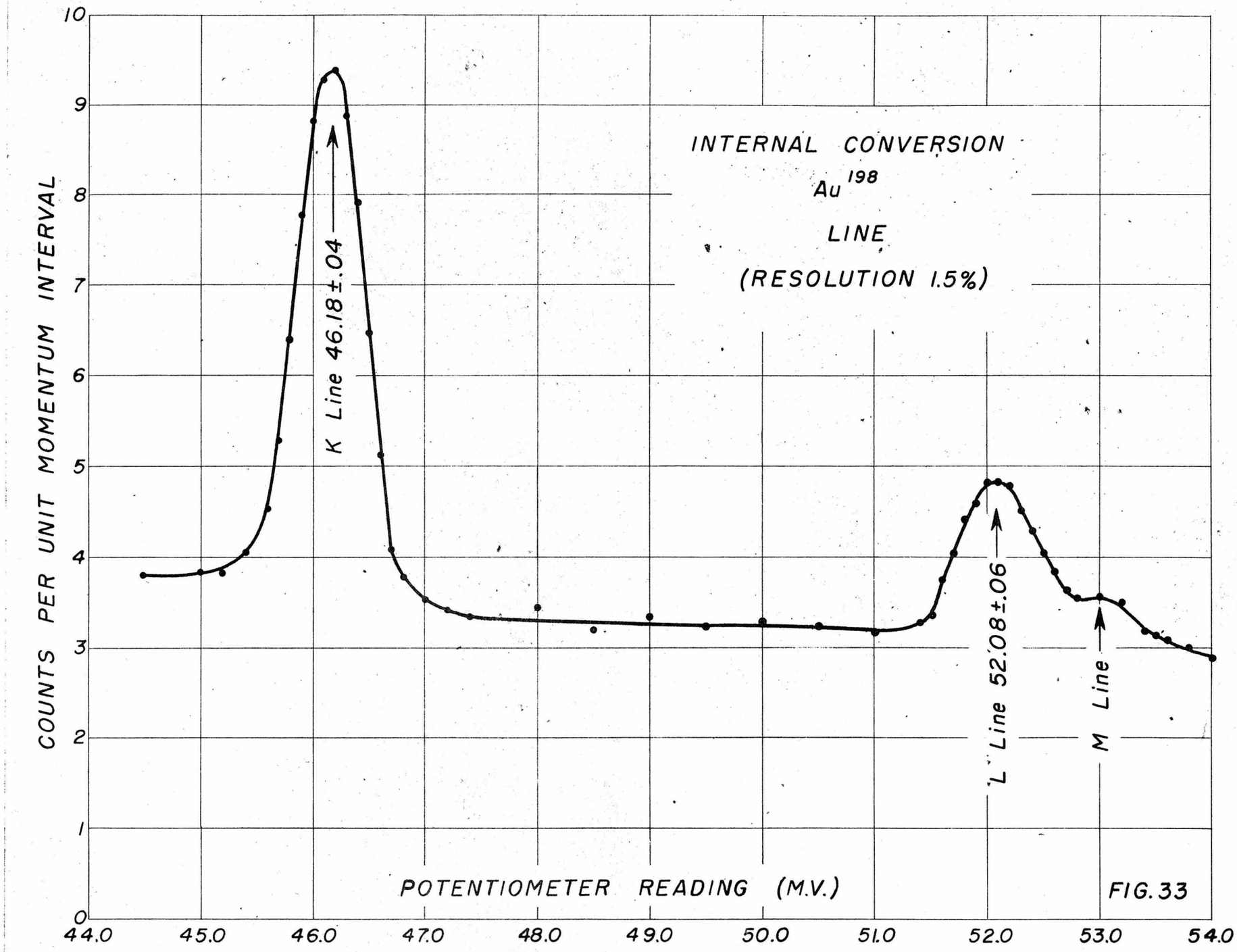
INTERNAL CONVERSION
Au 198
LINE
(RESOLUTION 1.5%)
K Line 46.18±.04
"L" Line 52.08±.06
M Line
COUNTS PER UNIT MOMENTUM INTERVAL
POTENTIOMETER READING (M.V.)
0
1
2
3
4
5
6
7
8
9
10
44.0
45.0
46.0
47.0
48.0
49.0
50.0
51.0
52.0
53.0
54.0

FIG. 33

calculated from Ellis' data. The close agreement of the calibrations attests to the accuracy of the method and provides a relative check on the two independent standards.*

Measurements were also made on the ThF and I lines, but the uncertainties in the stray magnetic field corrections limited the precision to about 0.5%. The values obtained were in agreement with the ratios quoted by Ellis within this accuracy.

For gamma ray sources in which no appreciable internal conversion occurs, photo electrons may be produced in an external converter of high atomic number as discussed before, using the arrangement of Fig. 14. To illustrate the effect of converter thickness on line shape at a comparatively low energy, experimental curves of the K conversion in thorium foils of the 411.2 kev gamma radiation of Au^{198} are shown in Fig. 34. The source used for this work consisted of a 1 mm square of activated Au foil. 001" thick placed on the back of a .030" copper absorber, to which were attached the thorium foils.** The copper absorb-

---

* If one uses the peak calibration for the Au^{198} to determine the X line value from this experiment, a value of 9998 gauss cm is obtained, corresponding to a gamma ray energy of 2.618 Mev with a probable error of 4 kev. The corresponding extrapolated edge value, which is in this case considered somewhat less reliable because of the overlapping with the X_a line, yields $B\rho$ = 9989 gauss cm or 2.615 ± .006 Mev. This comparison has been recently repeated with a resolution of 1.0%, resulting in a $B\rho$ value of 9982 gauss cm for the X line peak or an energy of 2.613 ± .004 Mev.

** Throughout this thesis the converter thicknesses quoted in inches are nominal thicknesses. By weighing these have been determined to be:

.00025 inches	7 mg/cm^2
.0005 "	16 "
.001 "	25 "
.002 "	57 "
.003 "	78 "
.004 "	113 "
.005 "	150 "

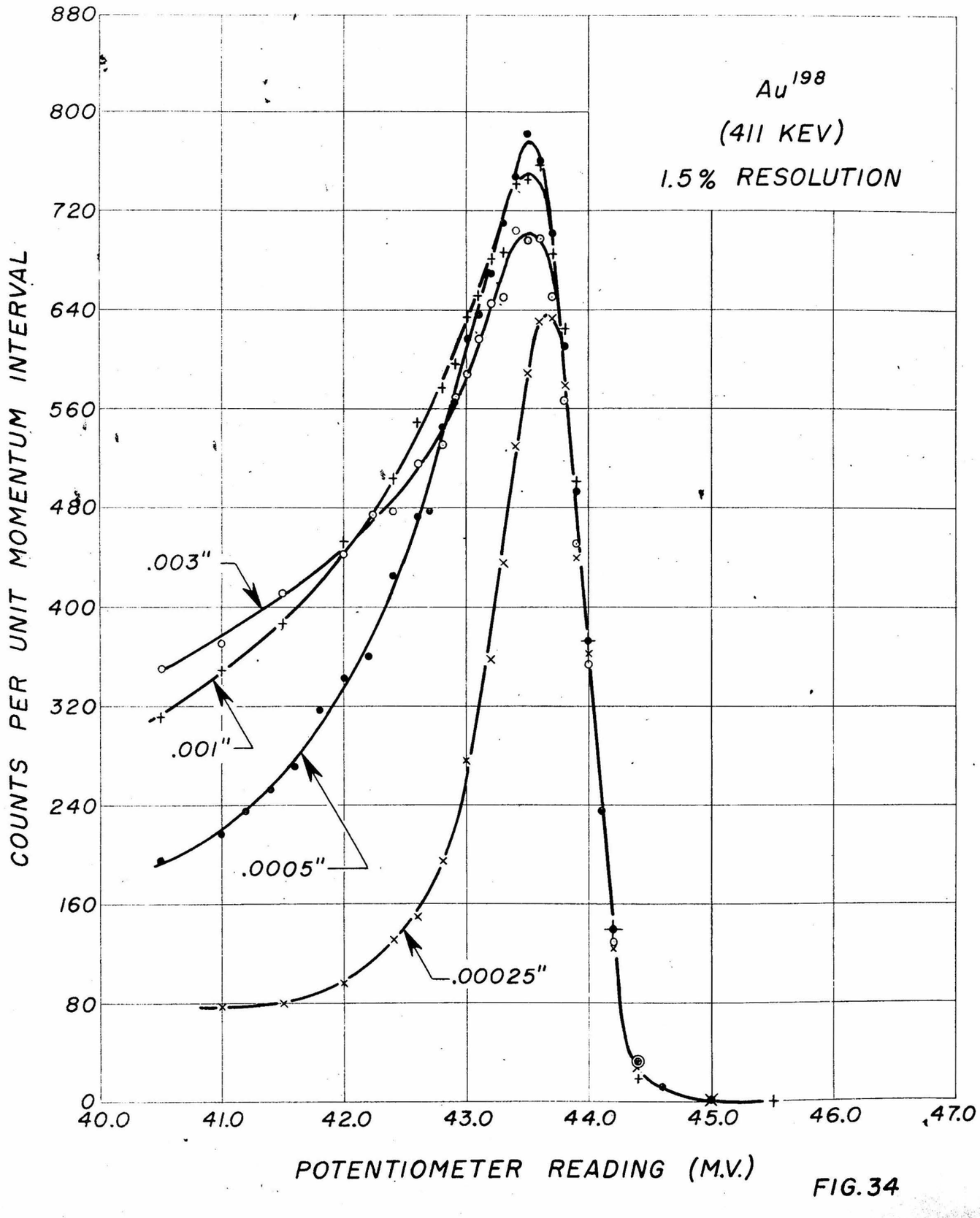
Au 198
(411 KEV)
1.5% RESOLUTION
COUNTS PER UNIT MOMENTUM INTERVAL
880
800
720
640
560
480
400
320
240
160
80
0
.003"
.001"
.0005"
.00025"
40.0
41.0
42.0
43.0
44.0
45.0
46.0
47.0
POTENTIOMETER READING (M.V.)

FIG. 34

TABLE F

Calibration Lines

Line	E_γ (kev)	E_e (kev)	$B\rho$	Edge † M.V.	Peak † M.V.	$(B\rho/M.V.)_e$	$(B\rho/M.V.)_p$
ThD K	2618 ± 4	2530	10,000.	211.1_0*	208.6_4*	47.37_0	47.92_9
Au^{198} decay K	411.2 ± .1	328.1	2,219.7	36.89	46.32	47.33_8	47.92_1
Au^{198} decay L	411.2 ± .1	396.7	2,502.1	52.90	52.22	47.29_9	47.91_5
					Calibration**:	$47.34_9 \pm .03$	$47.92_5 \pm .03$

† Corrected for axial component of stray field.

* Including 9 gauss om correction for cover foil; reduced to standard shunt readings.

** ThD values weighted 3 x; mean of three runs given in table.

er was used to suppress the continuous β radiation. The ordinates of the various curves have been adjusted only to the extent that backgrounds of the order of 30%, due partly to the tailing of the L and M lines at $\approx$ 51 M.V. and partly to general radiation, have been subtracted. The intensities plotted are for a constant source strength in all cases.

Perhaps the most significant feature of these curves, from the standpoint of their usefulness in energy determinations is the observation that the intersection of the extrapolated front edge with the background is apparently independent of converter thickness. A similar set of curves for the 717 kev gamma radiation from the reaction $Be^{9}(dn)B^{10*}$ is shown in Fig. 35. The curves of Fig. 36 illustrate the two high energy gamma rays accompanying the decay of Co^{60}, where the background has not been subtracted.* In all cases the extrapolated edge values for the K conversion lines were found to be independent of converter thickness to within about 0.2%. Reference to Table G shows that the value of the Au^{198} gamma ray deduced from the extrapolated edge agrees within 0.1 kev with the known value (using extrapolated edges of the internal conversion lines referred to above for calibration).

An inspection of the curve of Fig. 26 shows that observed lines having widths twice the resolution or more will have only

---

* The cobalt curves were run with only .001" Cu absorber; the abnormal intensity of the L lines is due to the superposition on them of the internal conversion K lines, shifted by the energy loss in the absorber.

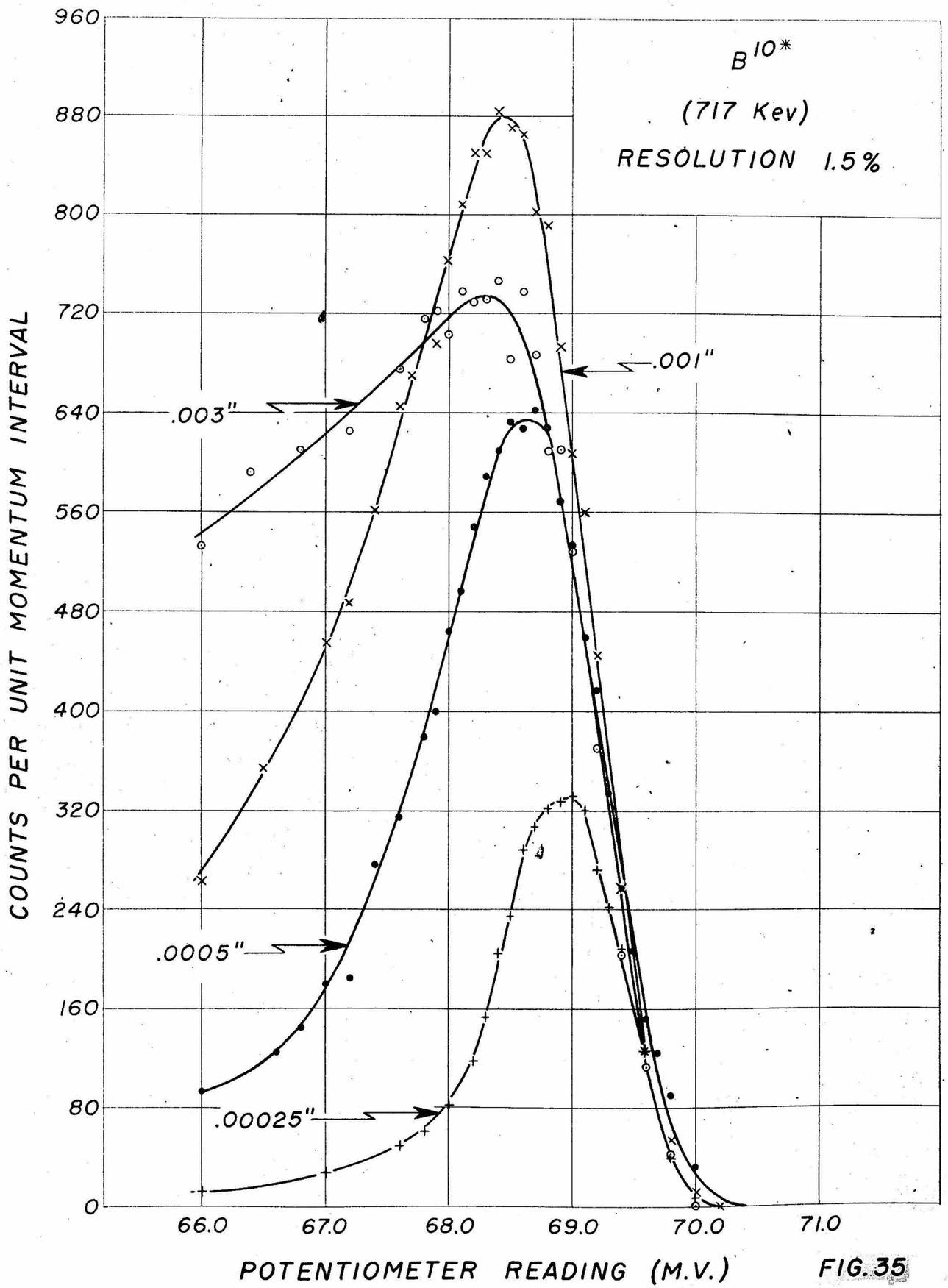
B^{10*}
(717 Kev)
RESOLUTION 1.5%
.001"
.003"
.0005"
.00025"
960
880
800
720
640
560
480
400
320
240
160
80
0
66.0
67.0
68.0
69.0
70.0
71.0
COUNTS PER UNIT MOMENTUM INTERVAL
POTENTIOMETER READING (M.V.)

FIG. 35

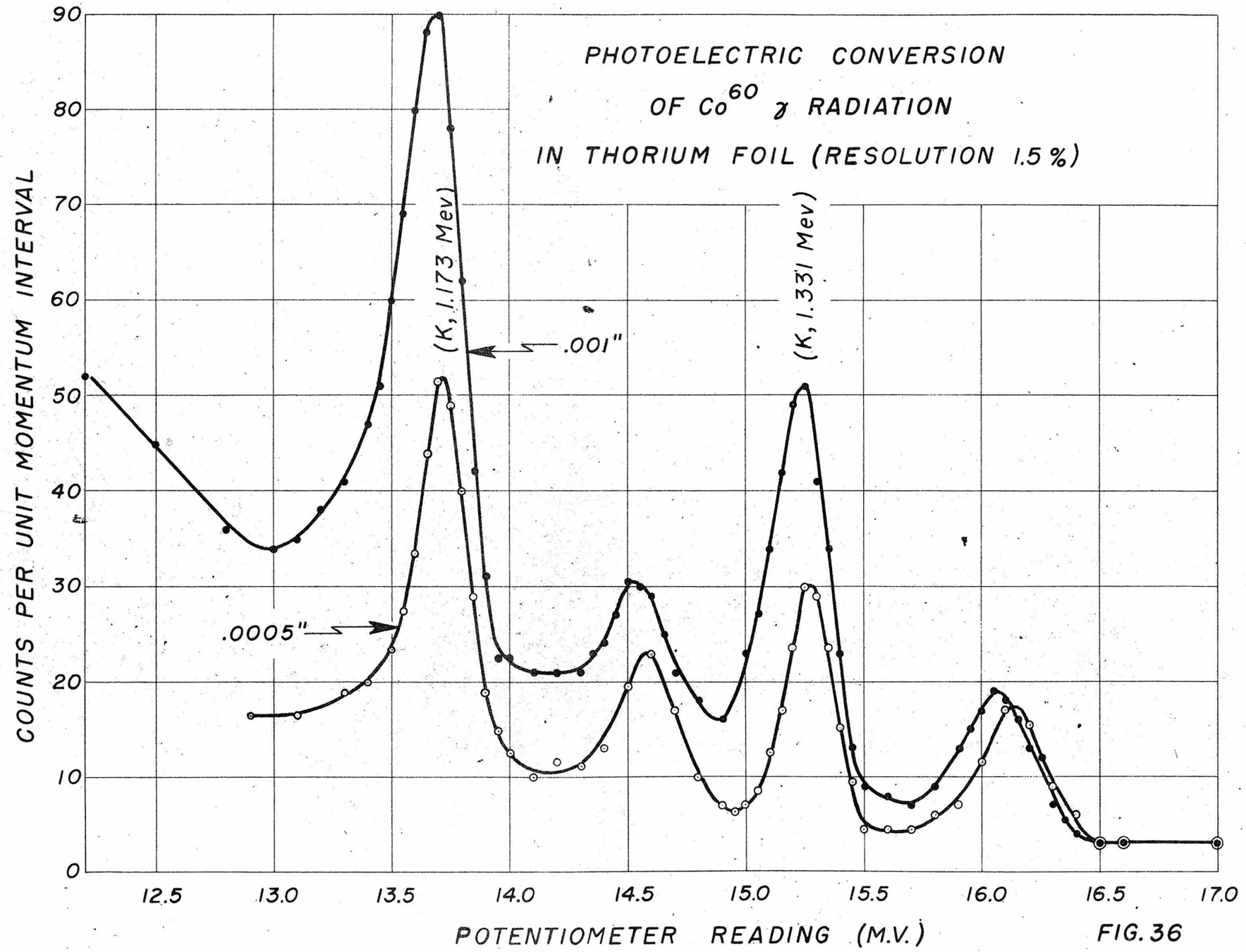
PHOTOELECTRIC CONVERSION
OF Co60 γ RADIATION
IN THORIUM FOIL (RESOLUTION 1.5 %)
(K, 1.173 Mev)
(K, 1.331 Mev)
.001"
.0005"
COUNTS PER UNIT MOMENTUM INTERVAL
POTENTIOMETER READING (M.V.)
0
10
20
30
40
50
60
70
80
90
12.5
13.0
13.5
14.0
14.5
15.0
15.5
16.0
16.5
17.0

FIG. 36

small variations in the location of the extrapolated edge. The calculated difference in the extrapolated edges for the .00025" and .003" curves for thethorium converted Au^{198} radiation of Fig. 34 is 0.053 M.V., which is less than the experimental error. However, an absolute shift in the extrapolated edge, based on Fig. 26, of 0.18 M.V. (2.0 kev) should have been observed for the .0005" data of Au^{198}. This discrepancy amounts to about 2.5 probable errors. An explanation of this discrepancy will become clear presently.

The height and location of the peaks and the magnitude of the low energy side of the distributions, on the other hand, are clearly affected by changes in the converter thickness. Between the .00025" and the .0005" curves in Fig. 34, one observes an increase of intensity and a shift of the maximum toward lower energy. As compared with the expected peak for zero converter thickness, the .00025" peak is shifted by 1.7 kev and the .0005" by 3.2 kev. For thicknesses greater than .0005" one observes no further shift or increase in peak intensity (the intensity actually decreases somewhat because of the absorption of the gamma radiation) and only the lower energy tail seems to be affected.

In an effort to ascertain the primary distribution of the electrons emerging from the converter, some of the experimental curves of Fig. 34, Fig. 35,and Fig. 36 have been "unfolded", i.e., the effect of finite resolution removed. The method described under a previous section on instrument resolution was

used to obtain a first approximation. Further successive approximations were made, at each stage the window curve was folded into the "candidate" primary spectrum as a test. This process was repeated until a satisfactory primary spectrum was obtained. Although such a procedure cannot in general be expected to reveal changes occurring in intervals small compared to the resolution width (7.3 kev), in this case the unfolding was facilitated by the fact that the upper limit of the primary spectrum in each case was known. The location of the upper limit for the Au^{198} was determined from the known calibration while upper limit for the B^{10*} and Co^{60} photolines was determined from the subsequent energy determinations. The curves of Fig. 37, which exhibit the inferred spectra for three converter thicknesses for Au^{198}, show that the number of electrons per unit momentum interval emerging from the converter drops very sharply in less than $\sim$ 3 kev and thereafter falls more gradually at a rate depending on converter thickness. The ordinates in these curves are in the same (arbitrary) units as those of Fig. 34, to facilitate comparison. As a check on the reliability of the inferred primary distribution, the .0005" converter curve was repeated at a resolution of 0.65%, using a smaller source, and introducing several other modifications in the spectrometer. The primary spectrum representing the best fit for the two resolutions is shown in Fig. 38, where the numerically integrated folds with gaussians of 0.65% and 1.5% are also shown, together with the experimental points. This inferred

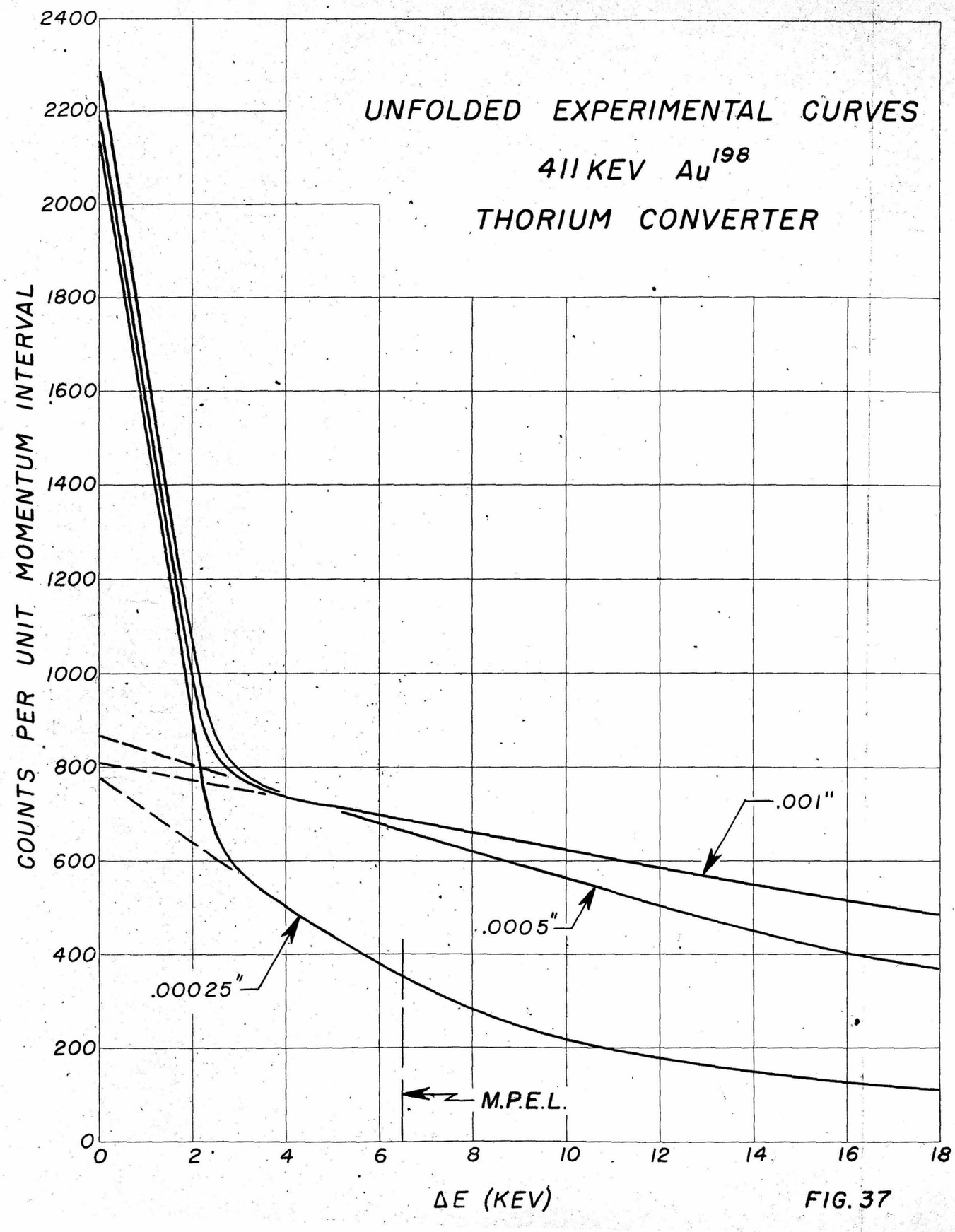
UNFOLDED EXPERIMENTAL CURVES
411 KEV Au198
THORIUM CONVERTER
COUNTS PER UNIT MOMENTUM INTERVAL
2400
2200
2000
1800
1600
1400
1200
1000
800
600
400
200
0
0
2
4
6
8
10
12
14
16
18
ΔE (KEV)
.001"
.0005"
.00025"
M.P.E.L.

FIG. 37

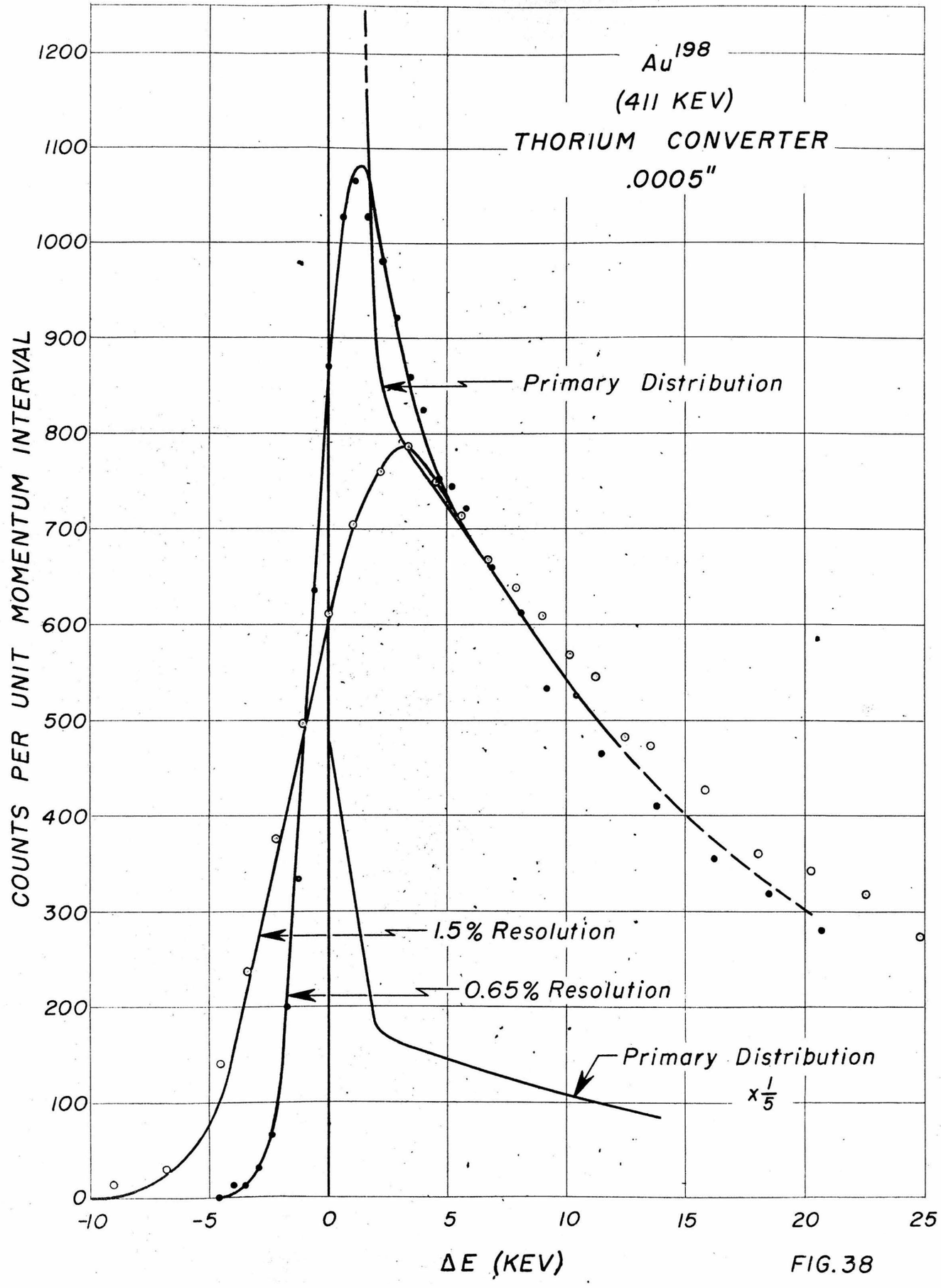
Au 198
(411 KEV)
THORIUM CONVERTER
.0005"
Primary Distribution
1.5% Resolution
0.65% Resolution
Primary Distribution
x 1/5
COUNTS PER UNIT MOMENTUM INTERVAL
ΔE (KEV)
0
100
200
300
400
500
600
700
800
900
1000
1100
1200
-10
-5
0
5
10
15
20
25

FIG. 38

distribution agrees well with the corresponding one in Fig. 37; the rapid change in slope of the curve is again very pronounced and permits a more accurate location of the break to be made as 2.5 1 kev. Figure 39 shows the unfolded curve for the .0005" converter thickness for the B^{10*} γ-radiation, and Fig. 40 gives the inferred primary spectrum for Co^{60} radiation and .001" converter. Again the ordinates of these curves have been kept the same as in Fig. 35 and Fig. 36 respectively. All the unfolded curves indicate that the area under the "spike" divided by the ordinate obtained by extrapolation of the slowly varying tail to zero energy loss is approximately independent of both the energy of the gamma ray and the thickness of the converter. The existence of this large number of electrons with small energy loss accounts for the fact that the extrapolated edge is relatively independent of converter thickness. However, with a considerably broader window curve, one might expect the influence of the back slope to become relatively more important, resulting in a detectable edge shift. A detailed comparison of the unfolded experimental curve for .0005" converter and Au^{198} radiation, with the various theories is made in Fig. 41. The curves were all normalized to give a constant area out to ΔE = 10 kev. The window curve is also given for comparison. It will be seen that the numerical integration of the White and Millington curves (smoothed out) and the curve based on the scattering absorption of Bothe's theory, coupled with a most probable energy loss associated with depth, are virtually co-

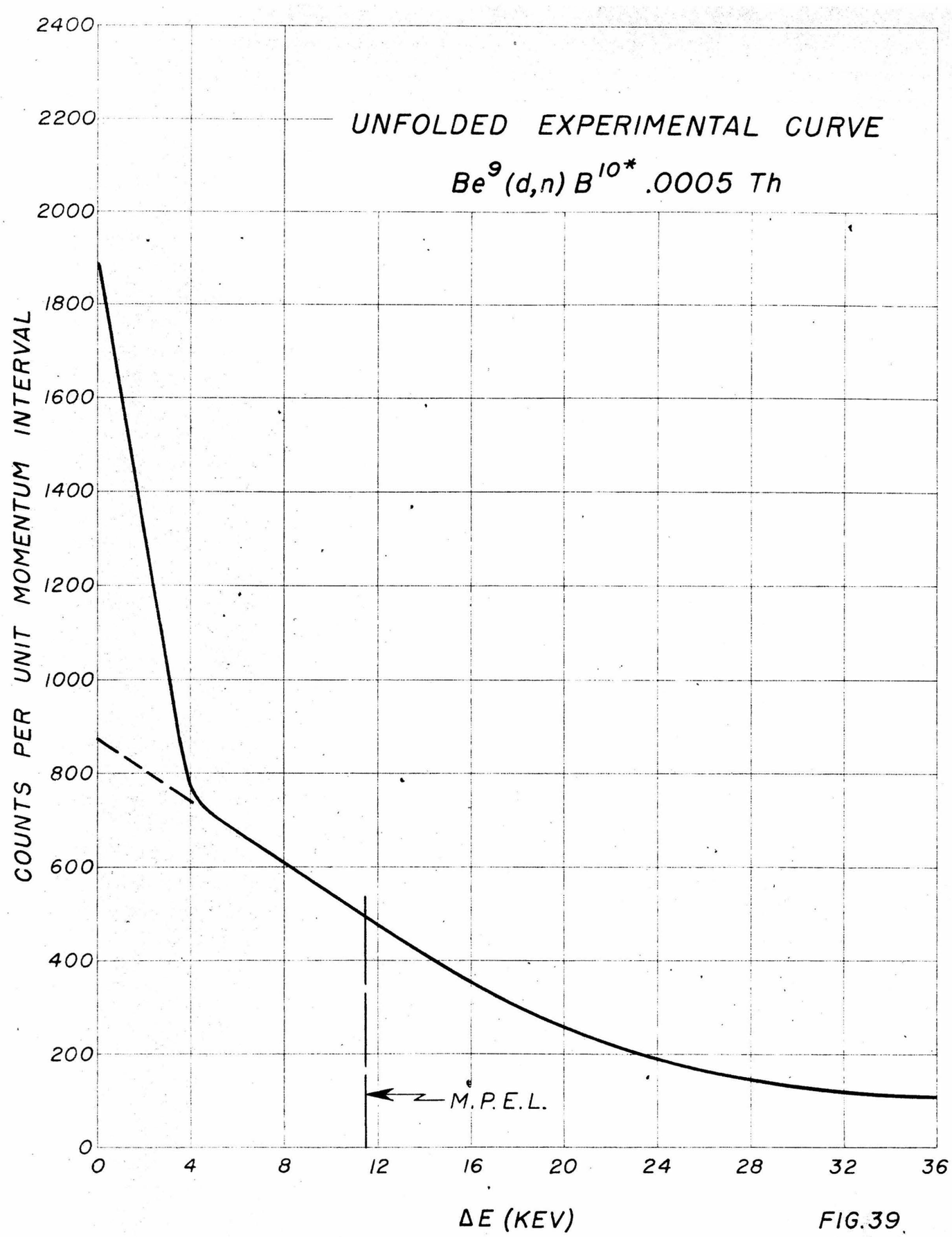
UNFOLDED EXPERIMENTAL CURVE
$Be^9(d,n)B^{10*}$ .0005 Th
COUNTS PER UNIT MOMENTUM INTERVAL
2400
2200
2000
1800
1600
1400
1200
1000
800
600
400
200
0
0
4
8
12
16
20
24
28
32
36
M.P.E.L.
ΔE (KEV)

FIG. 39

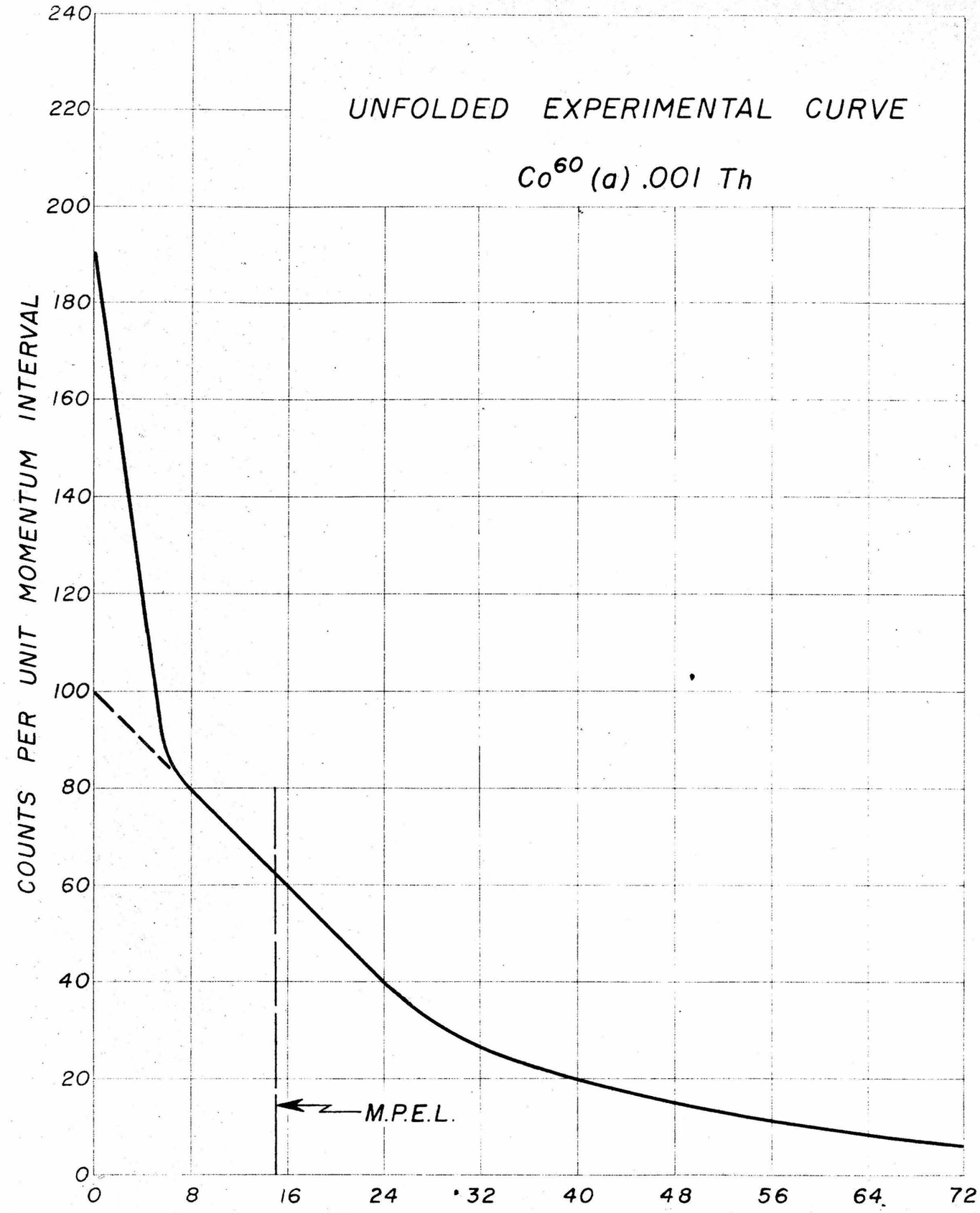
UNFOLDED EXPERIMENTAL CURVE
Co60 (a) .001 Th
COUNTS PER UNIT MOMENTUM INTERVAL
240
220
200
180
160
140
120
100
80
60
40
20
0
M.P.E.L.
0
8
16
24
32
40
48
56
64
72
ΔE (KEV)

FIG. 40

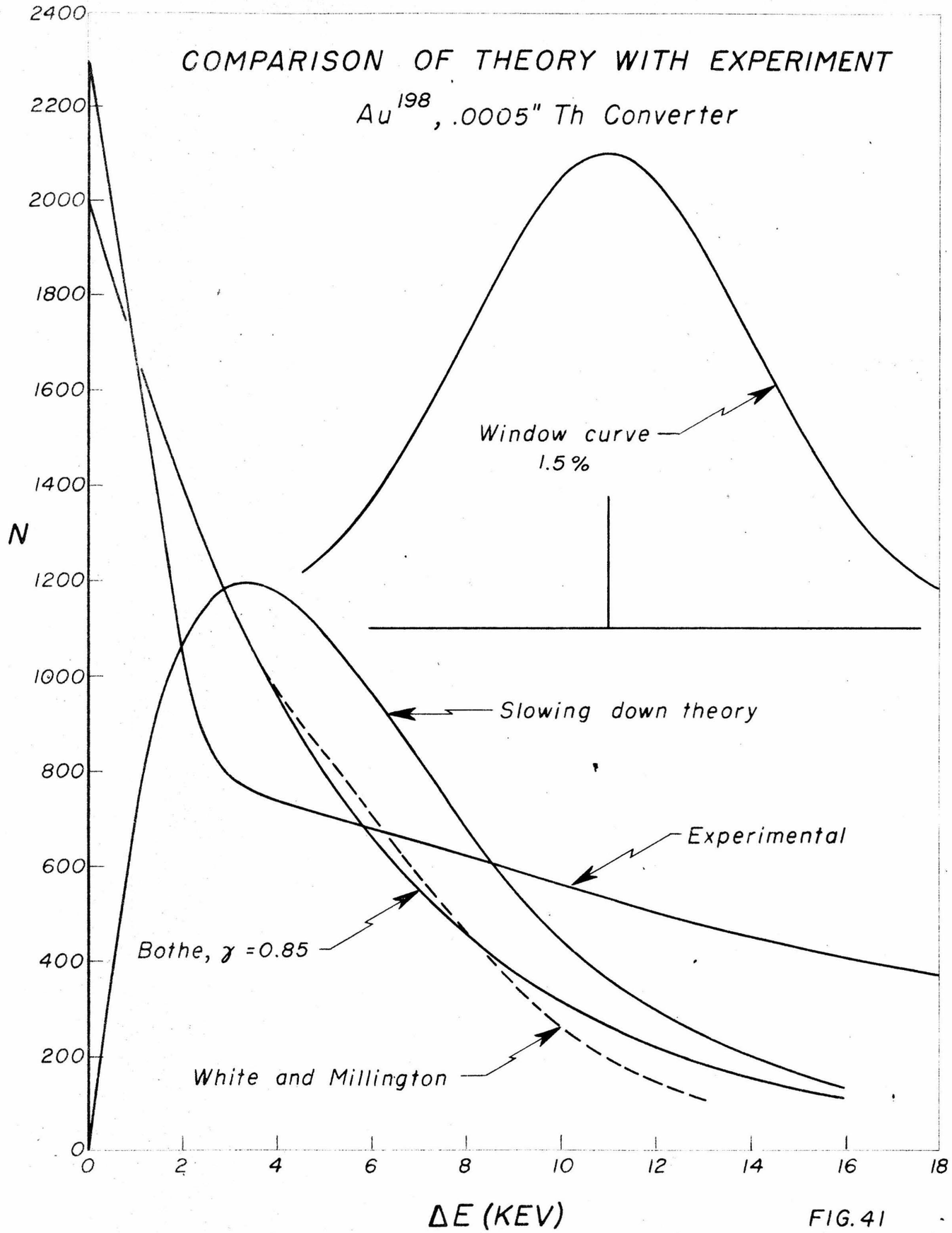
COMPARISON OF THEORY WITH EXPERIMENT
Au 198 , .0005" Th Converter
Window curve
1.5 %
Slowing down theory
Experimental
Bothe, γ =0.85
White and Millington
N
ΔE (KEV)
0
200
400
600
800
1000
1200
1400
1600
1800
2000
2200
2400
0
2
4
6
8
10
12
14
16
18

FIG. 41

incident. The free parameter γ in this latter curve was taken as 0.85 to match the observed peak shifts, to be discussed later. While neither of these curves are in particular agreement with the observed curve, they are womewhat better than the spectrum predicted by the "slowing down theory". All that will be required of the curve based on the absorption theory is that it give the proper interpolation of the peak shift function between the two extreme limiting cases that have been discussed. In spite of the apparent lack of agreement with observation as to the exact nature of the spectrum this theory gives the desired interpolation adequately well.

It is of some interest to investigate the extent to which the tails of the experimental inferred primary spectra (i.e. primary spectra with the "spikes" removed), can be represented as a set of universal curves. It will be recalled that theory was presented which indicated that if these spectra were plotted as a function of $\frac{\Delta E}{\epsilon_m \lambda_s}$ with a/λ_s as a parameter, such universal curves would result. Here a is the converter thickness, λ_s the scattering mean free path, ϵ_m the most probable energy loss per unit length, while ΔE is the energy loss for a specific portion of the spectrum. The various experimental curves of Fig. 42 are seen to interlace quite satisfactorily with a/λ_s increasing monotonically as the tailing becomes more pronounced.

The behavior of the distribution as a function of energy was studied using K photo electrons produced in a .0005" thorium foil by the following gamma rays:

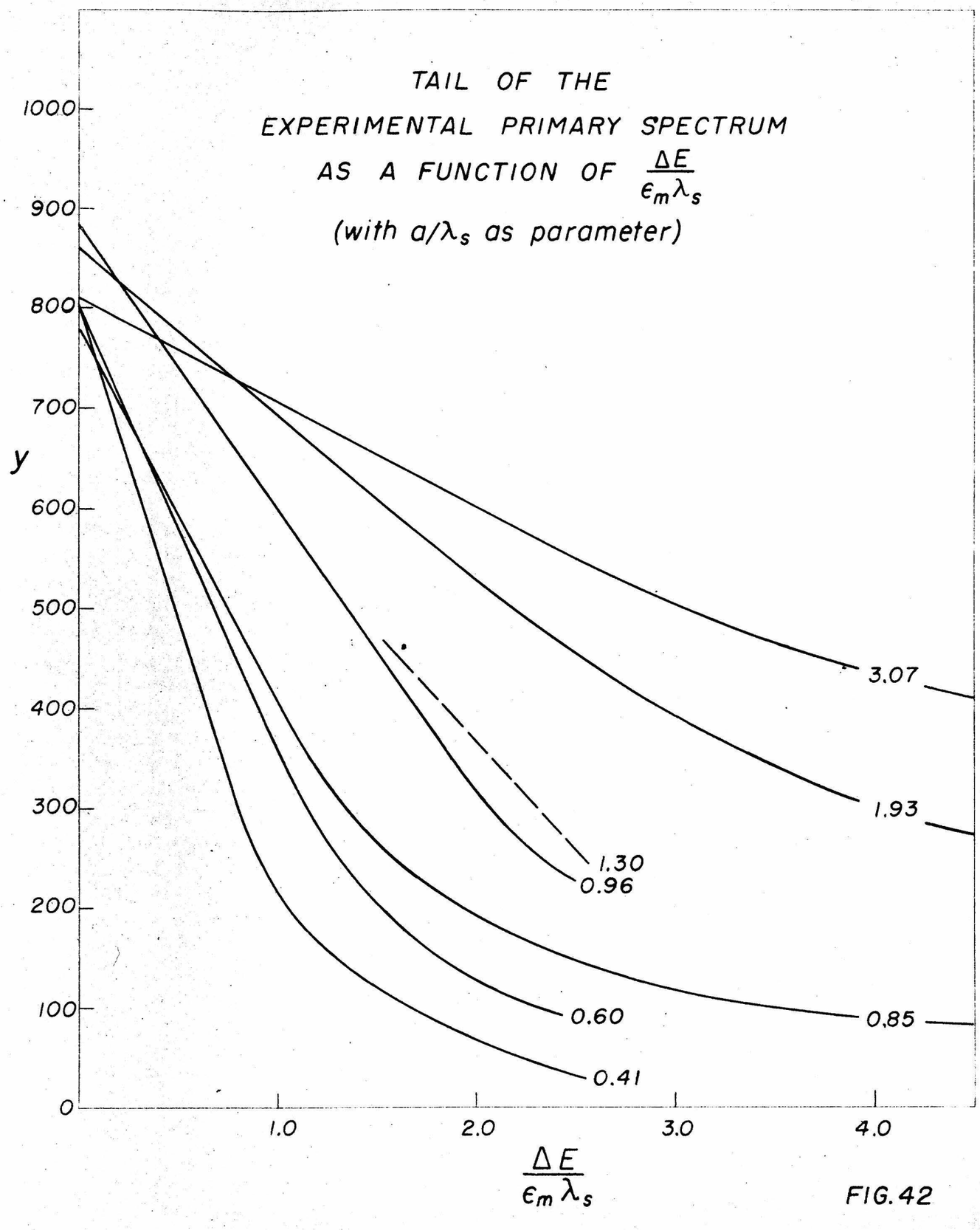
TAIL OF THE
EXPERIMENTAL PRIMARY SPECTRUM
AS A FUNCTION OF $\frac{\Delta E}{\epsilon_m \lambda_s}$
(with a/λ_s as parameter)
y
1000
900
800
700
600
500
400
300
200
100
0
1.0
2.0
3.0
4.0
$\frac{\Delta E}{\epsilon_m \lambda_s}$
3.07
1.93
1.30
0.96
0.85
0.60
0.41

FIG. 42

(a) Au^{198} radiation (411.2 kev) - .030" Cu absorber and .0005" Th converter.

(b) Li^{7*} radiation (478 kev) - produced by bombardment of a Li target by protons: same absorber and converter.

(c) Annihilation radiation (510.8 kev) - from 10 min N^{13} produced by bombarding a .010" thick graphite target with deuterons; same absorber and converter.

(d) B^{10*} (717 kev) - produced in the reaction $Be^{9}(dn)B^{10*}$ by deuteron bombardment of an .004" Be target with the .0005" Th converter only.

The observed spectra are illustrated in Fig. 43, where the momentum scales have been adjusted by multiplication to bring the front edges into coincidence. The location $B\rho/B\rho_0 = 1.000$ corresponds to the true position of the photoelectron line, determined absolutely for the Au^{198} radiation. In Table G, the gamma ray energies derived from the observed extrapolated front edges are presented, including the Co^{60} determinations from Fig. 36.

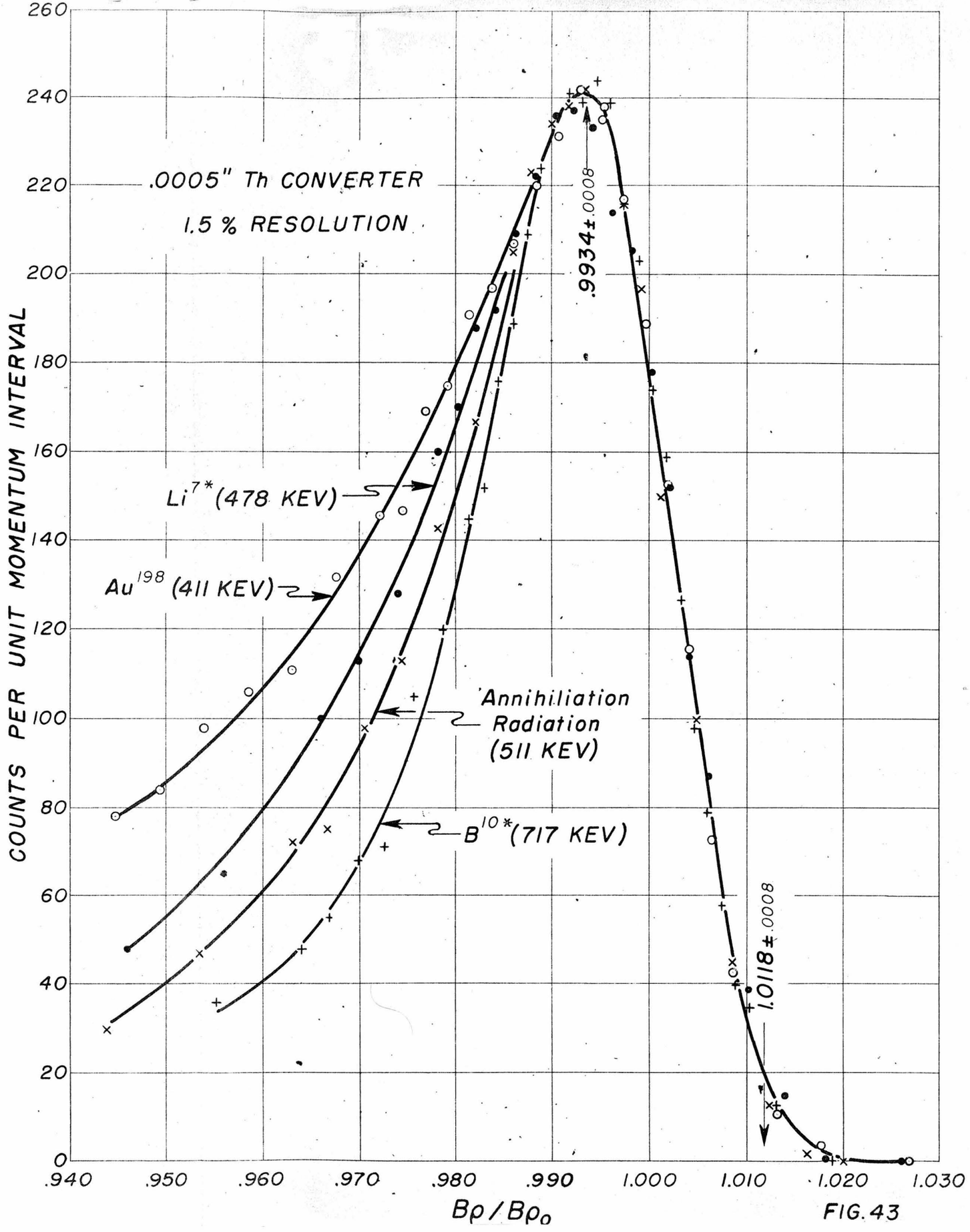
.0005" Th CONVERTER
1.5 % RESOLUTION
.9934±.0008
Li7* (478 KEV)
Au198 (411 KEV)
Annihiliation Radiation (511 KEV)
B10* (717 KEV)
1.0118±.0008
COUNTS PER UNIT MOMENTUM INTERVAL
Bρ/Bρo
0
20
40
60
80
100
120
140
160
180
200
220
240
260
.940
.950
.960
.970
.980
.990
1.000
1.010
1.020
1.030

FIG. 43

TABLE G

K-Line Extrapolated Edge Determinations - .005" Thorium Converter

resolution 1.5%

γ-Ray Source	M.V. (current)	M.V. † (current)	$B\rho$ ‡ (Gauss-cm)	E_e (kev)	$E_e + E_k$ (kev)
Au^{198} decay	44.34	44.48	2106.1	301.3	411.1 ± .6
Li^{7*}	50.28	50.42	2387.3	368.5	478.3 ± .7
e^+ annihilation	53.07	53.21	2519.4	401.0	510.8 ± .7
B^{10*}	69.90	70.04	3316.3	606.9	716.7 ± 1.0
Co^{60} decay (a)	13.932	104.8_6	4965	$1062._8$	$1172._6 \pm 2.5$
Co^{60} decay (b)	15.485	116.5_4	5518	$1220._4$	$1330._2 \pm 2.9$

† Values reduced to standard shunt readings, and corrected for axial component of stray fields by adding 0.14 M.V.

‡ Using as a calibration $B\rho/M.V. = 47.34_9 \pm .03$.

An independent check on the consistency of the data and support for the assumption that the extrapolated front edge does not, within the present uncertainty, require correction for converter thickness is provided by the close agreement of the observed value of the annihilation radiation to the known figure of 510.8 kev[33]. The probable errors indicated include estimates of uncertainties in matching the curves and subtracting background in addition to such systematic errors as appear in current measurement, source location, and stray field corrections.

Examination of the curves of Fig. 43 shows that, as the

energy is increased, the tail of the distribution becomes less prominent compared to the resolution of the instrument, which is given by a constant width on this plot. The peak locations for the four curves are identical within the experimental error of about 0.1% and indicate a displacement downward of 0.66% in momentum. That the peaks coincide in this case is to some extent fortuitous; a thinner converter would be expected to give a relatively smaller shift at the higher energy (compare Fig. 44).

It would appear from these experiments that, as long as variations in source diameter sufficient to affect the window curve are avoided, the extrapolated edge determination is to be preferred because of its relative independence of converter thickness. However, in many practical cases, uncertainties in the background and the interference of neighboring lines may make such determinations more difficult than the location of the peak.

As has already been pointed out, if peak values are to be used, allowance must be made for the converter effects. The corrections to be applied were roughly estimated from consideration of the effect of folding the window curve into the characteristic primary distribution. The limiting peak shift for "thin" converters is given in Fig. 44 by the dashed curves extending horizontally to the right. The limiting peak shift for "thick" converters is also given in Fig. 44, represented by the dashed diagonal line. The constant γ required for the interpolation formula has been adjusted to fit the experimentally de-

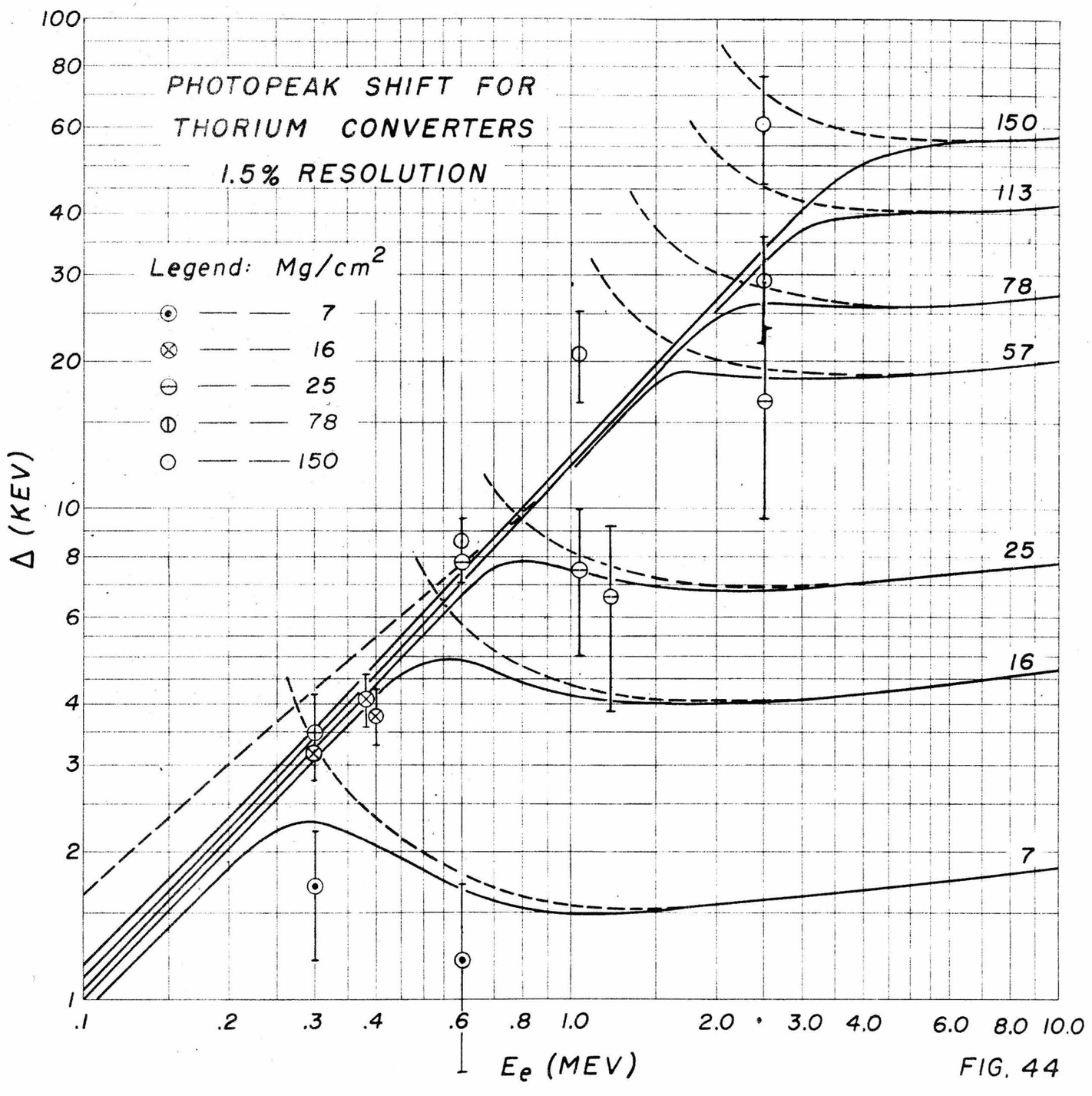
PHOTOPEAK SHIFT FOR
THORIUM CONVERTERS
1.5% RESOLUTION
Legend: Mg/cm²
7
16
25
78
150
Δ (KEV)
Eₑ (MEV)
100
80
60
40
30
20
10
8
6
4
3
2
1
.1
.2
.3
.4
.6
.8
1.0
2.0
3.0
4.0
6.0
8.0
10.0

FIG. 44

termined shifts for Au^{198} and annihilation radiation.

The extent to which these effects are applicable may be seen, at least qualitatively, from the distributions of Fig.34 and Fig. 37. Photo electrons that are produced at a depth within the converter such that the most probable energy loss suffered in emerging from the foil is less than approximately the resolution of the spectrometer will be the most effective in determining both the location and the intensity of the observed line peak. In the present case this amounts to energy losses less than 8 kev or a depth less than about .0003" of thorium. Thus it is observed that the increase of the peak intensity in going from .00025" to .0005" is comparatively slight although a shift in the location of the peak to a lower energy is apparent. Increasing the foil thickness beyond the "resolution depth" should however materially increase the prominence of the tail just below the peak until a thickness comparable to the transport mean free path is reached. The transport mean free path is estimated to be .0004" for this energy. After a thickness of the order of two or three times this value is reached, very few additional electrons are observed even in the tail. The "cut off" used in the theory is indicated in Fig. 37 for the .00025" foil thickness. The absence of any sharp discontinuity in the .00025" curve at this energy loss emphasizes the approximate nature of the theory used. The "cut off" is also given for the curves in Fig. 39 and Fig. 40.

At this point it may be profitable to give an example of a case in which using a foil of thickness greater than the

"saturation" thickness discussed above, results in an unfavorably large relative background and thus a subsequent loss in precision. Figure 45 shows the conversion of the Co^{60} γ-radiation in a .003" thorium foil, both including the large background. The shift in the peak location and the general distortion are apparent in this figure.

An illustration of a case in which it is difficult to suppress the background is shown in Fig. 46. Here the 2.62 Mev γ-radiation from ThD was converted in various thicknesses of thorium metal foils. Since this γ-ray is very strongly internally converted, sufficient copper absorber must be added between the source and the converter to shift the location of the internal conversion line that penetrates the converter, and which would otherwise obscure the external conversion line. The use of too large a thickness of absorber must be avoided, however, otherwise a large Compton background is introduced. The thickness of copper absorber used was .005", the curves of the figure are for .001", .003", and .005" of thorium converters.

In Table H are presented the observed peak locations for the various gamma rays converted in .0005" of thorium discussed earlier, together with the estimated shift values Δ (in parentheses) taken from Fig. 44. The peak shifts for the known lines are given along with the probable errors; these values are plotted in Fig. 44.

Auxiliary check points, to test the reliability of the

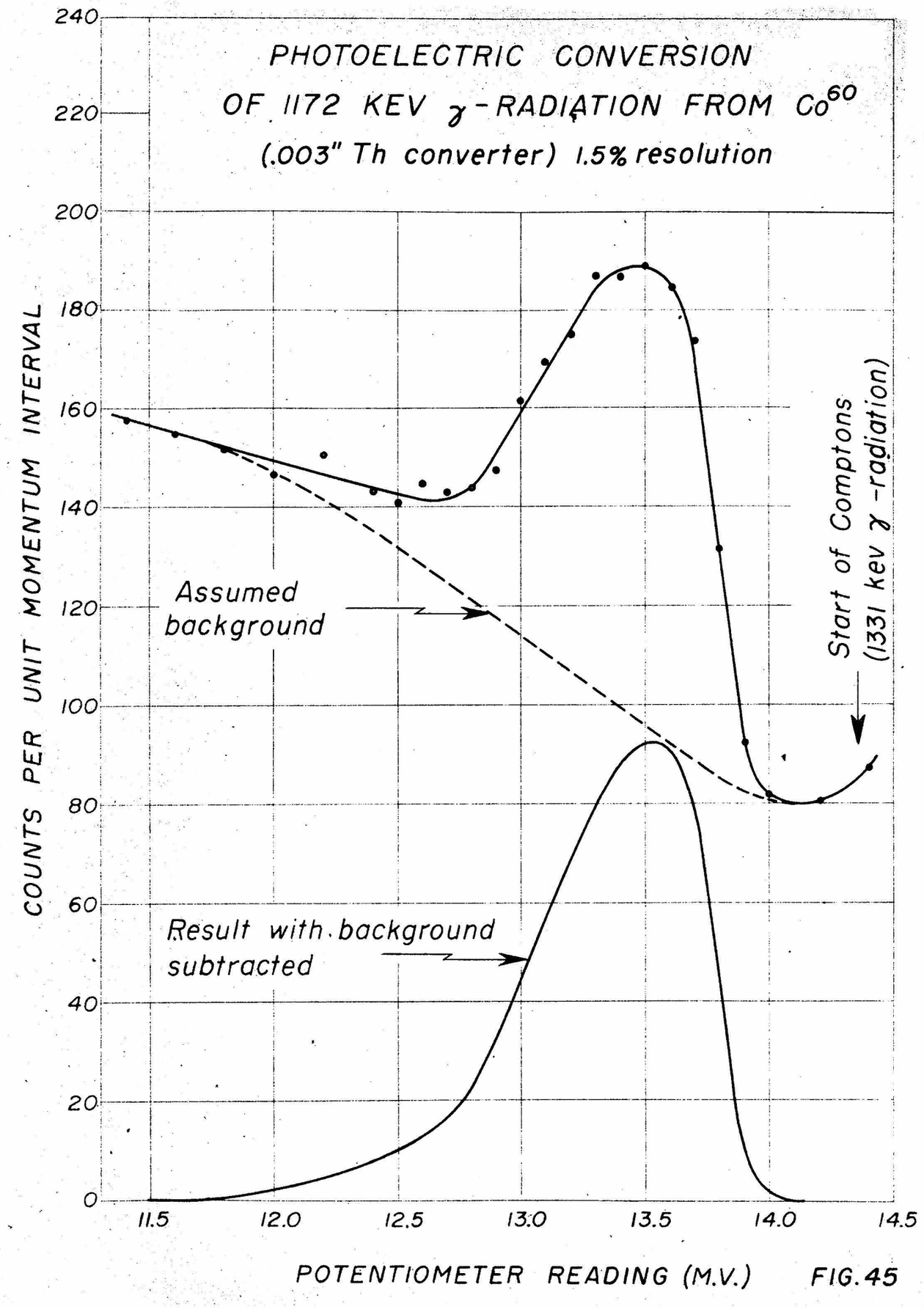
PHOTOELECTRIC CONVERSION
OF 1172 KEV γ-RADIATION FROM Co60
(.003" Th converter) 1.5% resolution
COUNTS PER UNIT MOMENTUM INTERVAL
240
220
200
180
160
140
120
100
80
60
40
20
0
Assumed background
Result with background subtracted
Start of Comptons (1331 kev γ-radiation)
11.5
12.0
12.5
13.0
13.5
14.0
14.5
POTENTIOMETER READING (M.V.)

FIG. 45

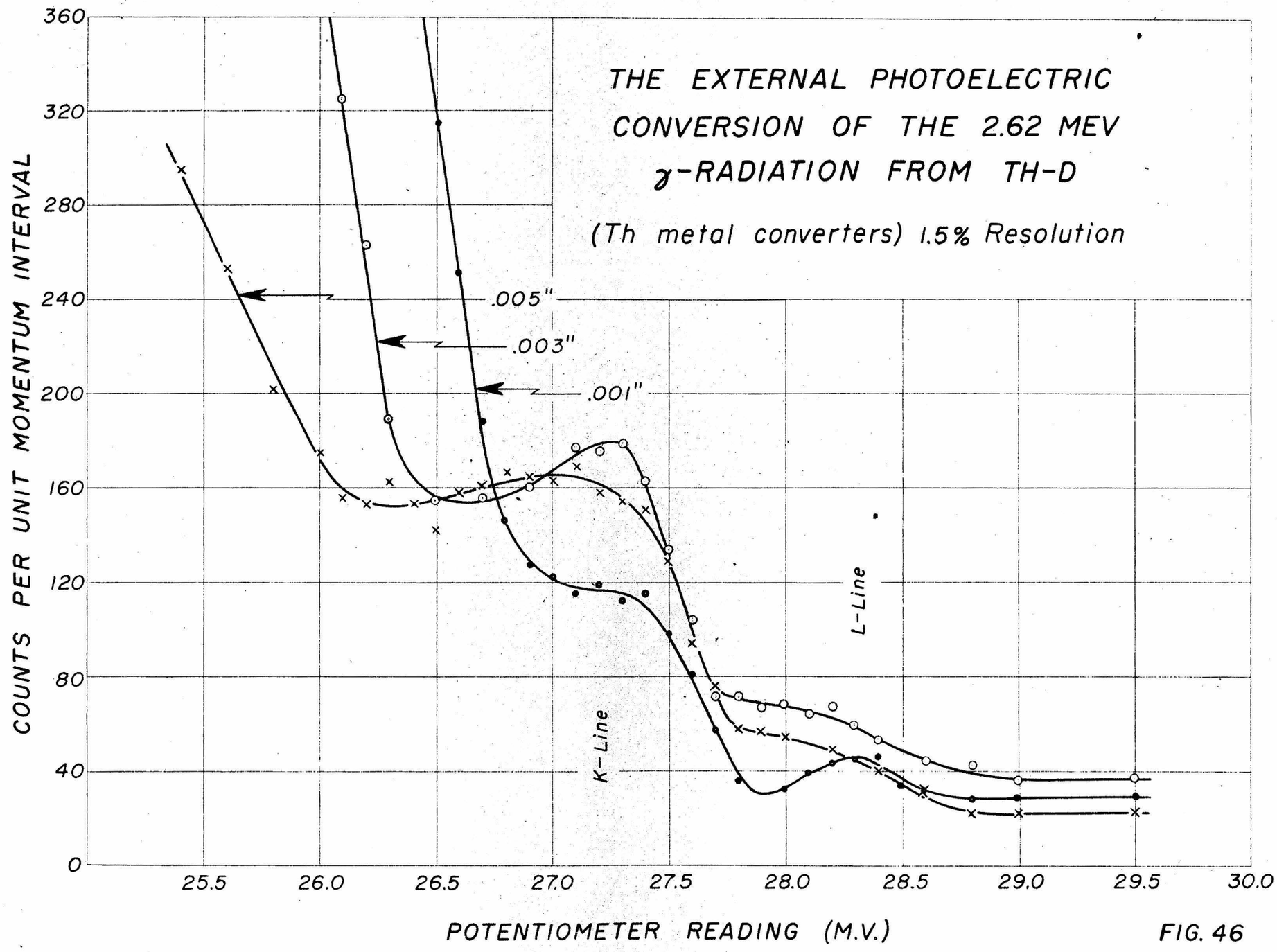
THE EXTERNAL PHOTOELECTRIC CONVERSION OF THE 2.62 MEV γ-RADIATION FROM TH-D
(Th metal converters) 1.5% Resolution
.005"
.003"
.001"
K-Line
L-Line
COUNTS PER UNIT MOMENTUM INTERVAL
POTENTIOMETER READING (M.V.)
0
40
80
120
160
200
240
280
320
360
25.5
26.0
26.5
27.0
27.5
28.0
28.5
29.0
29.5
30.0

FIG. 46

TABLE H

Peak Determinations, .0005" Thorium Converter, resolution 1.5%

γ-Ray Source	Line	M.V. (current)	M.V. † (current)	$B\rho$ ‡ (Gauss-cm)	E_e (kev)	$E_e + E_{K\ L}$ (kev)	Δ (kev)	$E\gamma$ (kev)
Au^{198} decay	K	43.53	43.67	2092.9	298.2	408.0	3.2	411.2
Li^{7*}	K	49.36	49.50	2372.3	364.8	474.6	(3.8)	478.4 ± .9
Au^{198} decay	L	51.24	51.38	2462.4	386.9	407.0	4.2	411.2
e^+ annihilation	K	52.10	52.24	2503.6	397.1	506.9	3.9	510.8
B^{10*}	K	68.63	68.77	3295.8	601.4	711.2	(4.9)	716.1 ± 1.3
Co^{60} decay (a)	K	13.718	103.2_6	4949.	$1058._2$	$1168._0$	(4.2)	$1172._2$ ± 2.5
Co^{60} decay (b)	K	15.275	114.9_6	5509.	$1217._8$	$1327._6$	(4.0)	$1131._6$ ± 2.9

† Values reduced to standard shunt reading, and corrected for axial component of stray fields by adding 0.14 M.V.

‡ Using as a calibration $B\rho/M.V. = 47.92_5 \pm .03$.

shift curves of Fig. 44 can be obtained from the data relating both the "known" and "unknown" lines converted in foil thicknesses other than .0005". The unknown γ-ray energies are determined by using the data in Tables G and H for .0005" converters, thus enabling one to calculate the shifts for the other foil thicknesses. Table I shows these values, also they have been plotted in Fig. 44. The agreement between the semi-empirical curve and the experimental points is on the whole satisfactory.

While no great claim to precision can be made in the arguments on which the peak shift corrections are based, a comparison of the values of Table G with those of Table H indicates satisfactory agreement between the two sets of determinations. It may be remarked that in the case of the Li^{7*} radiation, the fact that the line is bracketed between two known values makes the determination almost independent of the corrections adduced above. For the Co^{60}, a direct extrapolation, ignoring the peak shift would lead to values about 6 kev higher than those quoted in Table H.

We will now return to the experiments done with 3.0% resolution. These experiments will not be described in great detail, since in general this work is less precise than that carried out at the higher resolution. In its final low resolution configuration, the spectrometer again yielded a symmetric window curve, with a shape well approximated by a Gaussian function (Fig. 47), of half width 3.0%. The momentum calibration of the spectrometer for this configuration was determined

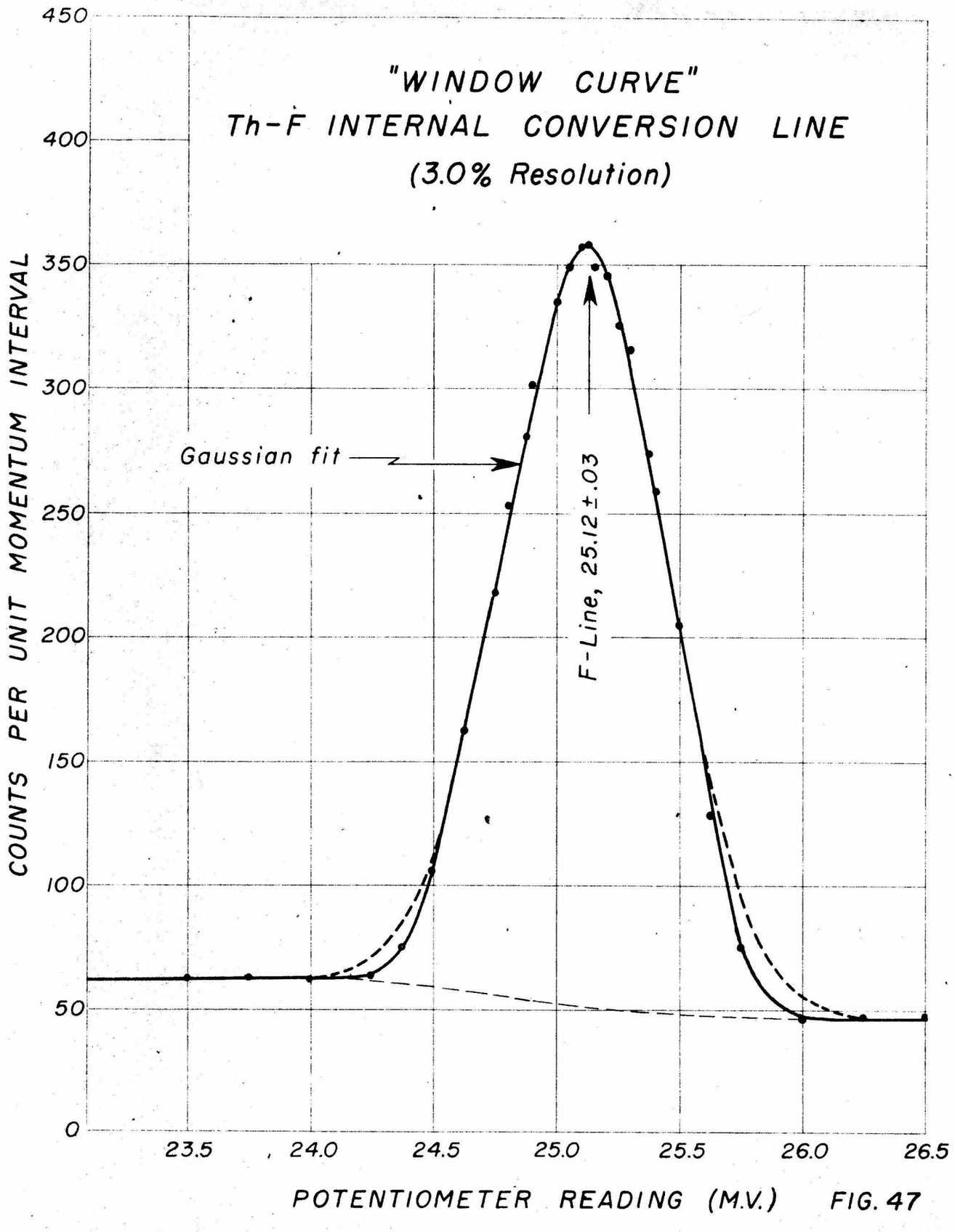
"WINDOW CURVE"
Th-F INTERNAL CONVERSION LINE
(3.0% Resolution)
Gaussian fit
F-Line, 25.12 ± .03
UNIT MOMENTUM INTERVAL
COUNTS PER
450
400
350
300
250
200
150
100
50
0
23.5
24.0
24.5
25.0
25.5
26.0
26.5
POTENTIOMETER READING (M.V.)

FIG. 47

TABLE I

Peak Shift Determinations for various γ-rays
(K-Lines, resolution 1.5%)

γ-Ray Source	Foil Thickness	M.V. (Current)	M.V. † (Current)	Bρ ‡ (Gauss cm)	E_e (Kev)	$E_e + E_{K,L}$ (Kev)	$E\gamma$ (Kev)	Δ (kev)
Au^{198} decay	.00025	43.66	43.80	2099.1	299.7	409.5	411.2	1.7± .9
"	.001	43.50	43.64	2091.4	297.9	407.7	411.2	3.5± 1.1
"	.003	43.50	43.64	2091.4	297.9	407.7	411.2	3.5± 1.4
B^{10}*	.00025	68.94	69.08	3310.7	605.4	715.2	716.4	1.2± 1.5
"	.001	68.44	68.58	3286.7	599.0	708.8	716.4	7.6± 1.7
"	.003	68.30	68.44	3280.0	597.2	707.0	716.4	8.6± 1.9
Co^{60} decay (a)	.001	13.690	103.05	4939.	1055.4	1165.2	1172.4	7.2± 3.3
"	.003	13.55	102.0	4888.	1041.	1151.	1172.4	21 ± 7
Co^{60} decay (b)	.001	15.240	114.70	5497.	1214.4	1324.2	1330.9	6.7± 3.6
ThD*	.001	27.37	205.89	9867.	2491.	2601.	2618.	17 ± 9
"	.003	27.26	205.06	9828	2479.	2589.	2618.	29 ± 8
"	.005	26.96	202.80	9719.	2447.	2557.	2618.	61 ± 17

† Values reduced to standard shunt reading, and corredted for axial component of stray fields by adding 0.14 M.V.

‡ Using as a calibration $B\rho/M.V. = 47.92_5 \pm .03$.

from the internal conversion "F" line (1385.8 Gauss cm) shown in this figure. The resulting peak calibration is 55.17 ± .2 Gauss cm per milli volt. As stated earlier no correction for the axial component of the stray fields was made, the magnitude of the correction that would have been appropriate was included as one of the sources of error.

In general the sources used in these experiments were of the same size and assembly as the corresponding ones in the higher resolution work. A typical low energy thorium converted line is the one shown in Fig. 48, for the γ-radiation from the excited state in Li^{7*} for a .001" thick converter. While an example of a high energy line is shown in Fig. 49 for the γ-radiation from the excited state of C^{13*} produced in the reaction $C^{12}(d,p)C^{13*}$, the converter thickness was .003".

The results of the several measurements made with various γ-rays and converter thicknesses, relating to peak determinations, are given in Table J. The normalization of the interpolation expression for peak shifts based on the Au^{198} and annihilation radiation points gave $\gamma = 0.85$, which is just the value obtained for the 1.5% resolution experiments. The curves of Fig. 50 show the peak shift correction as a function of electron energy and converter thickness. The normalization points are plotted. The value of the shifts for the "unknown" lines are taken from this figure and are given in Table J. The energy determinations for the B^{10*} and Li^{7*} γ-rays are

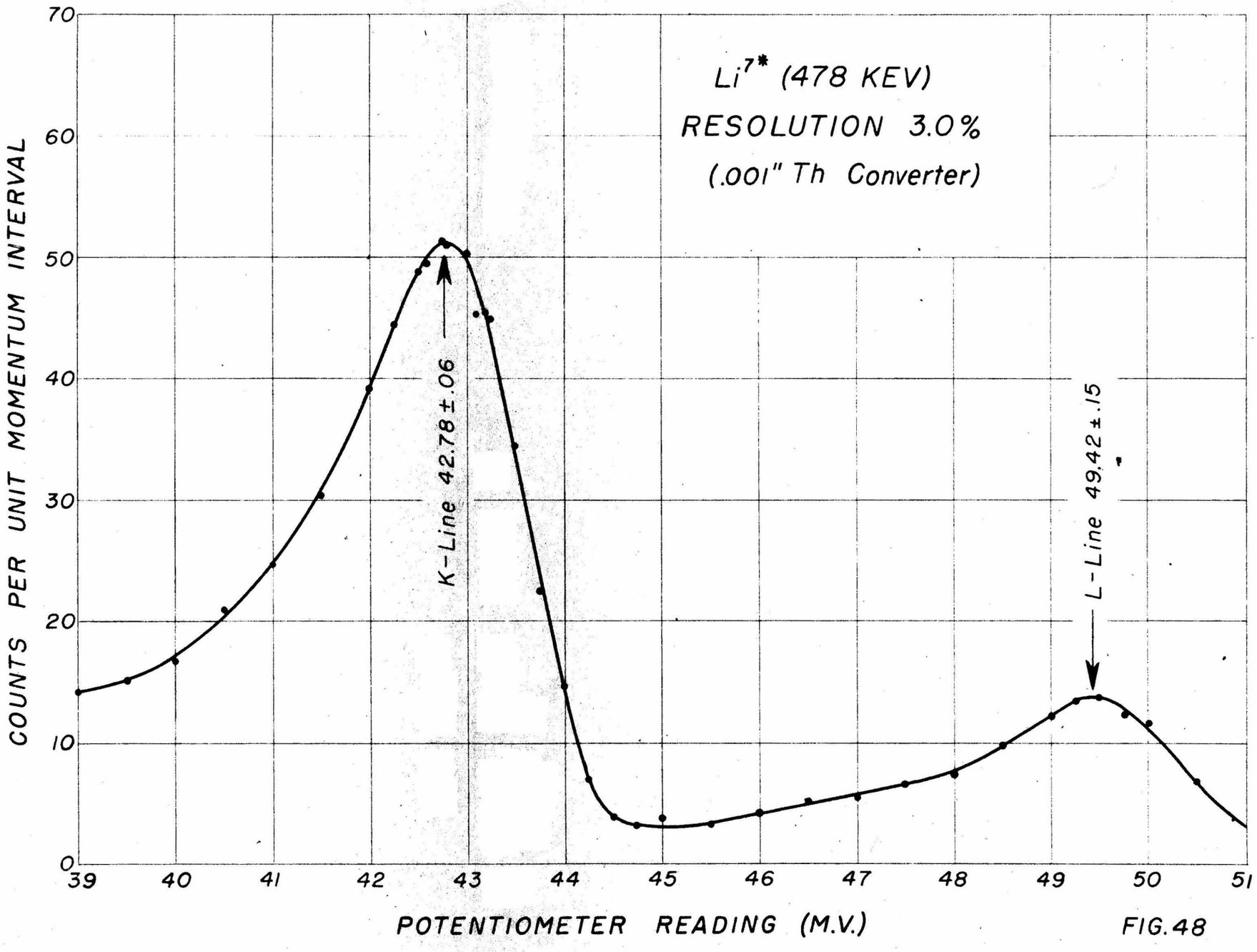
Li^{7*} (478 KEV)
RESOLUTION 3.0%
(.001" Th Converter)
K-Line 42.78 ± .06
L-Line 49.42 ± .15
COUNTS PER UNIT MOMENTUM INTERVAL
POTENTIOMETER READING (M.V.)
0
10
20
30
40
50
60
70
39
40
41
42
43
44
45
46
47
48
49
50
51

FIG. 48

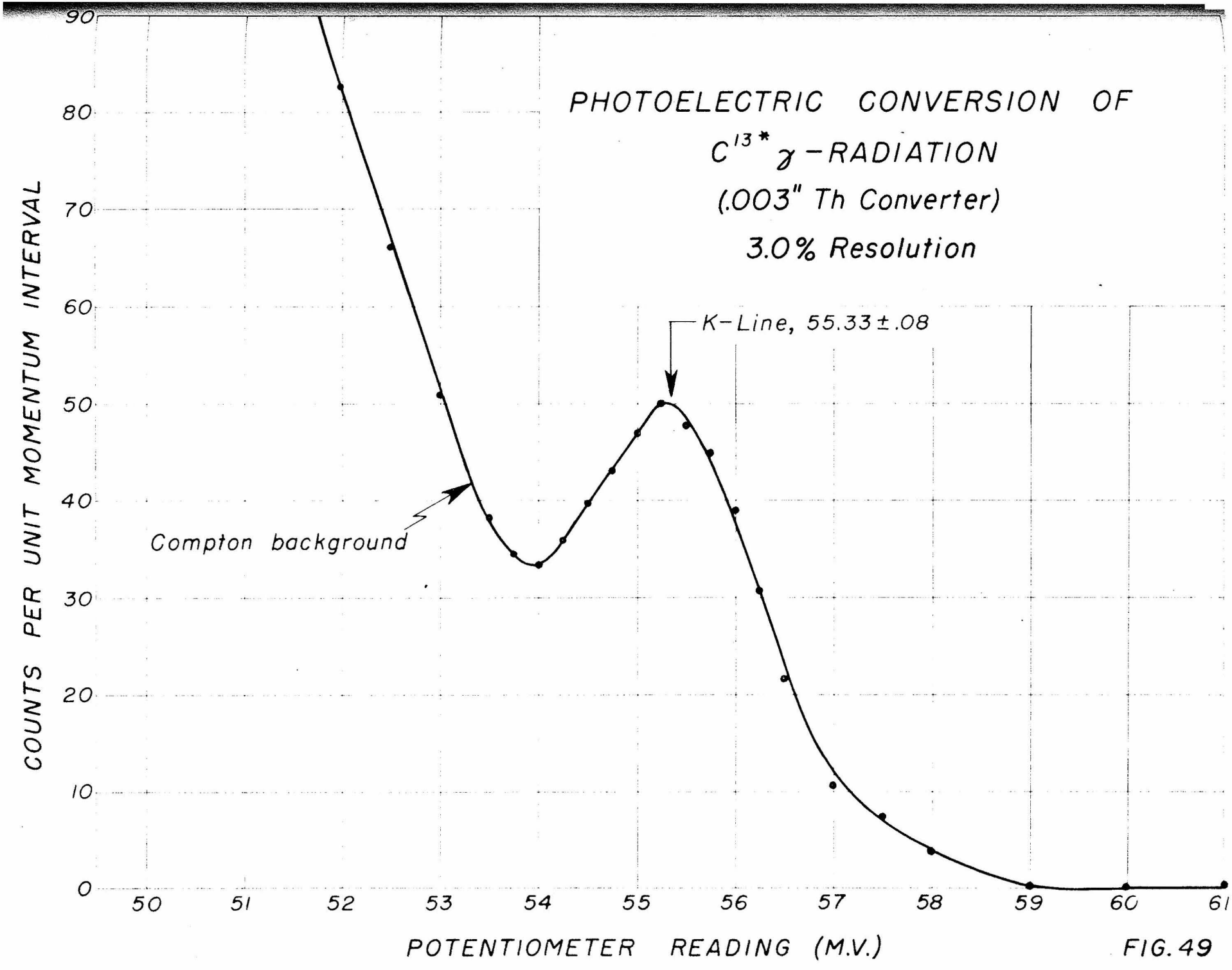
PHOTOELECTRIC CONVERSION OF
C^{13*} γ-RADIATION
(.003" Th Converter)
3.0% Resolution
K-Line, 55.33 ± .08
Compton background
COUNTS PER UNIT MOMENTUM INTERVAL
POTENTIOMETER READING (M.V.)
0
10
20
30
40
50
60
70
80
90
50
51
52
53
54
55
56
57
58
59
60
61

FIG. 49

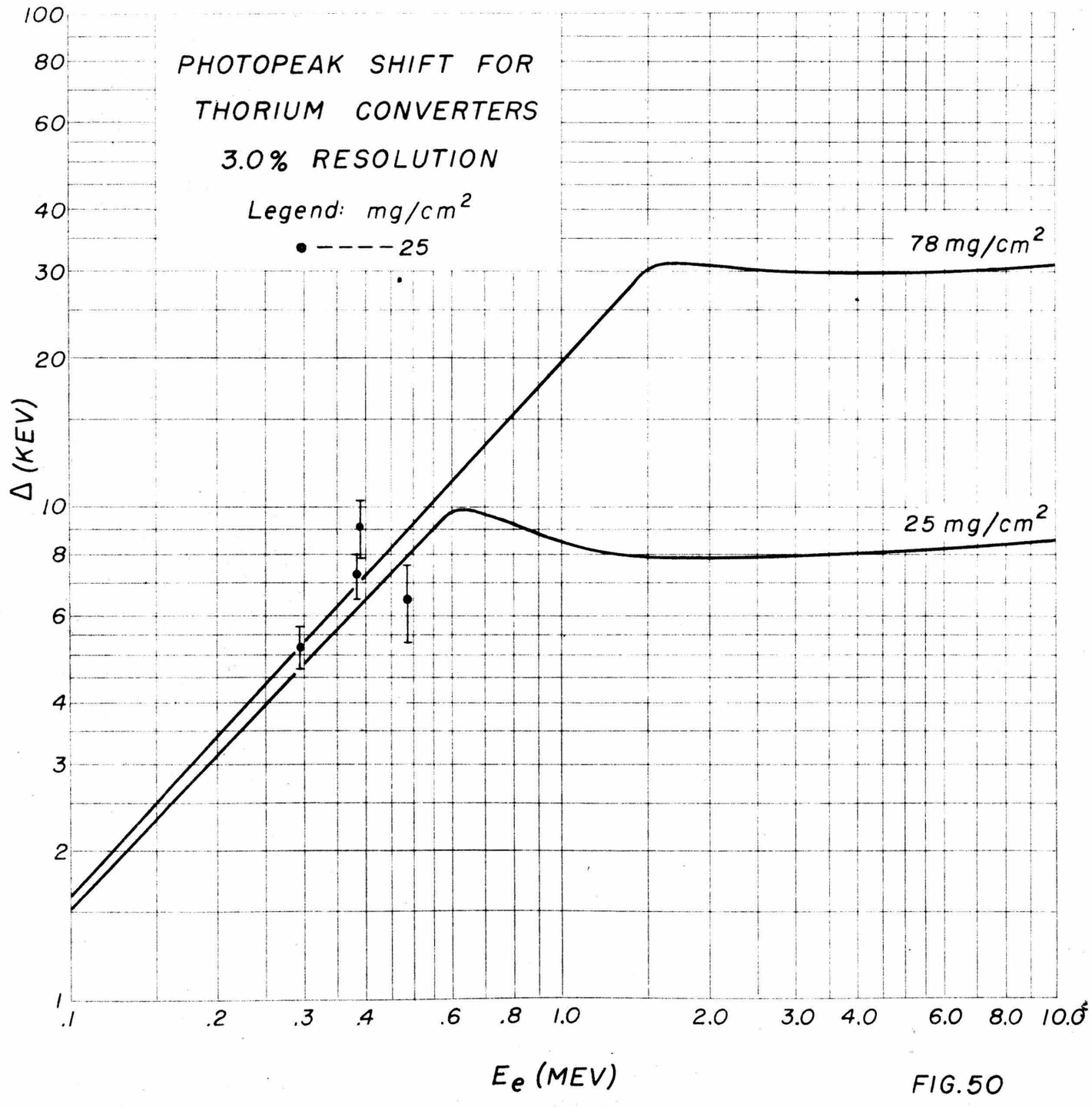
PHOTOPEAK SHIFT FOR
THORIUM CONVERTERS
3.0% RESOLUTION
Legend: mg/cm²
●----25
78 mg/cm²
25 mg/cm²
Δ (KEV)
100
80
60
40
30
20
10
8
6
4
3
2
1
.1
.2
.3
.4
.6
.8
1.0
2.0
3.0
4.0
6.0
8.0
10.0
Ee (MEV)

FIG. 50

TABLE J

Peak Determinations, resolution 3.0%

γ -Ray Source	Line	Foil Thickness	M.V. (Current)	$B\rho$ ‡ (Gauss cm)	E_e (Kev)	$E_e + E_{K\ L}$ (Kev)	Δ (Kev)	$E\gamma$ (Kev)
Au^{198} decay	K	.001	37.78	2084.	296.2	406.0	5.2 ± 1.0	411.2
"	L	.001	44.41	2450.	383.8	403.9	7.3 ± 1.4	411.2
e^+ annihilation	K	.001	45.00	2483.	391.9	501.7	9.1 ± 1.9	510.8
"	L	.001	51.63	2848.	484.2	504.3	6.5 ± 2.5	510.8
Li^{7*}	K	.001	42.78	2360.	361.8	471.6	(5.8)	477.4 ± 1.4
"	L	.001	49.42	2726.	453.0	473.1	(7.4)	480.5 ± 2.4
B^{10*}	K	.001	59.56	3286.	598.8	708.6	(9.8)	718.4 ± 3.1
"	K	.003	58.94 †	3252.	589.7	699.5	(11.1)	710.6 ± 4.0
C^{13*}	K	.003	207.3_2 †	11437.	2956.	3066.	(30.)	3096. ± 17

† Values reduced to standard shunt reading, using a shunt ratio of 3.747.

‡ Using as a calibration 55.17 ± .2 $B\rho$/M.V.

seen to be in good agreement with the values obtained in the higher resolution experiments.

If the extrapolated edge calibration of 53.73 ± .2 gauss cm per millivolt, based on the window curve of Fig. 47, is used in conjunction with the extrapolated edge observed for the K - line from the Au^{198} γ -radiation, a value of $E_e + E_K = 408.9 \pm$ 1.0 kev results. Thus an extrapolated edge shift of 3.3 ± 1.0 kev is required, since this γ-ray energy is known to be 411.2 kev. The observed half width at full maximum for this line was 7.0%, hence using the curve of Fig. 26, an edge shift of 2.5 kev would be expected. Thus as discussed before, when the window curve is broad enough to allow the back slope of the primary distribution to materially influence the observed spectrum near the front edge, an edge shift should appear.

The Doppler Effect and the Determination of Level Energies

In the cases of the Li^{7*}, B^{10*}, and C^{13*} radiations, an appreciable correction for Doppler effect is involved in the determination of the energy of the excited state because of the center of mass motion. The shift associated with a center of mass velocity along the spectrometer V is, neglecting effects of order V^2/c^2 and assuming isotropic disintegration,

$$\delta = \frac{V}{c} E_\gamma \overline{\cos\theta}$$

where $\overline{\cos\theta}$ is the mean cosine of the angle between the spectrometer axis and the gamma rays producing photo electrons in the acceptance cone. An estimate of $\overline{\cos\theta}$ can be made if the

scattering of the photoelectrons is neglected and if the angular distribution of the photoelectrons is simply taken to be a delta function at the angle

$$\omega = \cos^{-1}\beta_e$$

with the direction of the gamma ray, where β_e is the velocity of the photoelectron in units of the velocity of light. Then for the geometry in question, with θ_o the acceptance angle of the spectrometer

$$\overline{\cos\theta} = \sqrt{\cos(\theta_o+\omega)\cos(\theta_o-\omega)}$$

Table K gives the calculations leading to the values of δ, assuming that the residual nucleus has not been stopped before the emission of the gamma ray.

TABLE K

Doppler Shifts

Reaction	Bombarding Voltage (Mev)	$\frac{v}{c}$	ω	θ_o	$\overline{\cos\theta}$	δ (kev)
$Li^7(p\ p')Li^{7*}$	1.05	.0059	38.5°	13°	.78	2.2
$Be^9(d\ n)B^{10*}$	.96	.0058	27.1°	13°	.86	3.6
$C^{12}(d\ p)C^{13*}$	1.17	.0050	8.5°	30°	.85	13.

The scattering experienced by the photo electrons will in general reduce the Doppler shift, since radiation emitted at large angles to the center of mass motion will contribute to the spectrum. In an experimental comparison of the gamma ray from the

decay of Be^7 with that accompanying the inelastic scattering of protons by Li^7, the Doppler shift was found to be 1.6 kev[34] for the same geometrical arrangement used here. The calculated shift for B^{10*} has accordingly been reduced by the same proportion in the computation of the final values, even though at this higher energy the scattering is certainly less important. However, it is felt that the scattering is sufficiently less pronounced at 3.0 Mev, so that the full calculated Doppler shift should be used for the C^{13*} radiation. Table L presents the final values, using the means of Tables G and H, and including the estimated Doppler shifts.

TABLE L

Gamma Ray and Excitation Energies

Reaction	E_γ (kev)	δ (kev)	E_{level} (kev)
$Li^7(p\ p')Li^{7*}$	478.3 ± .6	1.6 ± .7	476.7 ± .9
$Be^9(d\ n)B^{10*}$	716.4 ± .8	2.6 ± 1.0†	713.8 ± 1.3
$Co^{60}(\beta^-)Ni^{60*}$ (a)	1172.4 ± 1.8	0	1172.4 ± 1.8
$Co^{60}(\beta^-)Ni^{60*}$ (b)	1330.9 ± 2.1	0	1330.9 ± 2.1
$C^{12}(d\ p)C^{13*}$	3096. ± 17	13. ± 5.	3083 ± 18

† Taken as $\frac{1.6}{2.2} \times 2.6$

The present value for the excited state of Li^7 is slightly lower than the value 478.5 ± 1.5 kev given by Elliott and Bell[35]

for $B^{10}(n\alpha)Li^{7*}$ but as the probable errors overlap, the difference is hardly significant. The Co^{60} values are about 20 kev higher than those obtained by Jensen, Laslett and Pratt[27]; the reason for this discrepancy is not clear. A preliminary crystal spectrometer determination for these lines, kindly communicated to me by Professor DuMond and Dr. Lind is in good agreement with the values quoted here.

III. GAMMA RAY ENERGY DETERMINATIONS USING THE COMPTON EFFECT

General Introduction

For a given intensity of γ-radiation from a source (i.e. number of quanta per second) and for a fixed thickness of photoelectric converter the yield of photo electrons decreases rapidly with an increase in the quantum energy. Heitler[16] calculated the dependence of the integrated cross-section per electron for the K shell photoelectric effect, on the energy of the γ-quantum and the atomic number Z of the converter atom. His results are illustrated in Fig. 51, where the unit of cross section ϕ_o is taken as the Thomson scattering cross section. (ϕ_o = .657 x 10^{-24} cm^2 or .657 barns). Curves for C, Al, Cu, Pb, and Th are given illustrating the rapid variation with Z, the variation being with the 5.0 power of Z. The total cross section per electron for Compton scattering is also shown in Fig. 51. An examination of this figure shows that the total cross section per atom for these two effects, for thorium becomes equal at approximately $h\nu$ = 400 Kev. Thus it would appear that while for γ-ray energies below this energy the photoelectric effect gives a more intense secondary electron spectrum, harder γ-radiation would be expected to give a more intense/Compton secondary spectrum and hence would be a more useful phenomenon from which to determine γ-ray energies. However, it must be remembered that the secondary spectrum from the photoelectric effect is a sharp line while

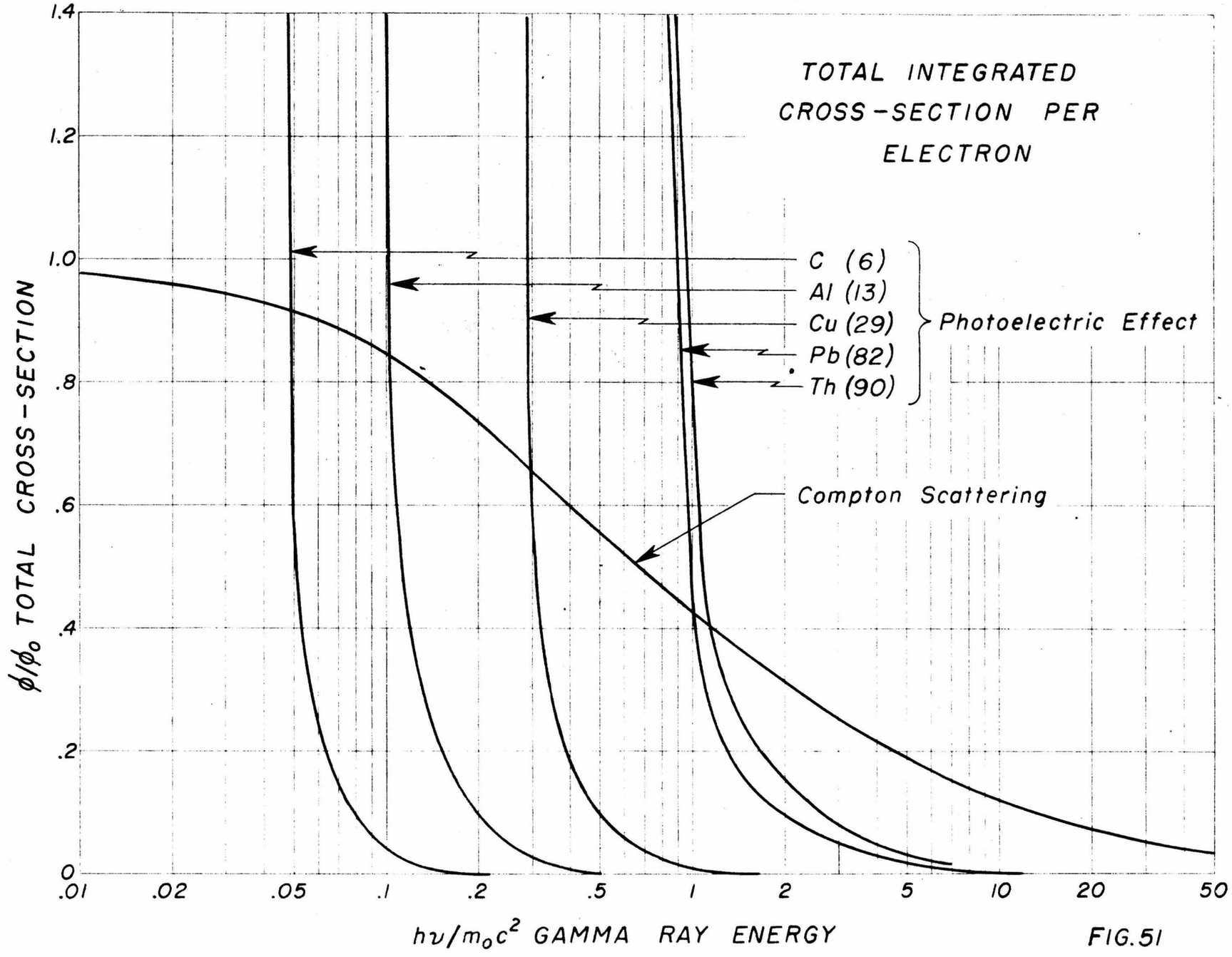
TOTAL INTEGRATED
CROSS-SECTION PER
ELECTRON
C (6)
Al (13)
Cu (29)
Pb (82)
Th (90)
Photoelectric Effect
Compton Scattering
ϕ/ϕ_o TOTAL CROSS-SECTION
1.4
1.2
1.0
.8
.6
.4
.2
0
.01
.02
.05
.1
.2
.5
1
2
5
10
20
50
$h\nu/m_oc^2$ GAMMA RAY ENERGY

FIG. 51

the Compton secondaries are distributed in a spectrum extending down to zero energy. It is true however that the Compton secondary electron spectrum which has its maximum at the maximum electron recoil energy becomes markedly sharper as the incident γ-ray energy is increased. Experimentally it is found that for instrument resolutions better than 5% the Compton effect above about 4 Mev is better suited to the determination of γ-ray energies. When it is intended to use the Compton effect it is of advantage to increase the contrast between the two effects by using a converter of atomic number of the order of Cu or less to prevent the overlapping of the weak photo line on the Compton distribution.

Source and Converter Geometry

The sources employed for hard γ-radiation when the energy determination is to be made employing the Compton effect generally consisted either of a thin target deposited on a copper converter or as in the case of the $C^{12}(d,p)C^{13*}$ reaction a thick target. In this latter case graphite targets ranging in thickness from .002" to .016" and approximately 5/16" on a side were used. In general all sources consisted of converters having roughly a mean diameter of 3/8" in addition to any other specific target material. Since the beam spot on the target was of the order of .080" in diameter, the γ-ray source may be considered as a point source placed on the back of a converter of thickness t; see Fig. 52a. The incident γ-radiation is then imagined to produce recoil Compton electrons throughout

SOURCE GEOMETRY

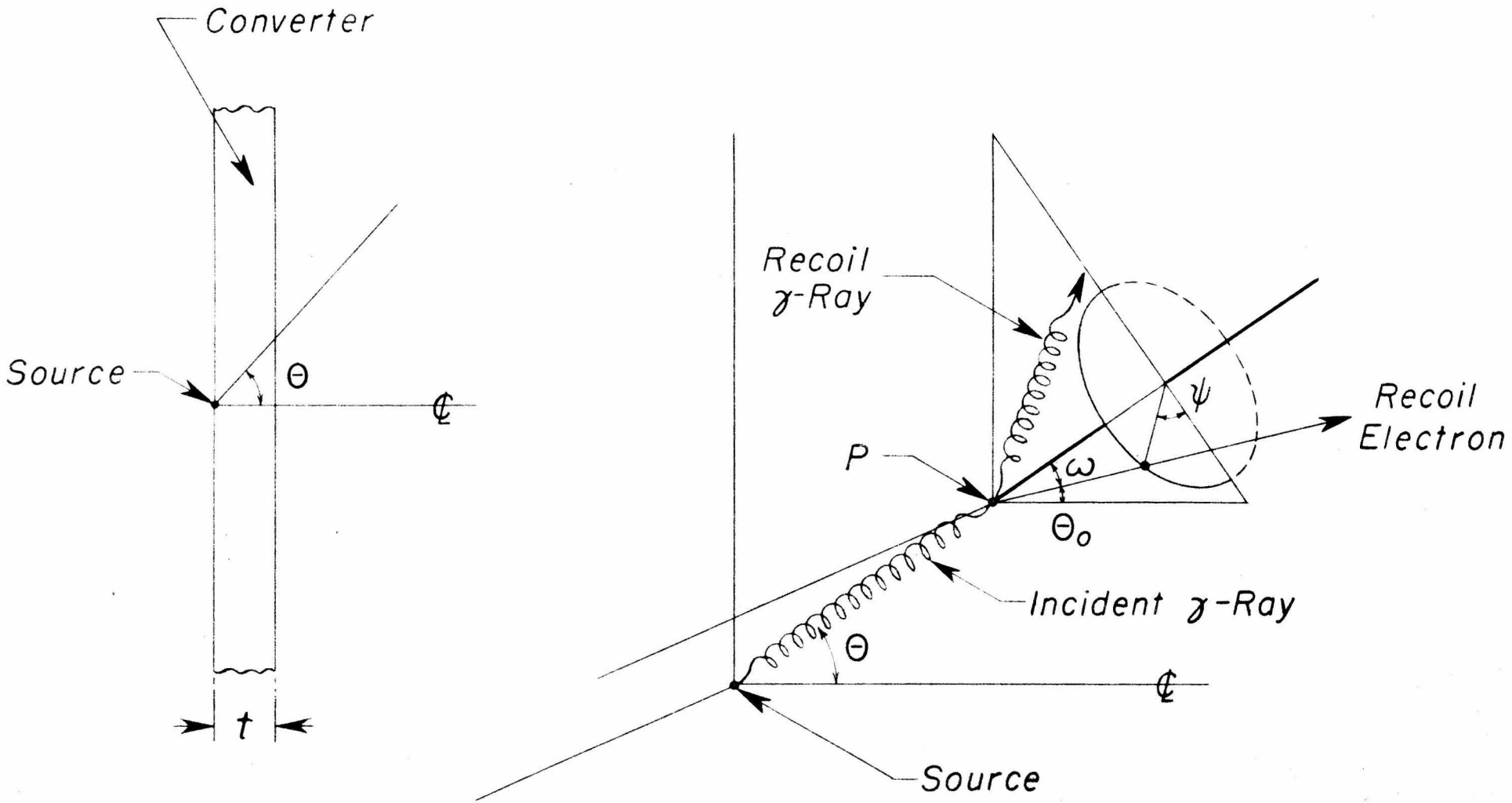

a

b

FIG. 52

the volume of the converter. The Fig. 52b illustrates schematically the production of a Compton electron at point P within the converter. The angle the incident γ-radiation makes with spectrometer axis is taken as θ while θ_0 and ω represent the angle of acceptance of the spectrometer and the angle the secondary electron makes with the direction of the incident γ-radiation. The azimuthal angle ψ completes the coordinate designation of recoil electron trajectory. For a given incident γ-ray energy the angle ω uniquely specifies the energy of the recoil electron. Hence for a given spectrometer current setting only the electrons with a specified ω will have the appropriate momentum to meet the focusing condition while the setting of the spectrometer stops determines the trajectory angle θ_0 which these electrons must have in addition to the requirement on ω. It is supposed in these considerations that at the electron energies discussed and for the thickness and atomic number of the converter used, scattering of the Compton electrons is negligible.

The probability then that a γ-ray per unit solid angle traveling in a direction θ produces a recoil electron at an angle ω per unit solid angle when the differential cross section is $P(\cos\omega)$ is

$$dI = \frac{Nt}{\cos\theta} \cdot 2\pi d(\cos\theta) \cdot P(\cos\omega)\, d(\cos\omega)\, d\psi \qquad (121)$$

where N is the density of electrons in the converter. In this expression the attenuation of the γ-ray flux due to absorption and scattering has been neglected. Now for the geometry described

$$\cos\theta_o = \cos\omega\cos\theta + \sin\omega\cos\psi\sin\theta \qquad (122)$$

Thus holding ω and θ fixed

$$d(\cos\theta_o) = -\sin\omega\sin\theta\sin\psi\, d\psi\,. \qquad (123)$$

Equation (122) may be used to determine $\sin\omega\sin\theta\sin\psi$ in terms of θ, θ_o, and ω which together with equation (123) gives

$$d(\cos\theta_o) = \left\{\left[\cos(\theta_o-\omega)-\cos\theta\right]\left[\cos\theta-\cos(\theta_o+\omega)\right]\right\} \qquad (124)$$

and hence from equation (1)

$$dI = \frac{2\pi Nt\, d(\cos\theta)\, P(\cos\omega)\, d(\cos\omega)\, d(\cos\theta_o)}{\cos\theta\left\{\left[\cos(\theta_o-\omega)-\cos\theta\right]\left[\cos\theta-\cos(\theta_o+\omega)\right]\right\}^{1/2}}\,. \qquad (125)$$

If we now let

$$\begin{aligned} x &= \cos\theta \\ a &= \cos(\theta_o+\omega) \\ b &= \cos(\theta_o-\omega) \end{aligned} \qquad (126)$$

in equation (125) the result may be integrated as

$$dI' = 4\pi Nt\, P(\cos\omega)\, d(\cos\omega)\, d(\cos\theta_o)\int_b^a \frac{dx}{x\sqrt{(x-a)(b-x)}}$$

or

$$dI' = \frac{4\pi^2 Nt\, P(\cos\omega)\, d(\cos\omega)\, d(\cos\theta_o)}{\sqrt{\cos(\theta_o+\omega)\,\cos(\theta_o-\omega)}}\,. \qquad (127)$$

It should be mentioned that the singularities in equation (127) correspond to a γ-ray angle $\theta = \frac{\pi}{2}$ which because of the assumption of no attenuation in connection with equation (121) produces this effect. Only the singularity $\omega+\theta_o = \frac{\pi}{2}$ is physically realizable, but does not however play a pronounced

role in the range of the distributions to be considered.

The Compton Distribution, and Experimental Results

To obtain the Compton electron distribution per unit momentum interval as a function of the momentum, $2\pi P(\cos\omega)d(\cos\omega)$ in equation (127) is replaced by the probability factor $\mathcal{P}(\phi)d\phi$ derived from the Klein-Nishina formula in Appendix V.

Thus using equations (57) and (59) from the Appendix we have in the notation employed there

$$dI' = \frac{4\pi^2 N t r_0^2 [(\gamma+1)^2+a]\left\{1+\left(\frac{a-1}{a+1}\right)^2+\frac{4\gamma^2}{(a+1)(a+1+2\gamma)}\right\} d\phi\, d\theta_0}{\gamma\mu(a+1+2\gamma+2\gamma^2)[(1+\gamma)^2\cot^2\theta_0 - a]^{1/2}} \quad (128)$$

$$\text{with } \frac{\phi}{\phi_{max}} = \frac{[(\gamma+1)^2+a]^{1/2}(2\gamma+1)}{[a+1+2\gamma](\gamma+1)} = \frac{\left[1+\frac{a}{(\gamma+1)^2}\right]^{1/2}}{1+\frac{a}{1+2\gamma}} . \quad (129)$$

When the range of the angle θ_0 accepted by the spectrometer is small equation (128) may be used directly to give the primary spectrum of electrons from the converter if energy loss and scattering for these electrons is neglected. When the range $\Delta\theta_0$ is large, fortunately equation (128) can be integrated giving

$$dI'' = \frac{4\pi^2 N t r_0^2 [(\gamma+1)^2+a]}{\gamma\mu(a+1+2\gamma+2\gamma^2)}\left\{1+\left(\frac{a-1}{a+1}\right)^2+\frac{4\gamma^2}{(a+1)(a+1+2\gamma)}\right\} \times$$

$$\times \ln\left|x+\left[x^2-\frac{a}{(1+\gamma^2)+a}\right]\right|_{\cos\theta_1}^{\cos\theta_2} d\phi . \quad (130)$$

In obtaining the spectrum $\frac{dI'}{d\phi}$ or $\frac{dI''}{d\phi}$ as a function of $\frac{\phi}{\phi_{max}}$ it is simpler to select values of a and use equation (129) to find $\frac{\phi}{\phi_{max}}$ while using either equation (128) or (130) to obtain

$\frac{dI'}{dp}$ or $\frac{dI''}{dp}$ respectively. The spectrum $\frac{dI'}{dp}$ for $\gamma = 6$ (i.e. $h\nu_0 = 3.1$ Mev) and $\theta_0 = 30^\circ$ with $\Delta\theta_0$ small is plotted in Fig. 53. The distribution has been arbitrarily normalized to give unity at $p/p_{max} = 1$.

To a first approximation the effect of the finite converter thickness is to produce an energy loss approximately proportional to the depth at which the Compton secondary electron is produced. This effect may be taken into account by folding a rectangular curve into the distributions of equation (128) or (130), this rectangle having a width

$$\frac{\Delta p}{p_{max}} = \left[\frac{1}{p_{max}}\frac{dp}{dE}\right]\frac{\epsilon t}{\cos\theta_0}\ , \qquad (131)$$

and unit area, where ϵ is the most probable energy loss per unit length. It will be remembered that ϵ is actually a function of thickness and energy; as an approximation a mean value in the range of thicknesses and energy of interest should be used. For example $\epsilon \approx 4.4$ Kev/mil and $\frac{\Delta p}{p_{max}} = .0016\, t$ (with t in mils), for the graphite target and converter used in studying the γ-radiation from the $C^{12}(dp)C^{13*}$ reaction; here

$$E_{max} \approx 2.9 \text{ Mev} \quad \text{and} \quad \theta_0 = 30^\circ.$$

The primary spectrum must be further modified by the fold of the window curve of the spectrometer in order to obtain the observed distribution. It must be borne in mind that if the distribution over a wide range of momentum is required the absolute resolution is proportional to the momentum of the electron that the spectrometer is set to focus. Fig. 54 shows the results

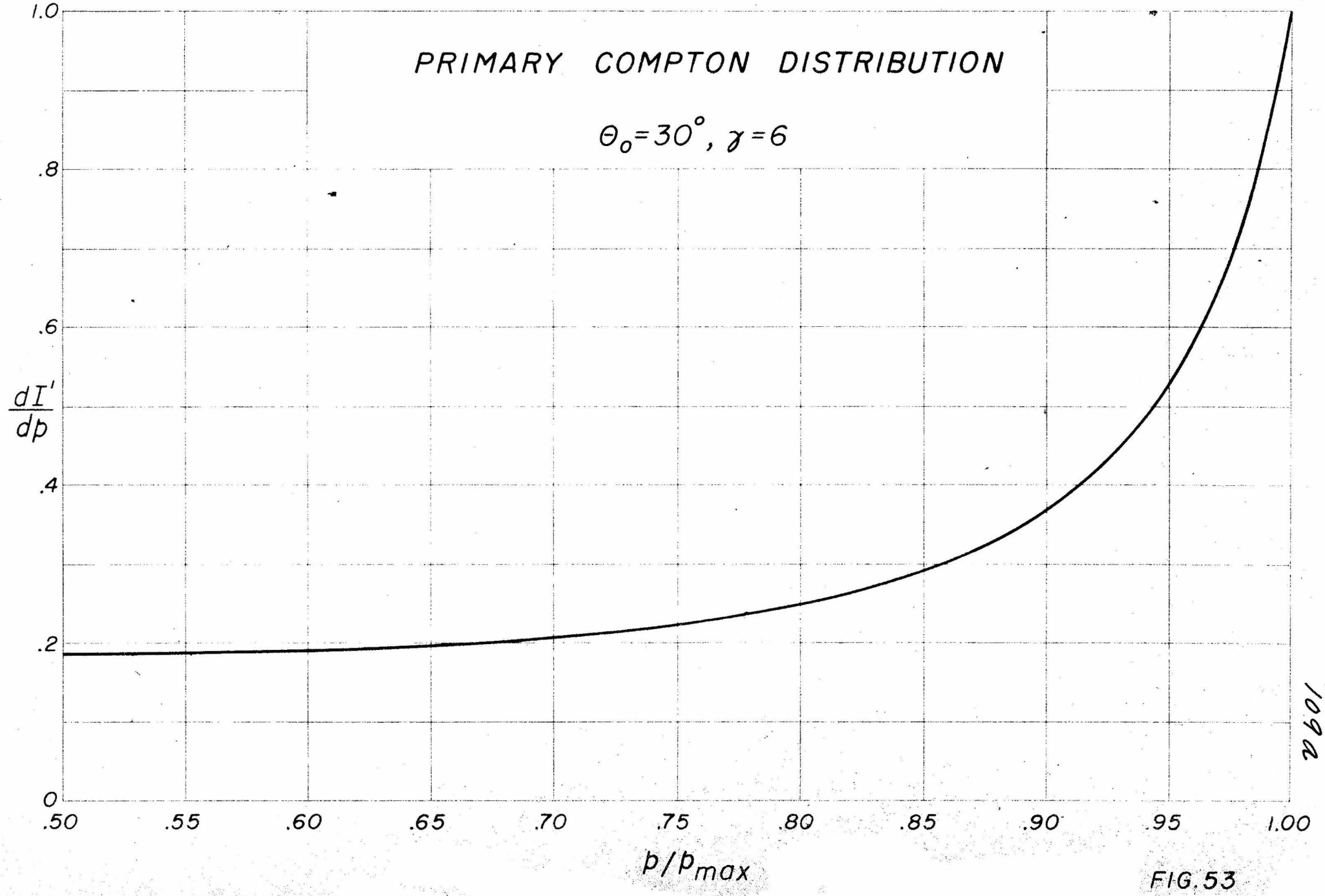
PRIMARY COMPTON DISTRIBUTION
$\theta_0 = 30°$, $\gamma = 6$
1.0
.8
.6
.4
.2
0
$\frac{dI'}{dp}$
.50
.55
.60
.65
.70
.75
.80
.85
.90
.95
1.00
p/p_{max}

FIG. 53

2601

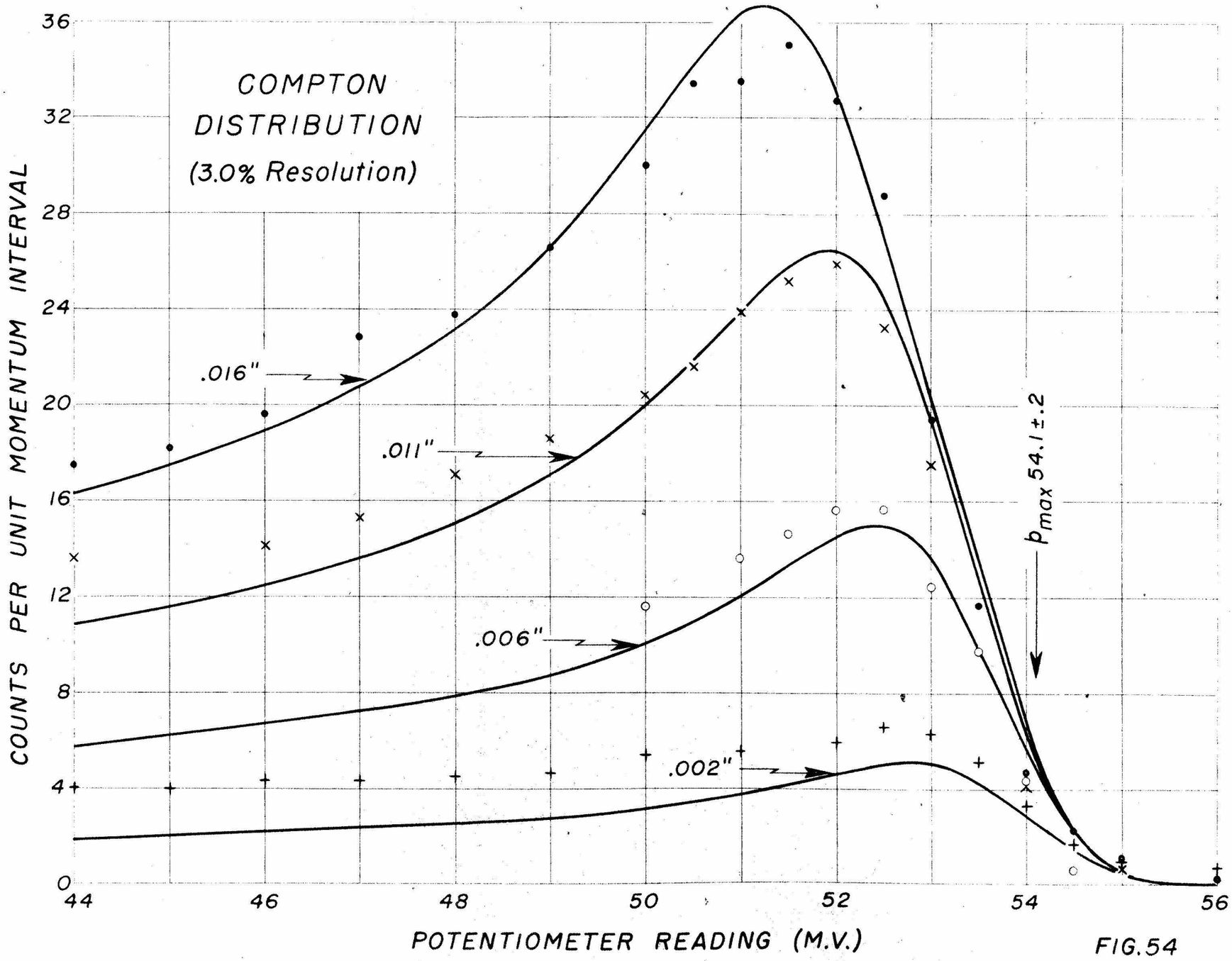
COMPTON
DISTRIBUTION
(3.0% Resolution)
.016"
.011"
.006"
.002"
p_{max} 54.1±.2
COUNTS PER UNIT MOMENTUM INTERVAL
POTENTIOMETER READING (M.V.)
0
4
8
12
16
20
24
28
32
36
44
46
48
50
52
54
56

FIG. 54

of folding a 3.0% resolution window curve, and energy loss curves determined from equation (131) for various thicknesses of graphites, into the spectrum of Fig. 53. The observed experimental points are also plotted. The height of the theoretical curves has been normalized to match the .011" thickness data, also ρ_{max} in millivolts reading on the potentiometer has been adjusted to match the high energy edge of the experimental points.

The thickness of the graphite sources were determined by micrometer measurements and are hence subject to a fairly large uncertainty particularly for the thinner sources. The internal conversion pairs[36] from this γ-ray start appearing at about 40 M.V. and may account for the relatively slower tailing off of the experimental points on the low energy side of the peak in the distribution. While only an approximate value of ρ_{max} was required to predict the observed distribution, a re-evaluation of ρ_{max} as above can be used to give an accurate determination of the γ-ray energy. The value of ρ_{max} determined in this way is $54.1_0 \pm .20$ M.V. or with the known calibration of the spectrometer from the ThC internal conversion "F" line, $\rho_{max} = 11{,}182 \pm 45$ gauss cm. This momentum corresponds to a maximum kinetic energy T_{max} of $2.88_0 \pm .013$ Mev. The γ-ray energy is obtained by adding the value of Δ given in equation (60) of the Appendix V to the maximum kinetic energy of Compton secondaries. The value of Δ as a function of the maximum kinetic energy T_{max} is given in Fig. 55. In the present case $\Delta = .23_4$ Mev thus $h\nu_0 = 3.11_4 \pm .01_4$ Mev. This determination compares

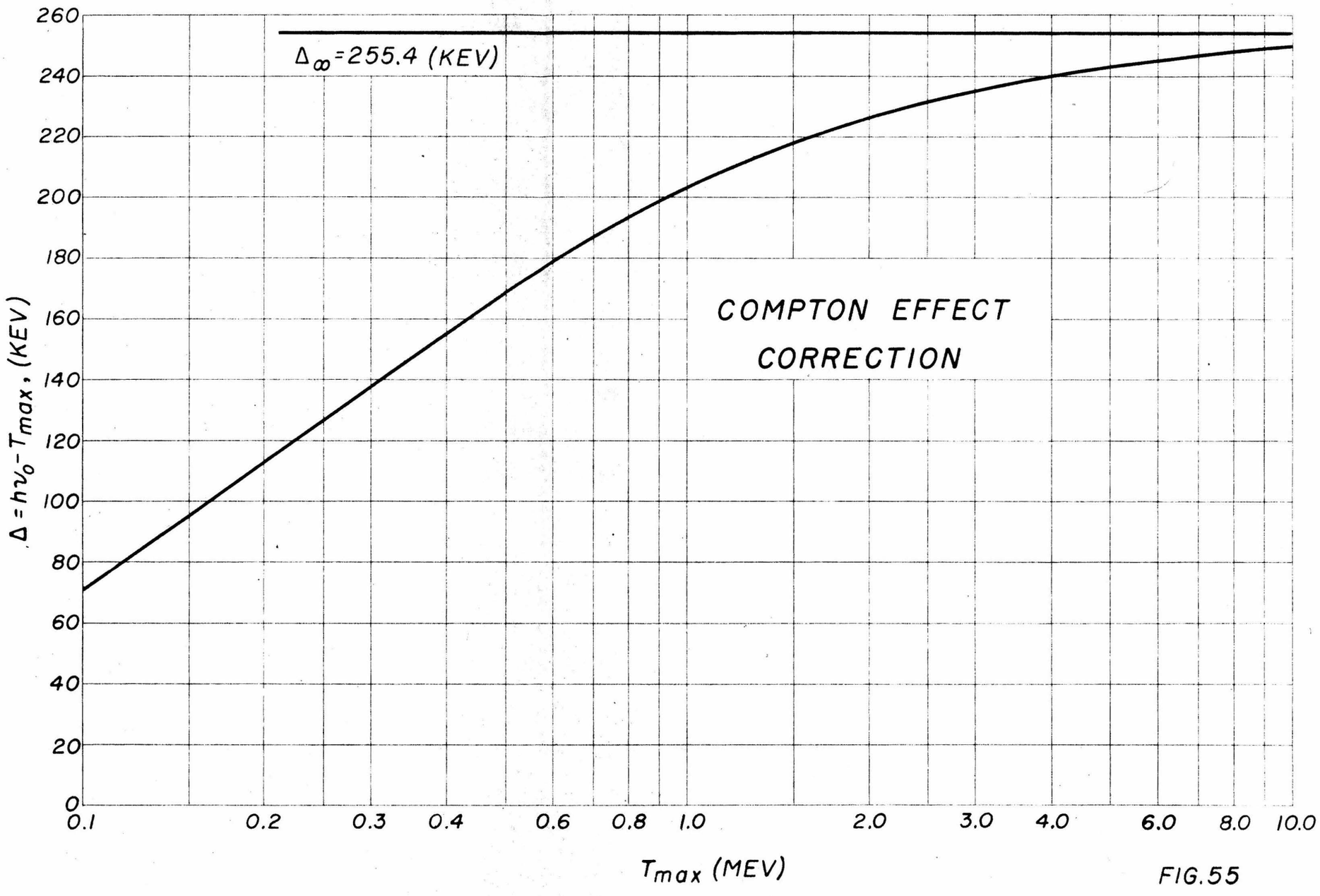
Δ_∞=255.4 (KEV)
COMPTON EFFECT
CORRECTION
$\Delta = h\nu_0 - T_{max}$, (KEV)
260
240
220
200
180
160
140
120
100
80
60
40
20
0
0.1
0.2
0.3
0.4
0.6
0.8
1.0
2.0
3.0
4.0
6.0
8.0
10.0
T_{max} (MEV)

FIG. 55

favorably with the value of $3.09_6 \pm .01_7$ Mev determined from the photoelectric effect. The mean of these values gives $3.10_5 \pm .011$ Mev for the γ-ray energy. When the Doppler shift of 13 ± 5 Kev is added, the value of the energy for the excited state in becomes $3.092 \pm .01_2$ Mev. This determination is in fair agreement with the values obtained by experiments measuring the energy of the proton groups in the reaction $C^{12}(d,p)C^{13*}$.(37)

IV. CONTINUOUS BETA SPECTRA

General Introduction

The discovery of the formation of radioactive Li^8 was made by Crane, Delsasso, Fowler, and Lauritsen* by a cloud chamber study of the disintegration of lithium by deuterons. The threshold reaction $Li^7(d,p)Li^8$, $Q = -0.20 \pm .03$ [38] involved in the discovery is the only convenient way of preparing Li^8 with an electrostatic accelerator. The Li^8 decays with a half life of 0.89 sec predominantly to a broad excited state in Be^8 at approximately 3 Mev., the transition to the ground state apparently being forbidden. The distribution of α -particles arising from the subsequent breakup of the Be^8 nucleus has been extensively studied[39]. Cloud chamber investigations of the β -decay electron spectrum have been carried out.

Radioactive B^{12} was discovered by E.O. Lawrence and R.L. Thornton employing the reaction $B^{11}(d,p)B^{12}$. Again the (d,p) reaction is the only one available for the preparation of B^{12} using an electrostatic accelerator. The decay of B^{12}, half life 0.025 sec. proceeds to the ground state and possibly excited states in C^{12}. The β -decay spectrum has been studied using cloud chambers.

Both β -decay processes are of considerable interest in that they may shed some light on the level structure in the daughter nuclei and because of the large disintegration energies

---

* References appearing before Nov., 1947 are summarized in ref. (37).

involved.

Experimental Method

In the investigation of these β -spectra the four coils of the spectrograph were used together as a unit centered between the source and the detector window. The spectrograph stops were set for ring focusing with a resolution of 2.6%. The helical baffle was used to reduce spurious counts from electrons scattered by the spectrometer. Further precautions taken against scattering included the use of the baffles described earlier. The momentum calibration was obtained using the internally converted "X" line. The compensation for the earth's magnetic field and other stray magnetic fields was checked at the end of the experiments. It was found that the compensation was satisfactory down to the internally converted Th"I" line or approximately 200 Kev. The beam from the electrostatic accelerator was brought directly into the vacuum chamber of the spectrometer to bombard suitable targets for the production of the radioactive elements.

Partly to check the extent to which the effects of electron scattering within the spectrometer had been eliminated, the positron spectrum of N^{13} (half life $10.1_3 \pm .1$ min) was run. The N^{13} was prepared by bombarding with deuterons a thin soot target sandwiched between two layers of 0.2 mg/cm^2 Be foil* employing the reaction $C^{12}(d,p)N^{13}$. The resulting momentum spectrum

---

* I am indebted to Dr. H. Bradner of the University of California for the Be foils.

after cosmic ray background has been subtracted is shown in Fig. 56. A background which is very slightly field sensitive and of the order of cosmic ray background is still left above the end point of the β -spectrum. This represents the amount of scattering by the spectrometer and possibly some slight diffusion of the radioactive nitrogen from the target. In connection with this latter point an appreciable increase in background was observed with non-sandwiched targets when the vacuum was allowed to rise to 10^{-2} mm by turning off the oil diffusion pump on the spectrometer. The half life observed for the sandwiched target was $10.05 \pm .05$ min thus indicating only slight diffusion of the radioactive nitrogen was present in this case.

When the slight correction for the residual background is made the Kurie plot of the data is seen in Fig. 57 to be linear from about 0.2 Mev kinetic energy to just below the end point. The curvature at the end point can be accounted for by the window curve of the spectrometer. The shape of the low energy end of the spectrum is in good agreement with the work of Cook, Langer, Price, and Sampson[40]. Table M gives the comparison of the end point observed in this experiment with other determinations.

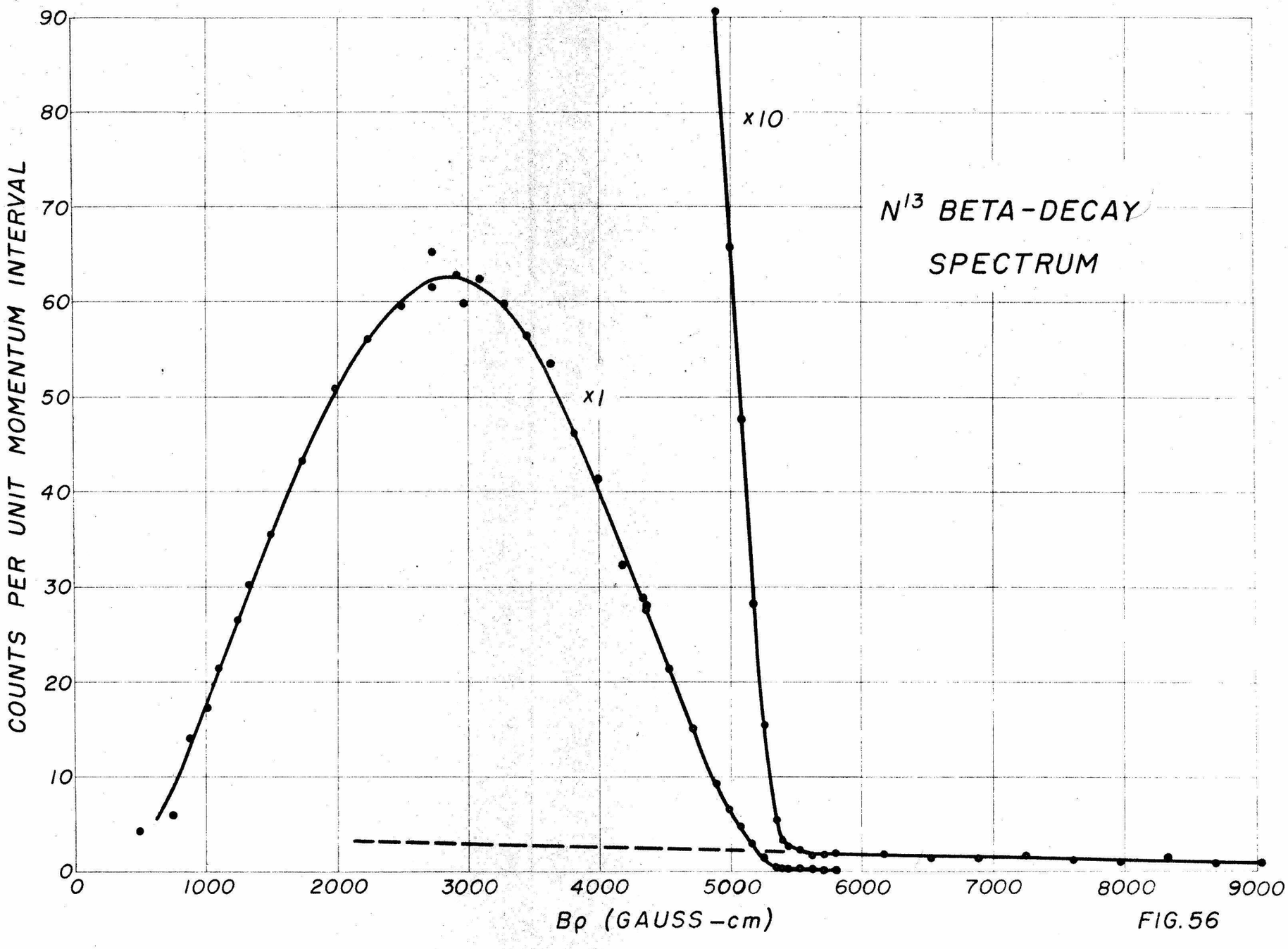
N13 BETA-DECAY SPECTRUM
x10
x1
COUNTS PER UNIT MOMENTUM INTERVAL
Bρ (GAUSS-cm)
0
10
20
30
40
50
60
70
80
90
1000
2000
3000
4000
5000
6000
7000
8000
9000

FIG. 56

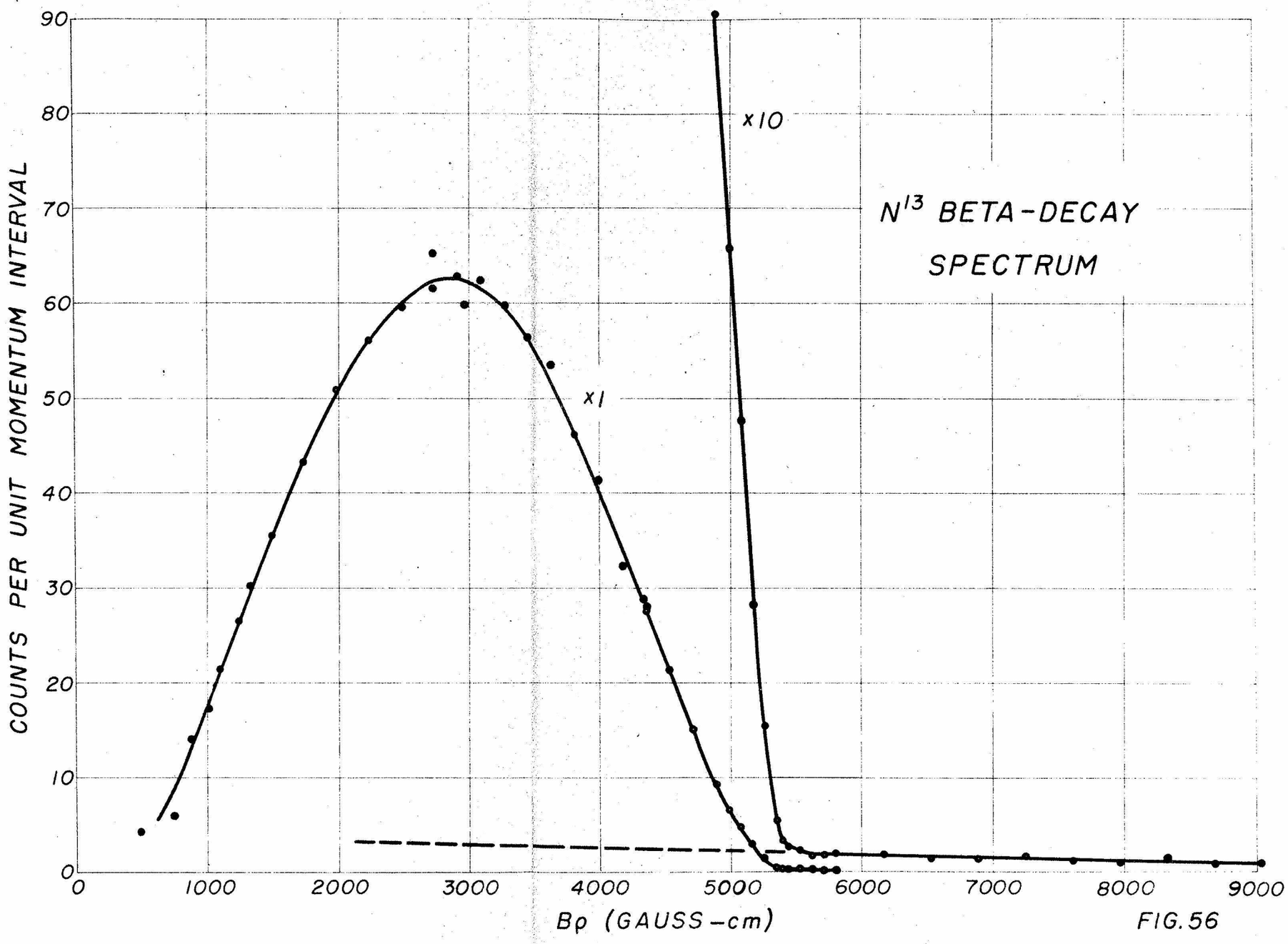
N13 BETA-DECAY SPECTRUM
x10
x1
COUNTS PER UNIT MOMENTUM INTERVAL
Bρ (GAUSS-cm)
0
10
20
30
40
50
60
70
80
90
1000
2000
3000
4000
5000
6000
7000
8000
9000

FIG. 56

TABLE M

End Point Mev.	Date	Ref.	Observers
(1) 1.198 ± 0.006	1939	41	Lyman
(2) 1.218 ± 0.004	1940	42	Townsend
(3) 1.24 ± 0.02	1945	43	Siegbahn and Slätis
(4) 1.25 ± 0.03	1948	40	Cook, Langer, Price and Sampson
(5) 1.202 ± 0.005	1948	This Thesis	

In the experiments on Li^8 and B^{12} the deuteron beam was periodically interrupted and the detector counter circuit was arranged to count only when the beam was off the target. This technique was adopted to eliminate the large neutron background from the prolific (d,n) reactions accompanying both main reactions and to eliminate background due to any prompt γ-radiation.

In the Li^8 experiment a motor driven switch with a 2-sec. period was used to operate a mechanical shutter which interrupted the beam for one second per cycle. The switch was also used to turn the recording circuit on and off. The sequence was carefully adjusted so that there was an adequate delay between the time when the beam was cut and the recording circuits turned on and also between the time when the recording circuits were turned off and the beam was allowed to strike the target. A schematic diagram of the arrangement appears in Fig. 58.

The shorter half life of B^{12} necessitated the use of an electrostatic deflector to interrupt the beam. For convenience

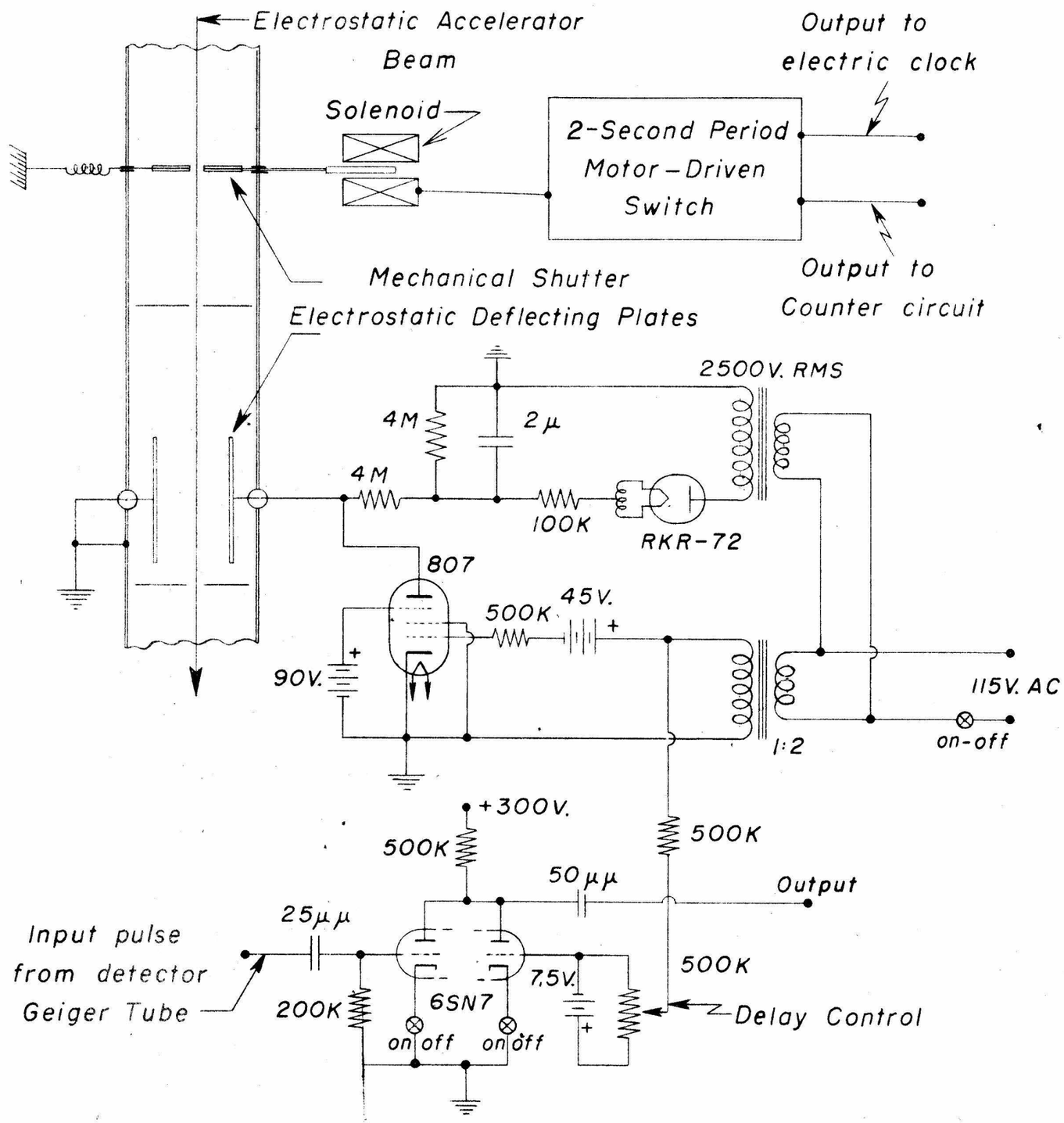

SCHEMATIC DIAGRAM FOR
SWITCHING CIRCUITS

FIG. 58

the already existing electrostatic analyzer plates[44] were used for this purpose. The beam was interrupted with a 1/60 sec period using the circuit diagram of Fig. 58. The same control voltage that switched a high voltage of 3000 volts on and off the deflector plates was used to operate a Rossi type coincidence circuit thus gating the pulses coming from the detector geiger tube. Again the delay between the switching operations was carefully set. To insure the fact that no spurious counts were introduced by the various transient effects a careful check on the cosmic ray background was made both with and without the electronic switch in operation. No extra counts were observed. The reproducibility of the switching cycle was checked and found to be satisfactory.

Targets were prepared by evaporating thin deposits of lithium metal and B_2O_3 on foils. Preliminary experiments were made to find a suitable foil support. Although thin aluminum foil has ideal physical properties and introduces negligible scattering, the 3 min Al^{28} formed by the reaction $Al^{27}(d,p)Al^{28}$ seriously distorts the spectra below 3.3 Mev kinetic energy. Copper foil of 9 mg/cm^2 thickness was found to be most convenient. No detectable activity was found from a bare copper foil at the deuteron energies used in this experiment. Since the decay electrons had to traverse the Cu foil before being focused in the spectrograph a check was made on the effect of scattering in the foil by using a target consisting of thin evaporated lithium metal sandwiched between two 0.2 mg/cm^2 Be

foils. A comparison of the low energy end of the Li^8 spectrum for these two backings showed no perceptible difference above $2000\mathcal{B}\rho$ ($\sim$ 280 Kev); see Fig. 59. Below $2000\mathcal{B}\rho$ for the Cu backing there are definite signs of scattering in the foil and of the presence of knock-on electrons ejected from the foil by the decay electrons.

While for the N^{13} experiment the conveniently long half life of N^{13} permitted the electrostatic accelerator beam to be completely shut off by removing the spray voltage during the run on the β -spectrum. This was not the case for the much shorter lived Li^8 and B^{12}. In these experiments the beam was interrupted as previously described but not turned off. During the off-target part of the cycle in each case the deuteron beam spent its energy against a quartz disc and thus produced a certain amount of neutron and soft γ-ray intensity. The resulting background in the β -spectrum runs was of the order of cosmic ray background. This background was constantly checked during the experiment and appropriate corrections were made in the data.

Experimental Results

The momentum spectrum of Li^8 is shown in Fig. 60 and that of B^{12} in Fig. 61. The spectrum of Fig. 60 has been compared with the experimental results of Bayley and Crane. The present curve is somewhat wider having a larger number of both low energy and high energy electrons relative to the number near the peak intensity. The peak intensity of the present curve occurs

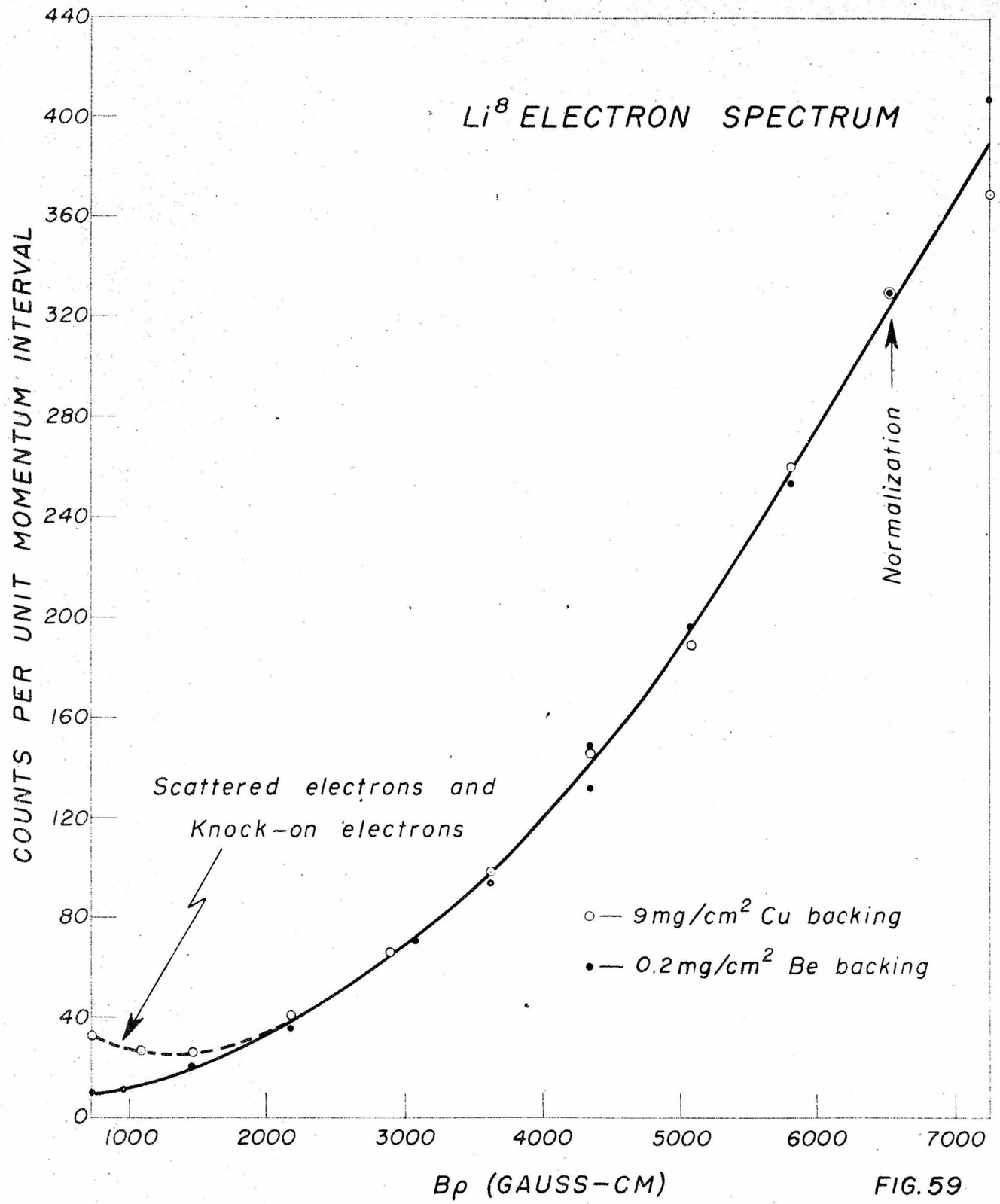
Li⁸ ELECTRON SPECTRUM
COUNTS PER UNIT MOMENTUM INTERVAL
440
400
360
320
280
240
200
160
120
80
40
0
Normalization
Scattered electrons and
Knock-on electrons
○— 9mg/cm² Cu backing
•— 0.2mg/cm² Be backing
1000
2000
3000
4000
5000
6000
7000
Bρ (GAUSS-CM)

FIG. 59

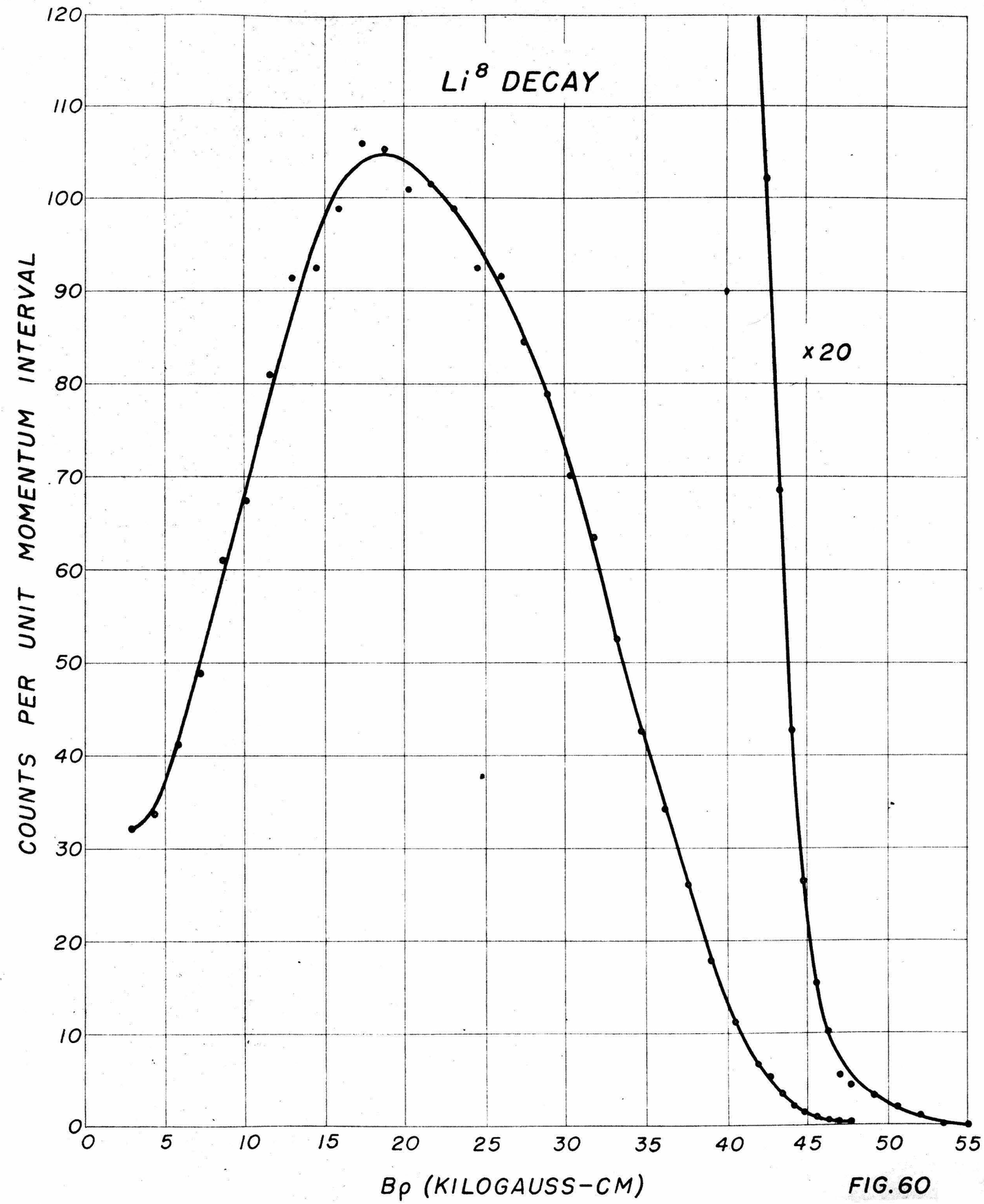
Li⁸ DECAY
x20
COUNTS PER UNIT MOMENTUM INTERVAL
Bρ (KILOGAUSS-CM)
0
10
20
30
40
50
60
70
80
90
100
110
120
0
5
10
15
20
25
30
35
40
45
50
55

FIG. 60

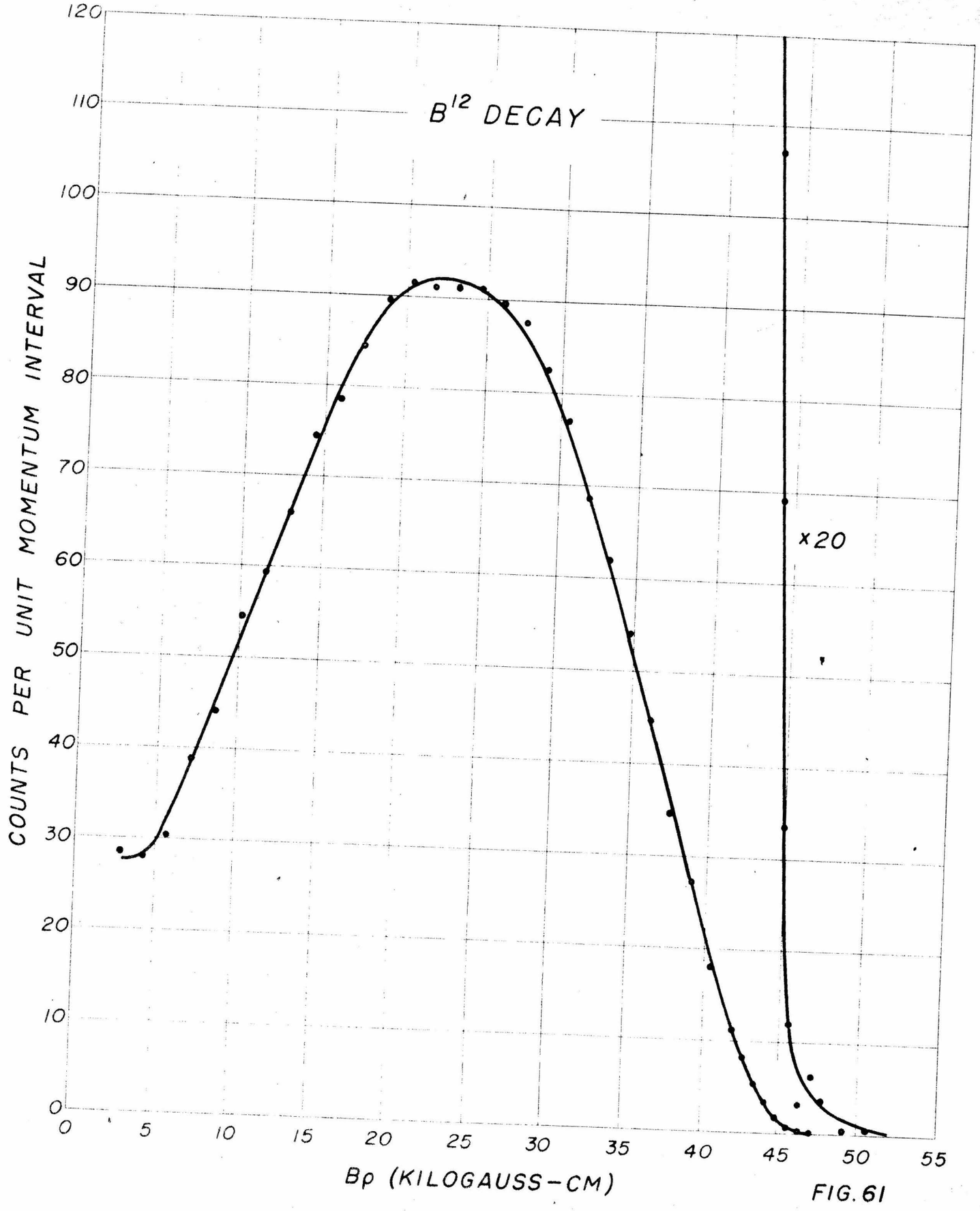
B12 DECAY
COUNTS PER UNIT MOMENTUM INTERVAL
Bρ (KILOGAUSS-CM)
x20
0
10
20
30
40
50
60
70
80
90
100
110
120
0
5
10
15
20
25
30
35
40
45
50
55

FIG. 61

at a slightly lower momentum. The agreement of the curve of Fig. 61 with the work of Bayley and Crane is far less favorable. The peak intensity of the present curve is at a considerably higher momentum and there are relatively many more high energy electrons. The present work and the results of Bayley and Crane should not however be considered in seri ous disagreement because of the large uncertainty attached to the cloud chamber data.

The Kurie plot of the B^{12} spectrum is given in Fig. 62 and 63. A straight line fits the higher energy end of the spectrum quite well from a total electron energy of 12 m_0c^2 to nearly the end point of 27.30 m_0c^2. The slight tail just at the high energy end of the spectrum can almost entirely be accounted for by the instrument resolution. The deviation of the plot from a straight line below a total energy of 12 m_0c^2 is very marked. The Kurie plot for the spectrum of Li^8 is shown in Figure 64 and 65. It will be seen that there is no extensive linear portion to the spectrum and in particular the deviation from linearity in the neighborhood of the end point is much more pronounced than for the B^{12} spectrum and cannot be ascribed to the instrumental resolution. As a first approximation the extrapolation of the best straight line fit to the spectrum may be taken as the "end point". The value thus obtained is $\sim$ 25.8 m_0c^2 ($\sim$ 12.7 Mev kinetic energy). Since the Li^8 - Be^8 mass difference from Q calculations is known to be 15.98 Mev[37] the indication is that the high energy transitions in the β -decay

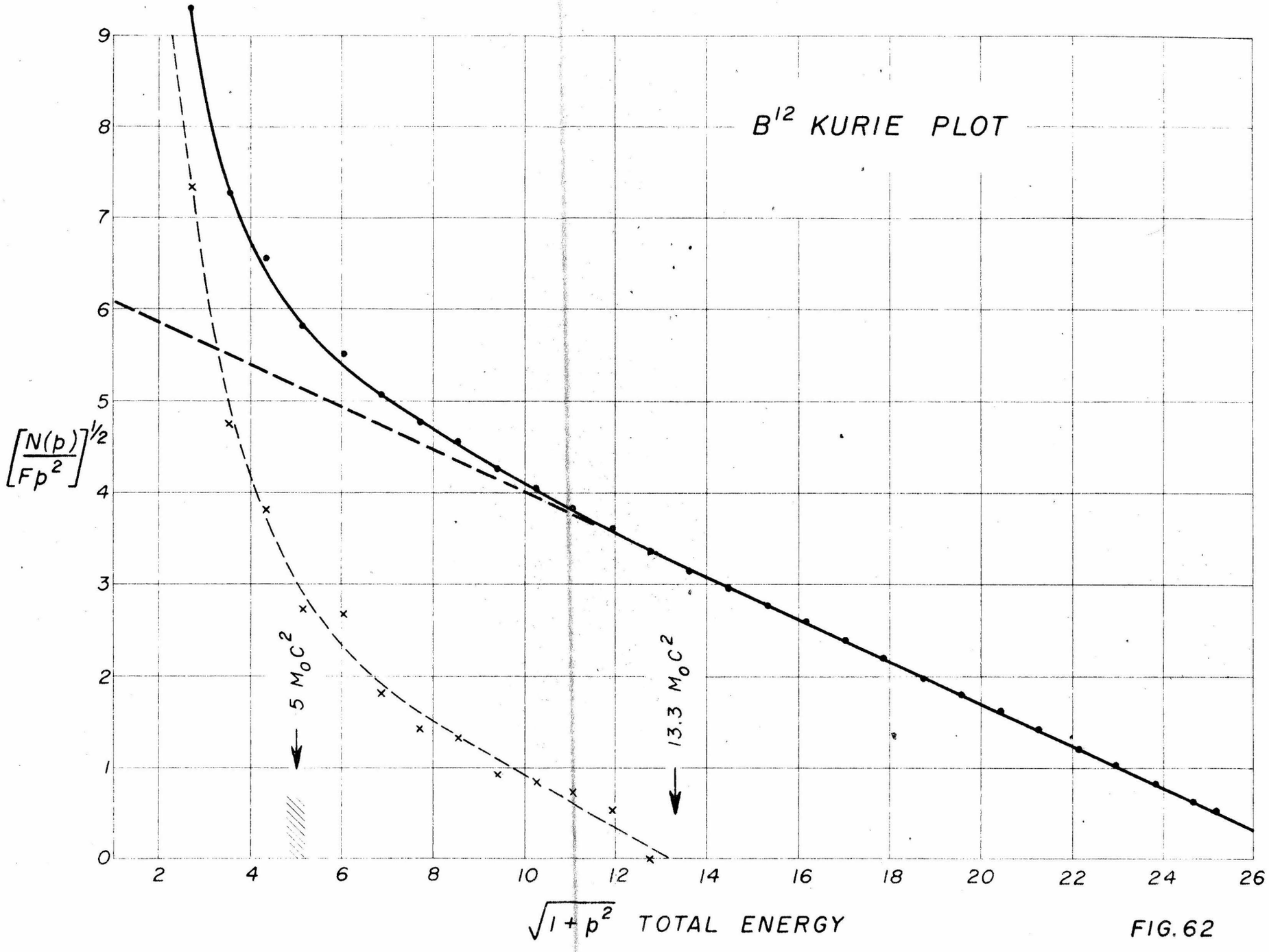
B12 KURIE PLOT
[N(p)/Fp2]1/2
0
1
2
3
4
5
6
7
8
9
2
4
6
8
10
12
14
16
18
20
22
24
26
5 M0C2
13.3 M0C2
√1 + p2 TOTAL ENERGY

FIG. 62

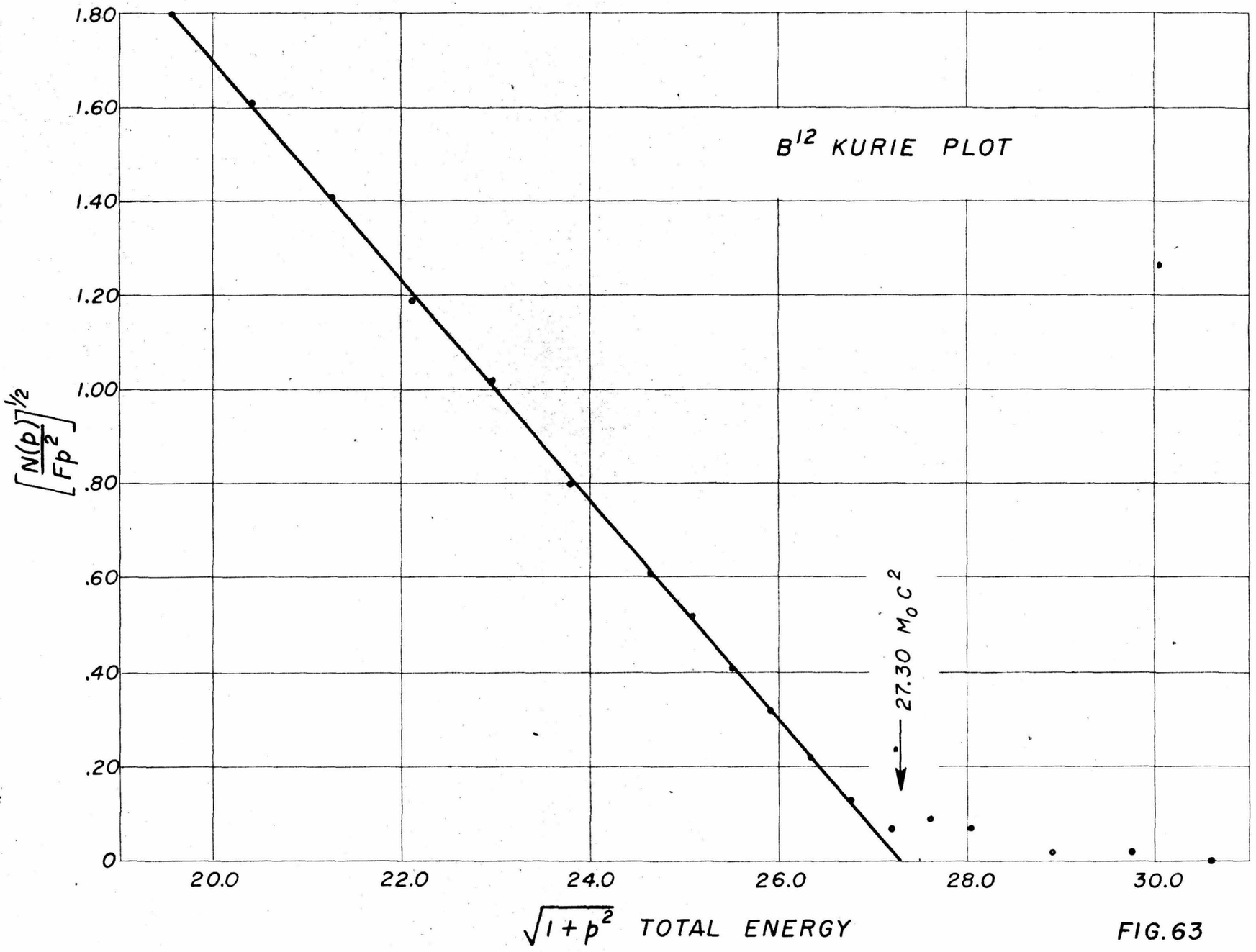
B^12 KURIE PLOT
1.80
1.60
1.40
1.20
1.00
.80
.60
.40
.20
0
20.0
22.0
24.0
26.0
28.0
30.0
27.30 M0 c2
[N(p)/Fp2]1/2
√1+p2 TOTAL ENERGY

FIG. 63

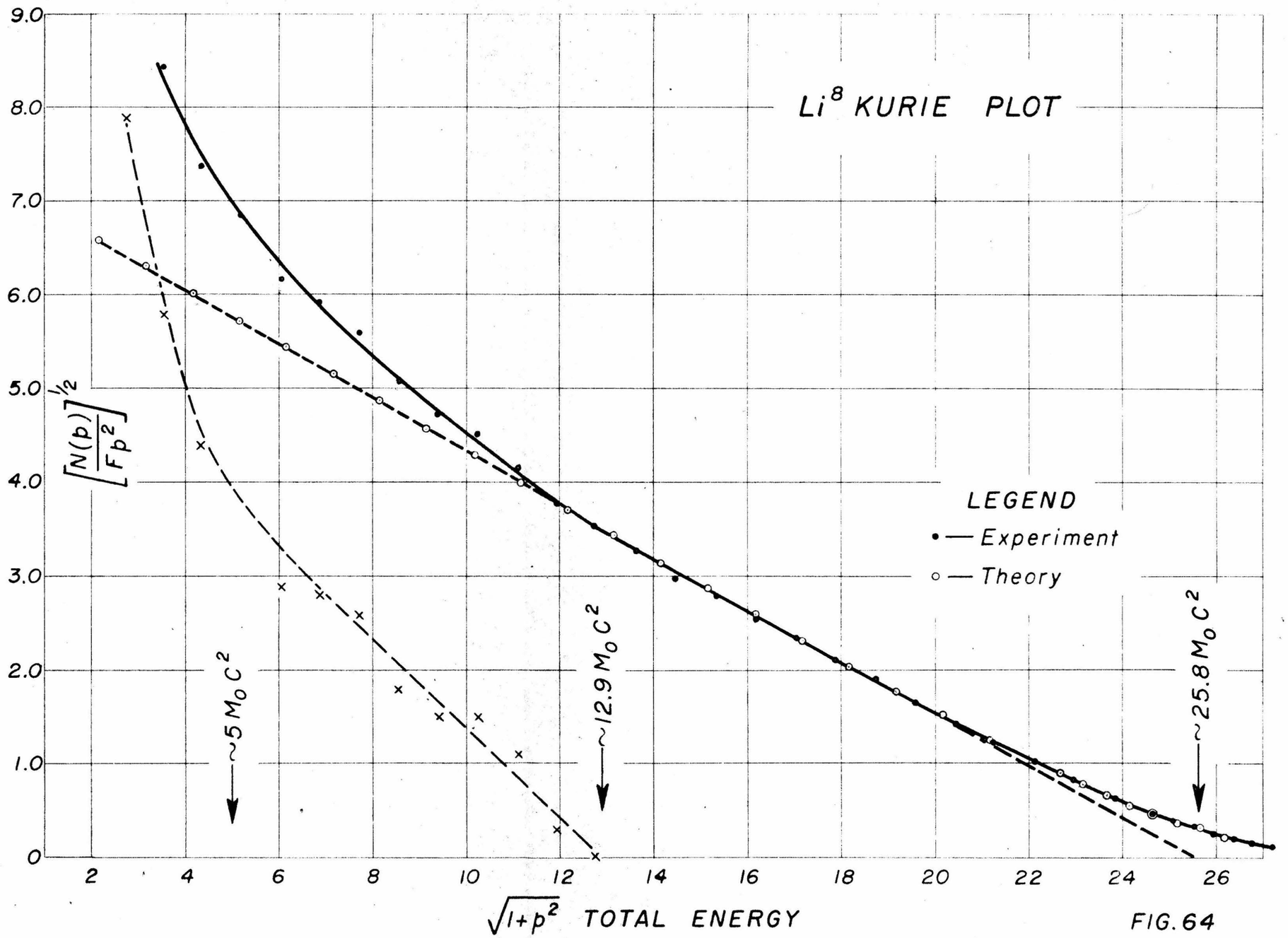
Li⁸ KURIE PLOT
LEGEND
• — Experiment
○ — Theory
$\left[\frac{N(p)}{Fp^2}\right]^{1/2}$
$\sqrt{1+p^2}$ TOTAL ENERGY
~5 M_0C^2
~12.9 M_0C^2
~25.8 M_0C^2
9.0
8.0
7.0
6.0
5.0
4.0
3.0
2.0
1.0
0
2
4
6
8
10
12
14
16
18
20
22
24
26

FIG. 64

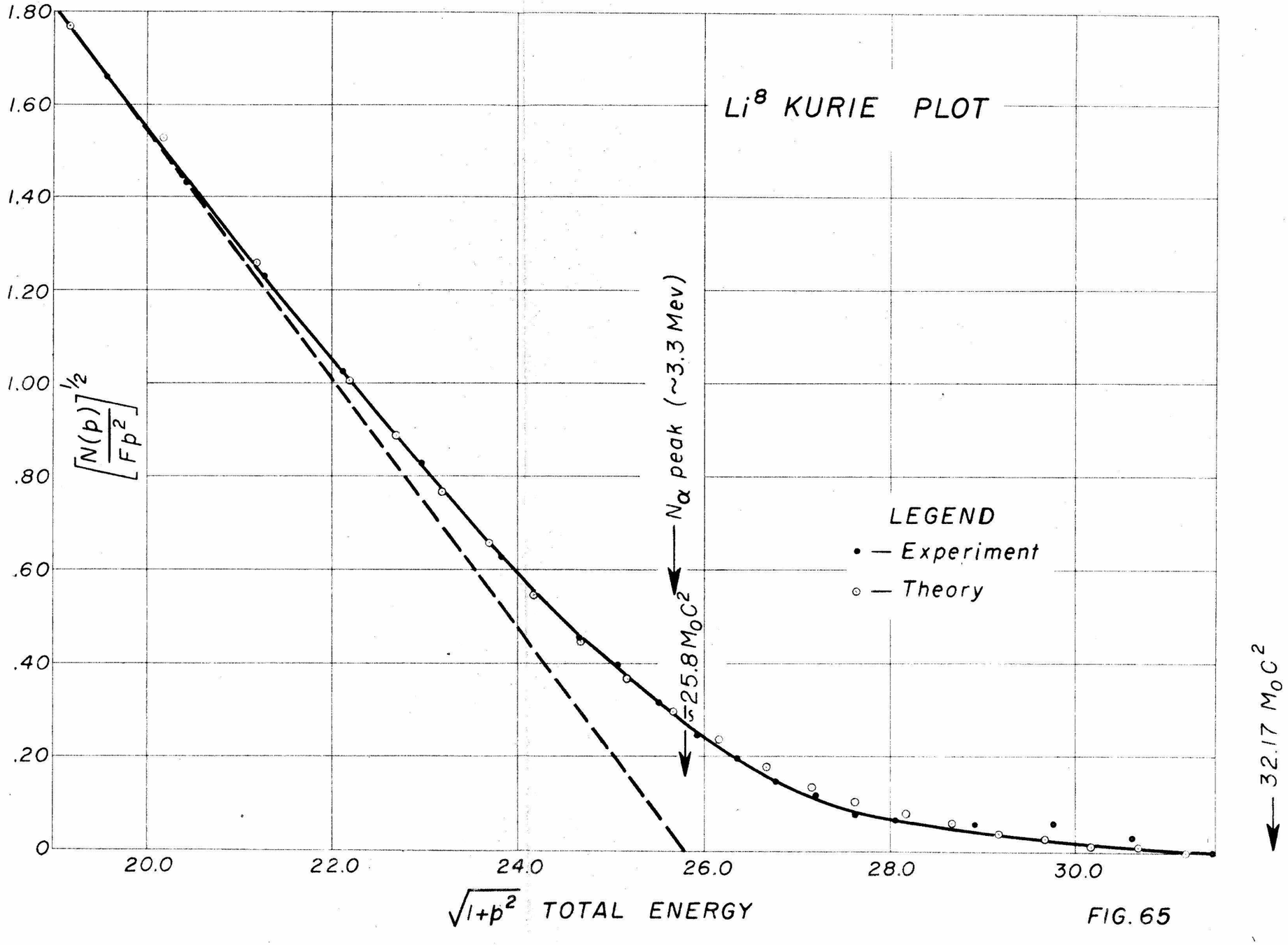
Li⁸ KURIE PLOT
LEGEND
• — Experiment
○ — Theory
$\left[\frac{N(p)}{Fp^2}\right]^{1/2}$
1.80
1.60
1.40
1.20
1.00
.80
.60
.40
.20
0
20.0
22.0
24.0
26.0
28.0
30.0
N_α peak (~3.3 Mev)
$\bar{s}$ 25.8 M_0C^2
32.17 M_0C^2
$\sqrt{1+p^2}$ TOTAL ENERGY

FIG. 65

of Li^8 are predominantly to an excited state in Be^8 at approximately (16.0 - 12.7 = 3.3) Mev rather than to the ground state. The non-linearity of the Kurie plot in this region indicates that this level is rather broad. These observations are in good agreement with the existing knowledge from other experiments. The deviation from linearity of the spectrum below a total energy of 12 m_0c^2 as in the case for B^{12} is quite marked.

Discussion of Results

The disintegration scheme for Li^8 is illustrated in Fig.66. The α -particle distribution has been observed to extend up to E_α = 7.75 Mev and to have a maximum intensity at 3.3 Mev.(39) By the analysis of the α -particle spectrum, Bonner et al(39) found that the spectrum can best be accounted for by taking the major part of the β -decay to an excited state in Be^8 at 3.1 Mev having a width Γ = 0.8 Mev. There was also some indication that a broad state at 7-9 Mev may be concerned in the decay scheme. The best estimate of the α -particle spectrum is shown in Fig. 67 and is based primarily on the work of Bonner, Evans, Malich, and Risser below $2E_\alpha \approx 6$ Mev and on the work of Rumbaugh, Roberts, and Hafstad above $2E_\alpha \approx 6$ Mev. The two experimental curves were normalized in the region of $4 < 2E_\alpha < 8$ Mev. The electron decay spectrum can be predicted from the α -particle distribution by assuming that the latter gives the density of states available in Be^8 for the β -transitions. This assumption is equivalent to stating that the principle mode of decay of the excited states in Be^8 is by α -particle emission and that γ -ra-

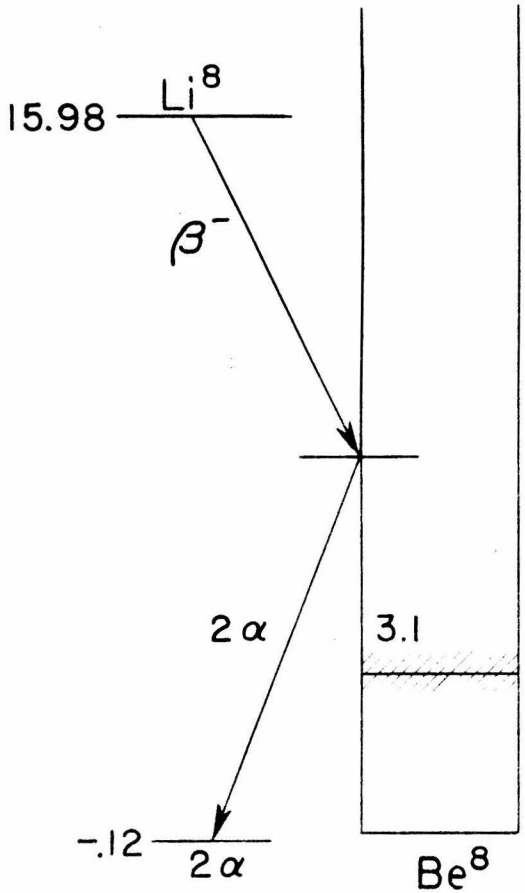

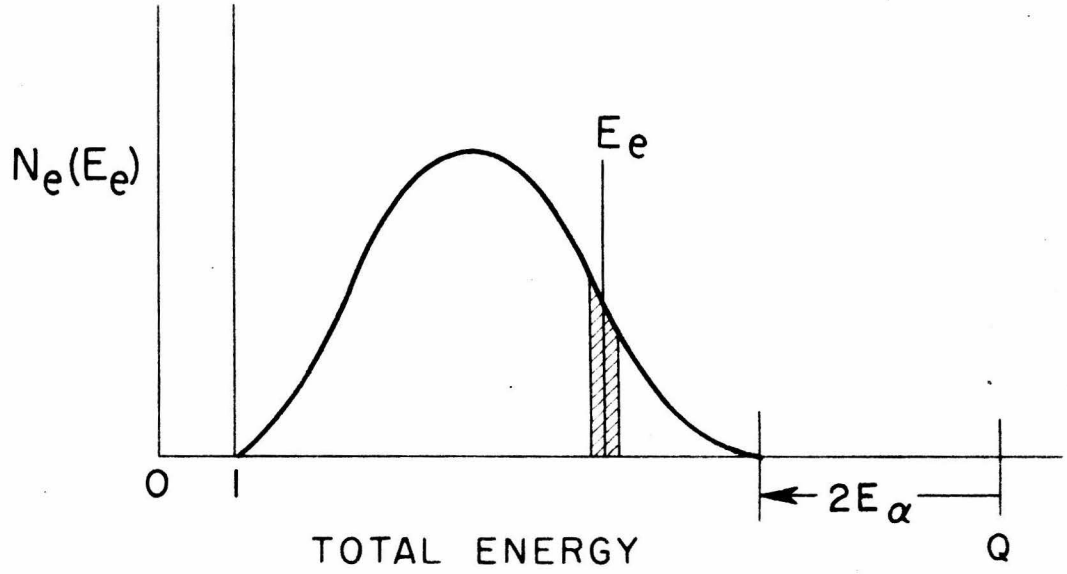

$$Q = \frac{15.98 + .12}{.5108} + 1 = 32.51$$

FIG. 66

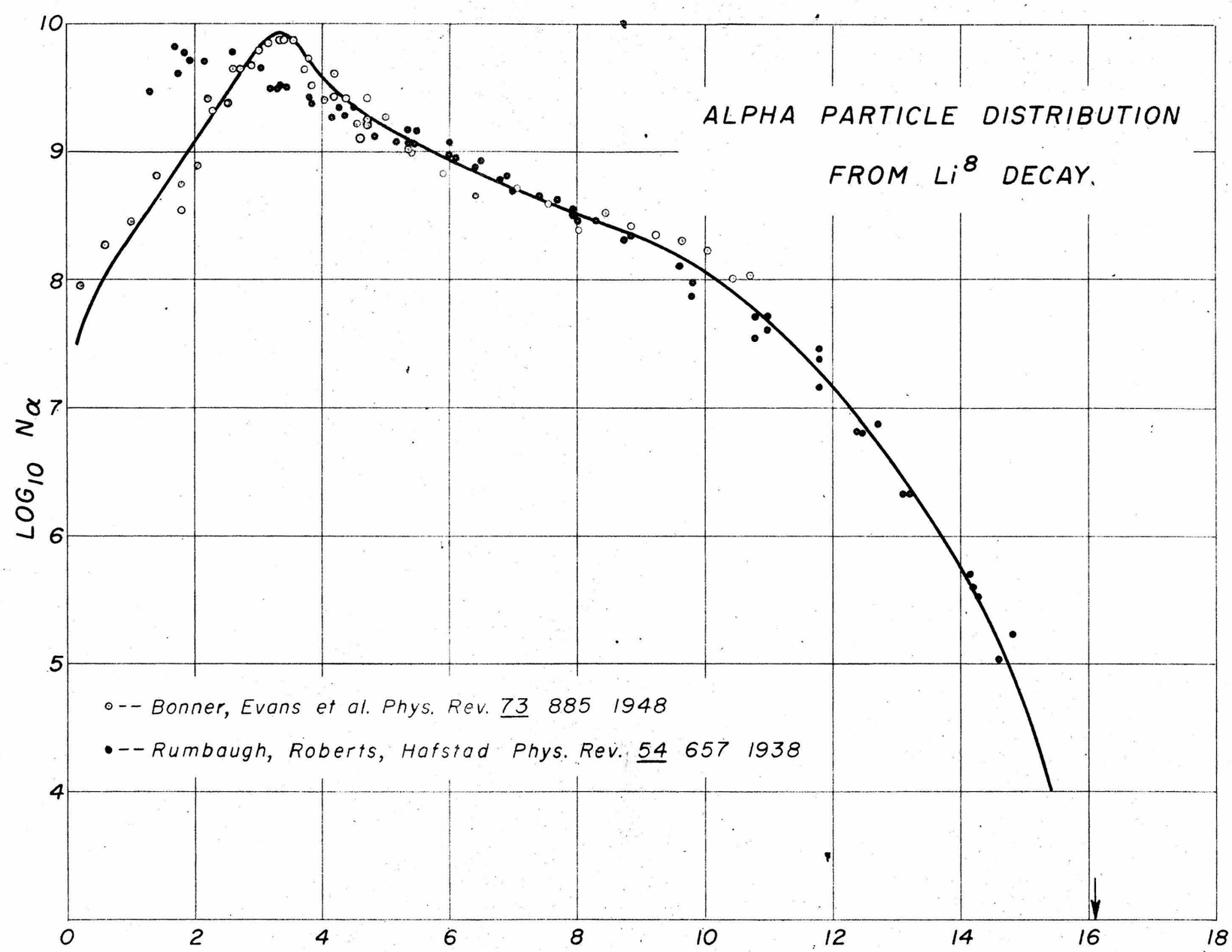
ALPHA PARTICLE DISTRIBUTION
FROM Li^8 DECAY.
$LOG_{10}\ N_\alpha$
10
9
8
7
6
5
4
0
2
4
6
8
10
12
14
16
18
$2E_\alpha$ (MEV)
o -- Bonner, Evans et al. Phys. Rev. 73 885 1948
• -- Rumbaugh, Roberts, Hafstad Phys. Rev. 54 657 1938

FIG. 67

diation can be neglected. The Fermi theory for allowed β-decay then gives the electron distribution

$$N_e(E_e)dE_e = C\,dE_e \int_0^{Q-E_e} N_\alpha(2E_\alpha)\left[Q-2E_\alpha-E_e\right]^2\left(E_e^2-1\right)^{1/2} E_e\, d(2E_\alpha) \quad (132)$$

where E_e is the total electron energy in units of m_0c^2 and E_α is the kinetic energy of one α-particle in units of m_0c^2 and Q is defined in Fig. 66 while $N_\alpha(2E_\alpha)$ is the α-particle distribution of Fig. 67.

Let $y = E_e$ and $x = 2E_\alpha$ then,

$$N_e(y)dy = C\,y\left(y^2-1\right)^{1/2}dy\left\{(Q-y)^2\int_0^{Q-y} N_\alpha(x)dx + \int_0^{Q-y} N_\alpha(x)x^2dx - 2(Q-y)\int_0^{Q-y} N_\alpha(x)\,x\,dx\right\} \quad (133)$$

and if p is the electron momentum in units of

$$\left[\frac{N_e(p)}{Cp^2}\right]^{1/2} = \left\{(Q-y)^2\int_0^{Q-y} N_\alpha(x)dx + \int_0^{Q-y} N_\alpha(x)x^2dx - 2(Q-y)\int_0^{Q-y} N_\alpha(x)\,x\,dx\right\}^{1/2} \quad (134)$$

with $y = \sqrt{1+p^2}$. Equation (134) is in the form ideally suited for comparison with the Kurie plot of the experimental β-spectrum. It is seen to involve only the quantity $Q-y$, the integral of $N_\alpha(x)$ and its first and second moments. The integrals have been evaluated numerically based on Fig. 67 and the result is plotted on Fig. 64 and 65 as open circles and labelled "theory". The value of Q which gave the best empirical fit was $32.2 \pm 0.2\ m_0c^2$ or a Li^8 - $2He^4$ mass difference of $15.9 \pm .1$ Mev, these values are to be compared with $32.51\ m_0c^2$ and 16.10 Mev, respectively obtained from reaction energies and mass values. The general agreement above a total energy of $12\ m_0c^2$ between the predicted and observed points is good

except perhaps for a range of energies just above 26 m_0c^2, corresponding to the α -particle distribution below the peak at $2E_\alpha = 3.3$ Mev, where the predicted values are too high. This discrepancy is somewhat further accentuated if the spectrometer window curve is folded into the predicted spectrum which has not been done in Fig. 65. This effect, however, is fairly small. Thus both the somewhat low value of Q and this slight discrepancy in the shapes near the end point may perhaps be taken to indicate that the α -particle spectrum of Fig. 67 has relatively too many low energy particles. Bonner, et al. themselves suggest that their spectrum over-estimates the number of low energy α -particles due to experimental difficulties.

An attempt has been made to determine the probability of β -decay to the ground state of Be^8. From the limit of error associated with the points just at the end point where the spectrum merges with the background it is estimated that less than 2% of the entire β -decay is to the ground state. A less certain estimate is that less than 5% of the β -decay is to the γ -ray emitting state at 4.8 Mev.

The deviation of the observed spectrum from the predicted spectrum below 12 m_0c^2 can be taken to indicate disintegrations to high excited states which do not decay by α -particle emission. The decomposition of the spectrum shown in Fig. 64 gives about 10% of the β -transitions to narrow states at $9.7 \pm .3$ and ~ 13 Mev excitation in Be^8. At present there is some evidence from other sources[37] for a level at approximately 9.8 Mev although there is none for the higher excitation.

An alternative explanation of the discrepancy below 12 m_0c^2 may be that the β -transition is of an unfavored nature. This could arise either by having the main bulk of the decay to the 3.1 Mev level be of an allowed type and with ~ 2% of the decay to the ground state being of a forbidden type, or by having the decay to the 3.1 Mev level itself of an unfavored nature. An investigation of the first of these possibilities showed that a spectrum shape correction which varied more rapidly with energy in the low energy range than that for a second forbidden scalar interaction type transition[45] was necessary even if as much as ~ 5% of the decay was to the ground state. In addition the width of the 3.1 Mev level would have to be taken much narrower than that indicated by the α -spectrum. The correction in the second of the above possibilities is much more difficult to evaluate but may be more successful in giving a fit of the observed spectrum.

The extrapolated end point of the Kurie plot for B^{12} gives 27.30 ± .10 m_0c^2 for the total energy or 13.43 ± .06 Mev kinetic energy. This value is in good agreement with the value 13.3 ± .5 Mev obtained by Hereford[46] using an absorption method to determine the end point energy. If the high energy end of the β -spectrum corresponds to a decay to the ground state of B^{12} then the above observed end point combined with the mass of C^{12} [47] gives 12.01827 ± .00009 amu. for the mass of B^{12}. From an analysis of the nuclear binding energies Barkas[48] predicts a mass of 12.0188 amu. for B^{12}. Continuing with this as-

sumption, if 5% of the β -decay is assumed to go to a narrow level in C^{12} at 7.1 ± .5 Mev and possibly a broad or composite level at ~ 11. Mev, the observed non-linearity of the Kurie plot below 12 m_0c^2 total energy can be accounted for. A decay of 5% or less to the 4.3 Mev level in C^{12} cannot be excluded. Again the lack of linearity of the Kurie plot below a total energy of 12 m_0c^2 may be due to an unfavored β -transition being involved rather than a complex decay scheme.

Again using the observed end point as the decay energy to the ground state of C^{12} and the mass tables of Flügge and Mattauch[49] the Q of the reaction $B''(d,p)B'^{2}$ is Q = 1.12 Mev. The early work of Cockcroft and Lewis[50] indicated that the bombardment of boron targets with deuterons of .55 Mev yielded no group with range greater than 2.7 cm indicating that the Q of this reaction is probably less than ~ .9 Mev. Recently Hudspeth and Swann[51] claim to have determined the Q of this reaction to be Q ≈ .15 Mev thus giving a discrepancy of about 1.0 Mev. The determination of Q = .15 Mev was based on both the analysis of the yield curve for B^{12} and the observation of the range of a particle group in a photographic plate ascribed to this reaction. Three possibilities suggest themselves to account for this discrepancy: First, since an unseparated boron target was used the charged particles observed may belong to the reaction $B^{10}(d,p)B''^{*}$ in which B'' is left in a highly excited state; second, both the charged particles and the excitation function observed may be from a $B''(d,p)B^{12*}$

reaction in which the B^{12} is excited to an energy of $\approx$ 1.0 Mev; third, the decay of B^{12} proceeds mainly to a level in C^{12} at $\approx$ 1.0 Mev, the transition to the ground state being forbidden. In connection with the first possibility it should be mentioned that at a bombarding voltage of .6 Mev the yield of B^{12} from an unseparated target is $\sim$ 20 times[52] that of the 91 cm proton group going to the ground state of B^{11}; this ought to afford a useful check on the origin of the short range group observed. Although no level in B^{11} is known in the region of 9 Mev excitation which is required by assumption, this region has not been well surveyed. In connection with the second possibility it should be remarked that in all probability the level density in B^{12} even at low excitation energies ought to be quite high, thus there is no difficulty in supposing that the decay of the C^{13} compound nucleus is to a level in B^{12} at $\sim$ 1.0 Mev which may successfully compete with the decay to the ground state of B^{12}. Finally in regards the third possibility it should be pointed out that from none of the other four reactions[37] which lead to excited states in C^{12} is there any evidence for a level in C^{12} near 1.0 Mev. If, however, the discrepancy is resolved by this third possibility then the estimated energy of the excited states involved in the possible complex decay of B^{12} must be raised from 7.1 to 8.1 Mev. and $\sim$11 to $\sim$ 12 Mev.

APPENDIX I

MAGNETIC LENS EQUATIONS AND ABERRATION CALCULATIONS

A charged particle moving in a static magnetic field will experience no change in energy since the force is always perpendicular to the line of motion. Thus the equations of motion for the relativistic case follow immediately from the non-relativistic case if the proper relativistic transverse mass is used. The equations of motion are using the notation of Fig. 1a

$$m\ddot{z} = H_r \frac{e}{c} r\dot{\theta} \tag{1}$$

$$m(\ddot{r} - r\dot{\theta}^2) = -\frac{e}{c} r\dot{\theta} H_z \tag{2}$$

$$\frac{m}{r}\frac{d}{dt}(r^2\dot{\theta}) = \frac{e}{c}\left[\dot{r}H_z - \dot{z}H_r\right] \tag{3}$$

where m is the transverse mass $m = \frac{m_0}{\sqrt{1 - v^2/c^2}}$, H_r and H_z are the radial and axial components of the field at the particle position and the dot represents differentiation with respect to time. Now for an axially symmetric magnetic field the field component at any point off the axis may be expressed in terms of the axial component of the field along the axis and its derivatives thus

$$\begin{aligned} H_z(r,z) &= H(z) - \frac{r^2}{4}H''(z) + \frac{r^4}{64}H^{IV}(z) + \cdots \\ H_r(r,z) &= -\frac{r}{2}H'(z) + \frac{r^3}{16}H'''(z) + \cdots \end{aligned} \tag{4}$$

where $' \equiv \frac{\partial}{\partial z}$.

Then equation (3) becomes, substituting (4)

$$d(r^2\dot\theta) = \frac{er}{mc}\left[H(z) - \frac{r^2}{4}H''(z) + \frac{r^4}{64}H^{IV}(z) + \cdots\right]dr$$

$$+ \frac{er}{mc}\left[\frac{r}{2}H'(z) - \frac{r^3}{16}H'''(z) + \cdots\right]dz$$

Multiplying the membrum on the right hand side by $\frac{dz}{dz}$ and integrating by parts gives

$$r^2\dot\theta = \frac{e}{mc}\left[\frac{r^2}{2}H(z) - \frac{r^4}{16}H''(z) + \cdots\right] + C_0$$

Now since at distances far removed from the region of the field $H(z)$ and its derivatives vanish and since $\dot\theta = 0$, $C_0 = 0$, thus this equation becomes

$$\dot\theta = \frac{e}{2mc}\left[H(z) - \frac{r^2}{8}H''(z) + \cdots\right] . \qquad (5)$$

From equation (1) we have, using equation (5)

$$\ddot z = -\frac{e^2r^2}{4m^2c^2}H(z)H'(z) + \cdots \qquad (6)$$

While from equation (2)

$$\ddot r = -\frac{er\dot\theta}{mc}\left[H(z) - \frac{r^2}{4}H''(z) + \cdots\right] + r\dot\theta^2$$

using (5)

$$= r\dot\theta\,\frac{e}{mc}\left[-H(z) + \frac{r^2}{4}H''(z) + \cdots + \frac{H(z)}{2} - \frac{r^2}{16}H''(z) + \cdots\right]$$

$$= r\dot\theta\,\frac{e}{mc}\left[-\frac{H(z)}{2} + \frac{3}{16}r^2H''(z) + \cdots\right]$$

and using (5) again

$$\ddot r = -\frac{re^2}{4m^2c^2}H(z)\left[H(z) - \frac{r^2}{2}H''(z) + \cdots\right] . \qquad (7)$$

Now from the symmetry $r = f(z)$ is the trajectory or

$$\dot{r} = \frac{dr}{dz}\dot{z} \tag{8}$$

and

$$\ddot{r} = \frac{d^2r}{dz^2}\dot{z}^2 + \frac{dr}{dz}\ddot{z} \quad . \tag{9}$$

Since there is no change in energy

$$\dot{z}^2 + \dot{r}^2 + r^2\dot{\theta}^2 = C_1$$

and substituting from equations (8) and (5),

$$\dot{z}^2\left[1 + \left(\frac{dr}{dz}\right)^2\right] = C_1 - r^2\dot{\theta}^2 = C_1 - \frac{r^2e^2}{4m^2c^2}H^2(z) + \cdots$$

or

$$\dot{z}^2 = \frac{C_1 - \frac{r^2e^2}{4m^2c^2}H^2(z)}{1 + \left(\frac{dr}{dz}\right)^2} \quad . \tag{10}$$

Hence equation (9) may be written, using equations (6),(7), and (10) as

$$-\frac{re^2}{4m^2c^2}H(z)\left[H(z) - \frac{r^2}{2}H''(z) + H(z)\left(\frac{dr}{dz}\right)^2 - rH(z)\frac{d^2r}{dz^2} - rH'(z)\frac{dr}{dz} + \cdots\right]$$

$$= C_1\frac{d^2r}{dz^2} \quad , \tag{11}$$

the terms in the bracket $-\frac{r^2}{2}H''(z)\left(\frac{dr}{dz}\right)^2 - rH'(z)\left(\frac{dr}{dz}\right)^3$ and terms of this order and higher being neglected. Expressing C_1 in terms of the momentum $B\rho$ for the electrons gives

$$-rH(z)\left[H(z) - \frac{r^2}{2}H''(z) + H(z)\left(\frac{dr}{dz}\right)^2 - rH(z)\frac{d^2r}{dz^2} - rH'(z)\frac{dr}{dz} + \cdots\right]$$

$$= 4(B\rho)^2\frac{d^2r}{dz^2} \quad . \tag{12}$$

The last three terms on the left hand side may be written,using the abbreviated notation as

$$I = \frac{r^2H^2r''}{2} + r^2HH'r' - rH^2r'^2 + \frac{r^2H^2r''}{2} = \frac{r^4}{2}\frac{d}{dz}\left(\frac{H^2r'}{r^2}\right) + \frac{r^2H^2r''}{2} \quad .$$

Thus equation (12) becomes:

$$-rH^2(z)+\frac{r^3}{2}H(z)H''(z)+\frac{r^4}{2}\frac{d}{dz}\left(\frac{H^2(z)}{r^2}\frac{dr}{dz}\right)+\frac{r^2H^2(z)}{2}\cdot\frac{d^2r}{dz^2}$$
$$=4(B\rho)^2\frac{d^2r}{dz^2}\quad . \tag{13}$$

The zero order equation

$$\frac{d^2r}{dz^2}=-\frac{rH^2(z)}{4(B\rho)^2} \tag{14}$$

is the one usually given for paraxial rays. The use of equation (13) represents the first approximation for the aberration terms. Scherzer[53] has made extensive calculations of the aberrations; his results are in a different form however. Equation (14) has been treated to some extent in the main body of this thesis.

A rough estimate of the order of magnitude of the aberrations may be obtained by using equation (13). The zero order equation (14) can be used to simplify equation (13) by substituting in the last term on the left, there results

$$-rH^2(z)+\frac{r^3}{2}H(z)H''(z)+\frac{r^4}{2}\frac{d}{dz}\left(\frac{H^2(z)}{r^2}\frac{dr}{dz}\right)-\frac{r^3H^4(z)}{8(B\rho)^2}=4(B\rho)^2\frac{d^2r}{dz^2} \tag{15}$$

Then for the thin lens approximation as in the body of the text multiply by dz and integrate from plane A to B (see Fig. Ib) then there results approximately

$$-r_0\int_{-\infty}^{\infty}H^2(z)dz+\frac{r_0^2}{2}\int_{-\infty}^{\infty}H(z)H''(z)dz+\frac{r_0^2}{2}\left|H^2(z)\frac{dr}{dz}\right|_A^B-\frac{r_0^3}{8(B\rho)^2}\int_{-\infty}^{\infty}H^4(z)dz$$
$$=4(B\rho)^2\left|\frac{dr}{dz}\right|_A^B \tag{16}$$

The third term on the left vanishes at both limits since

and comparing with equation (5) of the text

$$\Delta f_A = -\epsilon f^2$$

$$\epsilon \approx \frac{r_0^2}{8(B\rho)^2}\left[\frac{1}{4(B\rho)^2}\int_{-\infty}^{\infty} H^4(z)\,dz - \int_{-\infty}^{\infty} H(z)H''(z)\,dz\right] \tag{17}$$

where Δf_A is the change in focal length due to the aberrations. Equation (5) of the text shows that $f = \frac{const}{i^2}$ where i is the spectrometer current. Hence

$$\Delta f_I = -\frac{2f}{i}\Delta i \tag{18}$$

In a practical case f is fixed hence $\Delta f = \Delta f_A + \Delta f_I = 0$

Thus

$$\frac{\Delta i}{i} = -\frac{\epsilon f}{2} = -\frac{r_0^2}{4}\left\{\frac{\frac{1}{4(B\rho)^2}\int_{-\infty}^{\infty} H^4(z)\,dz - \int_{-\infty}^{\infty} H(z)H''(z)\,dz}{\int_{-\infty}^{\infty} H^2(z)\,dz}\right\} \tag{19}$$

here Δi is the change in focusing current to account for the aberrations. For a field shape $H(z) = H_0 e^{-z^2/b^2}$ and for the case of unit magnification $L = 4f$, where L is the distance from the source to the window, there results

$$\frac{\Delta i}{i} = -\frac{r_0^2}{b^2}\left[\frac{b}{L\sqrt{\pi}} + \frac{1}{4}\right] . \tag{20}$$

APPENDIX II

PARAXIAL RAY TRAJECTORIES

The trajectories for near paraxial rays for the field shape $\mu = 1$ discussed in the text has been carried out by Glaser[6] and is also presented by Zworykin et al[4]; this latter presentation will be followed here entirely. This solution is given here merely for the sake of completeness. Using the notation of the text in connection with equations (7) and (8)

$$\frac{d^2y}{dx^2} = -K_1^2 \frac{y}{(1+x^2)^2} \tag{21}$$

where $y = \frac{r}{a}$ (note that for $\mu = 1$, $a = d$); the other symbols as in the text. We now introduce $x = ctn\, w$ where upon

$$\frac{dy}{dx} = \frac{dy}{dw} \cdot \frac{dw}{dx} = -\frac{dy}{dw} \sin^2 w$$

$$\frac{d^2y}{dx^2} = \frac{d^2y}{dw^2} \sin^4 w + 2 \frac{dy}{dw} \sin^3 w \cos w \,. \tag{22}$$

Substituting this into equation (21) gives

$$\frac{d^2y}{dw^2} + 2\, ctn\, w \frac{dy}{dw} + K_1^2 y = 0 \,. \tag{23}$$

Letting $y = u(w)\, v(w) = uv$ gives

$$\frac{dy}{dw} = v \frac{du}{dw} + u \frac{dv}{dw}$$

$$\frac{d^2y}{dw^2} = v \frac{d^2u}{dw^2} + u \frac{d^2v}{dw^2} + 2 \frac{du}{dw} \cdot \frac{dv}{dw} \,. \tag{24}$$

Then equation (23) becomes

$$v \frac{d^2u}{dw^2} + \left[2 \frac{dv}{dw} + 2v\, ctn\, w\right] \frac{du}{dw} + \left[\frac{d^2v}{dw^2} + 2 \frac{dv}{dw} ctn\, w + K_1^2 v\right] u = 0, \tag{25}$$

taking the coefficient of $\frac{du}{dw} = 0$

$$-\frac{dv}{dw} = v \operatorname{ctn} w \qquad \text{or} \qquad -\ln v = \ln |\sin w|$$

with $w^2 < \pi^2$. Thus

$$v(w) = \frac{1}{\sin w} \tag{26}$$

and $$\frac{dv}{dw} = -\operatorname{ctn} w \csc w$$

$$\frac{d^2v}{dw^2} = \csc w + 2 \operatorname{ctn}^2 w \csc w \tag{27}$$

hence equation (25) becomes

$$\frac{d^2u}{dw^2} + (K_1^2 + 1) w = 0 \quad . \tag{28}$$

This equation has the well known solution

$$u = C_1 \sin\left[(K_1^2+1)^{1/2} w\right] + C_2 \cos\left[(K_1^2+1)^{1/2} w\right] \quad . \tag{29}$$

Thus the required solution is, combining equations (26) and (29)

$$r = \frac{1}{\sin w}\left\{C_1 \sin\left[(K_1^2+1)^{1/2} w\right] + C_2 \cos\left[(K_1^2+1)^{1/2} w\right]\right\} \tag{30}$$

with $w = \operatorname{arc\,ctn} x$ and $w^2 < \pi^2$.

APPENDIX III

COUNTER STATISTICS

Consider an infinite sequence of pulses which are a random function of time; take the time t to be zero at one such pulse taken as a reference. Let $\bar{n} = \frac{1}{\tau}$ be the long time average rate and let $P(t)$ be the probability that there is at least one pulse in the time interval $0-t$. Then $1-P(x)$ is the probability that there are no pulses up to the time X. From the random nature of the events $\frac{dx}{\tau}$ will be the probability that one pulse occurs within the time interval dx. Thus

$$P(t) = \int_0^t (1-P(x)) \frac{dx}{\tau} , \qquad (31)$$

differentiating there results

$$\tau P'(t) = 1-P(t) \qquad \text{or} \quad \frac{dP}{1-P} = \frac{dt}{\tau}$$

hence

$$1-P(t) = e^{-t/\tau} \qquad (32)$$

Now $P_0(t) = 1-P(t)$ is the probability that in the time interval t no pulse is counted and in general let $P_N(t)$ be the probability the precisely N pulses will be counted in the time interval t. Then

$$P_N(t) = \int_0^t P_{N-1}(x) \frac{dx}{\tau} P_0(t-x) . \qquad (33)$$

Since $P_{N-1}(x)$ is the probability of $N-1$ pulses up to the time X, $\frac{dx}{\tau}$ is the probability of a pulse at X within dx and $P_0(t-x)$ is the probability for no further pulses beyond X.

Now $P_0(t) = e^{-t/\tau}$ therefore

$$P_1(t) = \int_0^t e^{-\frac{x}{\tau}} \frac{dx}{\tau} e^{-\frac{(t-x)}{\tau}} = \frac{e^{-t/\tau}}{\tau} \int_0^t dx = \frac{t}{\tau} e^{-t/\tau}$$

and $$P_2(t) = \int_0^t \frac{x}{\tau} e^{-\frac{x}{\tau}} \frac{dx}{\tau} e^{-\frac{(t-x)}{\tau}} = \frac{e^{-t/\tau}}{\tau^2} \int_0^t x\,dx = \frac{t^2}{2\tau^2} e^{-t/\tau}$$

now assume $P_N = \frac{t^N}{N!\,\tau^N} e^{-t/\tau}$ then

$$P_{N+1}(t) = \int_0^t \frac{x^N}{N!\tau^N} e^{-t/\tau} \frac{dx}{\tau} e^{-\frac{(t-x)}{\tau}} = \frac{e^{-t/\tau}}{N!\,\tau^{N+1}} \int_0^t x^N dx = \frac{t^{N+1}}{(N+1)!} \frac{e^{-t/\tau}}{\tau^{N+1}}$$

hence by induction it follows that the assumed form is correct or

$$P_N(t) = \frac{t^N}{N!\,\tau^N} e^{-t/\tau} \tag{34}$$

is the probability for precisely N pulses in the time interval t. This relationship is known as Poisson's law.

For large N we may use Stirling's approximation

$N! = \sqrt{2\pi N}\, N^N e^{-N} \left(1 + \frac{1}{12N} + \cdots\right)$ whence equation (34) becomes

$$P_N(t) \approx \frac{t^N e^{N - t/\tau}}{\sqrt{2\pi N}\,(N\tau)^N} \,. \tag{35}$$

It is perhaps of some interest to note that if in addition $N \approx \bar{n} t$, we have letting $\xi = \bar{n} t - N$

$$P_N(\xi) = \frac{e^{-\frac{\xi^2}{2N}}}{\sqrt{2\pi N}} \left(1 + \frac{\xi^3}{3N^2} + \cdots\right) \tag{36}$$

which for small ξ gives essentially a Gaussian distribution.

APPENDIX IV

TABLE FOR ELECTRON MOMENTUM AS A FUNCTION OF ENERGY

When the kinetic energy W of an electron is expressed in Mev (absolute volts) the momentum $B\rho$ in gauss cm can be obtained from the expression

$$B\rho = \frac{10^4}{c}\sqrt{W(W+2m_0c^2)}$$

where m_0c^2 is the rest energy of the electron in Mev and c is the velocity of light in cm/sec. Using the atomic constant tables of DuMond and Cohen[33]

$$B\rho = \frac{10^4}{2.99776}\sqrt{W(W+1.02158)} \qquad (37)$$

The value of $B\rho$ is given in Table N for a range of energies from 0.1 to 20 Mev; the first differences are also tabulated to aid in interpolation.

Energy vs. Bρ, Table N

W (Mev)	Bρ (Gauss cm)	ΔBρ (Gauss cm)	W (Mev)	Bρ (Gauss cm)	ΔBρ (Gauss cm)
.10000	1117.2	59.7	1.050	4920.	176.
.11000	1176.9	57.8	1.100	5096.	176.
.12000	1234.7	56.1	1.150	5272.	175.
.13000	1290.8	54.4	1.200	5447.	
.14000	1345.2	53.2			348.
.15000	1398.4	52.1	1.300	5795.	347.
.16000	1450.5		1.400	6142.	346.
		100.9	1.500	6488.	344.
.18000	1551.4	97.5	1.600	6832.	343.
.20000	1648.9	94.5	1.700	7175.	343.
.22000	1743.4	92.1	1.800	7518.	342.
.24000	1835.5	90.1	1.900	7860.	341.
.26000	1925.6	88.2	2.000	8201.	
.28000	2013.8	86.7			680.
.30000	2100.5	85.2	2.200	8881.	678.
.32000	2185.7	84.0	2.400	9559.	677.
.34000	2269.7	82.9	2.600	10236.	676.
.36000	2352.6	81.9	2.800	10912.	675.
.38000	2434.5	81.0	3.000	11587.	
.40000	2515.5	80.2			1683.
.42000	2595.7	79.4	3.500	13270.	1680.
.44000	2675.1	78.8	4.000	14950.	1678.
.46000	2753.9	78.1	4.500	16628.	1676.
.48000	2832.0	77.6	5.000	18304.	1675.
.50000	2909.6	77.1	5.500	19979.	1673.
.52000	2986.7	76.5	6.000	21652.	1672.
.54000	3063.2	76.2	6.500	23324.	1673.
.56000	3139.4	75.7	7.000	24997.	1672.
.58000	3215.1	75.3	7.500	26669.	1670.
.60000	3290.4	75.0	8.000	28339.	
.62000	3365.4	74.6			3340.
.64000	3440.0	74.3	9.000	31680.	3340.
.66000	3514.3	74.0	10.000	35020.	3340.
.68000	3588.3	73.7	11.000	38360.	3340.
.70000	3662.0		12.000	41700.	3340.
		183.	13.000	45040.	3340.
.7500	3845.	182.	14.000	48380.	3330.
.8000	4027.	181.	15.000	51710.	3340.
.8500	4208.	179.	16.000	55050.	3340.
.9000	4387.	178.	17.000	58390.	3340.
.9500	4565.	178.	18.000	61730.	3330.
1.0000	4743.	177.	19.000	65060.	3340.
			20.000	68400.	3330.

$$B\rho = \frac{10^4}{2.99776}\sqrt{W(W + 1.02158)} \text{ Gauss cm}$$

APPENDIX V

THEORETICAL COMPTON DISTRIBUTION

An incident γ-ray of energy $h\nu_0$ is imagined scattered through an angle ε by a free electron and emerges with a reduced energy $h\nu_\varepsilon$. The electron recoils at an angle ω with a momentum ϕ. The scattered intensity of γ-radiation per electron I_ε (energy per unit solid angle per sec at an angle ε) is given by the Klein-Nishina formula for the Compton effect[16] as

$$\frac{I_\varepsilon}{I_0} = \frac{r_0^2}{2}\frac{1+\cos\varepsilon}{[1+\gamma(1-\cos\varepsilon)]^3}\left\{1+\frac{\gamma^2(1-\cos\varepsilon)^2}{(1+\cos^2\varepsilon)[1+\gamma(1-\cos\varepsilon)]}\right\}d\Omega \quad (38)$$

where I_0 = incident intensity (energy per/cm^{2}sec)

$r_0 = e^2/m_0c^2$

$\gamma = h\nu_0/m_0c^2$

Thus the probability that an incident quantum be scattered into a solid angle between the cone half angles ε and $\varepsilon+d\varepsilon$ is

$P(\varepsilon)d\varepsilon =$

$$2\pi\frac{r_0^2}{2}\frac{h\nu_0\,(1+\cos\varepsilon)d(\cos\varepsilon)}{h\nu_\varepsilon[1+\gamma(1-\cos\varepsilon)]^3}\left\{1+\frac{\gamma^2(1-\cos\varepsilon)^2}{(1+\cos^2\varepsilon)[1+\gamma(1-\cos\varepsilon)]}\right\} \quad (39)$$

Now since for every quantum scattered at an angle there is a recoil electron at an angle ω, we have

$$P(\varepsilon)d\varepsilon = P(\omega)d\omega \quad (40)$$

where $P(\omega)d\omega$ is the probability per incident γ quantum that a recoil electron appear within a solid angle between the cone

half angles ω and $\omega+d\omega$. It will be found useful to introduce the variable a defined as

$$a = \frac{1+\cos\varepsilon}{1-\cos\varepsilon} \quad , \quad \cos\varepsilon = \frac{a-1}{a+1} \quad . \tag{41}$$

Equation (40) may be extended then to

$$P(\varepsilon)d\varepsilon = P(\omega)d\omega = P(a)da \tag{42}$$

The equations of the conservation of momentum and energy for the Compton effect are

$$K \sin\varepsilon = p \sin\omega \tag{43}$$

$$K_0 - K\cos\varepsilon = p\cos\omega \tag{44}$$

$$K + E = K_0 + \mu \tag{45}$$

where relativistic units have been used with

$K_0 = h\nu_0$

$K_\varepsilon = h\nu_\varepsilon$

$\mu = m_0 c^2$

p = electron momentum x C

E = total electron energy.

Dividing the square of equation (43) by the square of equation (44) we have

$$\tan^2\omega = \frac{K^2\sin^2\varepsilon}{(K_0 - K\cos\varepsilon)^2} \quad , \tag{46}$$

while adding the square of these equations gives

$$p^2 = K^2 + K_0^2 - 2KK_0\cos\varepsilon \quad . \tag{47}$$

Solving equation (45) for E, squaring and using the relationship $E^2 = p^2 + \mu^2$ we have

$$p^2 = K_0^2 + K^2 - 2K_0K - 2K\mu + 2K_0\mu \quad . \tag{48}$$

Equating equations (47) and (48) gives

$$K = \frac{K_0 \mu}{\mu + K_0(1-\cos\varepsilon)} \quad . \tag{49}$$

When this equation is used to eliminate K in equation (46) after considerable simplification there results

$$(1+\gamma)^2 \tan^2 \omega = \frac{1+\cos\varepsilon}{1-\cos\varepsilon} = a \quad . \tag{50}$$

Note that

$$d(\cos\varepsilon) = \frac{2\,da}{(a+1)^2} \tag{51}$$

while using equations (49 and (41) gives

$$\frac{h\nu_0}{h\nu} = \frac{K_0}{K} = 1 + \gamma(1-\cos\varepsilon) = 1 + \frac{2\gamma}{a+1} \tag{52}$$

When equations (51), (52), and (41) are substituted into equation (39) $P(a)\,da$ as a function of a and γ may be found, thus $P(a)\,da =$

$$\frac{2\pi r_0^2}{(a+1+2\gamma)^2}\left\{1+\left(\frac{a-1}{a+1}\right)^2 + \frac{4\gamma^2}{(a+1)[a+1+2\gamma]}\right\} da \tag{53}$$

It now remains to find $\frac{d\phi}{da}$; we proceed by substituting equation (49) into equation (48) which gives after simplification

$$\phi^2 = \frac{K_0^2(1-\cos\varepsilon)}{\mu + K_0(1-\cos\varepsilon)}\left[\frac{K_0^2(1-\cos\varepsilon)}{\mu + K_0(1-\cos\varepsilon)} + 2\mu\right] .$$

Finally, if the transformation equation (41) is used to eliminate $\cos\varepsilon$ we get

$$\phi = \frac{2\gamma\mu}{(a+1+2\gamma)}\left[(\gamma+1)^2 + a\right]^{1/2} . \tag{54}$$

We note that when $a=0$, ϕ has its maximum value

$$\phi_{max} = \frac{2\gamma\mu(\gamma+1)}{2\gamma+1}$$

thus

$$\frac{\phi}{\phi_{max}} = \frac{[(\gamma+1)^2+a]^{1/2}(2\gamma+1)}{[a+1+2\gamma](\gamma+1)} = \frac{\left[1+\frac{a}{(\gamma+1)^2}\right]^{1/2}}{1+\frac{a}{1+2\gamma}} . \quad (55)$$

Differentiating equation (54) we get after simplification

$$\frac{d\phi}{da} = -\frac{(a+1+2\gamma+2\gamma^2)\gamma\mu}{(a+1+2\gamma)^2[(\gamma+1)^2+a]^{1/2}} . \quad (56)$$

In view of this equation, equation (53) becomes

$$|P(\phi)d\phi| = \frac{2\pi r_0^2[(\gamma+1)^2+a]^{1/2}}{\gamma\mu(a+1+2\gamma+2\gamma^2)}\left\{1+\left(\frac{a-1}{a+1}\right)^2+\frac{4\gamma^2}{(a+1)(a+1+2\gamma)}\right\}d\phi. \quad (57)$$

It is of importance to determine $[\cos(\theta_0+\omega)\cos(\theta_0-\omega)]^{1/2}$ as a function of θ_0, γ, and a. We have

$$[\cos(\theta_0+\omega)\cos(\theta_0-\omega)]^{1/2} = \sin\omega\sin\theta_0[\cot^2\theta_0\cot^2\omega-1]^{1/2} \quad (58)$$

The use of equations (43), (49), (50), (54), and the transformation equation (41) results in

$$[\cos(\theta_0+\omega)\cos(\theta_0-\omega)] = \sin\theta_0\frac{[(1+\gamma)^2\cot^2\theta_0-a]^{1/2}}{[(1+\gamma)^2+a]^{1/2}} . \quad (59)$$

From equation (45) we have that the incident γ-ray energy minus the kinetic energy of the recoil electron is

$$\delta = K_0-(E-\mu) = K$$

For the maximum recoil electron energy $\varepsilon = \pi$ in equation (49) hence if $\Delta = \delta_{max}$

$$\Delta = \frac{K_0}{1+2\gamma} = \frac{m_0c^2}{m_0c^2/h\nu_0+2} . \quad (60)$$

REFERENCES

1.	Deutsch, Elliott, and Evans	Rev. Sci. Inst. 15, 178 (1944).
2.	Witcher	Phys.Rev. 60, 32 (1941).
3.	Siegbahn	Phil. Mag. 37, 162 (1946).
4.	Zworykin, Morton, Ramberg, Hillier, and Vance	"Electron Optics and the Electron Microscope" (John Wiley and Sons, Inc., New York, 1945).
5.	Siegbahn	Arkiv. f. Math, Ast. Fys. 30, A No. 1 (1943).
6.	Glaser	Zeits. f. Phys. 117, 285 (1941).
7.	Eshbach	"Handbook of Engineering Fundamentals" (John Wiley and Sons, Inc., New York, 1944).
8.	Korff	"Electron and Nuclear Counters" (Van Nostrand Co., Inc., New York, 1946).
9.	Getting	Phys. Rev., 53, 103 (1938).
10.	Fry	"Probability and its Engineering Uses" (Van Nostrand Co., Inc., New York, 1928).
11.	Drude	"Theory of Optics" (Longmans, Green and Co., London, 1939).
12.	Cosslett	Rev. Sci. Inst. 17, 259 (1940).
13.	DuMond	Rev. Sci. Inst. 20, 160 (1949).
14.	Persico	Rev. Sci. Inst. 20, 191 (1949).
15.	Sauter	Ann. d. Phys. 11, 454 (1931).
16.	Heitler	"The Quantum Theory of Radiation" (Oxford University Press, London, 1947).
17.	Boltzmann	"Vorlesung uber Gas theorie" (J. Borth, Leipzig, 1923).

18.	Bothe	Zeits. f. Phys. 54, 161 (1929).
19.	Bethe, Rose, and Smith	Proc. Amer. Phil. Soc. 78, 573 (1938).
20.	Bothe	"Handbuch d Phys." Ch 1, vol. 22.2 (Edwards Bros., Ann Arbor, Mich, 1943).
21.	Kulchitsky and Latyshev	Jour. Phys. USSR 5, 249 (1941).
22.	Landau	Jour. Phys. USSR 8, 201 (1944).
23.	Bohr	Kgl. Dske. Vids. Selsk. Medd. 24, No. 19 (1948).
24.	Christy and Cohen	(to appear).
25.	White and Millington	Proc. Roy. Soc. A120, 701 (1928).
26.	Owen and Primakoff	Phys. Rev. 74, 1406 (1948).
27.	Jensen, Laslett, and Pratt	Phys. Rev. 75, 458 (1949).
28.	Lecture Series in Nuclear Physics MDDC 1175 ch. 6 (United States Atomic Energy Commission).	
29.	Ellis	Proc. Roy. Soc. A138, 318 (1932).
30.	Siegbahn	Arkiv. f. Ast. Math. Fys. 30A, No. 20 (1944).
31.	DuMond, Lind, and Watson	Phys. Rev. 73, 1392 (1948).
32.	Compton and Allison	"X-Rays in Theory and Experiment" (Van Nostrand Co., Inc., New York, 1935).
33.	DuMond and Cohen	Rev. Mod. Phys. 20, 82 (1948).
34.	Rasmussen, Lauritsen, and Lauritsen	Phys. Rev. 75, 199 (1949).
35.	Elliott and Bell	Phys. Rev. 74, 1869 (1948).
36.	Dougherty, Hornyak, Lauritsen, and Rasmussen	Phys. Rev. 74, 712 (1948).
37.	Hornyak and Lauritsen	Rev. Mod. Phys. 20, 191 (1948).

38. Van Atta and Buechner — M.I.T. Progress Reports ONR July 1, (1948).

39. Bonner, Evans, Malich, and Risser — Phys. Rev. 73, 885 (1948).

40. Cook, Langer, Price, and Sampson — Phys. Rev. 74, 502 (1948).

41. Lyman — Phys. Rev. 55, 234 (1939).

42. Townsend — Proc. Roy. Soc. A177, 357 (1941).

43. Siegbahn and Slatis — Arkiv. f. Ast. Math. Fys. 32A, No. 9 (1945).

44. Fowler, Lauritsen, and Lauritsen — Rev. Sci. Inst. 18, 818 (1947).

45. Konopinski — Rev. Mod. Phys. 15, 209 (1943).

46. Hereford — Phys. Rev. 74, 574 (1948).

47. Cohen and Hornyak — Phys. Rev. 72, 1127 (1947).

48. Barkas — Phys. Rev. 55, 691 (1939).

49. Flugge and Mattauch — Physik. Zeits. 44, 181 (1943).

50. Livingston and Bethe — Rev. Mod. Phys. 9, 326 (1937).

51. Hudspeth and Swann — Phys. Rev. 74, 1722 (1948).

52. Crane, Delsasso, Fowler, and Lauritsen — Phys. Rev. 47, 887 (1935).

53. Scherzer — "Calculation of the Third-order aberrations by the path method" in Busch and Bruche, Beitrage zur Elektronen optik (J. Barth, Leipzig, 1937).